論文 / 著書情報
Article / Book Information

題目(和文)	K中間子を用いた低エネルギーハドロン動力学におけるフレーバーSU(3) 対称性の破れの現象論的研究
Title(English)	Phenomenological study on SU(3) flavor symmetry breaking in low-energy hadron dynamics induced by kaon
著者(和文)	飯澤優太朗
Author(English)	Yutaro Iizawa
出典(和文)	学位:博士(理学), 学位授与機関:東京工業大学, 報告番号:甲第12308号, 授与年月日:2023年3月26日, 学位の種別:課程博士, 審査員:慈道 大介,伊藤 克司,関澤 一之,藤岡 宏之,須山 輝明
Citation(English)	Degree:Doctor (Science), Conferring organization: Tokyo Institute of Technology, Report number:甲第12308号, Conferred date:2023/3/26, Degree Type:Course doctor, Examiner:,,,,
学位種別(和文)	博士論文
Type(English)	Doctoral Thesis

Phenomenological study on SU(3) flavor symmetry breaking in low-energy hadron dynamics induced by kaon

(K 中間子を用いた低エネルギーハドロン動力学における
フレーバー SU(3) 対称性の破れの現象論的研究)

Yutaro Iizawa

Supervised by Prof. Daisuke Jido

Department of Physics,
School of Science,
Tokyo Institute of Technology

Abstract

In low-energy hadron physics, one can consider a global symmetry called isospin symmetry (SU(2) flavor symmetry) for the light quark sector, up and down quarks. We can also consider SU(3) flavor symmetry with the addition of further strange quarks for the light quark sector. SU(3) flavor symmetry as well as the symmetry breaking due to the difference among the quark masses are also important, and they appear in hadron phenomena. Among hadrons kaon is unique; it is a hadron that appears due to the dynamical breaking of chiral symmetry and reflects the large effect of explicit breaking of chiral symmetry due to the inclusion of the strange quark. In this dissertation, we study the flavor symmetry and its symmetry breaking phenomenologically via the hadron phenomena with strangeness induced by the kaon.

For the study of the isospin symmetry breaking, we propose to utilize the $K^- d \to \pi^- \Lambda p$ and $K^- d \to \pi^0 \Lambda n$ reactions in order to investigate the difference between the low-energy Λp and Λn scatterings. In these reactions, the Λp and Λn scatterings appear as final state interactions. The large isospin breaking in the ΛN system is proposed by the experiments of the hypernuclei. The low-energy property of Λp was studied by the $pp \to K^+ \Lambda p$ reaction, while that of the Λn has not yet been experimentally determined. We find that the ratio of the ΛN invariant mass spectra of the $K^- d \to \pi^- \Lambda p$ and $K^- d \to \pi^0 \Lambda n$ reactions is useful for studying the qualitative properties of isospin symmetry breaking in the low-energy ΛN scattering.

For the SU(3) flavor symmetry breaking, we discuss the density dependence of the chiral condensate with the strange quarks in the nuclear matter. In order to confirm the dynamical breaking of chiral symmetry, the partial restoration of the chiral symmetry in nuclear matter is investigated. The magnitude of the chiral condensate $\langle \bar{u}u + \bar{d}d \rangle$ is expected to decrease as chiral symmetry is restored in the nuclear matter. The partial restoration of the chiral symmetry in nuclear matter is confirmed by the decrease in the chiral condensate obtained experimentally through the pion-nucleus interactions, the pionic atom and the pion-nucleus scattering. For the systematic study on the partial restoration of the chiral symmetry, we derive the in-medium chiral condensate with strange components and discuss the behavior of in-medium chiral condensate with the obtained KN scattering amplitude. We obtain the KN scattering amplitude using chiral perturbation theory and the experimental data of the $K^+ N$ elastic scatterings. We propose the low-energy experiments of KN scattering in order to obtain the KN scattering amplitude more precisely and discuss the chiral condensate.

As well as the pion-nucleus interaction from the pionic atoms, the K^--nucleus interaction from kaonic atoms may be a phenomenological tool to prove the partial restoration of the chiral symmetry. A pionic atom is well-understood by theoretical and experimental studies. The fundamental π^--nucleon interaction is repulsive, and then the potential between π^- and a nucleus is also worked repulsively. Therefore the energy shift is seen repulsively in the pionic atoms. On the other hand, the K^--nucleus interaction is not as precisely understood as the pion-nucleus interaction at present. The energy shift in the kaonic atom is repulsive as well as that in the pionic atom, while the interaction between K^- and a nucleon is attractive, and the K^--nucleus potential is also attractive. We study the global feature of the K^--nucleus interaction in terms of the mechanism of the repulsive energy

shifts by the strong interaction in kaonic atoms. Naively, the effect of the level repulsion to the kaonic atom by the kaonic nuclei coupled to the atomic state yields the repulsive energy shift, however, in our study we find that the level repulsion by the nuclear bound states is not responsible for the repulsive shift and reconfirm that the imaginary part of the optical potential plays a significant role for the repulsive shift in the kaonic atom.

Through these phenomenological studies with the kaon, we conclude that a phenomenological approach to flavor symmetry and its breaking is an effective way.

Contents

List of Figures

List of Tables

Chapter 1

Introduction

One of the purposes of physics is to explore the origin of matter. Matter in this world consists of atoms, which are composed of a nucleus and elementary particles, electrons. The nucleus is made up of protons and neutrons. A proton and a neutron are composed of three quarks, which are elementary particles. The elementary particles that make up the matter at the present time, three of the four known fundamental forces (the electromagnetic, weak and strong interactions) in nature acting on them, and the elementary particles that mediate them are summarized as the Standard Model. The experimental property of elementary particles in the Standard Model is summarized in Review of Particle Physics [1] and shown in Fig. 1.1. In the Standard Model, elementary particles are quarks and leptons, which are matter particles, gauge bosons, which mediate forces, and Higgs bosons, which give particles mass. The forces in the Standard Model are electromagnetic, strong, and weak interactions. This dissertation will focus on the quarks, gluons, and hadrons composed of them that are involved in the physics of strong interaction.

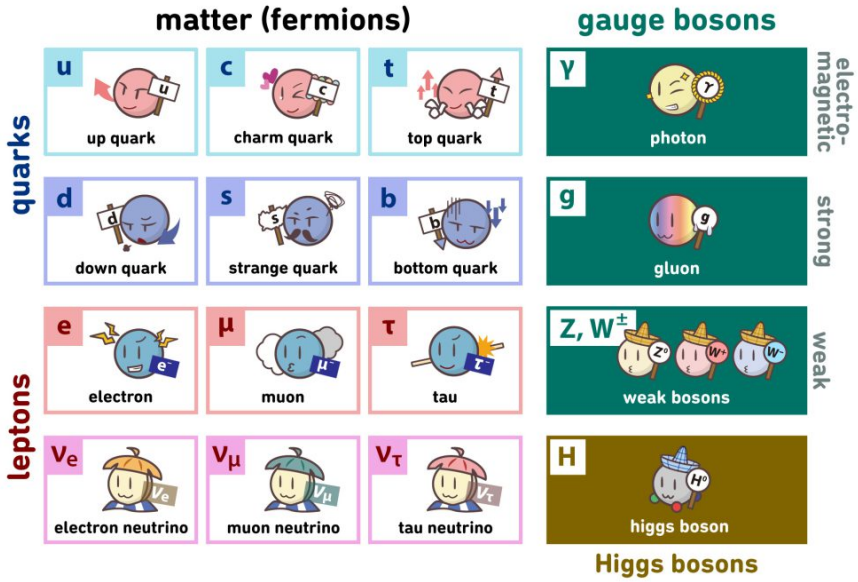

Fig.1.1 Elementary particles in the Standard Model. This figure is taken from Ref. [2].

The fundamental theory of the strong interaction is a SU(3) gauge theory called Quantum Chromo-

dynamics (QCD), in which the fundamental degrees of freedom are color-charged quarks and gluons. At high energies, the coupling constant of QCD is small enough to allow perturbation calculations and direct treatment of quarks and gluons, whereas at low energies, the coupling constant becomes large enough to make such calculations impossible. In this case, color confinement occurs and the quark-gluon exists as a combined bound state that is color-singlet. This state is the hadron, which is the fundamental degree of freedom in low-energy QCD. Although hadrons themselves are no longer the most fundamental particles in particle nuclear physics today, they are of interest as systems that reflect the non-perturbative nature of QCD in low-energy, the standard theory describing strong interactions. In other words, the study of hadrons is essential to investigate the nature of the strong interaction in low-energy, and hadron physics does just that.

The symmetries that the low-energy QCD Lagrangian possesses, such as flavor symmetry and chiral symmetry based on it, and their breaking appear in the hadron property, such as the hadron mass spectrum and interactions between hadrons. The flavor symmetry requires that strong interaction is invariant with respect to the transformation of the light quark sector, up and down quarks for flavor SU(2) (isospin symmetry), and up, down and strange quarks for flavor SU(3). SU(3) flavor symmetry is a functioning symmetry and plays an important role, for example, in the classification of baryon octet. On the other hand, the symmetry is not exact and is broken because of the large difference of the strange quark mass (94 MeV) compared to the masses of the up and down quarks (< 10 MeV). Compared to SU(3) flavor symmetry, isospin symmetry is a good symmetry. This is because the masses of both up and down quarks (~ 2 MeV and ~ 5 MeV) are significantly smaller than the typical energy scale of hadrons (~ 1 GeV) and can be considered as zero. However, it is not also an exact symmetry because there is a slight difference between them. Chiral symmetry plays an important role in low-energy QCD. Chiral symmetry is a symmetry that requires that flavor transformations can be performed independently for right- and left-handed quarks. The QCD Lagrangian has the exact chiral symmetry in the case where the current quark mass is zero. In the real world, the chiral symmetry is broken explicitly by the finite value of the current quark mass, and it is also broken spontaneously. Therefore, the QCD vacuum has a non-trivial structure that is not determined by a single point but is infinitely degenerate. The associated massless Nambu–Goldstone boson appears, but in fact the Nambu–Goldstone bosons also have nonzero mass because the current quark mass has a finite value. Among them, kaon is unique: one of Nambu–Goldstone bosons in flavor SU(3) chiral symmetry, reflects the large effect of the explicit breaking of chiral symmetry due to the inclusion of the strange quark and is a source of strangeness if used as a beam.

In this dissertation, we study the isospin symmetry breaking in the Λ-nucleon interaction, the density dependence of the chiral condensate with the strange quarks in the nuclear matter, and K^--nucleus interaction in terms of flavor symmetry breaking through each hadron reaction induced by the kaon. Each study is an independent project.

For the study of the isospin symmetry breaking in the Λ-nucleon interaction, we use $K^-d \to \pi\Lambda N$ reaction ($K^-d \to \pi^-\Lambda p$ and $K^-d \to \pi^0\Lambda n$) [3]. These are reactions of isospin partners, so if isospin symmetry holds exactly, the ratio of the cross sections of these reactions is $2:1$. The scattering amplitudes of these reactions are constructed in the same way by isospin symmetry. Isospin symmetry breaking can then be incorporated via hadronic masses and more fundamental two-body hadron

interactions appearing in the scattering amplitudes. By choosing the charge of the pion in the final-state, we can study two reactions with the same initial state K^-d, and different final states $\pi^-\Lambda p$ and $\pi^0\Lambda n$. The final-state interaction in the $K^-d \to \pi\Lambda N$ reaction involves the interaction between Λ and a nucleon N. While the scattering length of Λ-proton has been studied experimentally by the $pp \to K^+p\Lambda$ reaction [4], that of Λ-neutron has not yet been experimentally determined. Using this reaction we examine what the difference in the scattering length between Λ-proton and Λ-neutron would look like. Taking advantage of the fact that these reactions are isospin-partners, we can examine the isospin symmetry breaking in the Λ-nucleon by taking the ratio of the cross sections of the reactions.

For the study of the density dependence of the chiral condensate with the strange quarks in the nuclear matter, we use KN elastic scattering [5]. Chiral symmetry, which is dynamically broken in reality, is considered to be restored at high temperature and/or density due to the phase transition phenomena. The chiral condensate $\langle\bar{\psi}\psi\rangle$ is considered to be one of the order parameters of the spontaneous breaking of chiral symmetry, which is $\langle\bar{\psi}\psi\rangle \neq 0$ when it is spontaneously broken. The chiral symmetry is expected to move toward restoration even in finite density, though not completely, compared to the vacuum. In-medium chiral condensate of flavor SU(2), $\langle\bar{u}u + \bar{d}d\rangle$, is expected to be about 30% smaller than in vacuum at normal nuclear density. This prediction has been phenomenologically proven through hadronic phenomena such as pionic atoms [6–8], which are bound systems between a pion and a nucleus as a source of high density, and pion-nucleus scattering [9]. In our study, we focus on the in-medium chiral condensate with the strange quarks $\langle\bar{u}u + \bar{s}s\rangle$ for the systematic study of the partial restoration of chiral symmetry. The condensate with strange quarks is clearly different from SU(2) condensate $\langle\bar{u}u + \bar{d}d\rangle$. This is because nuclear matter does not contain any strange quarks, while the condensate contains strange quarks. We first derive $\langle\bar{u}u + \bar{s}s\rangle$ in the nuclear medium based on the correlation function approach [8, 10, 11] and the low-density theorem [12, 13]. Then the parameters included in the obtained formula are determined using KN elastic scattering. Once the parameters are determined, the behavior of the condensate in the nuclear matter can be obtained. Of course, it is possible to consider the chiral condensate in SU(3) flavor symmetric baryonic matter, and indeed we have included the calculations in Chapter 6.

For the study of the K^--nucleus interaction, we use a kaonic atom, which is one of the exotic atoms, and a bound state between a negatively charged kaon and a nucleus mainly by Coulomb potential but the strong force also works. A pionic atom, a bound state between a pion and a nucleus, is well-understood by theoretical and experimental studies. The fundamental π^--nucleon interaction is repulsive, and then the potential between π^- and the nucleus is also worked repulsively. Therefore the energy shift which is the correction to binding energy by Coulomb force due to strong force is seen repulsively in the pionic atom. On the other hand, the study of the kaonic atom is in progress. The energy shift in the kaonic atom is repulsive as well as that in the pionic atom, while the interaction between K^- and a nucleon is attractive, and the K^--nucleus potential is also attractive. Naively, this could be attributed to the existence of a kaonic nucleus below the energy spectrum of the kaonic atom due to attraction and the energy shift is repulsive due to its level repulsion, but on the other hand, the other mechanism is also possible: Even if the real part of the optical potential which describes the K^--nucleus interaction is attractive, if the imaginary part of it, which represents the effect of the kaon absorption to the nucleons, is large, the energy shift will be repulsive. In our study on the kaonic

atom, we focus on the mechanism of the repulsive shift induced by strong interaction in kaonic atoms.

This dissertation is based on Refs. [3, 5, 14]. The structure of this dissertation is as follows. Chapters 2 and 3 are the review part of research area. In Chapter 2, we discuss QCD which is the fundamental theory of strong interaction, its symmetries and breaking. In Chapter 3, we discuss symmetry breakings and related hadron phenomena. Chapter 4 describes theoretical tools used in this dissertation. Chapters 5 to 7 are the main results of this dissertation. In Chapter 5, we first show the theoretical formalism of the $K^- d \to \pi \Lambda N$ reaction and then perform the numerical calculations. We also take the ratio of the cross sections between $K^- d \to \pi^- \Lambda p$ and $K^- d \to \pi^0 \Lambda n$ reactions in order to discuss the isospin symmetry breaking in the low-energy Λ-nucleon scattering. Chapter 6 is devoted to the in-medium chiral condensate with the strange quarks and KN elastic scattering. Chapter 7 is devoted to the discussion of the mechanism of the repulsive energy shift in the kaonic atom. Finally, we summarize this dissertation in Chapter 8.

Chapter 2

Low-energy Quantum Chromodynamics and its symmetries

In this chapter, we give a brief overview of Quantum Chromodynamics in low-energy and related topics.

2.1 Quantum Chromodynamics

Strong interaction, one of the four fundamental forces in nature, is described by Quantum Chromodynamics (QCD). QCD is a SU(3) gauge theory with color charges as degrees of freedom. The matter fields are fermionic quarks with spin 1/2 and the gauge fields are bosonic gluons with spin 1. The quarks which correspond to the fundamental representation of SU(3) and the gluons which correspond to the adjoint representation of SU(3) have three different color charges r, b, g (anti-quarks have anti-color $\bar{r}, \bar{b}, \bar{g}$) and eight different pairs color and anti-color, respectively.

The Lagrangian of QCD is given by

$$\mathcal{L}_{\mathrm{QCD}} = -\frac{1}{4} G^a_{\mu\nu} G^{\mu\nu,a} + \sum_f \bar{q}_f (i\gamma^\mu D_\mu - m_f) q_f. \tag{2.1}$$

where q_f is the quark field and f is the quark flavor. m_f is the current quark mass of flavor f. For each flavor quark field, since quarks are the fundamental representation of $\mathrm{SU}(3)_c$, we have

$$q_f = \begin{pmatrix} q_{f,R} \\ q_{f,B} \\ q_{f,G} \end{pmatrix}. \tag{2.2}$$

$G^a_{\mu\nu}$ and D_μ are the field strength tensor and the covariant derivative defined as

$$G_{\mu\nu} = \partial_\mu A_\nu - \partial_\nu A_\mu - ig[A_\mu, A_\nu], \tag{2.3}$$
$$D_\mu = \partial_\mu - igA_\mu, \tag{2.4}$$

respectively. A^a_μ is the color SU(3) gauge field, which corresponds to the gluon fields, and g is the coupling constant between quarks and gluons.

Six flavors of quarks have been found: up, down, strange, charm, bottom, and top. Table 2.1 lists the mass, charge, and quantum number of each quark. Up, down, and strange quarks are called light quarks, and charm, bottom, and top quarks are called heavy quarks, relative to the proton mass (938

Table 2.1 Mass, charge and quantum number of each quark flavor. The quark masses of the light sector (up, down and strange) and the heavy sector (charm and bottom) are given by $\overline{\text{MS}}$ mass with the renormalization scale $\mu = 2$ GeV and with the renormalization scale $\mu = m_f$, respectively. The top quark mass here is given by an average of the top quark mass from several measurements. The values of quark masses here is taken from the 2022 version of Review of Particle Physics [1].

Flavor	Mass	Charge[e]	Quantum number
u	$2.16\ ^{+0.49}_{-0.26}$ MeV	$+2/3$	$I_z = +1/2$
d	$4.67\ ^{+0.48}_{-0.17}$ MeV	$-1/3$	$I_z = -1/2$
s	$93.4\ ^{+8.6}_{-3.4}$ MeV	$-1/3$	$S = -1$
c	1.27 ± 0.02 GeV	$+2/3$	$C = +1$
b	$4.18\ ^{+0.03}_{-0.02}$ GeV	$-1/3$	$B = -1$
t	172.69 ± 0.3 GeV	$+2/3$	$T = +1$

MeV) which is the typical scale for hadrons. Since the top quark decays by weak interaction and changes into other flavors before hadronization, only charm and bottom are actually considered when discussing the heavy quarks in the strong interaction. In this dissertation, we consider only the light quarks below.

2.2 Asymptotic freedom

In the previous section, we have introduced g as the coupling constant of QCD, but with quantum effects, the coupling constant g becomes dependent on the energy scale μ. That is, $g = g(\mu)$. Now we introduce $\alpha_s(\mu) = \frac{g^2(\mu)}{4\pi}$ as the coupling constant. The μ-dependence of $\alpha_s(\mu)$ can be computed perturbatively as

$$\mu^2 \frac{\mathrm{d}}{\mathrm{d}\mu^2}\alpha_s(\mu) = \beta(\alpha_s) = -b_0\alpha_s^2 - b_1\alpha_s^3 - \dots \tag{2.5}$$

where

$$b_0 = \frac{11 - 2N_f/3}{4\pi},\ b_1 = \frac{153 - 19N_f}{24\pi^2} \tag{2.6}$$

with N_f stands for the number of quark flavors considered here. Because of $\beta(\alpha_s) < 0$, we have $\alpha_s(\mu^2) \to 0$ together with $\mu \to \infty$. This behavior of α_s is called asymptotic freedom [15, 16]. Solving Eq. (2.5) for α_s yields

$$\alpha_s(\mu^2) = \frac{12\pi}{(33 - 2N_f)\ln\left(\mu^2/\Lambda^2_{\text{QCD}}\right)}\left[1 - \frac{6(153 - 19N_f)}{(33 - 2N_f)^2}\right]\frac{\ln\left(\ln\left(\mu^2/\Lambda^2_{\text{QCD}}\right)\right)}{\ln\left(\mu^2/\Lambda^2_{\text{QCD}}\right)} + \dots \tag{2.7}$$

where Λ_{QCD} is a parameter that stands for an energy scale that characterizes QCD and depends on N_f and a renormalization prescription. When $\overline{\text{MS}}$ scheme is used as the renormalization prescription, $\Lambda_{\text{QCD}} = (339 \pm 10)$ MeV when $N_f = 3$ (u, d, s quarks). Asymptotic freedom allows perturbation calculations to be performed for high-energy QCD, while in the low-energy region, α_s becomes large enough to make perturbation theory untenable. In the physics of strong interactions in the low-energy region treated in this dissertation, hadrons are treated as the fundamental degrees of freedom,

Table 2.2 Non-zero totally antisymmetric structure constants of SU(3)

abc	123	147	156	246	257	345	367	458	678
f^{abc}	1	$\frac{1}{2}$	$-\frac{1}{2}$	$\frac{1}{2}$	$\frac{1}{2}$	$\frac{1}{2}$	$-\frac{1}{2}$	$\frac{1}{2}\sqrt{3}$	$\frac{1}{2}\sqrt{3}$

and the interactions that appear are those between hadrons. With the increasing performance of computers, the method of numerically treating non-perturbative QCD (lattice QCD) is also a very efficient approach.

2.3 Symmetries of QCD

2.3.1 Color symmetry (SU(3) gauge symmetry)

Color symmetry is the exact and local symmetry of QCD. We confirm the invariance of QCD Lagrangian (2.1) under the $\mathrm{SU}(3)_c$ gauge transformation. The $\mathrm{SU}(3)_c$ gauge transformation to the quark, anti-quark and gluon fields is given as the following local transformation using the $\mathrm{SU}(3)_c$ unitary matrix $U(x)$ that satisfies $U(x)U^\dagger(x) = U^\dagger(x)U(x) = \mathbb{1}$ at each point in spacetime:

$$q_f(x) \to q'_f(x) = U(x)q_f(x) \equiv \exp\left[-i\sum_{a=1}^{8}\theta^a(x)\frac{\lambda^a}{2}\right]q_f(x) \tag{2.8}$$

$$\bar{q}_f(x) \to \bar{q}'_f(x) = \bar{q}_f(x)U^\dagger(x) \tag{2.9}$$

$$A_\mu(x) \to A'_\mu(x) = U(x)A_\mu(x)U^\dagger(x) - \frac{i}{g}(\partial_\mu U(x))U^\dagger(x). \tag{2.10}$$

Here λ^a, the so-called Gell-Mann matrices, is given by the following matrices:

$$\begin{aligned}
\lambda^1 &= \begin{pmatrix}0&1&0\\1&0&0\\0&0&0\end{pmatrix},\ \lambda^2 = \begin{pmatrix}0&-i&0\\i&0&0\\0&0&0\end{pmatrix},\ \lambda^3 = \begin{pmatrix}1&0&0\\0&-1&0\\0&0&0\end{pmatrix},\\
\lambda^4 &= \begin{pmatrix}0&0&1\\0&0&0\\1&0&0\end{pmatrix},\ \lambda^5 = \begin{pmatrix}0&0&-i\\0&0&0\\i&0&0\end{pmatrix},\ \lambda^6 = \begin{pmatrix}0&0&0\\0&0&1\\0&1&0\end{pmatrix},\\
\lambda^7 &= \begin{pmatrix}0&0&0\\0&0&-i\\0&i&0\end{pmatrix},\ \lambda^8 = \frac{1}{\sqrt{3}}\begin{pmatrix}1&0&0\\0&1&0\\0&0&-2\end{pmatrix},\ \lambda^0 = \sqrt{\frac{2}{3}}\begin{pmatrix}1&0&0\\0&1&0\\0&0&1\end{pmatrix}.
\end{aligned} \tag{2.11}$$

The commutation relations of the Gell-Mann matrices read

$$\left[\frac{\lambda^a}{2}, \frac{\lambda^b}{2}\right] = if^{abc}\frac{\lambda^c}{2} \tag{2.12}$$

where f^{abc} stands for the totally antisymmetric structure constants of SU(3) summarized in Table 2.2.

The anticommutation relations of the Gell-Mann matrices read

$$\left\{\frac{\lambda^a}{2}, \frac{\lambda^b}{2}\right\} = \frac{1}{3}\delta^{ab} + d^{abc}\frac{\lambda^c}{2} \tag{2.13}$$

where d^{abc} are the totally symmetric and summarized in Table 2.3.

Using Eq. (2.10), the $\mathrm{SU}(3)_c$ gauge transformation of the field strength $G_{\mu\nu}$ of the gluon fields and

Table 2.3 Non-zero totally symmetric d symbols of SU(3)

abc	118	146	157	228	247	256	338	344	355
d^{abc}	$\frac{1}{\sqrt{3}}$	$\frac{1}{2}$	$\frac{1}{2}$	$\frac{1}{\sqrt{3}}$	$-\frac{1}{2}$	$\frac{1}{2}$	$\frac{1}{\sqrt{3}}$	$\frac{1}{2}$	$\frac{1}{2}$
abc	366	377	488	558	668	778	888	000	$0ii(i \neq 0)$
d^{abc}	$-\frac{1}{2}$	$-\frac{1}{2}$	$-\frac{1}{2\sqrt{3}}$	$-\frac{1}{2\sqrt{3}}$	$-\frac{1}{2\sqrt{3}}$	$-\frac{1}{2\sqrt{3}}$	$-\frac{1}{\sqrt{3}}$	$\sqrt{\frac{2}{3}}$	$\sqrt{\frac{2}{3}}$

the covariant derivative for the quark fields $D_\mu q$ are respectively given as

$$\begin{aligned} G_{\mu\nu}(x) \to G'_{\mu\nu} &= \partial_\mu A'_\nu - \partial_\nu A'_\mu - ig\big[A'_\mu, A'_\nu\big] \\ &= \left[(\partial_\mu U)A_\nu U^\dagger + U(\partial_\mu A_\nu)U^\dagger + UA_\nu(\partial_\mu U^\dagger) - \frac{i}{g}\big[(\partial_\mu\partial_\nu U)U^\dagger + (\partial_\nu U)(\partial_\mu U^\dagger)\big]\right] \\ &- \left[(\partial_\nu U)A_\mu U^\dagger + U(\partial_\nu A_\mu)U^\dagger + UA_\mu(\partial_\nu U^\dagger) - \frac{i}{g}\big[(\partial_\nu\partial_\mu U)U^\dagger + (\partial_\mu U)(\partial_\nu U^\dagger)\big]\right] \\ &- ig\left[\left(UA_\mu U^\dagger - \frac{i}{g}(\partial_\mu U)U^\dagger\right), \left(UA_\nu U^\dagger - \frac{i}{g}(\partial_\nu U)U^\dagger\right)\right] \\ &= U[\partial_\mu A_\nu - \partial_\nu A_\mu - ig[A_\mu, A_\nu]]U^\dagger = U(x)G_{\mu\nu}(x)U^\dagger(x) \end{aligned} \tag{2.14}$$

$$\begin{aligned} D_\mu q(x) \to D'_\mu q'(x) = (\partial_\mu - igA'_\mu(x))q'(x) &= \left[\partial_\mu - ig\left(UA_\mu U^\dagger - \frac{i}{g}(\partial_\mu U)U^\dagger\right)\right]Uq \\ &= (\partial_\mu U)q + U(\partial_\mu q) - igUA_\mu q - (\partial_\mu U)q = U(\partial_\mu - igA_\mu)q \\ &= U(x)D_\mu q(x) \end{aligned} \tag{2.15}$$

where we use $U(\partial_\mu U^\dagger) = -(\partial_\mu U)U^\dagger$ which is derived by the unitarity of $U(x)$.

Finally we confirm that $\mathcal{L}_{\rm QCD}$ is invariant under the SU(3)$_c$ gauge transformation:

$$\mathcal{L}_{\rm QCD} \to \mathcal{L}'_{\rm QCD} = -\frac{1}{4}UG^a_{\mu\nu}U^\dagger UG^{\mu\nu,a}U^\dagger + \sum_f \bar{q}_f U^\dagger(i\gamma^\mu UD_\mu - m_f)q_f = \mathcal{L}_{\rm QCD}. \tag{2.16}$$

2.3.2 Flavor symmetry

Isospin symmetry

Isospin which was first introduced by Heisenberg [17] is a quantum number of the nucleon for the internal degree of freedom. The proton and neutron have different electroweak interactions but have almost the same mass. Thus the proton and neutron are regarded as different internal states (isospin) of the same particle called a nucleon denoted as N, and the proton and neutron are given isospin up and down directions, respectively. Namely, it is expressed as

$$N = \begin{pmatrix} p \\ n \end{pmatrix}. \tag{2.17}$$

This is an analogy for the spin of the electron. In QCD, the isospin is understood as the role of up and down quarks. SU(2) flavor symmetry or simply isospin symmetry is a symmetry with respect to rotation in isospin space and is a global SU(2) symmetry that mixes two flavors of quarks, up and down. Thus, assigning u and d quarks to the isospin 1/2 representation, it is expressed as

$$q = \begin{pmatrix} u \\ d \end{pmatrix} \to U\begin{pmatrix} u \\ d \end{pmatrix} \equiv e^{i\theta^a \frac{\tau^a}{2}}\begin{pmatrix} u \\ d \end{pmatrix} \tag{2.18}$$

where U is the isospin transformation matrix with the Pauli matrices τ^a. The masses of up and down quarks are very small relative to the nucleon mass which is the typical hadron scale and then can be considered as zero. Therefore, while the isospin symmetry is not exact, it is a very good symmetry. For example, the masses of the isospin doublet of the nucleon, and the masses of the isospin triplet of the pion are nearly equal, respectively.

Charge symmetry and charge independence are also presented in relation to the isospin symmetry. These are symmetries for the nucleons and nuclei and nuclear forces. Charge symmetry is defined as the invariance under the rotation by π about the y axis in isospin space, a symmetry that is narrower than isospin symmetry. Charge independence stands for the invariance in general transformations in isospin space. Charge symmetry yields the consequence that replacing all the protons and neutrons in a nucleus with neutrons and protons, or in QCD terms, replacing all the up and down quarks with each other, results in a little change in the observed value. For example, the excited states of mirror nuclei have the same energy level and spin-parity assignment.

SU(3) flavor symmetry

SU(3) flavor symmetry or simply flavor symmetry is a symmetry that extends the isospin symmetry to SU(3) to include strange quark in addition to up and down quarks as the light quarks as

$$q = \begin{pmatrix} u \\ d \\ s \end{pmatrix} \to U \begin{pmatrix} u \\ d \\ s \end{pmatrix} \equiv e^{i\theta^a \frac{\lambda^a}{2}} \begin{pmatrix} u \\ d \\ s \end{pmatrix} \tag{2.19}$$

where U is the flavor transformation matrix. The flavor symmetry is justified because the mass of the strange quark is smaller than that of the nucleon, whereas the symmetry breaking is considered to be greater than the isospin symmetry because it is heavier than that of the up and down quarks. The flavor symmetry and its breaking appear in the hadron mass spectrum and the hadron-hadron interaction as well as the isospin symmetry. The well-known examples are the classification of the pseudoscalar meson flavor octet, the $1/2^+$ baryon flavor octet shown in Fig. 2.1 and summarized in Table 2.4, and Gell-Mann–Okubo mass formula [18, 19]. Gell-Mann–Okubo mass formula shows that taking the SU(3) breaking up to the first-order perturbation of the strange quark mass and estimating the symmetry breaking effect in the hadron mass relates the hadron masses in the same representation, such as baryon octet:

$$\underbrace{M_\Sigma - M_N}_{\sim 254\ \text{MeV}} = \underbrace{\frac{1}{2}(M_\Xi - M_N) + \frac{3}{4}(M_\Sigma - M_\Lambda)}_{\sim 247\ \text{MeV}}. \tag{2.20}$$

Thus, although SU(3) flavor symmetry is broken by the large mass of the strange quark (~ 100 MeV), it is worth considering, and the effects of the breaking can be perturbatively incorporated into the discussion.

The chiral symmetry discussed in the next section is based on isospin or flavor symmetry.

Table 2.4 Mass and the quantum number of pseudoscalar meson octet and $1/2^+$ baryon octet. The values of hadron masses here are isospin-averaged values. Note that one strange quark is counted with strangeness -1, one anti-strange quark with strangeness $+1$.

Hadron	Mass	Isospin	Strangeness
π (π^-, π^0, π^+)	138 MeV	1	0
K (K^0, K^+)	496 MeV	1/2	$+1$
$\bar{K}$ $(K^-, \bar{K})$	496 MeV	1/2	-1
η	548 MeV	0	0
N (p, n)	939 MeV	1/2	0
Λ	1116 MeV	0	-1
Σ $(\Sigma^-, \Sigma^0, \Sigma^+)$	1193 MeV	1	-1
Ξ (Ξ^-, Ξ^0)	1318 MeV	1/2	-2

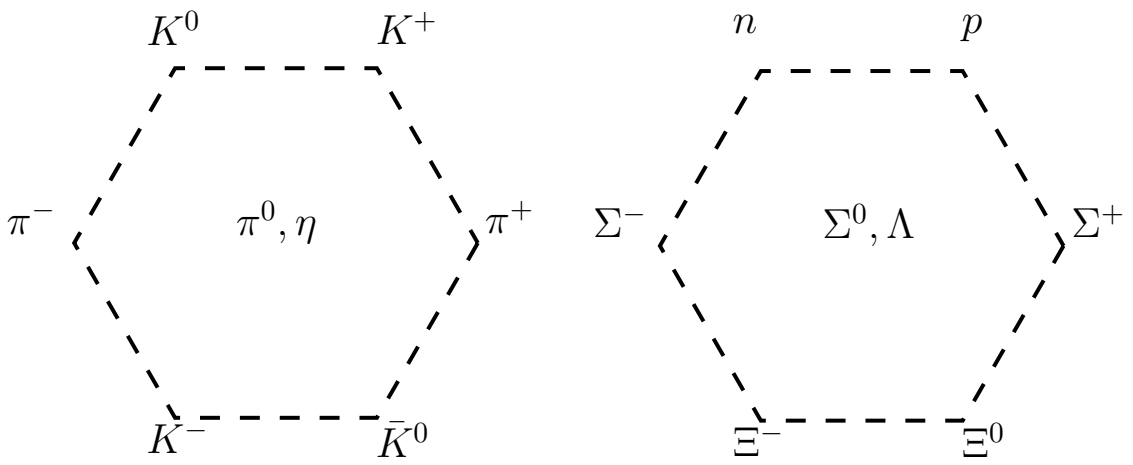

Pseudoscalar meson octet $1/2^+$ baryon octet

Fig.2.1 Pseudoscalar meson flavor octet and $1/2^+$ baryon flavor octet.

2.3.3 Chiral symmetry

We define chirality in order to discuss chiral symmetry. In general, the state with the eigenvalue -1 of γ_5 is called the left-handed and the state with eigenvalue $+1$ is called the right-handed for Dirac particles. The eigenvalue of γ_5 is called chirality. For the massless fermions or the fermions at the high-energy limit where mass is negligible, chirality matches helicity.

Projection operators with chirality of -1 (left-handed) and $+1$ (right-handed) are defined as

$$P_L \equiv \frac{1}{2}(\mathbb{1} - \gamma_5), \qquad P_R \equiv \frac{1}{2}(\mathbb{1} + \gamma_5), \tag{2.21}$$

respectively. Projection operators (2.21) satisfy the following relations:

$$P_L + P_R = \mathbb{1} \tag{2.22}$$

$$P_L^2 = \frac{1}{4}(\mathbb{1} - \gamma_5)^2 = \frac{1}{4}(2\mathbb{1} - 2\gamma_5) = P_L \tag{2.23}$$

$$P_R^2 = \frac{1}{4}(\mathbb{1} + \gamma_5)^2 = \frac{1}{4}(2\mathbb{1} + 2\gamma_5) = P_R \tag{2.24}$$

$$P_L P_R = P_R P_L = \frac{1}{2}(\mathbb{1} - \gamma_5)\frac{1}{2}(\mathbb{1} + \gamma_5) = \frac{1}{4}(\mathbb{1} - \gamma_5^2) = 0 \tag{2.25}$$

Now we define the left-handed quark field q_L and the right-handed quark field q_R by using the projection operators (2.21) as

$$q_L = P_L q, \qquad q_R = P_R q. \tag{2.26}$$

Confirm that they are the eigenstates of γ_5:

$$\gamma_5 q_L = \frac{1}{2}(\gamma_5 - \gamma_5^2)q = -\frac{1}{2}(\mathbb{1} - \gamma_5)q = -q_L \tag{2.27}$$

$$\gamma_5 q_R = \frac{1}{2}(\gamma_5 + \gamma_5^2)q = \frac{1}{2}(\mathbb{1} + \gamma_5)q = q_R. \tag{2.28}$$

Rewriting the quark field part of the QCD Lagrangian $\mathcal{L}_{\rm QCD}$, $\mathcal{L}^q_{\rm QCD}$ using q_L and q_R, we obtain

$$\begin{aligned}\mathcal{L}^q_{\rm QCD} &= \bar{q}(i\gamma^\mu D_\mu - \mathcal{M})q = \bar{q}(P_L + P_R)(i\gamma^\mu D_\mu - \mathcal{M})(P_L + P_R)q \\ &= \bar{q}_L(i\gamma^\mu D_\mu)q_L + \bar{q}_R(i\gamma^\mu D_\mu)q_R - \bar{q}_L\mathcal{M}q_R - \bar{q}_R\mathcal{M}q_L\end{aligned} \tag{2.29}$$

where $\mathcal{M}$ denotes the $\mathrm{SU}(3)_f$ quark mass matrix given as

$$\mathcal{M} = \begin{pmatrix} m_u & & \\ & m_d & \\ & & m_s \end{pmatrix} \tag{2.30}$$

with m_u, m_d and m_s denoting up, down and strange quark mass, respectively. As seen in Eq. (2.29), the kinetic term is split into the left- and right-handed, while the mass term is a mixture of the left- and right-handed. Namely, under the limit that quark mass is taken to zero (chiral limit), the QCD Lagrangian is invariant under the following independent flavor transformations discussed in the previous section for the left and right components, since the mass term vanishes, as

$$q_L \to U_L q_L, \qquad U_L = \exp\left(i\theta_L^a \frac{\lambda^a}{2}\right) \in \mathrm{SU}(3)_L, \tag{2.31}$$

$$q_R \to U_R q_R, \qquad U_R = \exp\left(i\theta_R^a \frac{\lambda^a}{2}\right) \in \mathrm{SU}(3)_R. \tag{2.32}$$

This invariance of the QCD Lagrangian under $\mathrm{SU}(3)_L \times \mathrm{SU}(3)_R$ is called chiral symmetry. The QCD Lagrangian is said to have chiral symmetry when the Lagrangian is invariant under chiral transformation. Actually, the quark masses are non-zero, then chiral symmetry is not exact symmetry. However given that the quark masses are sufficiently small compared with the proton mass, chiral symmetry serves well as a starting point for a discussion on the low-energy QCD, and furthermore, the effects of breaking by the finite quark mass can be introduced as we will see in the next chapter.

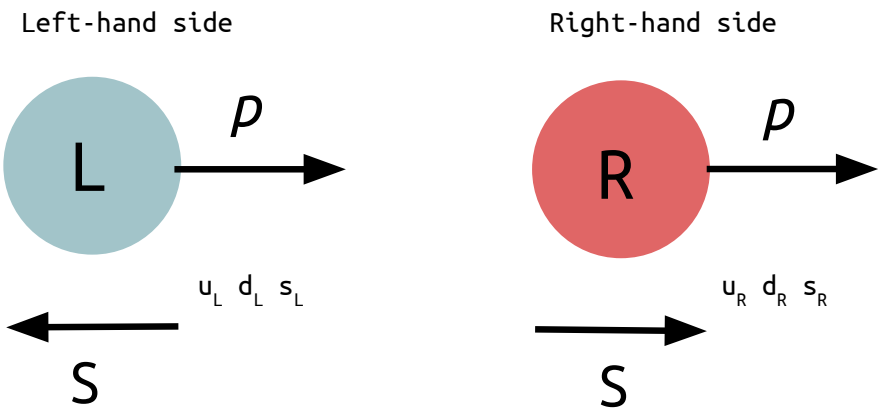

Fig.2.2 A schematic figure of the chiral transformation.

2.3.4 Noether's theorem

Let us introduce Noether's theorem in order to discuss the current and charge of the chiral symmetry. Noether's theorem states that if the Lagrangian is invariant under some continuous symmetry, then the currents associated with that symmetry exist and are conserved when the equation of motion derived from the Lagrangian is satisfied. In the following, we see Noether's theorem specifically.

We assume that the Lagrangian is written as the functional in terms of the n-independent fields ϕ_i and their derivatives $\partial_\mu \phi_i$ with $i = 1, 2, \ldots n$ as

$$\mathcal{L} = \mathcal{L}(\phi, \partial_\mu \phi). \tag{2.33}$$

The equations of motion is derived by the Lagrangian as

$$\frac{\partial \mathcal{L}}{\partial \phi_i} - \partial_\mu \frac{\partial \mathcal{L}}{\partial(\partial_\mu \phi_i)} = 0, \ \ i = 1, 2, \ldots n. \tag{2.34}$$

We assume that Eq. (2.33) is invariant under the transformation

$$\phi_i \to \phi_i' = U\phi_i \equiv e^{i\theta^a T^a} \tag{2.35}$$

with the real parameter $\theta^a = \theta^a(x)$ and the generator of the transformation T^a. The infinitesimal transformation of the fields is given by

$$\delta\phi_i = \phi_i' - \phi_i = i\theta^a T^a_{ij} \phi_j, \tag{2.36}$$

and its derivative is

$$\partial^\mu \delta\phi_i = iT^a_{ij} \partial^\mu(\theta^a \phi_j), \tag{2.37}$$

The variation of the Lagrangian is

$$\begin{aligned}
\delta\mathcal{L} &= \mathcal{L}(\phi', \partial_\mu\phi') - \mathcal{L}(\phi, \partial_\mu\phi) \\
&= \frac{\partial\mathcal{L}}{\partial\phi_i}\delta\phi_i + \frac{\partial\mathcal{L}}{\partial(\partial_\mu\phi_i)}\delta(\partial_\mu\phi_i) \\
&= \frac{\partial\mathcal{L}}{\partial\phi_i} i\theta^a T^a_{ij}\phi_j + \frac{\partial\mathcal{L}}{\partial(\partial_\mu\phi_i)} i(\partial_\mu\theta^a T^a_{ij}\phi_j) \\
&= \theta^a\left[i\frac{\partial\mathcal{L}}{\partial\phi_i}T^a_{ij}\phi_j + i\frac{\partial\mathcal{L}}{\partial(\partial_\mu\phi_i)}T^a_{ij}\partial_\mu\phi_j\right] + \partial_\mu\theta^a\left[i\frac{\partial\mathcal{L}}{\partial(\partial_\mu\phi_i)}T^a_{ij}\phi_j\right] \\
&\equiv \theta^a\partial_\mu J^\mu_a + (\partial_\mu\theta^a)J^\mu_a
\end{aligned} \tag{2.38}$$

where the so-called Noether's current J^μ_a is defined as

$$J^\mu_a \equiv i\frac{\partial\mathcal{L}}{\partial(\partial_\mu\phi_i)}T^a_{ij}\phi_j. \tag{2.39}$$

Taking the divergence of J^μ_a, we have

$$\begin{aligned}
\partial_\mu J^\mu_a &= \partial_\mu\frac{\partial\mathcal{L}}{\partial(\partial_\mu\phi_i)}T^a_{ij}\phi_j + i\frac{\partial\mathcal{L}}{\partial(\partial_\mu\phi_i)}T^a_{ij}\partial_\mu\phi_j \\
&= i\frac{\partial\mathcal{L}}{\partial\phi_i}T^a_{ij}\phi_j + i\frac{\partial\mathcal{L}}{\partial(\partial_\mu\phi_i)}T^a_{ij}\partial_\mu\phi_j
\end{aligned} \tag{2.40}$$

where we use the equations of motion. This is consistent with Eq. (2.38). From Eq. (2.38), we can derive the current and its derivative easily (the method of Gell-Mann and Lévy [20]):

$$J^\mu_a = \frac{\partial\mathcal{L}}{\partial(\partial_\mu\theta^a)}, \qquad \partial_\mu J^\mu_a = \frac{\partial\mathcal{L}}{\partial\theta^a}. \tag{2.41}$$

In the case of the global symmetry, the term $\partial_\mu\theta^a$ vanishes and the current J^a_μ conserved:

$$\partial^\mu J^a_\mu = 0. \tag{2.42}$$

2.3.5 Chiral algebra

Considering the infinitesimal transformation of the chiral symmetry given by

$$q_L \to \left(\mathbb{1} + i\theta^a_L\frac{\lambda^a}{2}\right)q_L, \qquad q_R \to \left(\mathbb{1} + i\theta^a_R\frac{\lambda^a}{2}\right)q_R, \tag{2.43}$$

we apply the method of Gell-Mann and Lévy discussed in the previous section and calculate the Noether's currents for each transformation as

$$L^a_\mu = \bar{q}_L\gamma_\mu\frac{\lambda^a}{2}q_L, \qquad \partial^\mu L^a_\mu = 0, \tag{2.44a}$$

$$R^a_\mu = \bar{q}_R\gamma_\mu\frac{\lambda^a}{2}q_R, \qquad \partial^\mu R^a_\mu = 0 \tag{2.44b}$$

Noether's charges corresponding to each transformation is calculated as

$$Q^a_L = \int \mathrm{d}^3x\, L^a_{\mu=0} = \int \mathrm{d}^3x\, \bar{q}_L\gamma_0\frac{\lambda^a}{2}q_L, \qquad \frac{\mathrm{d}Q^a_L}{\mathrm{d}t} = 0, \tag{2.45a}$$

$$Q^a_R = \int \mathrm{d}^3x\, R^a_{\mu=0} = \int \mathrm{d}^3x\, \bar{q}_R\gamma_0\frac{\lambda^a}{2}q_R, \qquad \frac{\mathrm{d}Q^a_L}{\mathrm{d}t} = 0. \tag{2.45b}$$

These charges satisfy the Lie algebra of SU(3) as follows

$$\left[Q_L^a, Q_L^b\right] = if^{abc}Q_L^c, \tag{2.46a}$$
$$\left[Q_R^a, Q_R^b\right] = if^{abc}Q_R^c, \tag{2.46b}$$
$$\left[Q_L^a, Q_R^b\right] = 0. \tag{2.46c}$$

Chiral transformations can be rewritten as a vector transformation with $\theta_V = \theta_L = \theta_R$ and an axial-vector transformations with $\theta_A = -\theta_L = \theta_R$ given by

$$q \to U_V q, \qquad U_V = \exp\left(i\theta_V^a \frac{\lambda^a}{2}\right), \tag{2.47a}$$
$$q \to U_A q, \qquad U_A = \exp\left(i\theta_A^a \gamma_5 \frac{\lambda^a}{2}\right), \tag{2.47b}$$

respectively. The currents associated with the transformations are obtained as

$$V_\mu^a = L_\mu^a + R_\mu^a = \bar{q}\gamma_\mu \frac{\lambda^a}{2} q, \qquad \partial^\mu V_\mu^a = 0, \tag{2.48a}$$
$$A_\mu^a = -L_\mu^a + R_\mu^a = \bar{q}\gamma_\mu\gamma_5 \frac{\lambda^a}{2} q, \qquad \partial^\mu A_\mu^a = 0, \tag{2.48b}$$

respectively.

The corresponding conserved charges are given by

$$Q_V^a = Q_L^a + Q_R^a = \int \mathrm{d}^3x\, \bar{q}\gamma_0 \frac{\lambda^a}{2} q, \tag{2.49a}$$
$$Q_A^a = -Q_L^a + Q_R^a = \int \mathrm{d}^3x\, \bar{q}\gamma_0\gamma_5 \frac{\lambda^a}{2} q. \tag{2.49b}$$

Considering Eq. (2.46c), we derive the commutation relations to Q_V^a and Q_A^a as

$$\left[Q_V^a, Q_V^b\right] = if^{abc}Q_V^c, \tag{2.50a}$$
$$\left[Q_A^a, Q_A^b\right] = if^{abc}Q_V^c, \tag{2.50b}$$
$$\left[Q_V^a, Q_A^b\right] = if^{abc}Q_A^c. \tag{2.50c}$$

These relations indicate that the algebra is closed under the vector transformation but not closed under the axial-vector transformation. Therefore the vector transformation forms a group, while axial transformation does not.

For the next section, we construct the scalar and pseudoscalar fields from the quark fields as

$$\phi^a = \bar{q}\lambda^a q \tag{2.51}$$
$$P^a = \bar{q}i\gamma_5\lambda^a q = i(\bar{q}_L\lambda^a q_R - \bar{q}_R\lambda^a q_L) \tag{2.52}$$

with $a = 0, 1, 2, \ldots, 8$, respectively.

We see how these composite fields are transformed by the vector and axial-vector transformations:

$$\left[Q_V^a, \phi^0\right] = 0 \tag{2.53}$$
$$\left[Q_V^a, \phi^b\right] = if^{abc}\phi^c, \ b = 1, 2, \ldots, 8 \tag{2.54}$$
$$\left[Q_V^a, P^0\right] = 0 \tag{2.55}$$
$$\left[Q_V^a, P^b\right] = if^{abc}P^c, \ b = 1, 2, \ldots, 8 \tag{2.56}$$

for the vector transformation and

$$\left[Q_A^a, \phi^0\right] = i\sqrt{\frac{2}{3}}P^a \tag{2.57}$$

$$\left[Q_A^a, \phi^b\right] = i\delta^{ab}\sqrt{\frac{2}{3}}P^0 + id^{abc}P^c,\ b = 1, 2, \ldots, 8 \tag{2.58}$$

$$\left[Q_A^a, P^0\right] = -i\sqrt{\frac{2}{3}}S^a \tag{2.59}$$

$$\left[Q_A^a, P^b\right] = -i\delta^{ab}\sqrt{\frac{2}{3}}\phi^0 - id^{abc}\phi^c,\ b = 1, 2, \ldots, 8 \tag{2.60}$$

for the axial-vector transformation. We can see that the axial-vector transformation is the parity transformation. This indicates that π, which couples with P^a, and σ, which couples with ϕ^0, are transferred to each other in the axial transformation. The hadrons that transfer to each other in the axial transformation are called chiral partners. As we will see later, under the chiral symmetry, the chiral partners are degenerate. In particular, choosing certain values for a and b yields the following equation:

$$\begin{aligned}
i[Q_A^1, P^1(0)] &= i[Q_A^2, P^2(0)] = i[Q_A^3, P^3(0)] \\
&= \sqrt{\frac{2}{3}}\phi^0(0) + d^{118}\phi^8(0) \\
&= \sqrt{\frac{2}{3}}\sqrt{\frac{2}{3}}(\bar{u}u + \bar{d}d + \bar{s}s) + \frac{1}{\sqrt{3}}\frac{1}{\sqrt{3}}(\bar{u}u + \bar{d}d - 2\bar{s}s) \\
&= \bar{u}u + \bar{d}d, \qquad (2.61a) \\
i[Q_A^4, P^4(0)] &= i[Q_A^5, P^5(0)] \\
&= \sqrt{\frac{2}{3}}\phi^0(0) + d^{443}\phi^3(0) + d^{448}\phi^8(0) \\
&= \sqrt{\frac{2}{3}}\sqrt{\frac{2}{3}}(\bar{u}u + \bar{d}d + \bar{s}s) + \frac{1}{2}(\bar{u}u - \bar{d}d) + (-\frac{1}{2\sqrt{3}})\frac{1}{\sqrt{3}}(\bar{u}u + \bar{d}d - 2\bar{s}s) \\
&= \frac{2}{3}(\bar{u}u + \bar{d}d + \bar{s}s) + \frac{1}{2}(\bar{u}u - \bar{d}d) - \frac{1}{6}(\bar{u}u + \bar{d}d - 2\bar{s}s) \\
&= \bar{u}u + \bar{s}s, \qquad (2.61b) \\
i[Q_A^6, P^6(0)] &= i[Q_A^7, P^7(0)] \\
&= \bar{d}d + \bar{s}s. \\
i[Q_A^8, P^8(0)] &= \frac{2}{3}(\bar{u}u + \bar{d}d + \bar{s}s) - \frac{1}{3}(\bar{u}u + \bar{d}d - 2\bar{s}s) \\
&= \frac{1}{3}\big(\bar{u}u + \bar{d}d + 4\bar{s}s\big). \qquad (2.61c)
\end{aligned}$$

We shall write these commutation relations notationally as

$$[Q_A^a, P^a(0)] = -i\left[\bar{\psi}\psi\right]^a. \tag{2.62}$$

2.4 Chiral symmetry breaking

2.4.1 Explicit breaking of chiral symmetry

In the previous chapter, we discussed the chiral symmetry under the chiral limit. In reality, however, the quark masses are finite. Therefore, the chiral symmetry is explicitly broken. Next, let us consider

the case of a finite quark mass. If the quark masses are equal (SU(3) limit), the Lagrangian is invariant under the vector transformations. Thus isospin symmetry for up and down quarks holds well, and flavor symmetry with the addition of strange quarks also holds approximately. On the other hand, if the quark mass is finite, the Lagrangian is not invariant under axial transformations. The infinitesimal axial-vector transformation is given by

$$q \to \left(\mathbb{1} + i\theta_A^a \frac{\lambda^a}{2}\gamma_5\right) q. \tag{2.63}$$

The variation of the mass term of QCD Lagrangian which break the chiral symmetry explicitly is calculated as

$$\delta\mathcal{L}_{\mathrm{QCD}} = i\theta_A^a \bar{q}\gamma_5 \left\{\mathcal{M}, \frac{\lambda^a}{2}\right\} q. \tag{2.64}$$

The divergence of the axial-vector current is given by

$$\partial^\mu A_\mu^a = i\bar{q}\gamma_5 \left\{\mathcal{M}, \frac{\lambda^a}{2}\right\} q, \tag{2.65}$$

or explicitly, setting $m = (m_u + m_d)/2 = m_s$, we have

$$\partial^\mu A_\mu^1 = i\bar{q}\gamma^5 \left\{\mathcal{M}, \frac{\lambda^1}{2}\right\} q = im\bar{q}\gamma^5\lambda^1 q = mP^1, \tag{2.66a}$$

$$\partial^\mu A_\mu^2 = i\bar{q}\gamma^5 \left\{\mathcal{M}, \frac{\lambda 2}{2}\right\} q = im\bar{q}\gamma^5\lambda^2 q = mP^2, \tag{2.66b}$$

$$\partial^\mu A_\mu^3 = i\bar{q}\gamma^5 \left\{\mathcal{M}, \frac{\lambda^3}{2}\right\} q = im\bar{q}\gamma^5\lambda^3 q = mP^3, \tag{2.66c}$$

$$\partial^\mu A_\mu^4 = i\bar{q}\gamma^5 \left\{\mathcal{M}, \frac{\lambda^4}{2}\right\} q = i\frac{m+m_s}{2}\bar{q}\gamma^5\lambda^4 q = \frac{m+m_s}{2}P^4, \tag{2.66d}$$

$$\partial^\mu A_\mu^5 = i\bar{q}\gamma^5 \left\{\mathcal{M}, \frac{\lambda^5}{2}\right\} q = i\frac{m+m_s}{2}\bar{q}\gamma^5\lambda^5 q = \frac{m+m_s}{2}P^5, \tag{2.66e}$$

$$\partial^\mu A_\mu^6 = i\bar{q}\gamma^5 \left\{\mathcal{M}, \frac{\lambda^6}{2}\right\} q = i\frac{m+m_s}{2}\bar{q}\gamma^5\lambda^6 q = \frac{m+m_s}{2}P^6, \tag{2.66f}$$

$$\partial^\mu A_\mu^7 = i\bar{q}\gamma^5 \left\{\mathcal{M}, \frac{\lambda^7}{2}\right\} q = i\frac{m+m_s}{2}\bar{q}\gamma^5\lambda^7 q = \frac{m+m_s}{2}P^7, \tag{2.66g}$$

$$\partial^\mu A_\mu^8 = i\bar{q}\gamma^5 \left\{\mathcal{M}, \frac{\lambda^8}{2}\right\} q = i\frac{m+2m_s}{3}\bar{q}\gamma^5\lambda^8 q = \frac{m+2m_s}{3}P^8. \tag{2.66h}$$

These equations are written collectively as follows:

$$\partial^\mu A_\mu^a = m^a P^a \tag{2.67}$$

with $m^{a=1\sim3} = m$, $m^{a=4\sim7} = (m+m_s)/2$ and $m^8 = (m+2m_s)/3$.

This equation is called the PCAC (partially conserved axial current) relation. When the quark mass is zero, the axial current is conserved, but even when the quark mass is non-zero, if the quark mass is sufficiently small, the chiral symmetry is still realized with breaking, and the explicit breaking is determined by Eq. (2.65). Flavor indices $a = 1 \sim 3$ are related to the pions, $a = 4$ and 5 are related to the kaons, $a = 6$ and 7 are related to the anti-kaon, and $a = 8$ is related to the octet component of the eta meson η_8, respectively. The eighth PCAC is modified as follows to include the zeroth component due to the ideal mixing induced by SU(3) flavor symmetry breaking, $m \neq m_s$:

$$\partial^\mu A_\mu^8 = \frac{m+2m_s}{3}P^8 + \frac{\sqrt{2}(m-m_s)}{3}P^0. \tag{2.68}$$

This mixes η_0 and η_8 in the ideal mixing. In the actual η and η', the η_0-η_8 mixing is suppressed due to $\mathrm{U}_A(1)$ anomaly, then we have $\eta \sim \eta_8$ identified as one of Nambu–Goldstone bosons and $\eta' \sim \eta_0$ which failed to become Nambu–Goldstone boson. In this dissertation, we do not treat the η' meson and do not mention $\mathrm{U}_A(1)$ anomaly anymore.

2.4.2 Dynamical breaking of chiral symmetry

In this section, we see that the chiral symmetry is spontaneously broken. Considering the charge Q_A^a of the axial vector transformation and the QCD vacuum $|0\rangle$, either of the following two is realized:

- Wigner–Weyl phase: chiral symmetry holds

$$Q_A^a |0\rangle = 0 \ \forall a \tag{2.69}$$

- Nambu–Goldstone phase: chiral symmetry is broken

$$Q_A^a |0\rangle \neq 0 \ \exists a \tag{2.70}$$

The latter case is not an accurate way to write it, and Q_A^a cannot be defined such that it satisfies the Wigner–Weyl phase.

In the case of the Wigner–Weyl phase, the chiral condensate is zero because we have

$$\langle 0| \left[Q_A^a, P^b\right] |0\rangle = \langle 0| \left(Q_A^a P^b - P^b Q_A^a\right) |0\rangle = i \langle 0| \left[\bar{\psi}\psi\right]^a |0\rangle = 0. \tag{2.71}$$

Moreover, if chiral symmetry holds, the parity partners of hadrons, which are called chiral partners, should be degenerate. This can be shown as follows. We introduce two states A and B:

$$|A\rangle = a^\dagger |0\rangle , \qquad |B\rangle = b^\dagger |0\rangle \tag{2.72}$$

where $a^\dagger$ and $b^\dagger$ are the creation operators for the state A and B, respectively. Suppose $a^\dagger$ and $b^\dagger$ belong to the same irreducible representation of as chiral symmetry, we have

$$\left[Q_A^a, a^\dagger\right] = b^\dagger \tag{2.73}$$

then

$$\begin{aligned} Q_A^a |A\rangle &= Q_A^a a^\dagger |0\rangle \\ &= a^\dagger Q_A^a |0\rangle + b^\dagger |0\rangle |0\rangle \\ &= |B\rangle \end{aligned} \tag{2.74}$$

where we use Eq. (2.69). Under the exact chiral symmetry, the Noether's charge of the axial-transformation Q_A^a exchanges with the QCD Hamiltonian H_{QCD}:

$$[Q_A^a, H_{\mathrm{QCD}}] = 0. \tag{2.75}$$

Thus the energy of B state E_B coincides with that of A state E_A:

$$\begin{aligned} E_B &= \langle B| H_{\mathrm{QCD}} |B\rangle \\ &= \langle B| H_{\mathrm{QCD}} Q_A^a |A\rangle \\ &= \langle B| Q_A^a H_{\mathrm{QCD}} |A\rangle \\ &= \langle A| H_{\mathrm{QCD}} |A\rangle \\ &= E_A. \end{aligned} \tag{2.76}$$

Therefore the chiral partners, such as π and σ, should be degenerate under the chiral symmetry. However, it is known that $\langle 0|\,\bar{\psi}\psi\,|0\rangle \neq 0$ for the real vacuum of QCD. This means that Eq. (2.90) is taken as the real vacuum of QCD, and the symmetry of the axial-vector transformation is broken spontaneously. On the other hand, the vector transformation is not. That is,

$$\mathrm{SU}(3)_L \times \mathrm{SU}(3)_R \to \mathrm{SU}(3)_V, \tag{2.77}$$

and then the chiral partners in the real world are not degenerate: a pseudoscalar meson π (~ 140 MeV) and a scalar meson σ ($400 - 550$ MeV) [*1]; a vector meson ρ (~ 770 MeV) and an axial-vector meson a_1 (~ 1260 MeV) as examples. As a result of the dynamical breaking of chiral symmetry, the Nambu–Goldstone bosons which have very light masses compared with other hadrons appear. Nambu–Goldstone theorem, which explains this mechanism, will be discussed next section.

2.5 Nambu–Goldstone theorem in QCD

We introduce the correlation functions between the axial-vector current $A^a_\mu(x)$ and the pseudoscalar field $P^a(x)$, and two pseudoscalar fields given by

$$\Pi^{ab}_{5\mu}(x,0) \equiv \langle 0|\,\mathbf{T}\big[A^a_\mu(x)P^b(0)\big]\,|0\rangle\,, \tag{2.78}$$
$$\Pi^{ab}(x,0) \equiv \langle 0|\,\mathbf{T}\big[P^a(x)P^b(0)\big]\,|0\rangle\,, \tag{2.79}$$
$$\Pi^{ab}_{5}(x,0) \equiv \partial^\mu\Pi^{ab}_{5\mu}(x,0) = \partial^\mu\,\langle 0|\,\mathbf{T}\big[A^a_\mu(x)P^b(0)\big]\,|0\rangle \tag{2.80}$$

where $\mathbf{T}$ denotes the time-ordered product and $|0\rangle$ represents the vacuum state. Taking the divergence of the operator part in Eq. (2.79), we have

$$\begin{aligned}
\partial^\mu\mathbf{T}\big[A^a_\mu(x)P^b(0)\big] &= \partial^\mu[\theta(x_0)A^a_\mu(x)P^b(0) + \theta(-x_0)P^b(0)A^a_\mu(x)] \\
&= \delta(x_0)\big[A^a_0(x)P^b(0) - P^b(0)A^a_0(x)\big] \\
&+ \big[\theta(x_0)(\partial^\mu A^a_\mu(x))P^b(0) + \theta(-x_0)P^b(0)(\partial^\mu A^a_\mu(x)\big] \\
&= \mathbf{T}\big[\partial^\mu A^a_\mu(x)P^b(0)\big] + \delta(x_0)\big[A^a_0(x), P^b(0)\big].
\end{aligned} \tag{2.81a}$$

This identity Eq. (2.81) is called the chiral Ward identity. Performing Fourier transformations to the momentum space (denoted by q) for Eq. (2.81) with the chiral Ward identity, we have

$$\begin{aligned}
\Pi^{ab}_5(q) &= \int \mathrm{d}^4x\, e^{iqx}\partial^\mu\Pi^{ab}_{5\mu}(x,0) \\
&= \int \mathrm{d}^4x\, e^{iqx}\partial^\mu\,\langle 0|\,\mathbf{T}\big[A^a_\mu(x)P^b(0)\big]\,|0\rangle \\
&= \int \mathrm{d}^4x\, e^{iqx}\,\langle 0|\,\big(\mathbf{T}\big[\partial^\mu A^a_\mu(x)P^b(0)\big] + \delta(x_0)\big[A^a_0(x), P^b(0)\big]\big)\,|0\rangle
\end{aligned} \tag{2.82}$$

[*1] The mass is taken from that of $f_0(500)$.

Taking the chiral limit and the soft limit $q_\mu \to 0$, we obtain

$$\begin{aligned}\lim_{q_\mu\to 0}\Pi_5^{ab}(q) &= \lim_{q_\mu\to 0}\int d^4x e^{iqx}\delta(x_0)\left\langle 0\right|\left[A_0^a(x),P^b(0)\right]\left|0\right\rangle \\ &= \lim_{q_\mu\to 0}\int \mathrm{d}^3x\, e^{-i\boldsymbol{q}\cdot\boldsymbol{x}}\left\langle 0\right|\left[A_0^a(0,\boldsymbol{x}),P^b(0)\right]\left|0\right\rangle \\ &= \left\langle 0\right|\left[\int \mathrm{d}^3x\, A_0^a(0,\boldsymbol{x}),P^b(0)\right]\left|0\right\rangle \\ &= \left\langle 0\right|\left[Q_A^a(0),P^b(0)\right]\left|0\right\rangle \\ &= -i\delta^{ab}\left\langle 0\right|\left[\bar{\psi}\psi\right]^b\left|0\right\rangle . \end{aligned} \tag{2.83}$$

Eq. (2.83) is known as one of the QCD identities. Here $\left[\bar{\psi}\psi\right]^a$ is given in Eq. (2.62).

Next performing the partial integration for the correlation function $\Pi_5^{ab}(q)$, we have

$$\begin{aligned}\Pi_5^{ab}(q) &= -iq^\mu\int \mathrm{d}^4x\, e^{iqx}\left\langle 0\right|T[A_\mu^a(x)P^b(0)]\left|0\right\rangle \\ &= -iq^\mu\Pi_{5\mu}^{ab}(q). \end{aligned} \tag{2.84}$$

We insert a complete set of hadronic states labeled as h given as

$$\mathbb{1} = \sum_h\int\frac{\mathrm{d}^3p_h}{2E_h(2\pi)^3}\left|h(p_h)\right\rangle\left\langle h(p_h)\right| \tag{2.85}$$

where $p_h = (E_h, \boldsymbol{p_h})$ is the four-momentum for the intermediate hadron h with the energy $E_h = \sqrt{M_h^2+E_h^2}$ into $\Pi_{5\mu}^{ab}(x,0)$ as

$$\begin{aligned}\Pi_{5\mu}^{ab}(x,0) &= \left\langle 0\right|T[A_\mu^a(x)P^b(0)]\left|0\right\rangle \\ &= \sum_h\int\frac{\mathrm{d}^3p_h}{2E_h(2\pi)^3}\big[\theta(x_0)\left\langle 0\right|A_\mu^a(x)\left|h(p_h)\right\rangle\left\langle h(p_h)\right|P^b(0)\left|0\right\rangle \\ &+ \theta(-x_0)\left\langle 0\right|P^b(0)\left|h(p_h)\right\rangle\left\langle h(p_h)\right|A_\mu^a(x)\left|0\right\rangle\big]. \end{aligned} \tag{2.86}$$

Since the operator P^b is the pseudoscalar operator with the same quantum number as the pseudoscalar states, the only state that this operator can couple to are the pseudoscalar states. Therefore the hadrons propagating the correlation function are pions and their excited states for the case of flavor SU(2), and pions, kaons and an eta meson and their excited states for the case of flavor SU(3). Then we have $\left|h(p_h)\right\rangle \to \left|h^a(p_h)\right\rangle$. The coupling constants between the state $\left|h^a(p_h)\right\rangle$ and the operators $P^a(x)$, and $A_\mu^a(x)$ are G_h and F_h, respectively. The pseudoscalar matrix element and the axial-vector matrix element are given by

$$\left\langle 0\right|P^a(x)\left|h^b(p_h)\right\rangle = \delta^{ab}G_he^{-ip_hx}, \tag{2.87}$$

$$\left\langle 0\right|A_\mu^a(x)\left|h^b(p_h)\right\rangle = \delta^{ab}iq_\mu F_he^{-ip_hx}. \tag{2.88}$$

The decomposition of the correlation function into each state using these matrix elements gives

$$\Pi_5^{ab}(q) = i\delta^{ab}\sum_h F_hG_h\frac{q^2}{q^2-M_h^2+i\epsilon}. \tag{2.89}$$

Taking soft limit $q_\mu \to 0$ for Eq. (2.89) and comparing Eq. (2.83), we have

$$\lim_{q_\mu\to 0} i\delta^{ab}\sum_h F_hG_h\frac{q^2}{q^2-M_h^2+i\epsilon} = -i\delta^{ab}\left\langle 0\right|\left[\bar{\psi}\psi\right]^b\left|0\right\rangle \tag{2.90}$$

We find that the left side of Eq. (2.90) converges to zero when $M_h \neq 0$ and has a finite value when $M_h = 0$. As mentioned in the previous section, the right side of Eq. (2.90) has a finite value when the dynamical breaking of chiral symmetry (DBχS) is spontaneously broken, there must always be a hadronic massless mode, which must be coupled to the axial-vector current. This massless particle is called the Nambu–Goldstone boson (NG boson). The number of NG bosons when the symmetry breaks corresponds to the number of generators for the broken symmetry. This is Nambu–Goldstone theorem. Three pseudoscalar mesons, $\pi_0,\ \pi^{\pm}$ in flavor SU(2) and eight pseudoscalar mesons, $\pi_0,\ \pi^{\pm},\ K^{\pm},\ K_0,\ \bar{K}_0,\ \eta$ in flavor SU(3), are considered as NG bosons. These hadrons have finite masses due to the explicit breaking of chiral symmetry, but they are less massive than the typical scale for the hadrons. Therefore they are identified as NG bosons associated with the dynamical breaking of chiral symmetry. As a result of considering the explicit breaking by finite quark masses, a relation can be established between physical quantities of quarks and these of hadrons. An example of this statement is the Gell-Mann–Oakes–Renner relation, which we will see next section.

2.6 Gell-Mann–Oakes–Renner relation

Since NG bosons labeled as Φ here are the pseudoscalar meson, they couple to the operators $P^a(x)$ and $A^a_\mu(x)$ as follows

$$\langle 0|\, P^a(x)\, |\Phi^b(p)\rangle = \delta^{ab} G_\Phi e^{-ipx},\ \langle 0|\, A^a_\mu(x)\, |\Phi^b(p)\rangle = \delta^{ab} i p_\mu F_\Phi e^{-ipx} \tag{2.91}$$

Here G_Φ and F_Φ are the coupling constants identified as the wavefunction renormalization and the decay constant for each NG boson, respectively. Now we use the PCAC relation Eq. (2.65):

$$\partial^\mu A^a_\mu = m^a P^a. \tag{2.92}$$

Both sides are sandwiched by the vacuum $\langle 0|$ and the intermediate NG boson state $|\Phi^b_5(p)\rangle$. The left-hand side is

$$\langle 0|\, \partial^\mu A^a_\mu\, |\Phi^b_5(p)\rangle = \delta^{ab} i p_\mu F_\Phi \partial^\mu e^{-ipx} = \delta^{ab} p^2 F_\Phi e^{-ipx} = \delta^{ab} M^2_\Phi F_\Phi e^{-ipx} \tag{2.93}$$

with the mass of NG boson $M_\Phi \neq 0$. The right-hand side is

$$m^a \langle 0|\, P^a\, |\Phi^b(p)\rangle = \delta^{ab} m^a G_\Phi e^{-ipx}. \tag{2.94}$$

Therefore we have

$$M^2_\Phi F_\Phi = m^a G_\Phi. \tag{2.95}$$

From Eq. (2.90), when the vacuum spontaneously breaks the chiral symmetry, we have

$$F_\Phi G_\Phi = -\langle 0|\, \bar{\psi}\psi\, |0\rangle\,. \tag{2.96}$$

This is Glashow–Weinberg relation [21]. Using Eqs. (2.95) and (2.96) to eliminate Z_ψ yields Gell-Mann–Oakes–Renner relation [22] as

$$M^2_\Phi F^2_\Phi = -m^a \langle 0|\, \bar{\psi}\psi\, |0\rangle \equiv -m^a \langle \bar{\psi}\psi\rangle \tag{2.97}$$

or explicitly,

$$M_\pi^2 F_\pi^2 = -m \left\langle \bar{u}u + \bar{d}d \right\rangle , \tag{2.98a}$$

$$M_K^2 F_K^2 = -\frac{m + m_s}{2} \left\langle \bar{u}u + \bar{s}s \right\rangle , \tag{2.98b}$$

$$M_{\eta_8}^2 F_{\eta_8}^2 = -\frac{m + 2m_s}{3} \frac{1}{3} \left\langle \bar{u}u + \bar{d}d + 4\bar{s}s \right\rangle \tag{2.98c}$$

where M_π and F_π, M_K and F_K, and M_{η_8} and F_{η_8} are the mass and the decay constant of the pion, the kaon, and the η_8, respectively. In the η_8-η_0 mixing due to $m \neq m_s$, the Gell-Mann–Oakes–Renner relation for the eta meson is modified as

$$M_\eta^2 F_\eta^2 = -\frac{m}{3} \left\langle \bar{u}u + \bar{d}d \right\rangle - \frac{4m_s}{3} \left\langle \bar{s}s \right\rangle \tag{2.99}$$

with the eta meson mass M_η and the decay constant of the eta meson F_η.

The Gell-Mann–Oakes–Renner relation relates the chiral condensate $\left\langle \bar{\psi}\psi \right\rangle$, which is not a direct observable, to physical quantities in hadrons, M_Φ and F_Φ, which are observables. Estimating the values of the in-vacuum chiral condensates with Eq. (2.98) yields

$$\left\langle \bar{u}u \right\rangle_0 \simeq \left\langle \bar{d}d \right\rangle_0 \sim -(288 \text{ MeV})^3 \tag{2.100a}$$

with $m = (m_u + m_d)/2 = 3.4$ MeV and $m_s = 93$ MeV. The subscript 0 stands for the in-vacuum value. The in-vacuum chiral condensates estimated by the lattice QCD [23] are given as

$$\left\langle \bar{u}u \right\rangle_0 \simeq \left\langle \bar{d}d \right\rangle_0 \sim -(283(2) \text{ MeV})^3 \tag{2.101a}$$

in the $\overline{\text{MS}}$ scheme at a renormalization scale of 2 GeV.

Chapter 3

Symmetry breaking and hadron phenomena

In this chapter, we show the symmetry breakings of QCD and the hadron reactions to study them.

3.1 Isospin symmetry breaking in hadron interaction

Isospin symmetry discussed in Section 2.3.2 comes from the fact that the electric charges are less relevant for the strong interaction. Due to the difference between the masses of up and down quarks, the isospin symmetry is broken. The effect of the breaking appears in the hadron masses such as the masses of proton and neutron, and the hadron-hadron interaction.

3.1.1 Isospin symmetry breaking in nucleon system

Thanks to the charge symmetry or, more generally, the isospin symmetry, the properties of nuclei and the nuclear force are very similar when all the protons and neutrons are replaced with neutrons and protons, respectively.

The breaking effect in the nuclei is seen in the mirror nuclei, for example, ^{3}H and ^{3}He. The binding energy of ^{3}H is 0.071 MeV deeper than that of ^{3}He after correcting the electromagnetic effects[*1] [24].

Another example we discuss here is the $I = 1$ nucleon-nucleon scattering length. The scattering amplitude f in the low energy is characterized by the scattering length a and effective range r in the effective range expansion of the S-wave phase shift $\delta(p)$ as follows:

$$f = \frac{1}{p\cot\delta(p) - ip} = \frac{1}{-\frac{1}{a} + \frac{1}{2}rp^2 + \mathcal{O}(p^4) - ip} \tag{3.1}$$

where p denotes the momentum of the nucleon in the center-of-mass frame. By our definition, the scattering length has a positive (negative) sign for repulsive (attractive) interaction. The experimentally obtained a and r parameters of the $I = 1$ nucleon-nucleon scattering correcting the electro-magnetic effects [25] are

$$\begin{aligned} a_{pp} &= -17.3 \text{ fm}, & r_{pp} &= 2.85 \text{ fm}, \\ a_{nn} &= -18.9 \text{ fm}, & r_{nn} &= 2.75 \text{ fm}, \\ a_{np} &= -23.7 \text{ fm}, & r_{np} &= 2.77 \text{ fm}. \end{aligned}$$

[*1] Including the electromagnetic effects, the difference is 0.7 − MeV

These are close values, which is one of evidence that the isospin symmetry is working. The difference of a_{pp} and a_{nn} is 1.6 fm due to charge symmetry breaking. Similarly, looking at the difference between a_{np} and $a_{nn}(a_{pp})$, 5.6 fm, this is due to the charge independence breaking. According to Ref. [25], the difference between a_{pp} and a_{nn} is caused by nucleon mass-splitting in two-pions exchange and pion and ρ meson-exchange contributions. As for the difference between a_{np} and $a_{nn}(a_{pp})$, the mass-splitting of the charged pion and the neutral pion scattering is a source of it. The reaction calculation of $\gamma d \to \pi^+ nn$ is performed to extract more precise a_{nn} and r_{nn} experimentally [26].

3.1.2 Isospin symmetry breaking in Λ-nucleon interaction and $K^- d \to \pi\Lambda N$ reaction

Λ-nucleon interaction

When the charge symmetry is extended to hyperon systems, the Λp and Λn scatterings are charge symmetric partners since the Λ baryon has $I = 0$. In the ΛN system, the charge symmetry coincidences with the isospin symmetry since the isospin of the ΛN system is 1/2. Isospin symmetry breaking in the ΛN system appears as a difference between the Λp and Λn interactions. Recently, a large isospin symmetry breaking effect has been suggested by experimental analysis for the $A = 4$ mirror hypernuclei, which are nuclei including the hyperon [27, 28]. From the experiments data, one finds the difference of the excitation energies from the 0^+ ground state to the 1^+ excited state of ${}^4_\Lambda$H and ${}^4_\Lambda$He to be 0.3 MeV, which is much larger than the binding energy difference of ^{3}H and ^{3}He, 0.071 MeV. The excitation energies of the first 1^+ states are different by 0.3 MeV between ${}^4_\Lambda$H and ${}^4_\Lambda$He (both the ground states have 0^+), while the difference between nuclear systems ^{3}H and ^{3}He is just 0.071 MeV after correcting the electromagnetic effects [24]. Namely, ${}^4_\Lambda$He has more binding energy of Λ than ${}^4_\Lambda$H. Thus, a large difference between the Λp and Λn interactions could be expected. It is the scattering length and effective range that determine the interaction in the low-energy region. The scattering length $a_{\Lambda p}$ and effective range $r_{\Lambda p}$ for Λp scattering were determined experimentally by analyzing the Λp final state interaction in the $pp \to K^+\Lambda p$ reaction [4] and their values were determined as

$$a^s_{\Lambda p} = -2.43^{+0.16}_{-0.25}\ \text{fm}, \qquad r^s_{\Lambda p} = 2.21^{+0.16}_{-0.36}\ \text{fm} \tag{3.2}$$

for the spin-singlet channel, and

$$a^t_{\Lambda p} = -1.56^{+0.19}_{-0.22}\ \text{fm}, \qquad r^t_{\Lambda p} = 3.7^{+0.6}_{-0.6}\ \text{fm} \tag{3.3}$$

for the spin-triplet channel. On the other hand, the low-energy Λn scattering parameters have not yet been experimentally determined due to the neutral system. Therefore, it is necessary to check whether isospin symmetry breaking in the ΛN interaction is significant, and it is important to know the direction of isospin symmetry breaking.

For theoretical approaches on the ΛN interaction, several phenomenological investigations of the ΛN interaction have been performed by using boson-exchange models (Nijmegen [29–31], Jülich [32–34] and Ehime [35, 36]), quark models [37–39], and hybrid model known as Kyoto-Niigata [40]. Effective field theory approaches also have investigated the ΛN interactions based on the flavor SU(3) chiral symmetry [41–51]. Among them the isospin symmetry breaking in the ΛN interactions was investigated in Ref. [51], giving a difference of the ΛN scattering lengths $\Delta a^{\rm ISB} \equiv a_{\Lambda p} - a_{\Lambda n}$ of 0.62 ± 0.08 fm for the spin-singlet state and -0.10 ± 0.02 fm for the spin-triplet state. Thus, the symmetry breaking

effect is calculated to be small compared with the nucleon-nucleon system. That is why it would be interesting if we find experimentally large symmetry breaking in the ΛN system, and even if not, a more precise description of the ΛN system is important for a precise discussion of hypernuclei.

$K^- d \to \pi\Lambda N$ reaction

In Chapter 5, we will propose the $K^- d \to \pi\Lambda N$ reaction in order to see the isospin symmetry breaking in Λ-nucleon scattering length by using the final state interaction of the $K^- d \to \pi\Lambda N$ reaction.

The $K^- d \to \pi^- \Lambda p$ reaction has been studied to investigate the Λp scattering and also the ΣN interaction with kaons at rest [52, 53] and in-flight [54–57]. There are many theoretical calculations of this reaction with kaons at rest so far [58–69]. Some of these works have mainly concerned a possible bound state below the ΣN threshold by considering Σ-Λ conversion in the intermediate states. Thus the nature of this reaction at the threshold ΣN was interesting.

Here, focusing on the Λp and Λn interactions, we revisit this reaction based on the formulation developed in Refs. [70–73] by using modern meson-baryon $\bar{K}N \to MB$ scattering amplitudes obtained by the chiral unitary approach [74–80] and introducing isospin symmetry breaking in the ΛN interaction and the scattering amplitudes. We include the kaon rescattering diagram together with the quasi-free production of the Λ baryon, which are the main sources of the background. By taking the cross section ratio of these two reactions based on isospin symmetrically constructed theory, we will study how the isospin symmetry breaking effects appear in the scattering parameters of the ΛN interaction.

3.2 Partial restoration of chiral symmetry in nuclei and exotic atom

3.2.1 Partial restoration of chiral symmetry in nuclei

We have seen in the previous chapter that the dynamical breaking of chiral symmetry results in massless Nambu–Goldstone bosons, non-zero chiral condensate in-vacuum, and that the Gell-Mann–Oakes–Renner relation is valid because of the explicit breaking of the chiral symmetry due to the non-zero quark mass. The dynamical breaking of chiral symmetry (DBχS) is considered to be a phase transition phenomenon. Thus the chiral condensate is one of the order parameters for DBχS. As the environment, here temperature T and density ρ, changes, the magnitude of the chiral condensate changes as

$$T,\ \rho \to \infty \Longrightarrow \left|\langle \bar{\psi}\psi \rangle\right| \to 0. \tag{3.4}$$

Therefore the chiral symmetry is expected to be restored by increasing the temperature T and the density ρ.

Chiral symmetry is thought to be incompletely restored or partially restored in finite densities such as nuclei, if not in high density. Taking in-medium chiral condensate

$$\left\langle \bar{u}u + \bar{d}d \right\rangle^* \equiv \langle \Omega | \, \bar{u}u + \bar{d}d \, | \Omega \rangle \tag{3.5}$$

with the in-medium grand state $|\Omega\rangle$ to the first order of nuclear density ρ_N under the low-density

approximation, we have

$$\left\langle \bar{u}u + \bar{d}d \right\rangle^* = \left\langle \bar{u}u + \bar{d}d \right\rangle + \left\langle N \right| \bar{u}u + \bar{d}d \left| N \right\rangle \rho_N. \tag{3.6}$$

Using πN sigma term [81]

$$\sigma_{\pi N} \equiv m \left\langle N \right| \bar{u}u + \bar{d}d \left| N \right\rangle \simeq 40 \sim 60 \text{ MeV} \tag{3.7}$$

and the Gell-Mann–Oakes–Renner relation (2.97), we obtain

$$\left\langle \bar{u}u + \bar{d}d \right\rangle^* = \left(1 - \frac{\sigma_{\pi N}}{M_\pi^2 F_\pi^2} \rho_N \right) \left\langle \bar{u}u + \bar{d}d \right\rangle_0 . \tag{3.8}$$

With the equation Eq. (3.8), the in-medium chiral condensate $\left\langle \bar{u}u + \bar{d}d \right\rangle^*$ at normal nuclear density $\rho_0 = 0.17$ fm^{-3} is expected to decrease by 30-40% compared with in-vacuum condensate $\left\langle \bar{u}u + \bar{d}d \right\rangle_0$. If there is a physical quantity of a hadron that is closely related to the chiral symmetry, we can experimentally study its change in the nuclear medium by binding and scattering nuclei and the hadron. If the physical quantity is changed in finite density compared with in-vacuum, then we have experimentally proved that the chiral symmetry is partially restored in finite density. In particular, pion and kaon, which are the Nambu-Goldstone bosons associated with the dynamical breaking of chiral symmetry, are expected to be susceptible to the partial restoration of the chiral symmetry. Beyond the linear density approximation has been calculated for in-medium chiral condensate by in-medium chiral perturbation theory [10, 11, 82]. These references show that up to normal nuclear density, the effect of nonlinear density is not very large and the effect of linear density is dominant. For pion in nuclei, it is confirmed that the chiral symmetry is recovered by about 30% in the nucleus by studies on the deeply bound pionic atom which shows the change in the value of in-medium pion decay constant F_π^* changes compared with the value of in-vacuum pion decay constant F_π, and the Gell-Mann–Oakes–Renner relation Eq. (2.97).

3.2.2 Pionic atom

The constituent particles of an atom, such as electrons and nuclei, are replaced by another particle with the same charge, which is called an exotic atom. The exotic atom, like a pionic atom, is bound by electromagnetic interactions to form an atomic state. For hydrogen-like (exotic) atoms, the Bohr radius a_B is inversely proportional to the reduced mass of the system μ as

$$a_B = \frac{\hbar c}{Z \alpha \mu c^2} \tag{3.9}$$

with the proton number Z.

The pionic atom is a system of negatively charged pion π^- bound to a nucleus and is a type of exotic atom. The π^--nucleon interaction is repulsive and therefore the π^--nucleus interaction is also considered to be repulsive. The π^--nucleus interaction is described as an optical potential, which is a complex potential with an imaginary part representing the pion absorption into the nucleus. The π^--nucleus optical potential consists of an S-wave component U_s and a P-wave component U_p, of which the S-wave component U_s is given as

$$U_s(r) = -\frac{2\pi}{M_\pi} \left[\left(1 + \frac{M_\pi}{M_N} \right) (b_0^* \rho_N(r) + b_1^* \delta\rho(r) + \left(1 + \frac{M_\pi}{2M_N} \right) B_0 \rho_N^2(r)) \right] \tag{3.10}$$

where $\rho_N = \rho_n + \rho_p$ and $\delta\rho = \rho_n - \rho_p$ are the nuclear density which is the sum of the neutron density ρ_n and the proton density ρ_p, and the difference between ρ_n and ρ_p, respectively. b_0^* and b_1^* stand for the isoscalar and isovector pion-nucleus scattering lengths, respectively. B_0 is the complex parameter that represents the absorption effect.

The pion-nuclear isovector scattering length b_1^* is associated with the chiral condensate in the medium as follows [7]. Firstly, the Gell-Mann-Oakes-Renner relation is valid in the nuclear medium under the low-density approximation [83] as

$$M_\pi^{*2} F_\pi^{*2} = -m \left\langle \bar{u}u + \bar{d}d \right\rangle^* . \tag{3.11}$$

Taking the ratio to the Gell-Mann-Oakes-Renner equation in-vacuum, we obtain

$$\frac{\left\langle \bar{u}u + \bar{d}d \right\rangle^*}{\left\langle \bar{u}u + \bar{d}d \right\rangle_0} = \frac{M_\pi^{*2}}{M_\pi{}^2} \frac{F_\pi^{*2}}{F_\pi{}^2} \simeq 1.04 \, \frac{F_\pi^{*2}}{F_\pi{}^2} \tag{3.12}$$

where we use the in-medium pion mass $M_\pi^* \sim M_\pi + 3$ MeV [83–85].

Next, we use the Weinberg-Tomozawa relation. The in-vacuum Weinberg-Tomozawa relation [86, 87] is given by

$$b_1 = -\frac{1}{4\pi\epsilon_1} \frac{M_\pi}{2F_\pi^2} \tag{3.13}$$

with $\epsilon_1 = 1 + M_\pi/M_N = 1.149$. According to Refs.[7, 8], the Weinberg-Tomozawa relation is extended to the nuclear matter as

$$b_1^*(\rho_N) = -\frac{1}{4\pi\epsilon_1} \frac{M_\pi}{2F_\pi^{*2}}. \tag{3.14}$$

Taking the ration between the isovector scattering length of pion-nucleus $b_1^*(\rho_N)$ and that of pion-nucleon b_1, we have

$$\frac{b_1}{b_1^*} \simeq \frac{F_\pi^{*2}}{F_\pi{}^2}. \tag{3.15}$$

Then we obtain

$$\frac{\left\langle \bar{u}u + \bar{d}d \right\rangle^*}{\left\langle \bar{u}u + \bar{d}d \right\rangle_0} \simeq 1.04 \, \frac{b_1}{b_1^*}. \tag{3.16}$$

From Eq. (3.16), the density dependence of the chiral condensate, a non-observable quantity, can be evaluated from the pion-nucleus isovector scattering length b_1^*, which is an observed quantity obtained by the precise measurement of the pion-nucleus system.

The ratio between b_1 and b_1^* was determined from the experiment on deeply bound states of the pionic atoms using Sn nuclei [6]. They reported

$$\frac{b_1}{b_1^*(\rho_N = 0.6\rho_0)} = 0.78 \pm 0.05. \tag{3.17}$$

An analysis of the $\pi^\pm$-nucleus scattering also gave a similar result for b_1^* [9]. Extrapolating this formula to $\rho_N = \rho_0$ under the assumption of the linear density approximation, they found that the chiral condensate is reduced by about 33% at the normal nuclear density ρ_0. This reproduced the

value of 30-40% expected in Section 3.2.1 and the experiment quantitatively showed that the chiral symmetry was partially restored.

Another calculation for the pion-nuclear isovector scattering and the chiral condensate is reported by Ref. [8]. The model-independent relation under the chiral limit is derived as

$$\frac{\langle \bar{u}u + \bar{d}d \rangle^*}{\langle \bar{u}u + \bar{d}d \rangle_0} \simeq Z_\pi^{*1/2} \left(\frac{b_1}{b_1^*} \right)^{1/2} \tag{3.18}$$

where $Z_\pi^{*1/2}$ the wavefunction renormalization of the pion in nuclear matter given by

$$Z_\pi^{*1/2} = 1 - \gamma \frac{\rho_N}{\rho_0} \tag{3.19}$$

with $\gamma \simeq 0.184$ estimated from the in-vacuum πN scattering amplitude. This analysis also gave the result that the chiral condensate was reduced by about 30% at the normal nuclear density ρ_0.

3.2.3 In-medium chiral condensate with strange quarks and KN elastic scattering

In-medium chiral condensate strange quarks

From a systematic point of view, we can also consider the chiral condensate with strange quarks in the nuclear matter $\langle \bar{u}u + \bar{s}s \rangle^*$. Here we assume the isospin symmetry. The chiral condensate contains strange quark components, whereas the nuclear matter does not contain any strange quarks, so the condensate breaks SU(3) flavor symmetry. As with $\langle \bar{u}u + \bar{d}d \rangle^*$ discussed in Section 3.2.1, the theoretical calculation for the low-density relation of $\langle \bar{u}u + \bar{s}s \rangle^*$ is first performed, and then the parameters included in the relation are estimated from experimental data as well as the $\sigma_{\pi N}$ term.

In Chapter 6, we will derive in-medium chiral condensate with strange quarks using the correlation function approach [10, 11, 70] and the low-density theorem [12, 13]. Details are given in Chapter 6, but as a result, the in-medium chiral condensate with strange quarks is expressed in terms of the KN scattering amplitude T_{KN} in the soft limit. In order to take the soft limit for the KN scattering amplitude, we employ the flavor SU(3) chiral perturbation theory. The in-medium condensate is obtained as a quantity including the low-energy constants (LECs) in the flavor SU(3) chiral perturbation theory as parameters [5, 88]

$$\frac{\langle \bar{u}u + \bar{s}s \rangle^*}{\langle \bar{u}u + \bar{s}s \rangle_0} = 1 + \frac{(3b^{I=1} + b^{I=0})}{F_K^2} \rho_N \tag{3.20}$$

with $b^{I=1} = b_0 + b_D$ and $b^{I=0} = b_0 - b_F$ where b_0, b_D and b_F are the LECs of the next-to-leading order of SU(3) chiral perturbation theory in Eq. (4.49).

KN elastic scattering

Just as πN scattering was used to study the behavior of $\langle \bar{u}u + \bar{d}d \rangle^*$, we will use KN scattering to evaluate that of $\langle \bar{u}u + \bar{s}s \rangle^*$.The advantage of the KN system is that $b^{I=0,1}$ can be determined directly from the experiments, not b_0, b_D and b_F. For determining the LECs, K^+N scatterings are preferable over K^-N scatterings since the $\Lambda(1405)$ resonance appears below the threshold and has a narrow decay width in $\bar{K}N$ system, while such resonance as $\Lambda(1405)$ does not exist. The K^+N scattering at low energy has been studied for a long time [89]. A recent study is done by Refs. [90, 91]. Reference [90] have constructed the K^+N scattering amplitude using chiral unitary approach and

discussed the presence of the broad resonance state with $I = 0,\ S = +1$ around $P_{\rm lab} = 600$ MeV. In Ref. [90], Aoki and Jido paid close attention to a sudden increase of the $I = 0$ total cross section around $P_{\rm lab} = 450$ MeV/c seen in the experimental data [92] (Carroll 1973). They constructed the K^+N scattering amplitudes using the chiral unitary approach and the model parameters were determined using observed cross sections of the K^+N elastic scattering up to $P_{\rm lab} = 800$ MeV. They found two best solutions for the K^+N amplitude with $I = 0$; in solution 1 the P_{01} amplitude provides a dominant contribution, while in solution 2 both P_{01} and P_{03} amplitudes contribute to the cross section. The former solution is more consistent with the Martin partial wave analysis [89]. Having performed analytic continuation of the obtained amplitudes into the complex energy plane, they found a resonance state in each solution. Solution 1 provides a resonance with 1617 MeV mass and 305 MeV width in the P_{01} partial wave, while solution 2 finds the resonance with 1678 MeV mass and 463 MeV width in the P_{03} partial wave. We will call the resonance in the former solution P_{01} resonance and the latter one P_{03} resonance in this paper.

It should be noted that the LECs in the chiral unitary approach are different from the original values as a result of the unitarization. And since the amplitude by chiral unitary approach is obtained numerically, it is not possible to perform the operation of taking the soft-limit. Therefore in order to achieve the purpose of determining the LECs, the K^+N scatterings need to be described by chiral perturbation theory, not the chiral unitary approach. Reference [91] has carried out the construction of the K^+N scattering amplitude using chiral perturbation theory up to the next-to-leading order, in which some terms are not considered.

In Chapter 6, we will construct K^+N scattering amplitudes using the chiral perturbation theory up to the next-to-leading order and some terms from the next-to-next-to-leading order which includes the strange quark mass, and estimate LECs using scattering data. Moreover, we will also consider the case of incorporating the P_{01} or P_{03} resonance states discussed in Ref.[90] to our amplitude obtained by chiral perturbation theory. The resonance state can influence the determination of the LECs. The determined LECs provide the behavior of the chiral condensate with strange in the nuclear matter.

We will also calculate the wavefunction renormalization of kaon in nuclei. In-medium property of NG bosons was investigated in terms of the wave function renormalization [7, 91, 93]. In Ref. [7], the wave function renormalization for the in-medium pion was discussed. Following that, the wave function renormalization for the in-medium kaon was calculated by constructing the K^+N amplitude in Ref. [91, 94]. Its result provided the wavefunction renormalization factor at the normal nuclear density was about 2 to 6% depending on the kaon momentum. This implied that the K^+N interaction got 2 to 6% enhancement in nuclear matter. On the other hand, the phenomenological study for the K^+-nucleus elastic scattering [95] indicated 14-34% enhancement. Thus Reference [91] suggested that the wave function renormalization gave a part of the in-medium effect for the kaon.

3.2.4 Kaonic atom and K^--nucleus interaction

As with the pionic atom discussed in Section 3.2.2, we can also consider a kaon atom which is the bound states of a K^- and a nucleus attracted mainly by the Coulomb interaction. From the kaonic atoms, the K^--nucleus interaction which is one of the important quantities in the investigation of the in-medium kaon can be extracted. The hadronic interactions by the K^--nucleus optical potential

shift the energy of the atomic state from that of the pure Coulombic bound state and provide the absorption widths. A schematic figure is shown in Fig. 3.1. The energy shift and the absorption width are extracted experimentally through the X-ray spectroscopy. The K^- K^- that stops around a nucleus is captured in an atomic orbit, is deexcited by emitting X-rays, and is absorbed into the nucleus. In experiments, the emitted X-rays are observed.

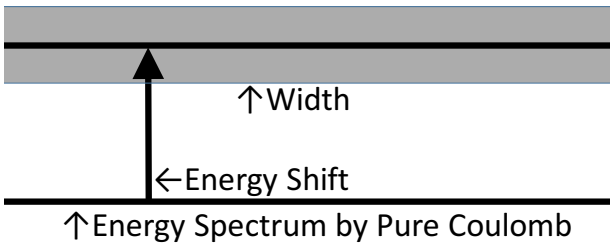

Fig.3.1 A schematic figure of the energy shift and absorption width. The arrows indicate the energy shift from the energy spectrum considering only the Coulomb interaction below, and the gray band over the upper spectrum indicates the absorption width.

So far, a lot of work has been done for the extraction of the optical potential of K^- in nucleus from the experimental data of kaonic atoms [96–105]. For instance, in Ref. [96], a global fit of the optical potential to the observed experimental data for the shift and width was performed, and the so-called phenomenological deep potential was obtained together with a shallower potential with a linear density approximation. There it was found that the imaginary part of the optical potential is comparably large to the real part to reproduce the observed data. Theoretical calculations have been also done in Refs. [106–128], for instance, using the chiral unitary approach [116]. The theoretical calculations support the shallower optical potential. Reference [129] showed that while both the phenomenological deep potential and the shallow potential based on the chiral unitary approach gave the same energy levels of ^{39}K kaonic atom for each angular momentum $L = 0, 1, 2, 3$, they produced the different energy spectrum for kaonic nuclear states of ^{39}K. We do not have enough information on kaonic atoms with small angular momentum that cannot be studied by X-ray spectroscopy. This is very different from the situation for the pionic atoms. For kaonic nuclei, the $\bar{K}NN$ state, in which one $\bar{K}$ and two nucleons are bound, was observed in the J-PARC E-15 experiment [130]. However, the existence of a nuclear state bounded with K^- in the medium-heavy nucleus has not been confirmed. The determination of the K^--nucleus interaction leads to in-medium K^- as well as the case of the pionic atom, however, this study is in progress.

In Chapter 7, apart from the big issue for the depth of the optical potential, we will investigate a global feature of the optical potential by arising the question of the origin of the repulsive shift seen in all of the observed kaonic atoms. It is well-known that the hadronic $\bar{K}N$ interaction is so attractive as to form $\Lambda(1405)$ as a bound state of $\bar{K}N$ with $I = 0$ [74, 75, 80, 131]. Nevertheless, in the kaonic atoms, the energy shift induced by the strong interaction is upwards repulsively. In other words, the scattering length of the $\bar{K}N$ with $I = 0$ is known to have repulsive nature. This is a consequence of the presence of the $\Lambda(1405)$ resonance below the $\bar{K}N$ scattering threshold, which induces the level repulsion due to the mixing of the $\Lambda(1405)$ resonance and the $\bar{K}N$ scattering states. The repulsive nature of the $\bar{K}N$ threshold may be kept even in the nuclear medium because the upward shift of the $\Lambda(1405)$ due to

the nucleon Pauli blocking [106–108] is compensated by the attraction for the in-medium $\bar{K}$ treated self-consistently into the $\bar{K}$ propagation in medium [112, 115]. There are two possible mechanisms for this puzzle of the repulsive shift in the atomic states. One is the level repulsion between the atomic and nuclear states as seen in the $\bar{K}N$ system. When the optical potential would be so strong as to provide a nuclear state close to the atomic state, with the coupling of these states level repulsion could take place and the atomic state could be pushed away upwards. The other mechanism is an effect of a large imaginary part of the optical potential $\mathrm{Im}V_{\mathrm{opt}}$, which works as repulsive interactions. The imaginary part provides nuclear absorption in 1st order perturbation, while in the 2nd order perturbation it gives repulsive interaction. The aim of our study in Chapter 7 is to find which mechanism is realized in the actual kaonic atoms. It is not the present intention here to extract the precise characteristics of the interaction between the kaon and the nucleus from the kaonic atom data. Rather, we are interested in finding the overall characteristics of the optical potential of the kaonic atom. To this end, we will employ a simple linear-density potential for the strong interaction between kaons and nucleus and consider the strength of the potential as an average aggregate from the atomic length scale. The origin of the microscopic nature of the potential is beyond the scope of our study.

Chapter 4

Theoretical tools

In this chapter, we describe the theoretical tools we use for each study. In Section 4.1, we summarize the kinematical formulations for the two-body calculation in order to discuss KN scattering used in Chapter 6, and for the two-body→three-body calculation in order to discuss the ΛN invariant mass spectrum of the $K^- d \to \pi\Lambda N$ reaction in Chapter 5. In Section 4.2, we introduce chiral perturbation theory for the construction of the KN scattering amplitude used in Chapter 6. In Section 4.3, we show the numerical method for solving the Klein-Gordon equation with the imaginary potential for the kaonic atom discussed in Chapter 7.

4.1 Kinematical formulation

In this section, we show the kinematical formulation for the two-body reaction and the three-body reaction.

4.1.1 Kinematics for two body reaction

In Chapter 6, we calculate the differential and total cross sections of $KN \to KN$ reaction. We introduce the general form of T-matrix for spin-0 boson (kaon) and spin-1/2 fermion (nucleon) scattering

$$T_{KN}(s,t) = \bar{u}(\boldsymbol{p}_4, s_4)\left[A(s,t) + \frac{1}{2}(\not{p}_1 + \not{p}_3)B(s,t)\right]u(\boldsymbol{p}_2, s_2). \tag{4.1}$$

The initial K^+ and nucleon momenta denote p_1 and p_2, respectively, while the final kaon and nucleon momenta stand for p_3 and p_4. $u(\boldsymbol{p}, s)$ is Dirac spinor with three-momentum $\boldsymbol{p}$ and spin s, which is normalized by $\bar{u}(\boldsymbol{p}, s)u(\boldsymbol{p}, s') = 2M_N\delta_{ss'}$ with nucleon mass M_N. $A(s,t)$ and $B(s,t)$ are two Lorentz-invariant functions of the two independent Mandelstam variables

$$\begin{aligned} s &= (p_1 + p_2)^2 \\ t &= (p_1 - p_3)^2. \end{aligned} \tag{4.2}$$

There is also a third Mandelstam variable, u defined as

$$u = (p_2 - p_3)^2. \tag{4.3}$$

Let us take the center-of-mass (c.m.) frame for partial wave decomposition. There we write the

T-matrix in terms of non-spin-flip amplitude f and spin-flip amplitude g as

$$T(s,t) = \chi^\dagger(\lambda_4)[f(W,\theta) - i(\boldsymbol{\sigma}\cdot\hat{\boldsymbol{n}})g(W,\theta)]\chi(\lambda_2) \tag{4.4}$$

where W and θ are the total energy of the system and the scattering angle between $\boldsymbol{p}_1$ and $\boldsymbol{p}_3$ in the center-of-mass frame, respectively, $\hat{\boldsymbol{n}}$ is the normal vector of the scattering plane defined by

$$\hat{\boldsymbol{n}} = \frac{\boldsymbol{p}_3 \times \boldsymbol{p}_1}{|\boldsymbol{p}_3 \times \boldsymbol{p}_1|}, \tag{4.5}$$

and $\chi(\lambda)$ is the Pauli spinor of a nucleon with helicity λ.

From Eq. (4.1) and Eq. (4.4), we obtain the relation of the Lorentz-invariant amplitudes A, B and the c.m. amplitudes f, g, as

$$f(W,\theta) = (E_N + M_N)(A + \omega B) + k^2 B + \frac{(E_N + M_N + \omega)B - A}{E_N + M_N}k^2\cos\theta, \tag{4.6}$$

$$g(W,\theta) = -\frac{(E_N + M_N + \omega)B - A}{E_N + M_N}k^2\sin\theta, \tag{4.7}$$

where E_N, ω and k stand for the nucleon energy, kaon energy and kaon momentum in the center-of-mass frame, respectively. For the detailed calculation, see Appendix A.

The amplitudes f and g are decomposed into the partial waves with Legendre polynomial $P_\ell(x)$ as

$$f(W,\theta) = \sum_{\ell=0}^{\infty} f_\ell(W)P_\ell(\cos\theta), \tag{4.8}$$

$$g(W,\theta) = \sum_{\ell=0}^{\infty} g_\ell(W)\sin\theta\frac{\mathrm{d}P_\ell(\cos\theta)}{\mathrm{d}\cos\theta}. \tag{4.9}$$

We introduce the amplitude of the total angular momentum $j = \ell \pm \frac{1}{2}$, $T_{\ell\pm}$ as

$$f_\ell(W) = (\ell+1)T_{\ell+}(W) + \ell T_{\ell-}(W), \tag{4.10}$$

$$g_\ell(W) = T_{\ell+}(W) - T_{\ell-}(W), \tag{4.11}$$

or equivalently

$$T_{\ell+}(W) = \frac{1}{2\ell+1}(f_\ell(W) + \ell g_\ell(W)), \tag{4.12}$$

$$T_{\ell-}(W) = \frac{1}{2\ell+1}(f_\ell(W) - (\ell+1)g_\ell(W)). \tag{4.13}$$

By taking the average of the initial nucleon spins and the summation of the final nucleon spins, the differential cross section in the center-of-mass frame is calculated as

$$\frac{\mathrm{d}\sigma}{\mathrm{d}\Omega} = \frac{1}{64\pi^2 s}\big(|f(W,\theta)|^2 + |g(W,\theta)|^2\big). \tag{4.14}$$

By integrating the differential cross section in terms of the solid angle Ω, we obtain the total cross section as

$$\sigma = \frac{1}{32\pi s}\int \mathrm{d}\cos\theta\big(|f(W,\theta)|^2 + |g(W,\theta)|^2\big). \tag{4.15}$$

Once the T-matrix can be calculated using chiral perturbation theory, it can be rewritten in the form A and B, or f and g to make it easier to use for calculating the cross section.

Coulomb correction

For the K^+p amplitude, we need to introduce the Coulomb correction. Here we follow the prescription done in Refs. [90, 91] originally given in Ref. [132]. The repulsive Coulomb amplitude is calculated as

$$f_C = -\frac{\alpha}{2kv\sin^2(\theta/2)}\exp\left[-i\frac{\alpha}{v}\ln\left(\sin^2\frac{\theta}{2}\right)\right] \tag{4.16}$$

with the scattering angle θ, the fine structure constant α and the K^+N relative velocity v defined by

$$v = \frac{k(E_K + E_p)}{E_K E_p}. \tag{4.17}$$

We add the Coulomb amplitude to the amplitudes calculated by the chiral perturbation theory. In addition, we multiply the Coulomb phase shift factor $e^{2i\Phi_\ell}$ with

$$\Phi_\ell = \sum_{n=1}^{\ell}\tan^{-1}\frac{\alpha}{nv} \tag{4.18}$$

for $\ell > 0$ ($\Phi_0 = 0$) to the strong interaction amplitudes. Finally, we have the amplitude with the Coulomb corrections as

$$f^{K^+p} = \sum_{\ell=0}^{\infty}\left[(\ell+1)T_{\ell+}^{I=1} + \ell T_{\ell-}^{I=1}\right]e^{2i\Phi_\ell}P_\ell(\cos\theta) - 8\pi\sqrt{s}f_C, \tag{4.19}$$

$$g^{K^+p} = \sum_{\ell=1}^{\infty}\left[T_{\ell+}^{I=1} - T_{\ell-}^{I=1}\right]e^{2i\Phi_\ell}\sin\theta\frac{\mathrm{d}P_\ell(\cos\theta)}{\mathrm{d}\cos\theta}. \tag{4.20}$$

4.1.2 Kinematics for three body reaction

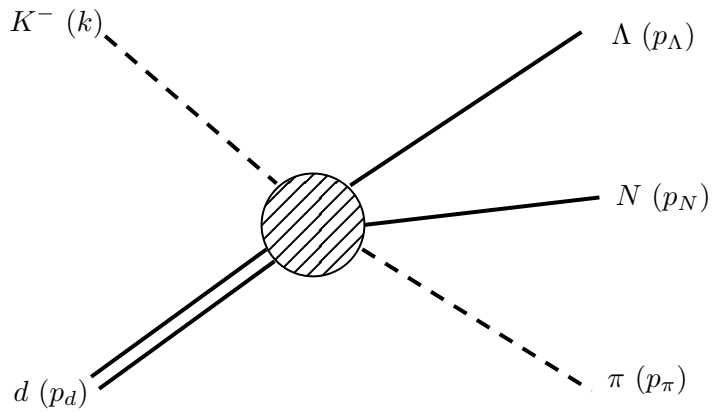

Fig.4.1 Kinematics of the $K^-d \to \pi\Lambda N$ reaction.

In Chapter 5, we will calculate the invariant mass spectrum of $K^-d \to \pi\Lambda N$ reaction. In preparation for this, we consider the kinematical formulation of the three body reaction. In general, n-body phase space $\mathrm{d}\Pi_n$ is given by

$$\mathrm{d}\Pi_n = (2\pi)^4\delta^{(4)}\left(P_{\mathrm{total}} - \sum_{i=1}^{n}p_i\right)\prod_{i=1}^{n}\frac{\mathrm{d}^3p_i}{(2\pi)^3}N_i \tag{4.21}$$

where P_{total} is the total momentum of the system, p_i is the momentum of the i-th particle in the final state and N_i stands for the normalization factor as

$$N_i = \begin{cases} \dfrac{1}{2\omega_i} & \text{for mesons,} \\ \dfrac{2M_i}{2E_i} & \text{for baryons,} \end{cases} \tag{4.22}$$

with the meson energy ω_i, the baryon energy E_i and the baryon mass M_i.

The cross section of two particles 1 and 2 in the initial state is given by

$$\mathrm{d}\sigma = \frac{1}{v_{\text{rel}}} N_1 N_2 \mathrm{d}\Pi_n |\mathcal{T}|^2 \tag{4.23}$$

where $\mathcal{T}$ is T-matrix of the reaction and v_{rel} is defined by

$$v_{\text{rel}} = \frac{\sqrt{(k_1 \cdot k_2) - m_1^2 m_2^2}}{k_1^0 k_2^0} \tag{4.24}$$

with k_i and m_i are the i-th momentum and mass in the initial state. In the center of mass frame, v_{rel} is transformed to

$$v_{\text{rel}} = \left| \frac{|k_{\text{c.m.}}|}{k_1^0} - \frac{-|k_{\text{c.m.}}|}{k_2^0} \right| = \frac{(k_2^0 + k_1^0) k_{\text{c.m.}}}{k_1^0 k_2^0} = \frac{E_{\text{c.m.}} k_{\text{c.m.}}}{k_1^0 k_2^0}. \tag{4.25}$$

Next, we formulate the invariant mass spectrum of the $K^- d \to \pi\Lambda N$ reaction. We assign the momentum variables shown in Fig. 4.1. We obtain the total cross section of the $K^- d \to \pi\Lambda N$ reaction as

$$\begin{aligned} \mathrm{d}\sigma =& \frac{1}{v_{\text{rel}}} N_1 N_2 \mathrm{d}\Pi_3 |\mathcal{T}|^2 \\ =& \frac{k^0 p_d^0}{k_{\text{c.m.}} E_{\text{c.m.}}} \frac{1}{2k^0} \frac{2M_d}{2p_d^0} \mathrm{d}\Pi_3 |\mathcal{T}|^2 \\ =& \frac{M_d}{k_{\text{c.m.}} E_{\text{c.m.}}} \frac{\mathrm{d}^3 p_\pi}{(2\pi)^3} \frac{1}{2\omega_\pi} \frac{\mathrm{d}^3 p_\Lambda}{(2\pi)^3} \frac{2M_\Lambda}{2E_\Lambda} \frac{\mathrm{d}^3 p_N}{(2\pi)^3} \frac{2M_N}{2E_N} \\ & \times (2\pi)^4 \delta^{(4)}(P_{\text{total}} - p_\pi - p_\Lambda - p_N) \, |\mathcal{T}|^2. \end{aligned} \tag{4.26}$$

The reaction $K^- d \to \pi\Lambda N$ requires five kinematical variables to fix the phase space of the three-body final state [1]. In this study we are interested in the mass spectra of the ΛN systems, thus we choose the following variables for unpolarized deuteron targets: the ΛN invariant mass $M_{\Lambda N}$ defined as

$$M_{\Lambda N} = \sqrt{(E_\Lambda + E_N)^2 - (\boldsymbol{p}_\Lambda + \boldsymbol{p}_N)^2}, \tag{4.27}$$

the solid angle of the final pion in the total center-of-mass (c.m.) frame Ω_π, and the solid angle of the final Λ in the Λ-nucleon c.m. frame Ω_Λ^*. Then the cross section (4.26) becomes

$$d\sigma = \frac{1}{(2\pi)^5} \frac{M_d M_\Lambda M_N}{4 k_{\text{c.m.}} E_{\text{c.m.}}^2} |\mathcal{T}|^2 |\boldsymbol{p}_\pi| \, |\boldsymbol{p}_\Lambda^*| \, dM_{\Lambda N} d\Omega_\Lambda^* d\Omega_\pi \tag{4.28}$$

where $E_{\text{c.m.}}$ is the total c.m. energy, $k_{\text{c.m.}}$ and $\boldsymbol{p}_\pi$ are the initial K^- and final π momenta in the total c.m. frame, respectively, $\boldsymbol{p}_\Lambda^*$ denotes the momentum of the final Λ in the Λ-nucleon c.m. frame, respectively, and $\mathcal{T}$ represents the T-matrix of the reaction.

The absolute value of the Λ momentum $\boldsymbol{p}^*_\Lambda$ in the Λ-nucleon c.m. frame can be fixed by the Λ-nucleon invariant mass as

$$|\boldsymbol{p}^*_\Lambda| = \frac{\lambda^{1/2}(M^2_{\Lambda N}, M^2_\Lambda, M^2_N)}{2M_{\Lambda N}}, \tag{4.29}$$

and similarly, the absolute value of the pion momentum $\boldsymbol{p}_\pi$ in the total c.m. frame can be fixed by the total energy of the reaction $E_{\text{c.m.}}$ as

$$|\boldsymbol{p}_\pi| = \frac{\lambda^{1/2}(E^2_{\text{c.m.}}, M^2_{\Lambda N}, M^2_\pi)}{2E_{\text{c.m.}}} \tag{4.30}$$

with the Källen function $\lambda(x, y, z) = x^2 + y^2 + z^2 - 2xy - 2yz - 2zx$.

4.2 Chiral perturbation theory

Chiral perturbation theory is a low-energy effective theory of QCD that describes a phenomenon in which the chiral symmetry is spontaneously broken. It describes the dynamics of hadrons such as the Nambu-Goldstone bosons that arise as a consequence of the dynamical breaking of chiral symmetry. In low-energy QCD, quarks and gluons compose hadrons due to the color confinement making it difficult to treat them as fundamental degrees of freedom, thus we construct a low-energy effective theory in which hadrons are fundamental degrees of freedom instead of quarks and gluons. In this section, we construct the effective chiral Lagrangian for mesons and meson-baryons. The chiral perturbation theory will be used in Chapter 6. The description in this section is based on References [133–138].

4.2.1 Effective field theory

An effective theory is a theoretical tool for describing low-energy physics, an approximation to a more fundamental underlying theory, such as QCD. The term "low energy" here refers to energies below a certain energy scale Λ. In the effective theory, only degrees of freedom related to low energy are used to construct the theory, and all information with energy above Λ is integrated and interpreted. As a result, they are included in the constants in the effective Lagrangian (called low-energy constants, LECs). The theoretical basis of the effective field theory was established by Weinberg [139] as a theorem as:

> *if one writes down the most general possible Lagrangian, including all terms consistent with assumed symmetry principles, and then calculates matrix elements with this Lagrangian to any given order in perturbation theory, the result will simply be the most general possible S-matrix consistent with analyticity, perturbative unitarity, cluster decomposition and the assumed symmetry principles.*

Based on this theorem, chiral perturbation theory was developed [140, 141].

4.2.2 Chiral perturbation theory

Chiral perturbation theory which is the low-energy effective theory of QCD is a theory built on the chiral symmetry, the symmetry of the original theory, and its dynamical breaking. In the dynami-

cally broken phase, the chiral symmetry cannot be expressed linearly but is expressed as a nonlinear transformation. Therefore the Nambu–Goldstone boson fields themselves are transformed nonlinearly.

Chiral Lagrangian for meson

Firstly, we construct chiral Lagrangian for meson. The dynamical symmetry breaking of the chiral symmetry is expressed by the groups as

$$G \equiv \mathrm{SU}(3)_L \times \mathrm{SU}(3)_R \xrightarrow{\mathrm{DB}\chi\mathrm{S}} H \equiv \mathrm{SU}(3)_V. \tag{4.31}$$

We denote $\phi^a (a = 1, 2, \ldots 8)$ as the Nambu–Goldstone boson fields in the coset space G/H, and choose a coset representative $\xi(\phi) \equiv (\xi_L(\phi), \xi_R(\phi)) \in G$. The transformation rules of the Nambu–Goldstone boson fields under chiral transformation $g \equiv (g_L, g_R) \in G$ are given via ξ as

$$\xi_L(\phi) \xrightarrow{G} g_L \xi_L(\phi) h^\dagger(\phi, g), \qquad \xi_R(\phi) \xrightarrow{G} g_R \xi_R(\phi) h^\dagger(\phi, g) \tag{4.32}$$

where $h(\phi, g) \in H$. Without loss of generality, we can put $\xi_L^\dagger(\phi) = \xi_R(\phi) = \xi(\phi)$, and the transformation rule of $\xi(\phi)$ is

$$\xi(\phi) \xrightarrow{G} h \xi(\phi) g_L^\dagger = g_R \xi(\phi) h^\dagger. \tag{4.33}$$

Introducing $U(\phi) \equiv \xi(\phi)^2$ which is called the chiral field, then we have the linear transformation rule for $U(\phi)$

$$U(\phi) \xrightarrow{G} g_R U(\phi) g_L^\dagger. \tag{4.34}$$

The meson fields $\Phi = \phi^a \lambda^a / \sqrt{2}$ are written in the SU(3) matrix form as

$$\Phi = \begin{pmatrix} \frac{\Phi_3}{\sqrt{2}} + \frac{\Phi_8}{\sqrt{6}} & \frac{\Phi_1 - i\Phi_2}{\sqrt{2}} & \frac{\Phi_4 - i\Phi_5}{\sqrt{2}} \\ \frac{\Phi_1 + i\Phi_2}{\sqrt{2}} & -\frac{\Phi_3}{\sqrt{2}} + \frac{\Phi_8}{\sqrt{6}} & \frac{\Phi_6 - i\Phi_7}{\sqrt{2}} \\ \frac{\Phi_4 + i\Phi_5}{\sqrt{2}} & \frac{\Phi_6 + i\Phi_7}{\sqrt{2}} & -\frac{2}{\sqrt{6}}\Phi_8 \end{pmatrix} \equiv \begin{pmatrix} \frac{\pi^0}{\sqrt{2}} + \frac{\eta}{\sqrt{6}} & \pi^+ & K^+ \\ \pi^- & -\frac{\pi^0}{\sqrt{2}} + \frac{\eta}{\sqrt{6}} & K^0 \\ K^- & \bar{K}^0 & -\frac{2}{\sqrt{6}}\eta \end{pmatrix}. \tag{4.35}$$

Here we use the Coleman–Callan–Wess–Zumino (CCWZ) parametrization for the chiral field U as

$$U = \exp\Big(i\sqrt{2}\Phi/F\Big) \tag{4.36}$$

where F is a normalization of the meson field Φ and corresponds to the meson decay constant.

In chiral perturbation theory, the most general Lagrangian involving the matrix $U(\phi)$ is constructed using chiral symmetry as a guide. When the Lagrangian has exact flavor $\mathrm{SU}(3)_L \times \mathrm{SU}(3)_R$ chiral symmetry, the Nambu–Goldstone bosons are massless, then the four-momentum of a Nambu–Goldstone boson on the mass shell is given by $p^\mu = (|p|, \boldsymbol{p})$. Therefore, when the spatial momentum can be regarded as sufficiently smaller than the chiral symmetry breaking scale $\Lambda_\chi = 4\pi F_\pi \sim 1$ GeV, the perturbation expansion by p^μ is a good approximation. In this sense, chiral perturbation theory is an effective field theory. When the flavor $\mathrm{SU}(3)_L \times \mathrm{SU}(3)_R$ symmetry is not exact, that is, when the quark has non-zero mass and then chiral symmetry is broken explicitly, the Nambu–Goldstone bosons have also non-zero mass. In this case, if the mass of the Nambu–Goldstone boson is small and p is also small, the perturbation expansion is valid in the same way as well as the case of the chiral limit. Under the above conditions, the Lagrangian is expanded in terms of powers of the momentum of the

Nambu–Goldstone boson (powers of the derivative for the Nambu–Goldstone fields). Since only even powers are allowed due to the conservation of parity, the effective Lagrangian which is called the chiral Lagrangian is given by

$$\mathcal{L}_{\text{eff}}(U) = \sum_n \mathcal{L}^{2n}. \tag{4.37}$$

In the low-energy region, the term with the minimum number of derivatives can be considered dominant. The term $\mathrm{Tr}\big[UU^\dagger\big]$ which is a non-derivative term but chiral invariant is constant because U is a unitary matrix.

The leading order of the chiral Lagrangian, which includes the Nambu–Goldstone field and an external source, is given by

$$\mathcal{L}_M^{(2)} = \frac{F^2}{4}\,\mathrm{Tr}\big\{D_\mu U^\dagger D^\mu U + \chi^\dagger U + \chi U^\dagger\big\} \tag{4.38}$$

where the field χ which contains the scalar and pseudoscalar external field, $s = s^a\lambda^a$ and $p = p^a\lambda^a$, is given by

$$\chi = 2B_0(s+ip), \qquad\qquad \chi^\dagger = 2B_0(s-ip), \tag{4.39}$$

where B_0 is a low-energy constant that is fixed by the relation

$$M_K^2 = B_0(m+m_s) \tag{4.40}$$

with the kaon mass M_K in this dissertation. The filed χ is transformed under the chiral transformation as

$$\chi \xrightarrow{G} g_R\chi g_L^\dagger. \tag{4.41}$$

The covariant derivative D_μ contains the vector and axial-vector external fields as

$$D_\mu U = \partial_\mu U - ir_\mu U + iU\ell_\mu \tag{4.42}$$

where $r_\mu = \frac{1}{2}(v_\mu + a_\mu)$ and $\ell_\mu = \frac{1}{2}(v_\mu - a_\mu)$ with the vector current v_μ and the axial-vector current a_μ. Using these external fields, the electromagnetic and semileptonic weak interactions, and the explicit breaking of chiral symmetry by the quark mass can be incorporated into the chiral Lagrangian. In particular, the explicit breaking of chiral symmetry due to the quark mass is introduced as $s = \mathcal{M} = diag(m, m, m_s)$.

Chiral perturbation theory for meson-baryon

Next, we construct chiral Lagrangian for meson-baryon. The octet of $\frac{1}{2}^+$ baryon fields B is introduced as

$$B = \begin{pmatrix} \frac{B_3}{\sqrt{2}} + \frac{B_8}{\sqrt{6}} & \frac{B_1 - iB_2}{\sqrt{2}} & \frac{B_4 - iB_5}{\sqrt{2}} \\ \frac{B_1 + iB_2}{\sqrt{2}} & -\frac{B_3}{\sqrt{2}} + \frac{B_8}{\sqrt{6}} & \frac{B_6 - iB_7}{\sqrt{2}} \\ \frac{B_4 + iB_5}{\sqrt{2}} & \frac{B_6 + iB_7}{\sqrt{2}} & -\frac{2}{\sqrt{6}}B_8 \end{pmatrix} \equiv \begin{pmatrix} \frac{\Sigma^0}{\sqrt{2}} + \frac{\Lambda}{\sqrt{6}} & \Sigma^+ & p \\ \Sigma^- & -\frac{\Sigma^0}{\sqrt{2}} + \frac{\Lambda}{\sqrt{6}} & n \\ \Xi^- & \Xi^0 & -\frac{2}{\sqrt{6}}\Lambda \end{pmatrix} \tag{4.43}$$

and its adjoint $\bar{B} = \bar{B}^a \lambda^a/\sqrt{2}$ by

$$\bar{B} = \begin{pmatrix} \frac{\bar{B}_3}{\sqrt{2}} + \frac{\bar{B}_8}{\sqrt{6}} & \frac{\bar{B}_1 - i\bar{B}_2}{\sqrt{2}} & \frac{\bar{B}_4 - i\bar{B}_5}{\sqrt{2}} \\ \frac{\bar{B}_1 + i\bar{B}_2}{\sqrt{2}} & -\frac{\bar{B}_3}{\sqrt{2}} + \frac{\bar{B}_8}{\sqrt{6}} & \frac{\bar{B}_6 - i\bar{B}_7}{\sqrt{2}} \\ \frac{\bar{B}_4 + i\bar{B}_5}{\sqrt{2}} & \frac{\bar{B}_6 + i\bar{B}_7}{\sqrt{2}} & -\frac{2}{\sqrt{6}}\bar{B}_8 \end{pmatrix} \equiv \begin{pmatrix} \frac{\bar{\Sigma}^0}{\sqrt{2}} + \frac{\bar{\Lambda}}{\sqrt{6}} & \bar{\Sigma}^- & \bar{\Xi}^- \\ \bar{\Sigma}^+ & -\frac{\bar{\Sigma}^0}{\sqrt{2}} + \frac{\bar{\Lambda}}{\sqrt{6}} & \bar{\Xi}^0 \\ \bar{p} & \bar{n} & -\frac{2}{\sqrt{6}}\bar{\Lambda} \end{pmatrix}. \tag{4.44}$$

Baryon fields are transformed under $G = \mathrm{SU}(3)_L \times \mathrm{SU}(3)_R$ as

$$B \xrightarrow{G} h(\phi, g) B h^\dagger(\phi, g). \tag{4.45}$$

The leading order of the SU(3) meson-baryon chiral Lagrangian reads

$$\mathcal{L}^{(1)}_{MB} = \mathrm{Tr}\big\{\bar{B}(i\not{D} - M_0)B)\big\} - \frac{D}{2}\,\mathrm{Tr}\big\{\bar{B}\gamma^\mu\gamma^5\{u_\mu, B\}\big\} - \frac{F}{2}\,\mathrm{Tr}\big\{\bar{B}\gamma^\mu\gamma^5[u_\mu, B]\big\}, \tag{4.46}$$

where M_0 is the baryon mass at the chiral limit.

The covariant derivative for the baryon field is introduced as

$$D_\mu B = \partial_\mu B + [\Gamma_\mu, B] \tag{4.47}$$

with the mesonic vector current called chiral connection given as

$$\Gamma_\mu = \frac{1}{2}(\xi^\dagger \partial_\mu \xi + \xi \partial_\mu \xi^\dagger)$$

where $\xi^2 = U$. The mesonic axial-vector current called chiral vielbein is introduced as

$$u_\mu = i(\xi^\dagger \partial_\mu \xi - \xi \partial_\mu \xi^\dagger). \tag{4.48}$$

The low-energy constants D and F are to be determined by fitting the semi-leptonic decay.

The next-to-leading order (NLO) of the chiral Lagrangian is given by

$$\begin{aligned}
\mathcal{L}^{(2)}_{MB} = {} & b_D\,\mathrm{Tr}\big\{\bar{B}\{\chi_+, B\}\big\} + b_F\,\mathrm{Tr}\big\{\bar{B}[\chi_+, B]\big\} + b_0\,\mathrm{Tr}\big\{\bar{B}B\big\}\,\mathrm{Tr}\{\chi_+\} + d_1\mathrm{Tr}\left(\bar{B}\{u_\mu, [u^\mu, B]\}\right) \\
& + d_2\mathrm{Tr}\left(\bar{B}[u_\mu, [u^\mu, B]]\right) + d_3\mathrm{Tr}\left(\bar{B}u_\mu\right)\mathrm{Tr}(u^\mu B) + d_4\mathrm{Tr}\left(\bar{B}B\right)\mathrm{Tr}(u^\mu u_\mu) \\
& - \frac{g_1}{8M_N^2}\mathrm{Tr}\left(\bar{B}\{u_\mu, [u_\nu, \{D^\mu, D^\nu\}B]\}\right) - \frac{g_2}{8M_N^2}\mathrm{Tr}\left(\bar{B}[u_\mu, [u_\nu, \{D^\mu, D^\nu\}B]]\right) \\
& - \frac{g_3}{8M_N^2}\mathrm{Tr}(\bar{B}u_\mu)\mathrm{Tr}(u_\nu, \{D^\mu, D^\nu\}B) - \frac{g_4}{8M_N^2}\mathrm{Tr}(\bar{B}\{D^\mu, D^\nu\}B)\mathrm{Tr}(u_\mu u_\nu) \\
& - \frac{h_1}{4}\mathrm{Tr}\left(\bar{B}[\gamma^\mu, \gamma^\nu]Bu_\mu u_\nu\right) - \frac{h_2}{4}\mathrm{Tr}\left(\bar{B}[\gamma^\mu, \gamma^\nu]u_\mu[u_\nu, B]\right) \\
& - \frac{h_3}{4}\mathrm{Tr}\left(\bar{B}[\gamma^\mu, \gamma^\nu]u_\mu\{u_\nu, B\}\right) - \frac{h_4}{4}\mathrm{Tr}(\bar{B}[\gamma^\mu, \gamma^\nu]u_\mu)\mathrm{Tr}(u_\nu B) + \mathrm{h.c.}
\end{aligned} \tag{4.49}$$

where b_i, d_i, g_i and h_i are the LECs of NLO. The terms that include b_i and d_i appear in the typical flavor SU(3) chiral Lagrangian such as in Ref. [80, 91], while the terms that include g_i and h_i are introduced as the extension of the flavor SU(2) chiral Lagrangian and used in Ref. [90].

The scalar and pseudoscalar sources are contained in $\chi_\pm$ as

$$\chi_\pm = \xi\chi^\dagger\xi \pm \xi^\dagger\chi\xi^\dagger. \tag{4.50}$$

In order to improve extrapolation in the strange quark sector for Chapter 6, we introduce some terms of the next-to-next-to-leading order (NNLO) of the chiral Lagrangian [142], which contain the

strange quark mass m_s in χ_- as

$$\begin{aligned}\mathcal{L}^{(3)}_{MB} &= v_1\,\mathrm{Tr}\big(\bar{B}\{\chi_-,\gamma_5 B\}\big) + v_2\,\mathrm{Tr}\big(\bar{B}[\chi_-,\gamma_5 B]\big)\\ &+ w_1\,\mathrm{Tr}\big(\bar{B}\gamma_\mu B[\chi_-,u^\mu]\big) + w_2\,\mathrm{Tr}\big(\bar{B}[\chi_-,u^\mu]\gamma_\mu B\big)\\ &+ w_3\big[\mathrm{Tr}\big(\bar{B}u^\mu\big)\,\mathrm{Tr}(\chi_-\gamma_\mu B) - \mathrm{Tr}\big(\bar{B}\chi_-\big)\,\mathrm{Tr}(u^\mu\gamma_\mu B)\big]\end{aligned} \tag{4.51}$$

where v_i and w_i are the LECs.

In-medium chiral perturbation theory

In-medium extension of chiral perturbation theory is done by Ref.[143] and further developed by Ref. [83]. In this theory, k_F/Λ_χ with the Fermi momentum k_F of the nucleon in nuclear matter is introduced as a new expansion parameter. k_F is related to the nuclear density ρ by $\rho = k_F^3/3\pi^2$. Therefore this theory allows for expansion by the nuclear density. Recent calculations by in-medium chiral perturbation theory are done in Ref. [144] for the in-medium pion property, Ref. [10] for SU(2) chiral condensate in symmetric nuclear matter and Ref. [11] for that in asymmetric nuclear matter.

Chiral unitarity approach

In chiral perturbation theory, the scattering amplitude is described by perturbative expansion, but the excited states of hadron cannot be represented by finite-order perturbation expansions. In order to represent the excited states in chiral perturbation theory, it is necessary to either explicitly incorporate them into chiral perturbation theory or dynamically generate them by non-perturbative conditions. Chiral unitarity approach [74–80] is the latter case. In the chiral unitarity approach, the unitarization for the scattering amplitude T is performed by solving the Lippmann-Schwinger equation:

$$T = V + VGT \tag{4.52}$$

where V is the interaction kernel derived by chiral perturbation theory and G is the loop function. As a result of the unitarization, the excited state is described as a pole of the obtained scattering amplitude. The $\Lambda(1405)$ resonance which is the excited state of the Λ baryon is described by the chiral unitarity approach [80].

4.2.3 Example

In the previous section, we introduced the chiral Lagrangian. In this section, we give a calculation example of the meson-baryon reaction using the chiral Lagrangian. To start, we need to clarify the reaction to be computed. Then, we expand the chiral Lagrangian from the meson field Φ in the chiral field U and the baryon field B to the specific hadron field, e.g., the kaon field π^+ and the proton field p, and extract only the parts that are relevant to the reaction we are dealing with. We consider the leading order of π^+p elastic scattering as an example. Here we do not consider the Coulomb correction. Expanding Eq. (4.46) and extracting the related terms, we find

$$\begin{aligned}\mathcal{L} &= \frac{1}{4F_\pi^2}\big[\bar{p}(i\partial\!\!\!/\pi^-)\pi^+ p - \bar{p}\pi^-(i\partial\!\!\!/\pi^+)p\big]\\ &+ \frac{D+F}{\sqrt{2}F_\pi}\big[\bar{n}(\partial\!\!\!/\pi^-)\gamma^5 p + \bar{p}(\partial\!\!\!/\pi^+)\gamma^5 n\big].\end{aligned} \tag{4.53}$$

Note that the outgoing baryon field is represented by $\bar{B}$, whereas the outgoing meson field is the complex conjugate of the incoming meson field, e.g. the outgoing π^+ is represented by π^- field in this example. The first term is a contact interaction of meson fields interacting with baryons at a single point, and the second term is the pseudovector meson-baryon coupling. They are the so-called Weinberg–Tomozawa term and Born term, respectively.

Fig.4.2 Feynman diagrams related to $\pi^+ p$ elastic scattering. The left diagram indicates the contact interaction. The right diagram means the u-channel Born term.

Let us calculate the T-matrix of two body meson-baryon scattering using the leading order of chiral Lagrangian. Firstly, we give the Weinberg–Tomozawa interaction $T_{\rm WT}$ which is the contact interaction derived by the leading order of the Lagrangian:

$$\begin{aligned} T_{\rm WT} &= -\bar{u}(\boldsymbol{p}_4, s_4)\big[\mathcal{L}_{\pi^+ p}\big]u(\boldsymbol{p}_2, s_2) \\ &= -\bar{u}(\boldsymbol{p}_4, s_4)\frac{1}{4F_\pi^2}(-\not{p}_3 - \not{p}_1)u(\boldsymbol{p}_2, s_2) \\ &= \frac{1}{4F_\pi^2}\bar{u}(\boldsymbol{p}_4, s_4)(\not{p}_1 + \not{p}_3)u(\boldsymbol{p}_2, s_2) \end{aligned} \tag{4.54}$$

where the minus sign over the whole equation is a notation. $[\mathcal{L}]$ is the vertex factor defined as

$$[\mathcal{L}_{\phi\ldots\chi}] = \frac{\delta}{\delta\phi}\cdots\frac{\delta}{\delta\chi}\mathcal{L}_{\phi\ldots\chi} \tag{4.55}$$

where $\phi\ldots\chi$ represents all the fields that interact at this vertex. The derivative with incoming meson gets replaced by $i\partial_\mu \to p_\mu$ and the derivative with outgoing meson is replaced with $i\partial_\mu \to -p_\mu$.

Similarly, next, let us consider the u-channel Born term given by

$$\begin{aligned} T_{\rm Born} &= -\bar{u}(\boldsymbol{p}_4, s_4)\big[\mathcal{L}_{\pi^+ np}\big]S_F^n(\boldsymbol{p}_2 - \boldsymbol{p}_3)\big[\mathcal{L}_{p\pi^+ n}\big]u(\boldsymbol{p}_2, s_2) \\ &= -\frac{(D+F)^2}{2F_\pi^2}\bar{u}(\boldsymbol{p}_4, s_4)\big(-i\not{p}_1\gamma^5\big)\frac{M_n + \not{p}_2 - \not{p}_3}{M_n^2 - (p_2 - p_3)^2}\big(i\not{p}_3\gamma^5\big)u(\boldsymbol{p}_2, s_2) \\ &= -\frac{g_A^2}{2F_\pi^2}\bar{u}(\boldsymbol{p}_4, s_4)\big(\not{p}_1\gamma^5\big)\frac{M_n + \not{p}_2 - \not{p}_3}{M_n^2 - (p_2 - p_3)^2}\big(\not{p}_3\gamma^5\big)u(\boldsymbol{p}_2, s_2) \end{aligned} \tag{4.56}$$

where S_F^B is a fermion propagator $S_F^B(q) = 1/(M_B + \not{q} - i\epsilon)$ with the baryon mass M_B. $g_A = D + F$ is the axial-vector coupling constant. The scattering length is given by the T-matrix at the threshold:

$$a_{\pi^+ p} = a^{I=3/2} = -\frac{1}{8\pi(M_{\pi^+} + M_p)}T_{\pi^+ p}^{\rm thr} = 0.126 \text{ fm} \tag{4.57}$$

where we use $g_A = 1.267$. The experimental value is given by

$$\begin{aligned} a_{\rm ex}^{I=3/2} &\equiv -(b_0^{\rm ex} + b_1^{\rm ex}) \\ &= -(-0.1 \times 10^{-3}\ M_\pi^{-1} - 88.5 \times 10^{-3}\ M_\pi^{-1}) \\ &= 0.125 \text{ fm} \end{aligned} \tag{4.58}$$

where the values of the isoscalar and isovector scattering length of πN, $b_0^{\rm ex} = -0.1 \times 10^{-3}\ M_\pi^{-1}$ and $b_1^{\rm ex} = -88.5 \times 10^{-3}\ M_\pi^{-1}$ are taken from Ref. [145]. We find that we obtain a good value by the leading order of chiral perturbation theory and chiral perturbation theory works well.

At the end of this section, we give the rules of calculation using the chiral Lagrangian:

1. Draw the Feynman graphs of the reaction one needs.
2. Expand the chiral Lagrangian and extract the terms related to the reaction one considers.
3. Calculate the vertex factor from the Lagrangian.
4. Attach the building blocks (the vertex, the propagator, the spinor...) to the Feynman diagram
5. If necessary, organize the obtained equation using the Klein-Gordon equation, Dirac equation, on-shell condition, etc.

4.3 Numerical calculation of the Klein-Gordon equation with the complex optical potential

We refer to Reference [146] in writing this section. In this section, we show the numerical calculation of the Klein-Gordon equation with the complex optical potential. The form of the equation we will consider is given by

$$[-\{E - V_c(r)\}^2 - \nabla^2 + \mu^2 + 2\mu V_{\rm opt}(r)]\phi(\boldsymbol{r}) = 0 \tag{4.59}$$

where $E \equiv \mu - E_B - i\Gamma/2$ is the energy with the reduced mass μ, the binding energy E_B and the absorption width Γ, $V_c(r)$ and $V_{\rm opt}(r)$ stand for the Coulomb and the optical potentials, respectively. $\phi(\boldsymbol{r})$ is the wavefunction we will consider. We do not consider angle dependence for the potential. Removing the angular dependence from the wavefunction, we obtain the radial direction part of the equation as

$$\left[-\{E - V_c(r)\}^2 - \frac{{\rm d}^2}{{\rm d}r^2} + \frac{\ell(\ell+1)}{r^2} + \mu^2 + 2\mu V_{\rm opt}(r)\right]\chi(r) = 0 \tag{4.60}$$

where $\chi(r)$ is defined as $\chi(r) = rR(r)$ with the radial direction part of the wavefunction $R(r)$. The angle-dependent part of the wavefunction is obtained as a spherical harmonic function.

The optical potential in Eq. (4.60) is generally a complex potential. Thus the eigenenergy of the equation is also the complex eigenvalue. We describe the numerical solution of the equation of motion with such complex eigenvalues. Let us consider the following general form of the equation of motion:

$$\left(-\frac{{\rm d}^2}{{\rm d}r^2} + \tilde{V}(r)\right)\chi(r) = -k^2\chi(r) \tag{4.61}$$

where k^2 is the complex eigenvalue and $\tilde{V}(r)$ is a complex potential function that goes to zero sufficiently early at $r \to \infty$. In the case of Eq. (4.60), $\tilde{V}(r)$ includes not only $V_{\rm opt}(r)$ but also $V_c(r)$ and a centrifugal barrier.

For a bound state, we consider finding the eigenvalue k^2 numerically. Imposing $\chi(r) \propto r^{\ell+1}$ as a boundary condition at $r \sim 0$ and assuming a certain k, $\chi(r)$ can be calculated numerically at any r. We assume that $\chi(r)$ can be expressed as follows:

$$\chi(r) = A(k)f(r) + B(k)g(r) \tag{4.62}$$

where $f(r)$ and $g(r)$ is two independent solution of Eq. (4.61). From the condition $\tilde{V}(r \to \infty) = 0$, they satisfy

$$f(r \to \infty) \to \exp(-kr),\ g(r \to \infty) \to \exp(+kr). \tag{4.63}$$

$A(k)$ and $B(k)$ depend on the eigenvalue k, but not on r. The problem here is whether $\chi(r)$ is the wavefunction of the bound system, namely converges at infinity. Taking $\mathrm{Re}\, k > 0$, the first term of Eq. (4.62) converges at infinity and the second term diverges at infinity. Then $k = k_{\mathrm{sol}}$ which satisfies the condition $B(k_{\mathrm{sol}}) = 0$ is the eigenvalue of the bound system for the equation. In practice, the behavior of the wavefunction at infinity cannot be calculated numerically, but we can find k such that the absolute value of the wavefunction $(\chi(r_{\mathrm{max}}))^2$ is minimized for $r = r_{\mathrm{max}}$ sufficiently larger than the system under consideration[*1]. k_{sol} is k when $(\chi(r_{\mathrm{max}}))^2$ takes a minimum value. When performing a numerical calculation, instead of the absolute value of the wavefunction $\chi^2(r_{\mathrm{max}})$, the function

$$v(k) = \frac{\chi^2(r_{\mathrm{max}})}{\exp(2(\mathrm{Re}\, k) r_{\mathrm{max}})} \tag{4.64}$$

is used for the finding of k_{sol}. Organizing Eq. (4.60) in the form (4.61) yields

$$\left(-\frac{\mathrm{d}^2}{\mathrm{d}r^2} + \tilde{V}(r)\right)\chi = -\left[-(\mu - E_B)^2 + \mu^2 + \frac{\Gamma^2}{4} + i\Gamma(\mu - E_B)\right]\chi \equiv -k^2\chi \tag{4.65}$$

where $\tilde{V}(r)$ is the sum of the terms containing the potential and the centrifugal force potential. In Chapter 7, we will examine the optical potential by solving the equation Eq. (4.65) backward, giving the energy as the initial value.

[*1] Note that the length scales are very different at the atomic or nuclear scale.

Chapter 5

Isospin symmetry breaking in Λ-nucleon interaction investigated with $K^-d \to \pi\Lambda N$ reaction

5.1 Introduction

The difference between the Λ-proton (Λp) and Λ-neutron (Λn) is interesting in terms of the isospin symmetry breaking in the system that includes strangeness. Recently a large isospin symmetry breaking effect has been suggested by experimental analysis for the $A = 4$ mirror Λ-hypernuclei [27, 28]. From the experimental data, one finds the difference of the excitation energies from the 0^+ ground state to the 1^+ excited state of ${}^{4}_{\Lambda}$H and ${}^{4}_{\Lambda}$He to be 0.3 MeV, which is much larger than the binding energy difference of ^{3}H and ^{3}He, 0.071 MeV. While the isospin symmetry breaking of the Λ binding energy to the nucleus in the Λ hypernuclei, the isospin symmetry breaking of the elementary process of that, the ΛN system is not fully understood. In particular, the Λn scattering is not enough understood, while the Λp scattering was extracted from the $pp \to K^+\Lambda p$ reaction [4]. In any case, there is little information on the ΛN system and more experimentation should be done for discussion on the isospin symmetry breaking in ΛN.

In this chapter, we propose the $K^-d \to \pi\Lambda N$ reaction with stopped kaons as a useful tool to study the isospin symmetry breaking in the ΛN interaction, how different $a_{\Lambda p}$ and $a_{\Lambda n}$ are, from the final state interactions of the reaction. Theoretically, the formulation of the $K^-d \to \pi\Lambda N$ scattering amplitude is constructed in the same way due to the isospin symmetry, and the effect of symmetry breaking can be put into the components of amplitudes, such as the ΛN scattering parameters. Information about scattering parameters may be derived by comparing sensitivities to scattering parameters in the spectra with experiments. Furthermore, for the qualitative discussions such as whether $a_{\Lambda p}$ or $a_{\Lambda n}$ is larger, by taking the ratio of the spectra of the two reactions, the effect of isospin symmetry breaking can be visualized. Experimentally, two reactions, $K^-d \to \pi^-\Lambda p$ and $K^-d \to \pi^0\Lambda n$ are initiated as the same K^-d and is distinguished by the charge of the pion in the final state. We formulate the scattering amplitudes of the $K^-d \to \pi^-\Lambda p$ and $K^-d \to \pi^0\Lambda n$ reactions. Then we discuss the possibility to extract the ΛN scattering parameters and the isospin symmetry breaking from the reactions.

5.2 Kinematics of $K^-d \to \pi\Lambda N$ reaction

Since we are interested in the invariant mass spectrum of ΛN for the $K^-d \to \pi\Lambda N$ reaction, we utilize the kinematical formulation introduced in Section 4.1. In the $K^-d \to \pi\Lambda N$ reaction, the deuteron is a probe so is at rest in the lab frame. The kaon beam is incident on the deuteron. In our study, we take the stopped kaon as the incident kaon which means that the momentum of the incident kaon is taken as zero at the lab. frame. Considering stopped kaons that have no directions, namely no direction in the initial state due to both the kaon and deuteron having no momentum, we can take the final pion momentum as a reference of the spatial coordinate for the final state without loss of generality.

In addition, taking the stopped kaon, the spin configuration of the ΛN system is fixed as the spin-triplet in the $K^-d \to \pi\Lambda N$ reaction. The spin of the ΛN system is either singlet or triplet. If one considers stopped kaons, the spin-triplet configuration dominates the ΛN final state interaction around its production threshold because the deuteron has spin 1 and the non-spin-flip S-wave interactions are the main contributions in the low-energy region. This is a good feature to fix the spin configuration of the ΛN system. It is also reported in Refs. [60, 147] that, thanks to the finite size of the deuteron, K^- in the atomic p-orbit is also absorbed by the S-wave K^-N interaction.

Moreover, once one fixes the reaction plane, the scattering amplitude does not depend on the azimuthal angle of Ω^*_Λ for unpolarized deuterons.

In our calculation, since the incident kaon momentum in the laboratory frame is fixed at 0 MeV/c, we introduce the ΛN invariant mass spectrum without $k_{\text{c.m.}}$ as

$$\begin{aligned} \mathcal{S}_N(M_{\Lambda N}) &\equiv k_{\text{c.m.}} \frac{\mathrm{d}\sigma}{\mathrm{d}M_{\Lambda N}} \\ &= \frac{M_d M_\Lambda M_N}{16\pi^3 E^2_{\text{c.m.}}} |\boldsymbol{p}_\pi| \, |\boldsymbol{p}^*_\Lambda| \int |\mathcal{T}_{\pi\Lambda N}|^2 \mathrm{d}\cos\theta^*_\Lambda \end{aligned} \tag{5.1}$$

where θ^*_Λ denotes the polar angle of the final Λ in the Λ-nucleon c.m. frame. The $K^-d \to \pi\Lambda N$ scattering amplitude $\mathcal{T}_{\pi\Lambda N}$ will be discussed in the next section.

5.3 Formulation of K^-d scattering amplitudes

In this section, we formulate the scattering amplitudes of the $K^-d \to \pi\Lambda N$ reactions by following Refs. [70–73] which is developed in order to study the hyperon resonance. One of the good advantages of the reaction is that it is initiated by the same K^-d system and includes $\pi^-\Lambda p$ and $\pi^0\Lambda n$ in the final states, which are isospin partners. Thus, we can use the same theoretical framework for these two final states and the formulation can be fixed by a better-known Λp channel to apply the uncertain Λn channel.

The Feynman diagrams that we consider in our calculation are given in Fig. 5.1 for the $K^-d \to \pi^-\Lambda p$ process (hereafter referred to as the Λp process) and Fig. 5.2 for the $K^-d \to \pi^0\Lambda n$ process (hereafter referred to as the Λn process). The initial K^- is absorbed by one of the nucleons in the deuteron as $K^-N \to \pi Y$ or $K^-N \to \bar{K}N$. In Dia. 1, the Λ hyperon produced by the K^- absorption scatters with another nucleon. This diagram, which we call Λ-exchange diagram, is our target diagram that contains

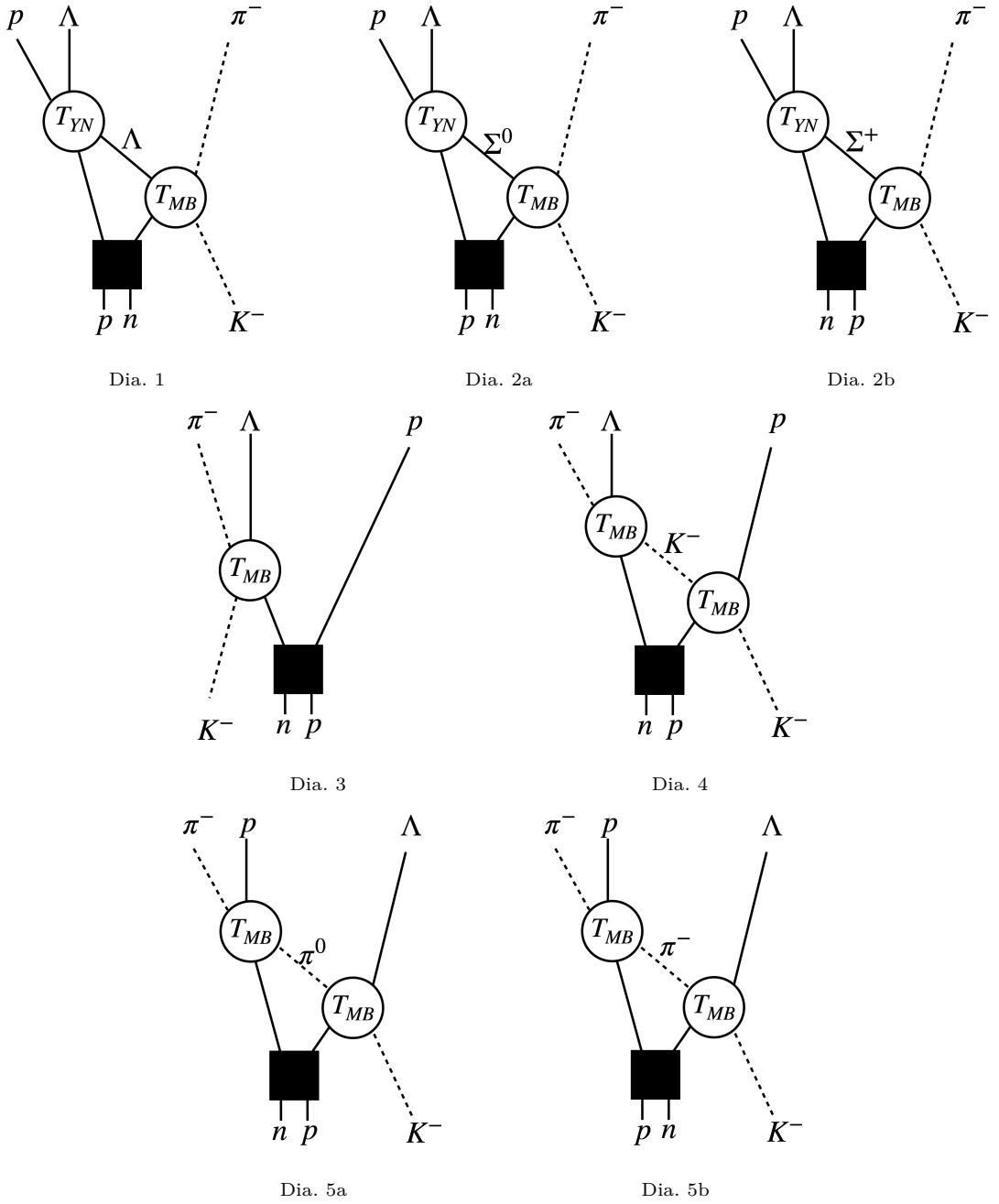

Fig.5.1 Feynman diagrams used for the calculation of the Λp process. In the diagrams, T_{MB} (T_{YN}) denotes the meson-baryon (hyperon-nucleon) amplitude scattering amplitude.

the final state interaction of ΛN. Diagram 2 has the Σ hyperon exchange and contains a transition amplitude of $\Sigma N \to \Lambda N$. In Dia. 3, which we call impulse approximation, the K^- absorption takes place without the final state interaction. In Dia. 4 the initial K^- scatters with one of the nucleons in the deuteron and rescatters with another nucleon. We call this diagram kaon-exchange. Diagrams 3 and 4 will turn out to be the main sources of the backgrounds. Diagram 5 has the pion-exchange with the final state interaction between a pion and a nucleon. We will see later that the pion-exchange diagram is negligibly small. The c.m. energies of these processes are low enough and one may use S-wave amplitudes. We use the observed hadron masses given in the Review of Particle Physics [1] in the following calculation.

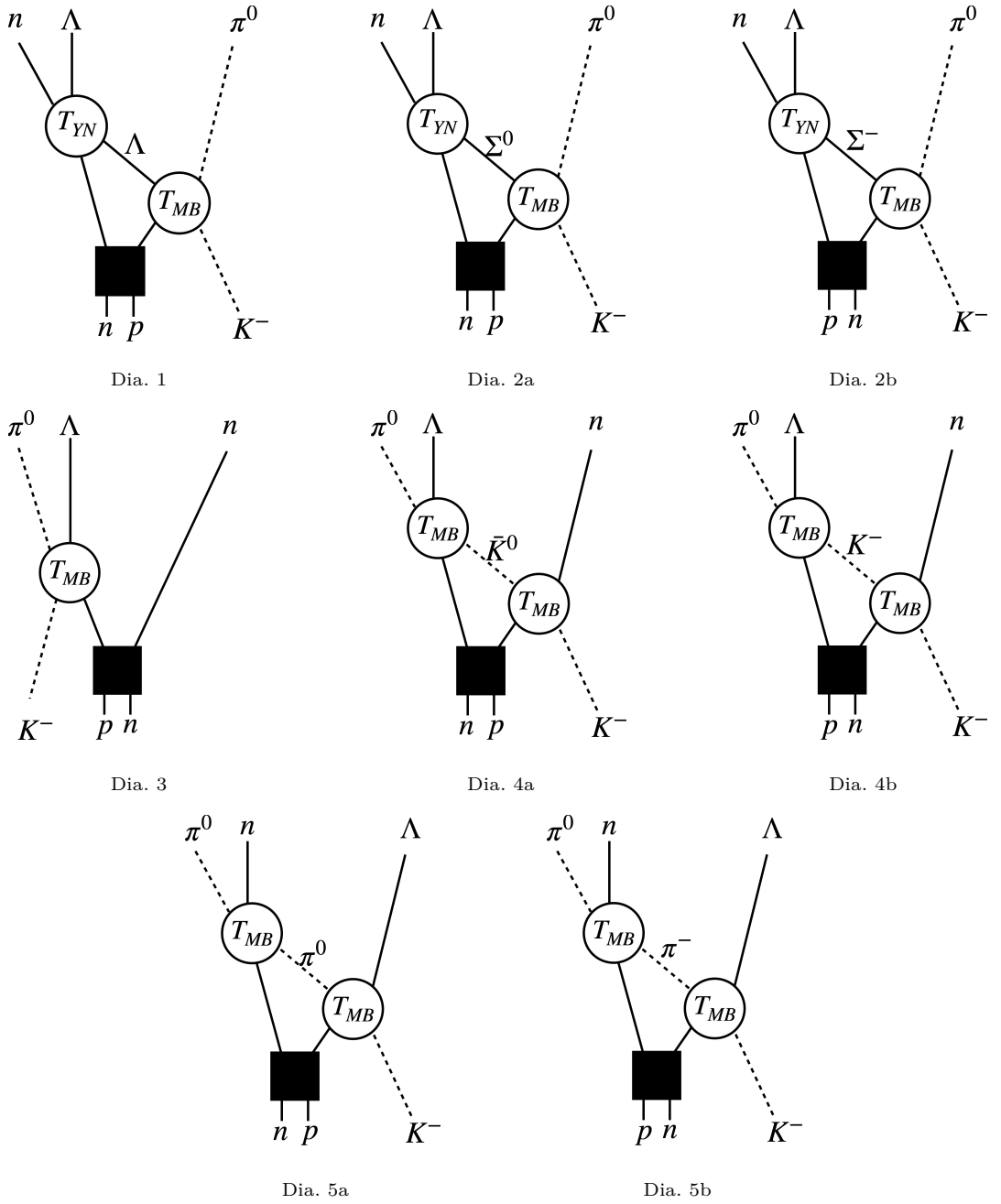

Fig.5.2 Same as in Fig. 5.1 but for the Λn process.

Diagram 1: Λ-exchange diagram as a example of T-matrix amplitude calculation

First, we formulate the amplitude of the Λ-exchange diagrams Dia. 1 in Figs. 5.1 and 5.2. We follow Ref. [71] which was the first work to develop this formulation. Here we explain the details of this formulation using this calculation as an example of T-matrix amplitude calculation.

We perform the calculation of the S-matrix of Dia. 1. Given the wavefunctions of the incoming kaon and the particles in the final state as plane waves, and writing the wavefunctions of the nucleons

in the deuteron as φ_i $(i = 1, 2)$, we find

$$S = 1 - \left(\prod_i \mathcal{N}_i\right) \int \mathrm{d}^4x_1 \int \mathrm{d}^4x_2 \int \frac{\mathrm{d}^4q}{(2\pi)^4} \frac{e^{-iq\cdot(x_1-x_2)}}{q_0 - \sqrt{\boldsymbol{q}^2 + M_\Lambda^2} + i\epsilon}$$
$$\times e^{ip_\Lambda\cdot x_1} e^{ip_N\cdot x_1} e^{ip_\pi\cdot x_2} e^{-ik\cdot x_2} e^{-ip_1^0 x_1^0} \varphi_1(\boldsymbol{x}_1)$$
$$\times e^{-ip_2^0 x_2^0} \varphi_2(\boldsymbol{x}_2)(-i)T_{K^-N\to\pi\Lambda}\,(-i)T_{\Lambda N}. \tag{5.2}$$

where $T_{K^-N\to\pi\Lambda}$ and $T_{\Lambda N}$ are the T-matrices of the $K^-N \to \pi\Lambda$ and the Λ-nucleon reactions, respectively. p_1 and p_2 are the momenta of nucleons inside the deuteron. The plane waves are normalized in a box with a unit volume, and the normalization factors of them are given by

$$\mathcal{N}_i = \begin{cases} \sqrt{\dfrac{1}{2\omega_i}} & \text{for mesons,} \\ \sqrt{\dfrac{2M_i}{2E_i}} & \text{for baryons.} \end{cases}$$

The integrations with respect to the time components x_1^0 and x_2^0 give energy conservations:

$$\int \mathrm{d}x_1^0\, e^{-i(p_1^0+q^0-p_\Lambda^0+p_N^0)} = 2\pi\delta(p_1^0 + q^0 - p_\Lambda^0 + p_N^0),$$
$$\int \mathrm{d}x_2^0\, e^{-i(p_2^0+k^0-q^0+p_\pi^0)} = 2\pi\delta(p_2^0 + k^0 - q^0 + p_\pi^0),$$

respectively. Furthermore, integrating with respect to q^0

$$\int \frac{\mathrm{d}q^0}{2\pi} \int \mathrm{d}x_1^0\, e^{-i(p_1^0+q^0-p_\Lambda^0+p_N^0)} \int \mathrm{d}x_2^0\, e^{-i(p_2^0+k^0-q^0+p_\pi^0)}$$
$$= \int \frac{\mathrm{d}q^0}{2\pi} 2\pi\delta(p_1^0 + q^0 - p_\Lambda^0 + p_N^0) 2\pi\delta(p_2^0 + k^0 - q^0 + p_\pi^0)$$
$$= 2\pi\delta(k^0 + p_d^0 - p_\Lambda^0 - p_N^0 - p_\pi^0), \tag{5.3}$$

we obtain the total energy conservation $k^0 + p_d^0 = p_\Lambda^0 + p_N^0 + p_\pi^0$. and q^0 has been fixed as $q^0 = k^0 + p_2^0 - p_N^0 = p_\Lambda^0 + p_\pi^0 - p_1^0$. Here we use again $p_1^0 + p_2^0 = p_d^0$.

For the spacial integrals, we introduce the relative coordinate between $\boldsymbol{x}_1$ and $\boldsymbol{x}_2$ as $\boldsymbol{R} = (\boldsymbol{x}_1 + \boldsymbol{x}_2)/2$ and $\boldsymbol{r} = \boldsymbol{x}_1 - \boldsymbol{x}_2$, and the deuteron wavefunction of the relative motion $\varphi(\boldsymbol{r})$. We assume that the deuteron wavefunction of the center of mass motion is the plane wave. In order to perform the spacial integrals, the two nucleon wavefunctions inside the deuteron, $\varphi_1(\boldsymbol{x}_1)$ and $\varphi_2(\boldsymbol{x}_2)$ are replaced to the deuteron wavefunctions as

$$\mathcal{N}_1\mathcal{N}_2\varphi_1(\boldsymbol{x}_1)\varphi_2(\boldsymbol{x}_2) \to \mathcal{N}_d e^{i\boldsymbol{p}_d\cdot\boldsymbol{R}}\varphi(\boldsymbol{r}) \tag{5.4}$$

where the deuteron wavefunction is normalized as

$$\int \mathrm{d}^3r\, |\varphi(\boldsymbol{r})|^2 = 1. \tag{5.5}$$

The integration in terms of $\boldsymbol{R}$ gives the total momentum conservation, while the integration of $\boldsymbol{r}$ gives the Fourier transformation of the deuteron wavefunction $\varphi(\boldsymbol{r})$ as

$$\int \mathrm{d}^3r\, \varphi(r)\, e^{i(-\boldsymbol{k}+\boldsymbol{p}_\pi-\boldsymbol{p}_\Lambda-\boldsymbol{p}_N+2\boldsymbol{q})\cdot\frac{\boldsymbol{r}}{2}} = \tilde{\varphi}(\boldsymbol{q} + \boldsymbol{p}_\pi - \boldsymbol{k}) \tag{5.6}$$

where we use the total momentum conservation. Note that $\tilde{\varphi}$ is defined in the deuteron rest frame same as the lab. frame, then $\boldsymbol{p}_d$ is dropped and the argument of $\tilde{\varphi}$ should be given in the lab. frame.

Here we introduce a specific form of the deuteron wave function in the momentum space $\tilde{\varphi}(\boldsymbol{r})$ which is used in this study. We neglect the small d-wave component of the deuteron wavefunction and use a parameterization of the S-wave component given by an analytic function in the CD-Bonn potential [148] as

$$\tilde{\varphi}(p) = \frac{1}{\sqrt{(2\pi)^3}} \sum_{j=1}^{11} \frac{C_j}{p^2 + m_j^2} \tag{5.7}$$

where C_j and m_j were determined in Ref. [148]. The argument of $\tilde{\varphi}$ in Eq. (5.9) is fixed by the momentum conservation of the vertex of the first-scattering.

Finally we obtain the S-matrix for the diagram 1 as

$$\begin{aligned} S = 1 - i\left(\prod_i \mathcal{N}_i\right)(2\pi)^4\delta^{(4)}(k + p_d - p_\Lambda - p_N - p_\pi) \\ \times T_{\Lambda N} \int \frac{d^3q}{(2\pi)^3} \frac{\tilde{\varphi}(\boldsymbol{q} + \boldsymbol{p}_\pi - \boldsymbol{k})}{q_0 - \sqrt{\boldsymbol{q}^2 + M_\Lambda^2} + i\epsilon}\, T_{K^- N \to \pi\Lambda}. \end{aligned} \tag{5.8}$$

Since in general the T-matrix is defined by

$$S = 1 - i\left(\prod_i \mathcal{N}_i\right)(2\pi)^4\delta^{(4)}(k + p_d - p_\Lambda - p_N - p_\pi)\mathcal{T},$$

we obtain the T-matrix corresponding to the diagram 1 $\mathcal{T}^{(1)}_{\pi\Lambda N}$ as

$$\begin{aligned} \mathcal{T}^{(1)}_{\pi\Lambda N} =& T_{\Lambda N}(M_{\Lambda N}) \int \frac{d^3q}{(2\pi)^3} \frac{2M_\Lambda}{q^2 - {M_\Lambda}^2 + i\epsilon} \\ & \times \tilde{\varphi}(\boldsymbol{q} + \boldsymbol{p}_\pi)\; T_{K^- N \to \pi\Lambda}(W) \end{aligned} \tag{5.9}$$

where $M_{\Lambda N}$ is the invariant mass of Λ and N in the final state, q is the momentum of the exchange Λ, $\tilde{\varphi}$ is the S-wave deuteron wavefunction in the momentum space, and W denotes the invariant mass of the initial kaon and the nucleon inside the deuteron. The amplitude $T_{\Lambda N}$ and $T_{K^- N \to \pi\Lambda}$ stand for the S-wave scattering amplitudes of the $\Lambda N \to \Lambda N$ and $K^- N \to \pi\Lambda$ processes, respectively. The charges of N and π are fixed in each process as shown in Figs. 5.1 and 5.2. For instance, $K^- N \to \pi\Lambda$ for the Λp process corresponds to $K^- n \to \pi^- \Lambda$.

The nonrelativistic propagator is extended to a relativistic one as

$$\frac{1}{q_0 - \sqrt{\boldsymbol{q}^2 + M^2} + i\epsilon} \simeq \frac{2M}{q^2 - M^2 + i\epsilon}$$

for simplicity of the calculation. With this approximation, we can perform the momentum integral of Eq. (5.9) analytically, which reduces the calculation costs a lot. For the detail of the momentum integral, see Appendix B.

For the baryon exchange diagrams, Dia. 1 and 2, q^0 and W are fixed as

$$q^0 = M_{K^-} + M_d - \left(M_2 - \frac{B_d}{2}\right) - p_\pi^0 \tag{5.10}$$

$$W = \left(M_1 - \frac{B_d}{2}\right) + M_{K^-} \tag{5.11}$$

where B_d is the binding energy of deuteron, $M_1(M_2)$ is the participant (spectator) nucleon mass in $K^-N \to \pi\Lambda$, and p^0_π is the energy of the final-state pion.

Diagram 2: Σ-exchange diagram

Next, as well as the foreground diagram, the Σ-exchange diagrams given by Dia. 2 in Figs. 5.1 and 5.2 are formulated as

$$\begin{aligned}\mathcal{T}^{(2)}_{\pi\Lambda N} = T_{\Sigma N\to\Lambda N}(M_{\Lambda N}) \int \frac{d^3q}{(2\pi)^3} \frac{2M_\Sigma}{q^2 - {M_\Sigma}^2 + i\epsilon} \\ \times \tilde{\varphi}(\boldsymbol{q} + \boldsymbol{p}_\pi)\ T_{K^-N\to\pi\Sigma}(W).\end{aligned} \tag{5.12}$$

Here q_0 and W are fixed as we do in Eqs. (5.10) and (5.11).

Due to charge conservation, the charge of the exchange Σ differs depending on which nucleon in the deuteron the kaon reacts with. As seen in Dia.2a of Fig. 5.1, the initial kaon reacts with the neutron in the deuteron and the charge of the pion in the final state is fixed as a negative charge, then the charge of Σ should be fixed as neutral charge. In the same way, the charge of the exchange Σ is specified in Dia.2a and b of Figs. 5.1 and 5.2.

Diagram 3: Impulse approximation

We consider the amplitudes of the impulse approximation given by Dia. 3. In this diagram, the nucleon in the deuteron which does not interact with the initial kaon is treated as a spectator. The amplitudes are calculated as

$$\mathcal{T}^{(3)}_{\pi\Lambda N} = T_{K^-N\to\pi\Lambda}(M_{\pi\Lambda})\ \tilde{\varphi}(\boldsymbol{p}_N) \tag{5.13}$$

where $\boldsymbol{p}_N$ is the momentum of the spectator nucleon in the rest frame of the deuteron.

Diagram 4: Kaon-exchange diagram

The kaon-exchange processes given by Dia. 4 can be calculated as

$$\begin{aligned}\mathcal{T}^{(4)}_{\pi\Lambda N} = T_{\bar{K}N\to\pi\Lambda}(M_{\pi\Lambda}) \int \frac{d^3q}{(2\pi)^3} \frac{\tilde{\varphi}(\boldsymbol{q} + \boldsymbol{p}_N)}{q^2 - M^2_{\bar{K}} + i\epsilon} \\ \times T_{K^-N\to\bar{K}N}(W).\end{aligned} \tag{5.14}$$

For $K^-d \to \pi^-\Lambda p$, the exchanged kaon is only K^-, while for $K^-d \to \pi^0\Lambda n$, K^- and $\bar{K}^0$ are allowed as the exchanged kaon due to charge conversion. For the kaon-exchange diagrams, q^0 is fixed as

$$q^0 = M_{K^-} + M_d - \left(M_2 - \frac{B_d}{2}\right) - p^0_N \tag{5.15}$$

with p^0_N the energy of the final-state nucleon and W is the same as Eq. (5.11).

Diagram 5: Pion-exchange diagram

We obtain the amplitudes for the pion-exchange processes given by Dia. 5 as

$$\begin{aligned}\mathcal{T}^{(5)}_{\pi\Lambda N} =& T_{\pi N\to\pi N}(M_{\pi N})\int\frac{d^3q}{(2\pi)^3}\frac{\tilde{\varphi}(\boldsymbol{q}+\boldsymbol{p}_\Lambda)}{q^2-M_\pi^2+i\epsilon}\\ &\times T_{K^-N\to\pi\Lambda}(W)\end{aligned} \tag{5.16}$$

where both π^0 and π^- are allowed as the exchanged pion for each process, $\boldsymbol{p}_\Lambda$ is the momentum of the final-state Λ baryon in the total c.m. frame. For the pion-exchange diagrams, q^0 is fixed as

$$q^0 = M_{K^-} + M_d - \left(M_2 - \frac{B_d}{2}\right) - p^0_\Lambda \tag{5.17}$$

with p^0_Λ the energy of the final-state Λ baryon and W is the same as Eq. (5.11).

Total, foreground and background amplitudes

The total amplitude for $K^-d\to\pi\Lambda N$ is defined by the sum of all amplitudes described above as

$$\mathcal{T}_{\pi\Lambda N} = \sum_j \mathcal{T}^{(j)}_{\pi\Lambda N}. \tag{5.18}$$

The amplitude of primary interest (the foreground amplitude) in our calculation for $K^-d\to\pi\Lambda N$ is given by the Λ-exchange diagram (Dia. 1 in Figs. 5.1 and 5.2) as

$$\mathcal{T}^{\rm FG}_{\pi\Lambda N} = \mathcal{T}^{(1)}_{\pi\Lambda N}, \tag{5.19}$$

and the background amplitude is defined by removing the foreground amplitude from the total amplitude as

$$\mathcal{T}^{\rm BG}_{\pi\Lambda N} = \sum_{j\neq 1} \mathcal{T}^{(j)}_{\pi\Lambda N}. \tag{5.20}$$

The relative phases of these amplitudes are safely fixed within the formulation. In the next section, we show the fundamental amplitudes included in the amplitudes we have obtained above. The meson-baryon scattering amplitudes are calculated by using the chiral unitary approach in which the amplitudes are obtained by resumming the interaction kernel given by the chiral perturbation theory. The interaction kernels are obtained at the tree level, having real values. The baryon-baryon interactions are parametrized by the effective range expansion and the values at the threshold are given by the scattering length which is real for the ΛN interaction. In this way, the phases of the two-body amplitudes are fixed without any ambiguities.

The isospin breaking effects on the T-matrix of the reaction $\mathcal{T}$ are introduced by using the observed masses for the exchanged particles and through the amplitudes of the absorption processes and the final state interactions. The details of the isospin breaking of these amplitudes are described below.

5.3.1 Hyperon-nucleon and meson-baryon amplitudes

In this section, we explain the fundamental amplitudes which constitute K^-d scattering amplitudes, such as the hyperon-nucleon and meson-baryon amplitudes.

Λ-nucleon amplitude

We parametrize the low-energy S-wave ΛN scattering amplitude by the scattering length $a_{\Lambda N}$ and the effective range $r_{\Lambda N}$ given by

$$T_{\Lambda N} = \mathcal{N} \frac{1}{-\frac{1}{a_{\Lambda N}} + \frac{1}{2} r_{\Lambda N} p_\Lambda^{*2} - i p_\Lambda^*} \tag{5.21}$$

where p_Λ^* is the momentum in the Λ-nucleon c.m. frame, and the kinematic factor $\mathcal{N}$ is given by

$$\mathcal{N} = -\frac{8\pi M_{\Lambda N}}{\sqrt{(2M_Y)(2M_2)(2M_f)(2M_\Lambda)}} \tag{5.22}$$

for the $YN_2 \to \Lambda N_f$ process, where M_Y, M_2 and M_f are the masses of Y, N_2 and N_f, respectively. We use the observed baryon masses for each channel, and this kinematic factor is also used for the $\Sigma N \to \Lambda N$ transition.

In our formulation, the spin-flip of the baryon-baryon interaction does not occur due to the stopped kaon thus we can only consider the spin-triplet of the ΛN interaction. The experimentally obtained $a_{\Lambda N}$ and $r_{\Lambda N}$ of the spin-triplet Λ-proton are $a_{\Lambda p}^t = -1.56^{+0.19}_{-0.22}$ fm and $r_{\Lambda p}^t = 3.7^{+0.6}_{-0.6}$ fm, respectively via the $pp \to K^+\Lambda p$ reaction [4]. On the other hand, the Λ-neutron interaction is not measured separately. The same value as the parameters of Λp is tentatively used as that of Λn. If there is the isospin symmetry breaking in the ΛN system, there should be a difference between $a_{\Lambda p}$ and $a_{\Lambda n}$, and $r_{\Lambda p}$ and $r_{\Lambda n}$. The sensitivity of the ΛN scattering parameters to the cross section of the reaction will be discussed in Section 5.4.4.

$\Sigma N \to \Lambda N$ transition amplitude

For the $\Sigma N \to \Lambda N$ transition amplitude $T_{\Sigma N \to \Lambda N}$, we employ the unitarity of S-matrix in the isospin-doublet ΛN and ΣN channels. With the diagonal ΛN and ΣN amplitudes given, we determine the off-diagonal amplitude $\Sigma N \to \Lambda N$ according to the unitarity. The diagonal ΛN and ΣN amplitudes at their threshold are fixed by the scattering lengths. For the ΣN amplitude, we first adopt $a_{\Sigma N} = 1.68 - i2.35$ fm which is obtained by the Nijmegen NSC97f potential [29]. We also compare the results with $a_{\Sigma N} = -3.83 - i3.01$ fm taken from the Jülich '04 potential [34].

The unitarity is implemented to the normalized transition amplitude f, which is defined by $T \equiv \mathcal{N} f$ with the kinematical factor $\mathcal{N}$ given in Eq. (5.22), as

$$F = \left(-V^{-1} - iP\right)^{-1} \tag{5.23}$$

where F, V, and P stand for the matrices of the scattering amplitudes, the interaction kernels, and the momenta, respectively, and are defined as

$$F = \begin{pmatrix} f_{\Lambda N} & f_{\Sigma\Lambda} \\ f_{\Sigma\Lambda} & f_{\Sigma N} \end{pmatrix}, \tag{5.24}$$

$$V = \begin{pmatrix} v_{11} & v_{12} \\ v_{12} & v_{22} \end{pmatrix}, \tag{5.25}$$

$$P = \begin{pmatrix} p_\Lambda^* & 0 \\ 0 & p_\Sigma^* \end{pmatrix}. \tag{5.26}$$

Table 5.1 Model parameters in a unit of MeV^{-1}

$a_{\Sigma N}$	$1.68 - i2.35$ fm (NSC97f)	$-3.83 - i3.01$ fm (Jülich '04)
v_{11}	8.3×10^{-5}	2.1×10^{-2}
v_{12}	6.5×10^{-3}	4.4×10^{-2}
v_{22}	8.8×10^{-3}	7.1×10^{-2}

Here, p^*_Λ and p^*_Σ in P are the momenta of Λ and Σ in the Λ-nucleon c.m. frame, respectively. Note that p^*_Σ is pure imaginary when one considers the energy region below the ΣN threshold. Here we assume that each v_{ij} model parameter is constant.

By using Eq. (5.23), we obtain the off-diagonal amplitude $f_{\Sigma N\to\Lambda N}$ from the unitarity of S-matrix. The model parameters are determined so as to reproduce the scattering lengths of the ΛN and ΣN at their thresholds:

$$f_{\Lambda N} = -a_{\Lambda N}, \tag{5.27}$$
$$f_{\Sigma N} = -a_{\Sigma N} = -(A - iB) \tag{5.28}$$

with the spin-triplet isospin-doublet ΛN scattering length $a_{\Lambda N}$ and ΣN scattering length $a_{\Sigma N} = A - iB$ where A and B are real. We obtain the matrix V:

$$v_{11} = \frac{-\kappa_\Sigma B + a_{\Lambda N}\kappa_\Lambda(1 - \kappa_\Sigma A)}{\kappa_\Lambda(1 - \kappa_\Sigma A + \kappa_\Sigma B a_{\Lambda N}\kappa_\Lambda)}, \tag{5.29}$$

$$v_{12} = -\frac{\sqrt{B(1 - 2\kappa_\Lambda A + \kappa_\Sigma^2 A^2 + \kappa_\Sigma^2 B^2)(1 + a_{\Lambda N}^2\kappa_\Lambda^2)}}{\sqrt{\kappa_\Lambda}(1 - \kappa_\Sigma A + \kappa_\Sigma a_{\Lambda N} B\kappa_\Lambda)}, \tag{5.30}$$

$$v_{22} = \frac{A - \kappa_\Sigma A^2 - \kappa_\Sigma B^2 + a_{\Lambda N} B\kappa_\Lambda}{1 - \kappa_\Sigma A + \kappa_\Sigma a_{\Lambda N} B\kappa_\Lambda} \tag{5.31}$$

where $\kappa_\Lambda = p^*_\Lambda$ at the ΣN threshold and $\kappa_\Sigma = -ip^*_\Sigma$ at the ΛN threshold. All the v_{ij} parameters are real. The determined v_{ij} parameters are summarized in Table 5.1. In these calculations, we use the isospin-averaged masses to obtain the kinematical variables and find $\kappa_\Lambda = 283.8$ MeV and $\kappa_\Sigma = 282.6$ MeV. In the following calculations, we introduce the known isospin breaking effect into the transition amplitude $T_{\Sigma N\to\Lambda N}$ through the kinematic factor $\mathcal{N}$ given in Eq. (5.22). Anyhow the isospin breaking effects on the transition amplitude are irrelevant to the cross sections of the $K^- d \to \Lambda N$ reactions around the ΛN threshold because the Σ-exchange diagram itself provides little contribution there as we will see below in the next section.

$\bar{K}N \to MB$ amplitude

The $\bar{K}N \to \bar{K}N$, $\bar{K}N \to \pi\Lambda$ and $\bar{K}N \to \pi\Sigma$ amplitudes are given by the chiral unitary approach using the parameters in Ref. [77] similarly to Refs. [70–73]. The isospin breaking of these amplitudes is introduced by using the physical hadron masses in the loop functions and kinematic factors of the chiral unitary approach. The interaction kernels are given by the Weinberg-Tomozawa interaction and do not contain explicit flavor symmetry breaking. The subtraction constants are also determined in an isospin symmetric way. In Fig. 5.3, we plot the modules of the $\bar{K}N$ scattering amplitudes used in

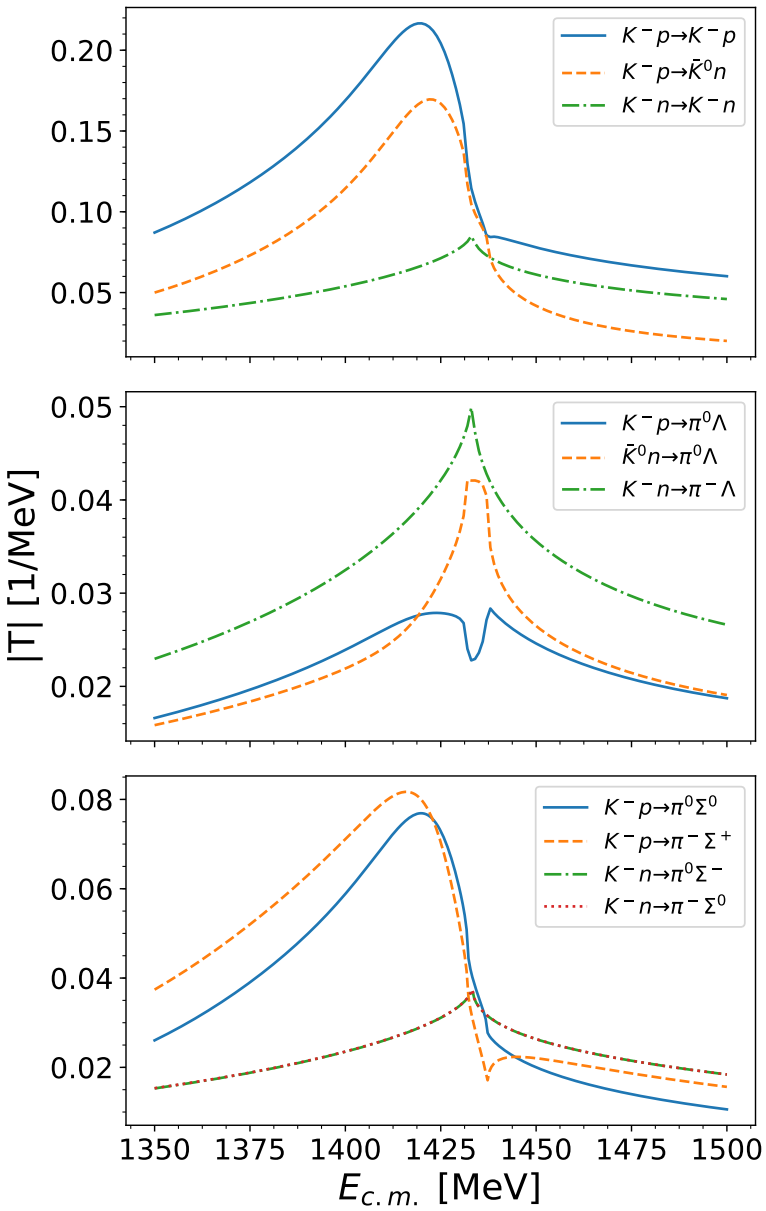

Fig.5.3 Modules of $\bar{K}N \to \bar{K}N$, $\bar{K}N \to \pi\Lambda$ and $\bar{K}N \to \pi\Sigma$ scattering amplitude obtained in the chiral unitary approach using the parameters in Ref. [77]

this work. The isospin breaking of the $\bar{K}N$ thresholds is properly introduced by using the observed masses in the loop functions. It is known that the chiral unitary amplitudes reproduce the observed scattering cross sections of $K^-p \to K^-p$ and to various channels, say $\pi^-\Sigma^+$ and $\pi^+\Sigma^-$, in the low-energy region well. (See, for instance, Ref. [80].) Around the $\bar{K}N$ thresholds the isospin breaking effects look large. There, the theoretical description of the $\bar{K}N$ scattering amplitudes could be less reliable, because isospin breaking was not considered in the interaction kernels, although the isospin breaking effects may be enhanced around the thresholds.

πN amplitude

For $\pi N \to \pi N$ scattering, we use the empirical amplitude $t_{\pi N}$ [149] which is based on the available scattering data. It has been constructed isospin-symmetrically. Our amplitude $T_{\pi N}$ is obtained by

Table 5.2 The values of the hadron masses we use in this chapter.

M_p	M_n	M_Λ	M_{Σ^+}	M_{Σ^0}	M_{Σ^-}
938.272 MeV	939.565 MeV	1115.683 MeV	1189.370 MeV	1192.642 MeV	1197.449 MeV
	M_{K^-}	$M_{\bar{K}^0}$	M_{π^-}	M_{π^0}	
	493.677 MeV	497.611 MeV	139.570 MeV	134.977 MeV	

$t_{\pi N}$ with a kinematic factor as follows:

$$T_{\pi N} = -\frac{8\pi M_{\pi N}}{\sqrt{k_i}\sqrt{k_f}\sqrt{2M_i}\sqrt{2M_f}} t_{\pi N} \tag{5.32}$$

where $M_{\pi N}$ in the invariant mass of πN, $k_i(k_f)$ is the momentum of the initial (final) pion, $M_i(M_j)$ is the mass of the initial (final) nucleon. The isospin breaking effect in the πN amplitude $T_{\pi N}$ comes from the kinematic factor. We will see below that the contributions of the π-exchange are negligible, and thus the introduction of the isospin breaking in the πN amplitudes is not important.

5.4 Results

In this section, we show numerical results of the calculation for the $K^- d \to \pi^- \Lambda p$ and $K^- d \to \pi^0 \Lambda n$ reactions. Since we do not incorporate the Coulomb correction to the amplitude, our calculations give quantities that should be compared to the experimental values corrected for the effect of Coulomb.

We use the most probable values of the observed spin-triplet Λ-proton scattering parameters $a_{\Lambda p}^{\rm ex} = -1.56$ fm and $r_{\Lambda p}^{\rm ex} = 3.7$ fm as both the Λ-proton and Λ-neutron scattering parameters in Eq. (5.21), and use $a_{\Sigma N} = 1.68 - i2.35$ fm (NSC97f). The parameter sensitivity will be discussed later. We use the observed hadron masses given in the Review of Particle Physics [1] in the following calculation to incorporate the isospin symmetry breaking effect in hadron masses. The hadron masses are summarized in Table 5.2

5.4.1 Tests of our formulation: Comparison to the previous experiment of $K^- d \to \pi^- \Lambda p$ reaction

In order to check the consistency of our formulation with existing experimental data, we first compare our calculation with the past experiments of $K^- d \to \pi^- \Lambda p$ with stopped K^-.

First, we show the proton kinetic energy $T_p = E_p - M_p$ spectrum in Fig. 5.4 together with the experimental data in Ref. [52]. Our calculation is multiplied by a constant to adjust the height to the data. In Ref. [52], they have shown the number counts on the $K^- d \to \pi^- \Lambda p$ reaction with stopped K^- as a function of the kinetic energy of the emitted proton, T_p. In their result, a bump structure was found around $T_p = 30$ MeV, but it was not reproduced in the previous theoretical calculation [60]. Reference [52] mentioned that the bump structure would be explained by the effect of the $\Sigma(1385)$ resonance. Nevertheless, it is unnatural that $\Sigma(1385)$ resonance, coupling to $K^- N$ in the P-wave, appears in the relevant energy region of this reaction. Our calculation reproduces nicely the bump structure seen in the experimental data without introducing the $\Sigma(1385)$ resonance. In our

calculation, we take into account several diagrams with their interference and the bump structure is actually explained by the interference between the Σ-exchange and other contributions coming from the foreground, the impulse and the kaon-exchange diagrams. The theoretical line shown in Ref. [52] considered only the impulse and Σ-Λ conversion effects without their interference. Our calculation shows that one does not have to introduce the Σ(1385) resonance in the calculation of such low-energy $\bar{K}N$ scattering.

Next, we show the Λp invariant mass spectrum in comparison with the experimental data [53] as plotted in Fig. 5.5. In Ref. [53], they have measured the number of counts on the $K^- d \to \pi^- \Lambda p$ reaction with stopped K^- and shown it as a function of the Λp invariant mass. It was pointed out in Refs. [67, 68] that only events with proton recoil momenta more than 75 MeV/c were counted in Ref. [53]. Thus, in order to compare our result with the experimental data given in Ref. [53], we make a similar cut on proton momenta in our calculation. Our calculation reproduces well the rapid increase at the threshold observed in the experimental data. The Λp invariant mass spectrum without the proton momentum cutoff will be shown in Fig. 5.6 of the next section.

The comparison of the two experimental results with our formulation shows that our formulation works well.

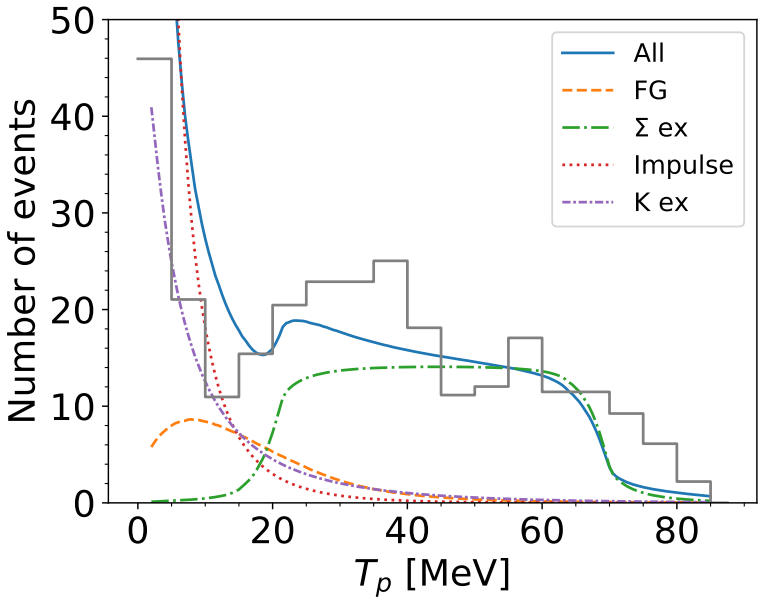

Fig.5.4 Proton kinetic energy T_p spectrum for $K^- d \to \pi^- \Lambda p$ reaction in comparison with the experimental data taken from Ref. [52].

5.4.2 Invariant mass spectrum and background reduction

We are interested to see if we can extract the information on the scattering parameters of the ΛN from the spectrum of the $K^- d \to \pi \Lambda N$ reaction. In particular, it is important that whether the contribution of the foreground diagram which includes the ΛN amplitude is seen in the spectrum. We show the ΛN invariant mass spectra for the Λp process and Λn process where θ^*_Λ is integrated from 0 to π in Fig. 5.6. Here we use the excitation energy $E_{\Lambda N}$ defined from the threshold as

$$E_{\Lambda N} \equiv M_{\Lambda N} - (M_\Lambda + M_N) \tag{5.33}$$

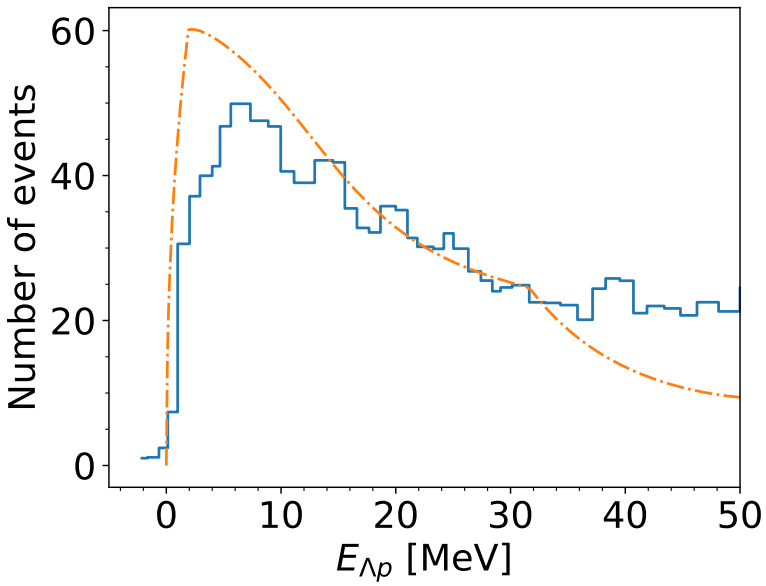

Fig.5.5 Λp invariant mass spectrum for $K^- d \to \pi^- \Lambda p$ reaction in comparison with the experimental data taken from Ref. [53]. The theoretical spectrum is obtained by removing the events with the proton momentum less than 75 MeV/c.

instead of the invariant mass itself. The foreground and background separated spectra are also plotted in Fig. 5.6. As can be seen in these plots, the background contribution dominates the total spectrum. Therefore, it may be difficult to extract the scattering properties of ΛN from the invariant spectrum. We decompose the spectra into their components and look for appropriate kinematic conditions to reduce the background contribution.

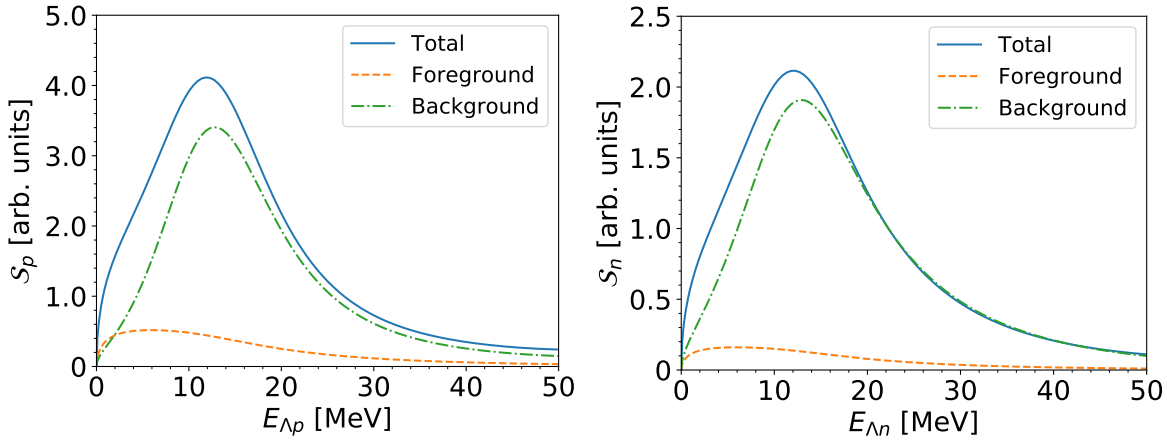

Fig.5.6 Λp invariant mass spectra for the Λp process (above) and the Λn process (below) with stopped kaons. The horizontal axis represents the excitation energy from the threshold in a unit of MeV. The solid, dashed, dash-dotted lines indicate the contributions of the total amplitudes, the foreground amplitude (only Dia. 1 in Figs. 5.1 and 5.2), the background amplitudes (the diagrams other than Dia. 1).

In Fig. 5.7, we show the decomposed components of the spectra. As seen in the figure the impulse diagram gives the largest contribution and dominates the background. The contribution from the kaon-exchange diagram is the second largest and is comparable with the foreground diagram. The Σ and π-exchange diagrams give tiny contributions. In particular, the π-exchange contribution is found

to be negligibly small in the range of the excitation energy which we consider here. For the excitation energy higher than 40 MeV, the contribution from the Σ-exchange diagram becomes comparable to the foreground but now we only focus on the threshold of ΛN so it does not matter.

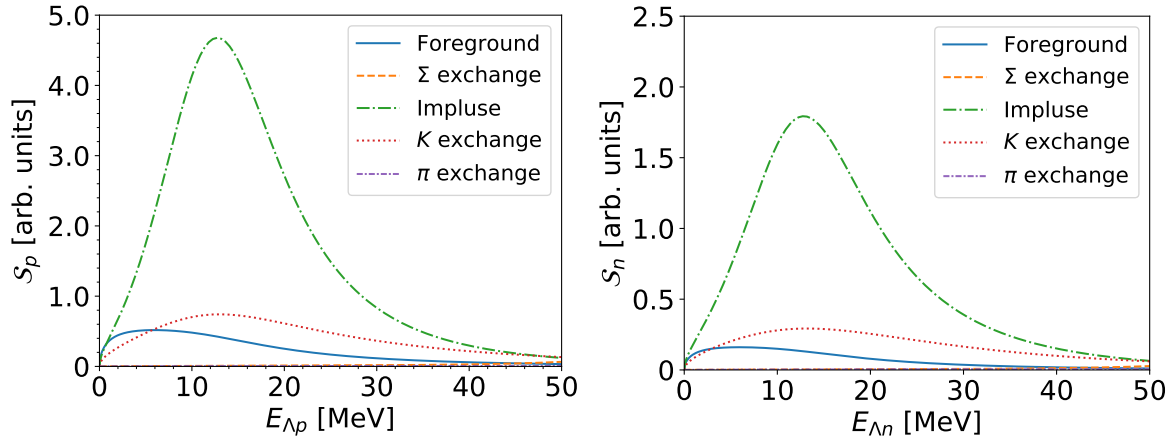

Fig.5.7 Decomposed background contributions of the Λp and Λn processes. The solid, dashed, dash-dotted, dotted, dash-dotted, and density dash-dotted lines show the contributions from the foreground, Σ-exchange, impulse, K exchange, and π-exchange diagrams, respectively.

In order to better see the contribution of the foreground diagram, it is necessary to reduce the background effects. We discuss the background reduction in the ΛN invariant mass spectrum for the $K^- d \to \pi\Lambda N$ reaction by controlling the kinematical condition.

Let us examine the angular dependence of the cross section for the impulse diagram. With a stopped kaon the final pion is emitted in the opposite direction to the Λ in the laboratory frame because the initial nucleon in the deuteron has a small Fermi momentum thanks to the small deuteron binding energy. Thus, the impulse diagram gives a larger contribution for larger θ^*_Λ. The kaon-exchange diagram has also similar angular dependence because the exchange kaon also has a small momentum for a stopped initial kaon. Therefore, the main background diagrams, Dias. 3 and 4, have a smaller contribution for smaller θ^*_Λ. This can be checked by plotting a ratio defined by

$$\mathcal{R}_B = \frac{|\mathcal{T}^{\rm BG}_{\pi\Lambda N}|^2}{|\mathcal{T}^{\rm FG}_{\pi\Lambda N}|^2}. \tag{5.34}$$

As seen in Fig. 5.8, $\mathcal{R}_B$ is large at $\theta^*_\Lambda > 3\pi/4$. In order to reduce the background, we should avoid this region. In $E_{\Lambda N} \gtrsim 40$ MeV, $\mathcal{R}_B$ is large independently of θ^*_Λ. This is because the contribution of Σ-exchange increases as $E_{\Lambda N}$ approaches the ΣN threshold seen in Fig. 5.7.

In order to reduce the background contributions, let us propose to restrict the integral region of the angle θ^*_Λ as 0 to $\pi/2$. In Fig. 5.9, we show the total, foreground, and background ΛN mass spectra for the Λp process integrated within the range $[0, \pi/2]$. From Fig. 5.9, it can be seen that the background contributions are substantially suppressed for $E_{\Lambda p} < 30$ MeV. We also plot the ΛN mass spectrum for each contribution in Fig. 5.10, showing that the foreground contribution dominates over the other contributions of $E_{\Lambda p} < 40$ MeV. In particular, the contribution of the pion-exchange diagram is negligibly small. The Σ-exchange contribution is also quite small $E_{\Lambda p} < 30$ MeV, but it gets comparable to the foreground contribution for $E_{\Lambda p} > 40$ MeV. Hereafter the integral of θ^*_Λ is performed from 0 up to $\pi/2$. We also take $\pi/2$ for the upper limit of the angular integrals of the Λn process.

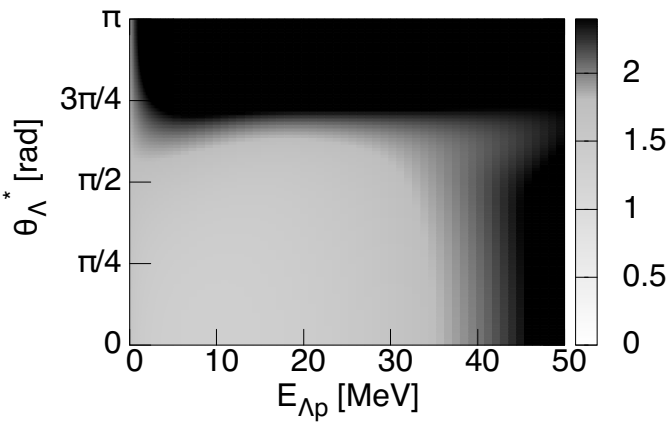

Fig.5.8 Two dimensional plot of $\mathcal{R}_B$ as a function of θ^*_Λ and $E_{\Lambda N}$ for the Λp process.

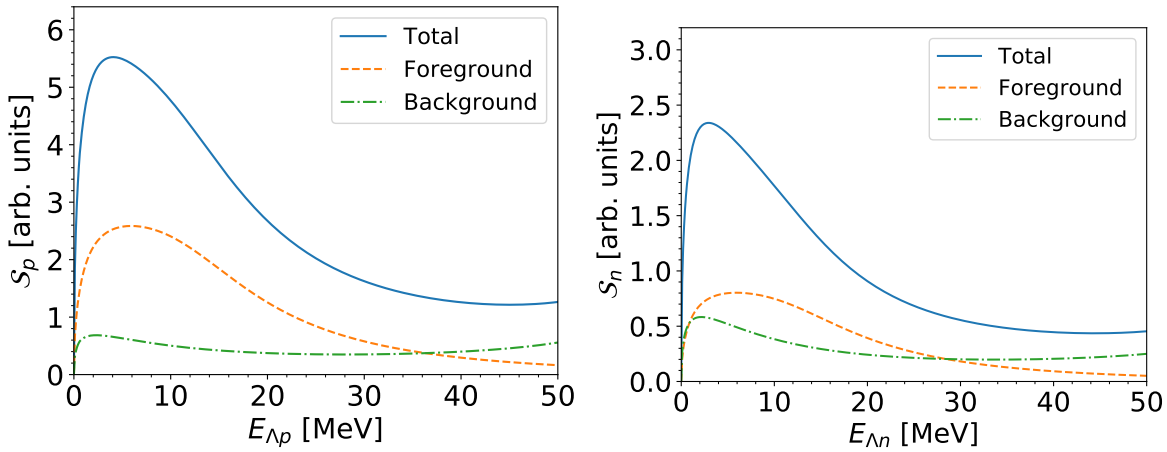

Fig.5.9 Λp mass spectra for the Λp process (above) and the Λn process (below) integrated in the range $[0, \pi/2]$ with stopped kaon. The horizontal axis represents the excitation energy from the threshold in a unit of MeV. The solid, dashed, dash-dotted lines indicate the contributions of the total amplitudes, the foreground amplitude (only Dia. 1 in Figs. 5.1 and 5.2), the background amplitudes (the diagrams other than Dia. 1).

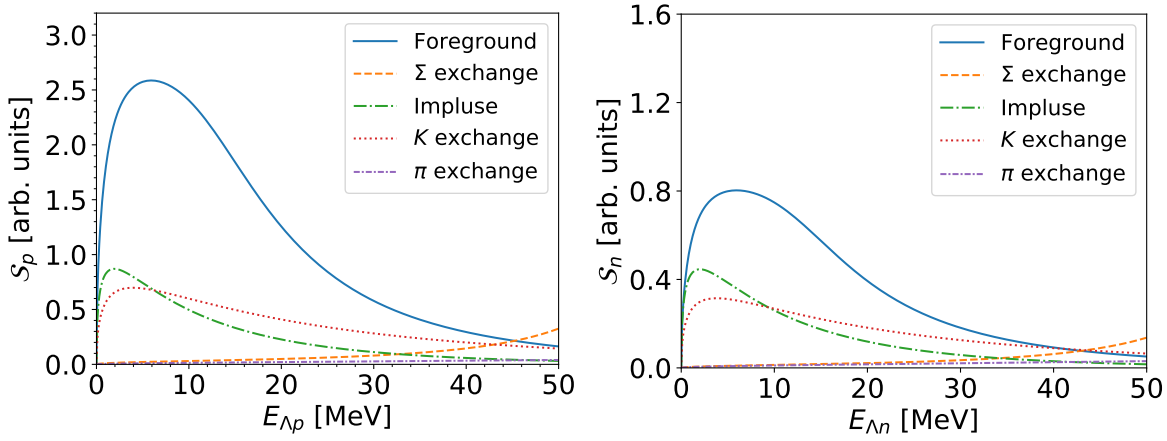

Fig.5.10 Decomposed background contributions of the Λp process (above) and Λn process (below) integrated in the range $[0, \pi/2]$. The solid, dashed, dash-dotted, dotted, dash-dotted, and density dash-dotted lines show the contributions from the foreground, Σ-exchange, impulse, K exchange, and π-exchange diagrams, respectively.

The purpose of this study is to see isospin symmetry breaking in the ΛN interaction. It is very important to control the isospin symmetry breaking effects from other sources. In particular, there is a large isospin breaking effect around the $\bar{K}N$ thresholds in the $\bar{K}N \to MB$ amplitudes as seen in Fig. 5.3. If possible, it is better to avoid this energy region by controlling the kinematical variables of the final state. In the diagrams expect the impulse approximation (Dia. 3) in Figs. 5.1 and 5.2, the energy of the first scattering is determined by those of the initial kaon and the participant nucleon in the deuteron. Thus, the first scattering cannot be controlled by the final state kinematics. For the second scattering, on the other hand, the c.m. energy is dependent on the kinematics of the final state and is controllable.

In order to see isospin breaking of the $\bar{K}N \to \pi\Lambda$ amplitudes, let us plot the following ratio of the $\bar{K}N \to \pi\Lambda$ amplitudes in Fig. 5.11:

$$\mathcal{R}_V(W) = \frac{|T_{K^-p\to\pi^0\Lambda} - T_{\bar{K}^0n\to\pi^0\Lambda}|}{\sqrt{2}|T_{K^-n\to\pi^-\Lambda}|}. \tag{5.35}$$

The ratio should be unity if the amplitude is isospin symmetric. This figure shows the large isospin breaking effect around the threshold region, 1420 MeV $< W <$ 1450 MeV. The c.m. energy of the second scattering is determined by the final state momenta. In order to find kinematic conditions in the final state corresponding a large isospin breaking effect in the $\bar{K}N \to \pi\Lambda$ amplitudes, we show the c.m. energy W of $\pi\Lambda$ as a function of θ^*_Λ in Fig. 5.12 for several $E_{\Lambda p}$. One can see that if one wants to avoid the large isospin breaking area 1420 MeV $< W <$ 1450 MeV for the $\bar{K}N \to \pi\Lambda$ amplitudes, smaller angles are favorable, such as $\theta^*_\Lambda < \pi/2$. This implies that our integral region of θ^*_Λ is in this safe range.

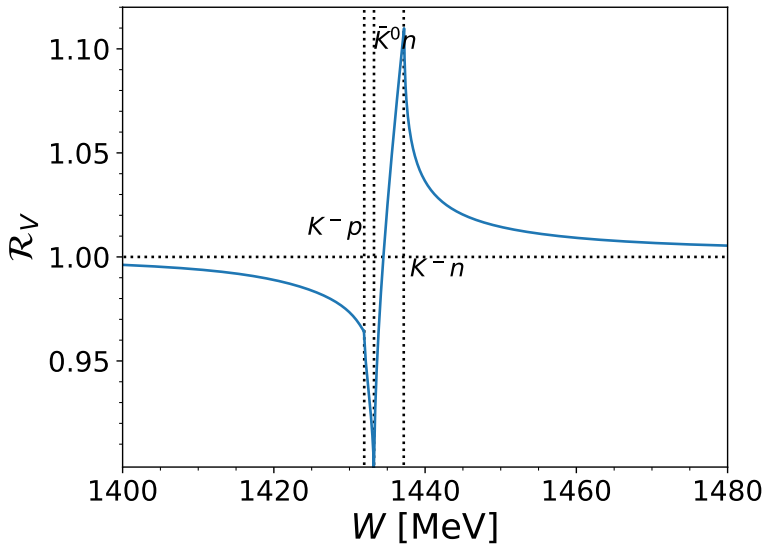

Fig.5.11 Ratio (5.35) for the $\bar{K}N \to \pi\Lambda$ amplitudes as a function of the c.m. energy of $\pi\Lambda$. The thresholds of K^-p, $\bar{K}^0n$ and K^-n are at 1431.95, 1433.24 and 1437.18 MeV, respectively.

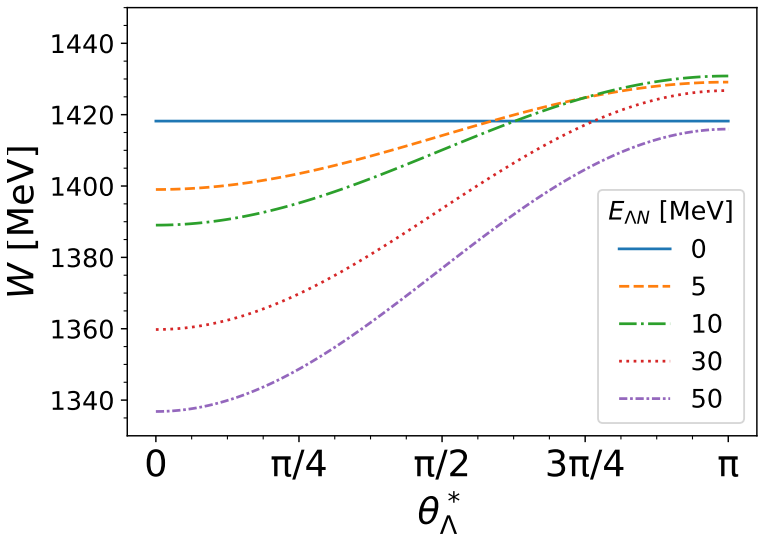

Fig.5.12 Center-of-mass energy W of $\pi\Lambda$ as a function of θ^*_Λ for several $E_{\Lambda p}$.

5.4.3 Sensitivity to $a_{\Lambda N}$, $r_{\Lambda N}$ and $a_{\Sigma N}$

In the previous section, the background effect and the effect of the isospin symmetry breaking in $\bar{K}N \to \pi\Lambda$ could be reduced by restricting the angle of integration to the range of 0 to $\pi/2$ in order to see the foreground contribution more clearly in the ΛN invariant mass spectrum. In this section, we discuss the sensitivity of $a_{\Lambda N}$, $r_{\Lambda N}$ and $a_{\Sigma N}$ after restricting the angle.

First, we evaluate the sensitivity of the invariant mass spectra of the Λp process by changing the values of $a_{\Lambda p}$ and $r_{\Lambda p}$ within the experimental errors in order to see the experimental uncertainties on the Λp scattering parameters. The result is shown in Fig. 5.13 using $a_{\Sigma N} = 1.68 - i2.35$ fm (NSC97f) and Fig. 5.14 using $a_{\Sigma N} = -3.83 - i3.01$ fm (Jülich '04). In each upper plot, we change the value of the scattering length within $a_{\Lambda p} = -1.56^{+0.19}_{-0.22}$ fm with fixing the effective range as $r_{\Lambda p} = 3.7$ fm, while we vary the value of the effective range within $r_{\Lambda p} = 3.7^{+0.6}_{-0.6}$ fm with $a_{\Lambda p} = -1.56$ fm in each lower plot. From Figs. 5.13 and 5.14, one can see that the Λp mass spectrum changes in the regions of the lower excitation energies $0 < E_{\Lambda p} < 15$ MeV when $a_{\Lambda p}$ is varied, and it changes in $5 < E_{\Lambda p} < 30$ MeV when $r_{\Lambda p}$ is varied.

Comparing Figs. 5.13 and 5.14, we find that the two models have little difference in the low-energy region now we consider, while at $E_{\Lambda p} > 40$ MeV the spectrum using $a_{\Sigma N} = 1.68 - i2.35$ fm (NSC97f) increases as increase of $E_{\Lambda p}$ and that using $a_{\Sigma N} = -3.83 - i3.01$ fm (Jülich '04) does not.

Next, we calculate the sensitivity of the invariant mass spectra of the Λn process. In order to see isospin symmetry breaking, we change the scattering parameters for the Λn process, $a_{\Lambda n}$ and $r_{\Lambda n}$, within $\pm 10\%$ of the experimentally determined values for Λp scattering. In Fig. 5.15 and Fig. 5.16 we show the calculated spectra with different $a_{\Lambda n}$ and $r_{\Lambda n}$ for the Λn process. In each upper plot, we change $a_{\Lambda n}$, while we vary $r_{\Lambda n}$ in each lower plot. One can see from the plots the invariant mass spectra change significantly in the regions $0 < E_{\Lambda n} < 15$ MeV for the scattering length and less significantly $5 < E_{\Lambda p} < 30$ MeV for the effective range. Again we also compare the results with different values from NSC97f in Fig. 5.15 and Jülich '04 in Fig. 5.16.

We can see that the shapes of the spectra with NSC97f and Jülich '04 are different above 40 MeV,

which is approaching the ΣN threshold, while they are almost the same below 40 MeV. Thus, we could determine the ΛN scattering properties insensitively to the value of $a_{\Sigma N}$ from the invariant mass spectra for $E_{\Lambda N} < 40$ MeV.

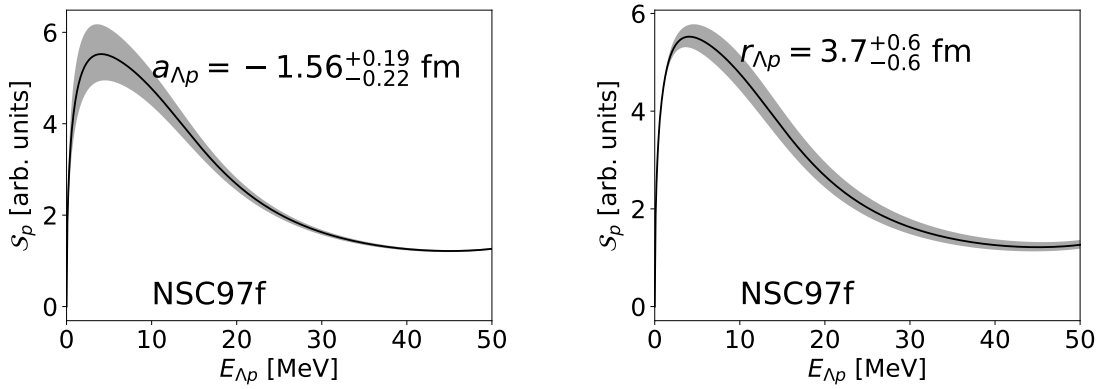

Fig.5.13 Λp invariant mass spectra calculated with different $a_{\Lambda p}$ and $r_{\Lambda p}$ values for the Λp process. In the upper plot the value of the scattering length is changed within $a_{\Lambda p} = -1.56^{+0.19}_{-0.22}$ fm, while the value of the effective range varies within $r_{\Lambda p} = 3.7^{+0.6}_{-0.6}$ fm in the lower plot. For the two plots $a_{\Sigma N} = 1.68 - i2.35$ fm (NSC97f) is used.

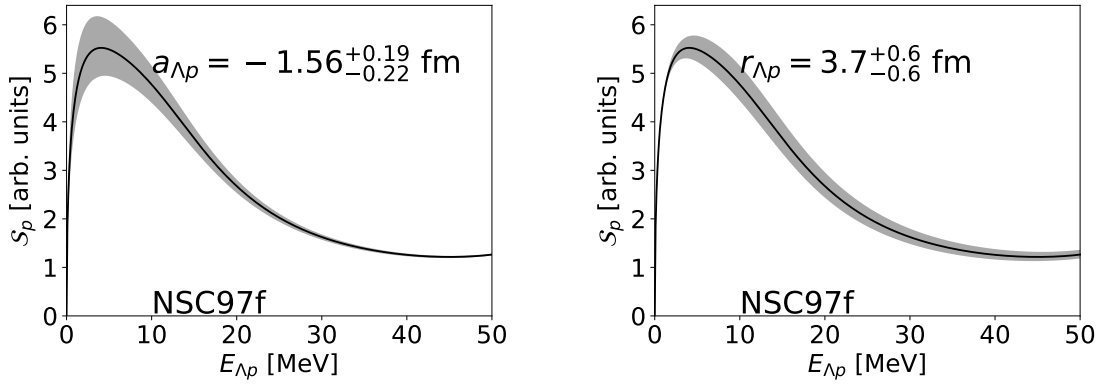

Fig.5.14 Same as Fig. 5.13 but $a_{\Sigma N} = -3.83 - i3.01$ fm (Jülich '04) is used.

5.4.4 Ratio between two reactions

It may be difficult to extract the properties of the low-energy ΛN scattering by comparing directly the line shapes of the ΛN invariant mass spectra obtained in experiments to that from the theoretical calculation in the previous section. Therefore, as a complementary calculation to the one in the previous section, we would like to propose taking the ratio of the cross sections as a function of the excitation energy $E_{\Lambda N}$ between the Λn and Λp processes:

$$\mathcal{R}_S = 2\frac{\mathcal{S}_n}{\mathcal{S}_p} \tag{5.36}$$

where factor 2 is introduced to normalize the ratio to be unity regardless of the excitation energy when the isospin symmetry is satisfied. This is due to isospin symmetric formulation. Using $\mathcal{R}_S$,

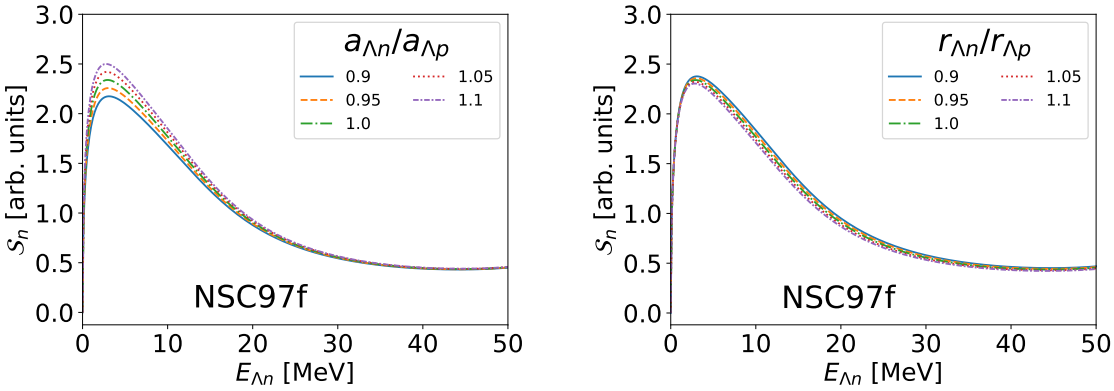

Fig.5.15 Λn invariant mass spectra calculated with different $a_{\Lambda n}$ and $r_{\Lambda n}$ values for the Λn process. In the upper plot, the value of the scattering length is changed within $\pm 10\%$ of the observed Λp scattering $a_{\Lambda p} = -1.56$ fm, while the value of the effective range varies within $\pm 10\%$ of the observed Λp effective range $r_{\Lambda p} = 3.7$ fm in the lower plot. For the two plots $a_{\Sigma N} = 1.68 - i2.35$ fm (NSC97f) is used.

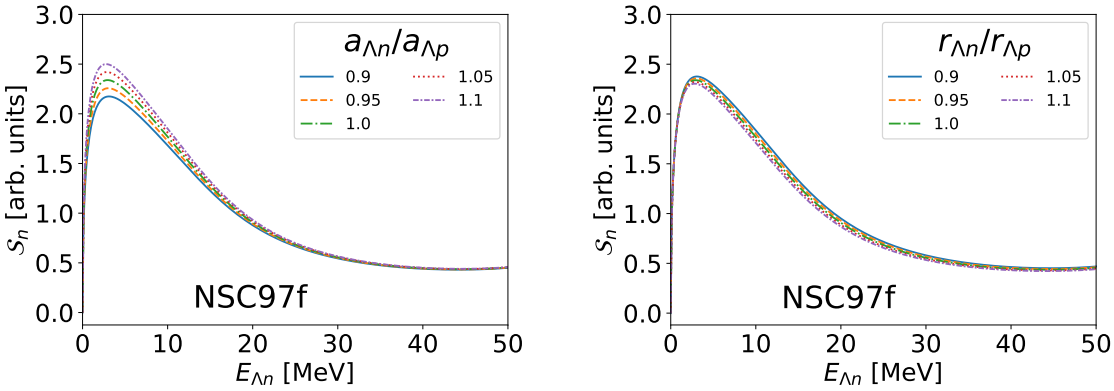

Fig.5.16 Same as Fig. 5.15 but $a_{\Sigma N} = -3.83 - i3.01$ fm (Jülich '04) is used.

we expect to extract relative difference between the Λn and Λp scattering properties, that is isospin symmetry breaking. We note that the isospin breaking from other sources is modeled by introducing the observed hadron masses when we calculate the energy-momenta of particles and the kinematic factors. It is also noted that because the Σ and π-exchange diagrams do not contribute visibly around the ΛN threshold, the isospin breaking in the ΣN transition and πN amplitudes is not important in this calculation.

First of all, we show the ratio calculated only with the foreground diagram in order to check the feasibility of extracting the isospin symmetry breaking effects in the ΛN interaction from $\mathcal{R}_S$. In Fig. 5.17 we show $\mathcal{R}_S$ for several $a_{\Lambda n}$ values within range of $\pm 10\%$ of $a_{\Lambda p}$. This range must be much wider than the typical uncertainty in the difference between $a_{\Lambda n}$ and $a_{\Lambda p}$ from isospin symmetry breaking. We fix the other ΛN parameters: $a_{\Lambda p} = -1.56$ fm, $r_{\Lambda n} = r_{\Lambda p} = 3.7$ fm. Figure 5.17 shows that for $a_{\Lambda n}/a_{\Lambda p} < 1.0$ the ratio $\mathcal{R}_S$ tends to go down as the excitation energy approaches to the ΛN threshold, which for $a_{\Lambda n}/a_{\Lambda p} > 1.0$ it tends to be enhanced. Thus isospin symmetry breaking effect on the ΛN scattering could be clearly seen particularly around the threshold if one could observe only the foreground contribution. We find that $\mathcal{R}_S$ works for extracting the isospin symmetry breaking in the

ΛN scattering length. We see that even though $\mathcal{R}_S$ for the isospin symmetric case with $a_{\Lambda n}/a_{\Lambda p} = 1$ is almost constant against the excitation energy, it deviates from unity. This is because of the isospin symmetry breaking of the $K^- N \to \pi\Lambda$ amplitudes (the first scattering in Dia. 1), which is independent of the excitation energy.

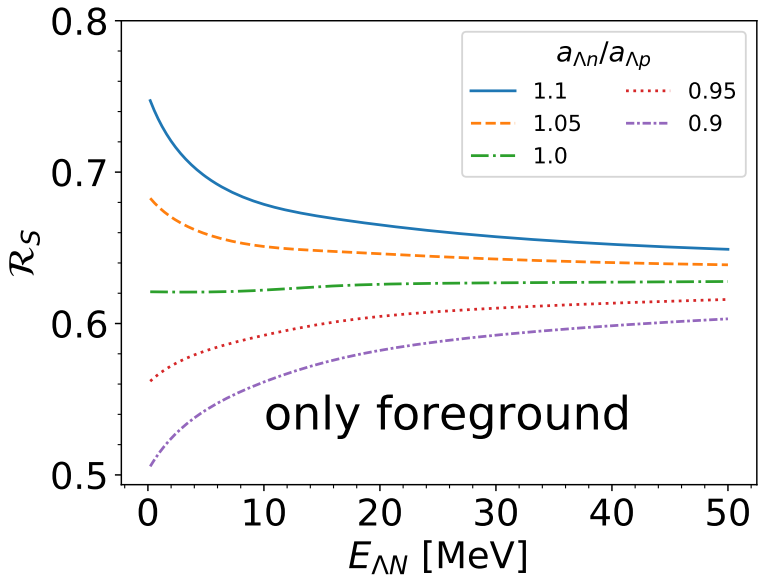

Fig.5.17 Ratio $\mathcal{R}_S$ calculated only with the foreground diagram as a function of the excited energy $E_{\Lambda N}$. We take several $a_{\Lambda n}$ values within $\pm 10\%$ of $a_{\Lambda p}$, while the other ΛN parameters are fixed at $a_{\Lambda p} = -1.56$ fm, and $r_{\Lambda n} = r_{\Lambda p} = 3.7$ fm.

Next, we calculate the ratio $\mathcal{R}_S$ by incorporating all the background contributions. We change the Λn scattering length $a_{\Lambda n}$ within $\pm 10\%$ of the Λp scattering length $a_{\Lambda p} = -1.56$ fm and fix the effective range as $r_{\Lambda n} = r_{\Lambda p} = 3.7$ fm again. The results are shown in Fig. 5.18. The upper panel of Fig. 5.18 is calculated with $a_{\Sigma N} = 1.68 - i2.35$ fm (NSC97f) while the lower panel of Fig. 5.18 is with $a_{\Sigma N} = -3.83 - i3.01$ fm (Jülich '04).

These figures show that the interference to the background contributions gives an enhancement of $\mathcal{R}_S$ at the vicinity of the threshold. Still, we find qualitative sensitivity to the change of the ratio $a_{\Lambda n}/a_{\Lambda p}$ in a wide range of the excitation energy $0 \leq E_{\Lambda p} < 30$ MeV, in which the ratio $\mathcal{R}_S$ gets enhanced with larger $a_{\Lambda n}/a_{\Lambda p}$. Unfortunately, we do not find qualitative sensitivity as seen in Fig. 5.17.

Comparing Figs. 5.17 and 5.18, we find that the interference between the foreground and backgrounds is substantially large even if we reduce the background effects by making the angular cut on θ^*_Λ. In order to enhance the interference, we calculate the ratio $\mathcal{R}_S$ without the angular cut. The results are shown in Fig. 5.19. The difference between $a_{\Lambda n}$ and $a_{\Lambda p}$ can be seen more qualitatively than Fig. 5.18. It should be noted that the difference is seen only near the threshold up to $E_{\Lambda p} = 10$ MeV. For $a_{\Lambda n}/a_{\Lambda p} < 1.0$, $\mathcal{R}_S$ tends to go down significantly as the excitation energy approaches the threshold, while for $a_{\Lambda n}/a_{\Lambda p} > 1.0$ it tends not to go down so much. This behavior is due to the effect of interference between the foreground and impulse diagrams, with the background contribution being the largest. This may help to extract the nature of the isospin symmetry breaking in the ΛN interaction. At least we could find out the direction of the isospin symmetry breaking of the Λn scattering length against Λp.

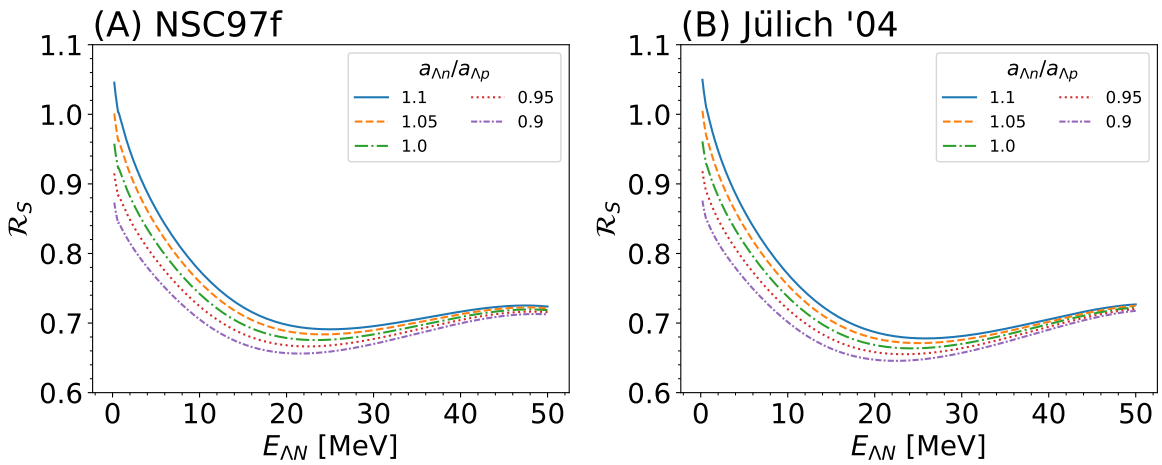

Fig.5.18 Same as Fig. 5.17 but for incorporating the background contributions. The upper and lower panels show the ratios obtained by using the $a_{\Sigma N}$ values in NSC97f and Jülich '04, respectively.

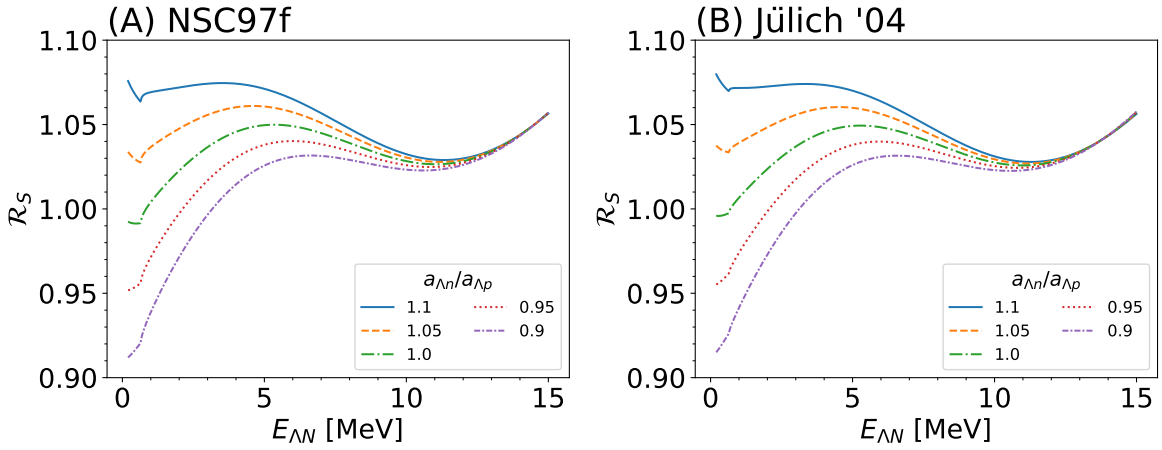

Fig.5.19 Same as Fig. 5.18 but the cutoff of θ^*_Λ is not applied. The upper and lower panels show the ratios obtained by using the $a_{\Sigma N}$ values in NSC97f and Jülich '04, respectively.

5.5 Summary

In this chapter, we have proposed that the $K^- d \to \pi\Lambda N$ reaction has an advantage for the study of isospin symmetry breaking in the ΛN scattering because both isospin partners, Λp and Λn, are possible in the final state and we can observe Λp and Λn final state interactions with the same initial condition by selecting the charge of the final-state pion. We have formulated the $K^- d \to \pi\Lambda N$ scattering amplitudes by considering not only the foreground contribution which contains the ΛN final state interaction but also the background contributions which include the impulse contribution, the Σ, K and π-exchange contributions. These background diagrams contain the $\pi\Lambda$ and πN final state interactions. For stopped kaons, the ΛN interaction is dominated by the spin-triplet configuration because of the deuteron spin and S-wave dominance of low-energy scattering. In order to reduce the background effects, we have examined the dependence of the amplitude to the angle of Λ in the final state and have found that the background effects can be suppressed for narrower angles between Λ and π. We have found that the ΛN invariant mass spectra both for the Λp and Λn processes are

sensitive to the ΛN scattering properties around the ΛN threshold, $E_{\Lambda p} < 30$ MeV and that one may extract the scattering lengths and the effective ranges from these spectra. It has also been found that the $\Sigma N \to \Lambda N$ transition effect is less important around the ΛN threshold and the π exchange contribution is negligibly small. We have suggested that the ratio of the invariant mass spectra for the Λn and Λp processes works well to extract the qualitative tendency of the isospin symmetry breaking effects between the low-energy Λp and Λn scatterings.

Chapter 6

In-medium chiral condensate with strange quarks estimated from K^+N scattering

6.1 Introduction

As mentioned in Section 3.2.3, the purpose of this chapter is to evaluate the chiral condensate extended to flavor SU(3).

In order to confirm the dynamical breaking of chiral symmetry (DBχS), the partial restoration of the chiral symmetry in nuclear matter which has a finite density is investigated. For the flavor SU(2) case, the magnitude of $\langle \bar{u}u + \bar{d}d \rangle$ is expected to decrease as chiral symmetry is restored in nuclear matter. It was predicted by a model-independent low-density theorem [12, 13]. With the πN-σ term $\sigma_{\pi N} = 40 \sim 60$ MeV which is determined by πN scattering, the in-medium condensate decreases by $30 - 40\%$ at the normal nuclear density compared to the in-vacuum one. Of particular interest are Nambu-Goldstone bosons (NG bosons) such as pion, which are appeared by the dynamical breaking of chiral symmetry. Hence the property of the NG boson is sensitive to DBχS. The partial restoration of DBχS has been confirmed, especially for pion in nucleus [6–9]. Systematic studies of other hadronic systems are needed to firmly establish that chiral symmetry is partially restored in finite density. For this reason, we would like to consider NG bosons with strangeness.

In this chapter, we focus on chiral condensate with strange quarks in nuclear matter in order to study a systematic study of the partial restoration of chiral symmetry. In our calculation, we derive the chiral condensate with strange quarks, $\langle \bar{u}u + \bar{s}s \rangle^*$ based on the correlation function approach and the low-density theorem. We then obtain $\langle \bar{u}u + \bar{s}s \rangle^*$ in terms of KN scattering amplitude in soft-limit. We construct the KN scattering amplitudes using the chiral perturbation theory and determine the low-energy constants from the K^+N elastic scattering in the same way that $\sigma_{\pi N}$ was determined by πN scattering. Since the KN system contains a strange quark unlike the πN system, we utilize the leading order, the next-to-leading order and some terms from the next-to-next order which includes the strange quark mass of chiral perturbation theory to incorporate the SU(3) flavor symmetry breaking effect due to the strange quark. The determined KN scattering amplitudes provide the behavior of $\langle \bar{u}u + \bar{s}s \rangle^*$ in nuclear matter.

6.2 In-medium chiral condensate with strange

In this section, we construct the chiral condensate based on the correlation function approach [8, 10, 11] and the low-density theorem [12, 13].

6.2.1 Correlation function approach

Following Refs. [8, 10, 11], we recall the divergence of the following time-ordered product discussed in Eq. (2.81)

$$\partial^\mu \mathbf{T}\left[A^a_\mu(x)P^b(0)\right] = \mathbf{T}\left[\partial^\mu A^a_\mu(x)P^b(0)\right] + \delta(x_0)\left[A^a_0(x), P^b(0)\right]. \tag{6.1}$$

where the axial-vector current $A^a_\mu(x)$ and the pseudoscalar fields $P^a(x)$ which were introduced in Section 2.5.

We can use the partially-conserved axial current (PCAC) relation for the kaon sector Eq. (2.65) as

$$\partial^\mu A^a_\mu(x) = \frac{m+m_s}{2}P^a(x) \tag{6.2}$$

for flavor index $a = 4, 5$. We use the isospin-symmetric quark mass m and the strange quark mass m_s. In our approach, we consider the extension of the correlation functions defined in Section 2.5 to in the nuclear matter, which means replacing the vacuum state $|0\rangle$ with the in-medium grand state $|\Omega\rangle$ in Eq. (2.79). We evaluate Eq. (6.2) by the in-medium vacuum $|\Omega\rangle$ as

$$\partial^\mu \Pi^{ab}_{5\mu}(x,0;\rho_N) = \frac{m+m_s}{2}\Pi^{ab}(x,0;\rho_N) + \delta(x^0)\left\langle\Omega\right|\left[A^a_0(x), P^b(0)\right]\left|\Omega\right\rangle, \tag{6.3}$$

where we introduce the in-medium correlation functions

$$\Pi^{ab}_{5\mu}(x,0;\rho_N) = \left\langle \mathbf{T}A^a_\mu(x)P^b(0)\right\rangle^* \equiv \left\langle\Omega\right|\mathbf{T}A^a_\mu(x)P^b(0)\left|\Omega\right\rangle, \tag{6.4}$$

$$\Pi^{ab}(x,0;\rho_N) = \left\langle \mathbf{T}P^a(x)P^b(0)\right\rangle^* \equiv \left\langle\Omega\right|\mathbf{T}P^a(x)P^b(0)\left|\Omega\right\rangle. \tag{6.5}$$

Performing the Fourier transformation to the momentum space and taking the soft limit $q^\mu \to 0$, we obtain

$$\delta^{ab}\langle\bar{u}u + \bar{s}s\rangle^* = -i\frac{m+m_s}{2}\Pi^{ab}(q=0;\rho_N) \tag{6.6}$$

with indices $a, b = 4, 5$. Taking the linear combination for the indices, we obtain the in-medium condensate in terms of the linear combination of the pseudoscalar fields:

$$\begin{aligned}
\langle\bar{u}u + \bar{s}s\rangle^* &= -i\frac{m+m_s}{4}\left(\Pi^{44}(q=0;\rho_N) + \Pi^{55}(q=0;\rho_N)\right) \\
&= -i\frac{m+m_s}{4}\left\langle P^4(0)P^4(0) + P^5(0)P^5(0)\right\rangle^* \\
&= -i\frac{m+m_s}{2}\left\langle\left(\frac{P^4(0)+iP^5(0)}{\sqrt{2}}\right)\left(\frac{P^4(0)-iP^5(0)}{\sqrt{2}}\right)\right\rangle^* \\
&\equiv -i\frac{m+m_s}{2}\Pi^{4+i5,4-i5}(q=0;\rho_N).
\end{aligned} \tag{6.7}$$

Taking $\rho_N = 0$, the in-vacuum condensate is represented in terms of the in-vacuum correlation function:

$$\langle\bar{u}u + \bar{s}s\rangle_0 = -i\frac{m+m_s}{2}\Pi^{4+i5,4-i5}(q=0;\rho_N=0). \tag{6.8}$$

6.2.2 Low-density theorem

In the low-density theorem [12, 13], we can expand the in-medium matrix element of an operator O as

$$\langle\Omega|\, O\,|\Omega\rangle = \langle 0|\, O\,|0\rangle + \rho_N \langle N|\, O\,|N\rangle + \mathcal{O}(\rho_N^{n>1}). \tag{6.9}$$

Applying this theorem to $\Pi^{4+i5,4-i5}(q;\rho_N)$, we obtain

$$\Pi^{4+i5,4-i5}(q;\rho_N) = G_K^2 \langle 0|\, K^-(q)K^+(q)\,|0\rangle + \rho_N G_K^2 \langle N|\, K^-(q)K^+(q)\,|N\rangle + O(\rho_N^{n>1}) \tag{6.10a}$$

$$= \Pi^{4+i5,4-i5}(q;\rho_N=0) + \rho_N G_K^2 \langle N|\, K^-(q)K^+(q)\,|N\rangle + O(\rho_N^{n>1}), \tag{6.10b}$$

$$\Pi^{4+i5,4-i5}(q;\rho_N=0) = G_K^2 \langle 0|\, K^-(q)K^+(q)\,|0\rangle = \frac{iG_K^2}{q^2-M_K^2} \tag{6.10c}$$

where G_K is the in-vacuum coupling defined as $\langle 0|\, \frac{P^4-iP^5}{\sqrt{2}}\,|K^+\rangle \equiv G_K$. $\langle 0|\, K^-(q)K^+(q)\,|0\rangle$ stands for the in-vacuum kaon propagator. The matrix element $\langle N|\, K^-(q)K^+(q)\,|N\rangle$ is written by the kaon-nucleon scattering amplitude $T_{KN}(q)$ using the reduction formula [86] as

$$\langle N|\, K^-(q)K^+(q)\,|N\rangle = \frac{i}{q^2-M_K^2}\frac{1}{q^2-M_K^2}\left(-\frac{T_{KN}(q)}{2M_N}\right). \tag{6.11}$$

Finally, the chiral condensate with the strange quarks is given in terms of the kaon-nucleon scattering amplitude T_{KN} in the soft limit using Eqs. (6.7), (6.8), (6.10) and (6.11) as

$$\langle\bar{u}u+\bar{s}s\rangle^* = -i\frac{m+m_s}{2}\Pi^{4+i5,4-i5}(q=0;\rho_N) \tag{6.12}$$

$$= -i\frac{m+m_s}{2}\Pi^{4+i5,4-i5}(0;0)\left(1+\frac{\rho_N}{M_K^2}\frac{T_{KN}(q=0)}{2M_N}\right) \tag{6.13}$$

$$\frac{\langle\bar{u}u+\bar{s}s\rangle^*}{\langle\bar{u}u+\bar{s}s\rangle_0} = \left(1+\frac{\rho_N}{M_K^2}\frac{T_{KN}(q=0)}{2M_N}\right). \tag{6.14}$$

Here, in order to evaluate the chiral condensate, it is necessary to take the soft limit for T_{KN}, and for this purpose, T_{KN} is constructed using chiral perturbation theory for the next section.

6.3 Formulation of KN amplitudes

In order to estimate the in-medium chiral condensate with strange quarks $\langle\bar{u}u+\bar{s}s\rangle^*$ based on Eq. (6.12), we construct the kaon-nucleon scattering amplitude T_{KN} from the observed data of the K^+N scattering using chiral perturbation theory introduced in Sec. 4.2. We use the kinematical formulation given in Section 4.1 and the Coulomb correction is taken into K^+p amplitude obtained in chiral perturbation theory by way given in Section 4.1.1.

6.3.1 KN scattering amplitude in chiral perturbation theory

The K^+N scattering amplitudes in the particle basis $T^{K^+p\to K^+p}$, $T^{K^+n\to K^+n}$ and $T^{K^+n\to K^0p}$ are constructed by those in the isospin basis T^I $(I=0,1)$ as

$$T^{K^+p\to K^+p} = T^{I=1}, \tag{6.15}$$

$$T^{K^+n\to K^+n} = \frac{1}{2}\left(T^{I=1}+T^{I=0}\right), \tag{6.16}$$

$$T^{K^+n\to K^0p} = \frac{1}{2}\left(T^{I=1}-T^{I=0}\right). \tag{6.17}$$

In this section, we construct the tree-level amplitude of the K^+N elastic scattering using the chiral perturbation theory based on Section 4.2.3 as

$$T^{KN} = T_{\rm WT} + T_{\rm Born} + T_{\rm NLO} + T_{\rm NNLO}. \tag{6.18}$$

The leading order contribution contains the amplitudes of the contact Weinberg-Tomozawa interaction $T_{\rm WT}$ and the u-channel Born terms of the hyperons with the KYN Yukawa interactions $T_{\rm Born}$. The loop diagrams contribute from the next-to-next-to-leading order (NNLO).

Fig.6.1 Feynman diagrams related to K^+N elastic scattering. The left diagram indicates the contact interaction. The right diagram means the u-channel Born term.

Leading order: Weinberg-Tomozawa term

The invariant amplitudes for the Weinberg-Tomozawa diagrams in the isospin basis are calculated as

$$T^{I=0}_{\rm WT} = 0,\ T^{I=1}_{\rm WT} = \frac{1}{2F_K^2}\bar{u}(\boldsymbol{p}_4,s_4)(\not{p}_1+\not{p}_3)u(\boldsymbol{p}_2,s_2) \tag{6.19}$$

and their corresponding invariant amplitudes read

$$A^{I=0}_{\rm WT} = B^{I=0}_{\rm WT} = A^{I=1}_{\rm WT} = 0,\ B^{I=1}_{\rm WT} = \frac{1}{F_K^2} \tag{6.20}$$

with the kaon decay constant F_K.

Leading order: Born term

The invariant amplitudes for the u-channel Born terms in the isospin basis are evaluated as

$$\begin{aligned} T^{I=0}_{\rm Born} =& -\frac{3}{4}\frac{(D-F)^2}{F_K^2}\bar{u}(\boldsymbol{p}_4,s_4)\not{p}_1\gamma_5\frac{M_\Sigma+(\not{p}_2-\not{p}_3)}{M_\Sigma^2-(p_2-p_3)^2-i\epsilon}\not{p}_3\gamma_5 u(\boldsymbol{p}_2,s_2) \\ &+\frac{1}{12}\frac{(3F+D)^2}{F_K^2}\bar{u}(\boldsymbol{p}_4,s_4)\not{p}_1\gamma_5\frac{M_\Lambda+(\not{p}_2-\not{p}_3)}{M_\Lambda^2-(p_2-p_3)^2-i\epsilon}\not{p}_3\gamma_5 u(\boldsymbol{p}_2,s_2), \end{aligned} \tag{6.21}$$

$$\begin{aligned} T^{I=1}_{\rm Born} =& -\frac{1}{4}\frac{(D-F)^2}{F_K^2}\bar{u}(\boldsymbol{p}_4,s_4)\not{p}_1\gamma_5\frac{M_\Sigma+(\not{p}_2-\not{p}_3)}{M_\Sigma^2-(p_2-p_3)^2-i\epsilon}\not{p}_3\gamma_5 u(\boldsymbol{p}_2,s_2) \\ &-\frac{1}{12}\frac{(3F+D)^2}{F_K^2}\bar{u}(\boldsymbol{p}_4,s_4)\not{p}_1\gamma_5\frac{M_\Lambda+(\not{p}_2-\not{p}_3)}{M_\Lambda^2-(p_2-p_3)^2-i\epsilon}\not{p}_3\gamma_5 u(\boldsymbol{p}_2,s_2) \end{aligned} \tag{6.22}$$

where Σ baryon mass M_Σ and Λ baryon mass M_Λ and their corresponding invariant amplitudes read

$$A^{I=0}_{\rm Born} = \frac{3}{4}\frac{(D-F)^2}{F_K^2}\frac{(M_N+M_\Sigma)(M_N^2-u)}{u-M_\Sigma^2} - \frac{1}{12}\frac{(3F+D)^2}{F_K^2}\frac{(M_N+M_\Lambda)(M_N^2-u)}{u-M_\Lambda^2}, \tag{6.23}$$

$$B^{I=0}_{\rm Born} = -\frac{3}{4}\frac{(D-F)^2}{F_K^2}\frac{u+M_N^2+2M_\Sigma M_N}{u-M_\Sigma^2} + \frac{1}{12}\frac{(3F+D)^2}{F_K^2}\frac{u+M_N^2+2M_\Lambda M_N}{u-M_\Lambda^2}, \tag{6.24}$$

$$A^{I=1}_{\rm Born} = \frac{1}{4}\frac{(D-F)^2}{F_K^2}\frac{(M_N+M_\Sigma)(M_N^2-u)}{u-M_\Sigma^2} + \frac{1}{12}\frac{(3F+D)^2}{F_K^2}\frac{(M_N+M_\Lambda)(M_N^2-u)}{u-M_\Lambda^2}, \tag{6.25}$$

$$B^{I=1}_{\rm Born} = -\frac{1}{4}\frac{(D-F)^2}{F_K^2}\frac{u+M_N^2+2M_\Sigma M_N}{u-M_\Sigma^2} - \frac{1}{12}\frac{(3F+D)^2}{F_K^2}\frac{u+M_N^2+2M_\Lambda M_N}{u-M_\Lambda^2} \tag{6.26}$$

with the Σ baryon mass M_Σ, the Λ baryon mass M_Λ and the Mandelstam variable $u=(p_2-p_3)^2 = 2M_N^2+2M_K^2-s-t$. We use the isospin-averaged hadron masses for the calculation in this chapter.

Next-to-leading order

The next-to-leading order of the K^+N scattering amplitudes for $I=0,1$ is calculated as

$$\begin{aligned} T^I_{\rm NLO} =& \left[\frac{4B_0}{F_K^2}(\hat{m}+m_s)b^I + \frac{2}{F_K^2}(p_1\cdot p_3)d^I + \frac{(p_2\cdot p_1)(p_2\cdot p_3)+(p_4\cdot p_1)(p_4\cdot p_3)}{2M_N^2F_K^2}g^I\right] \\ &\times\bar{u}(\boldsymbol{p}_4,s_4)u(\boldsymbol{p}_2,s_2) - \frac{h^I}{2F_K^2}p_1^\mu p_3^\nu\,\bar{u}(\boldsymbol{p}_4,s_4)[\gamma_\mu,\gamma_\nu]u(\boldsymbol{p}_2,s_2), \end{aligned} \tag{6.27}$$

where we have introduced the LECs in the isospin basis, b^I, d^I, g^I and h^I, which are defined by the LECs, b_i, d_i, g_i and h_i appearing in the chiral Lagrangian 4.49 as

$$b^{I=0} = b_0 - b_F, \qquad b^{I=1} = b_0 + b_D, \tag{6.28}$$

$$d^{I=0} = 2d_1 + d_3 - 2d_4, \qquad d^{I=1} = -2d_2 - d_3 - 2d_4, \tag{6.29}$$

$$g^{I=0} = 2g_1 + g_3 - 2g_4, \qquad g^{I=1} = -2g_2 - g_3 - 2g_4, \tag{6.30}$$

$$h^{I=0} = h_1 + h_2 + h_3 + h_4, \qquad h^{I=1} = h_1 - h_2 - h_3 - h_4. \tag{6.31}$$

The corresponding invariant amplitudes to Eq. (6.27) read

$$\begin{aligned} A^I_{\rm NLO} =& \frac{4B_0}{F_K^2}(m+m_s)b^I + \frac{2}{F_K^2}(p_1\cdot p_3)d^I \\ &+\frac{(p_2\cdot p_1)(p_2\cdot p_3)+(p_4\cdot p_1)(p_4\cdot p_3)}{2M_N^2F_K^2}g^I + \frac{p_1\cdot(p_2+p_4)}{F_K^2}h^I \end{aligned} \tag{6.32}$$

$$B^I_{\rm NLO} = -\frac{2M_N}{F_K^2}h^I. \tag{6.33}$$

Some terms from next-to-next-to-leading order

In order to improve extrapolation in the strange quark sector, we introduce some terms from the next-to-next-to-leading order (NNLO) of the chiral Lagrangian Eq. (4.51) which contain the strange quark mass.

The K^+N scattering amplitudes obtained by using Eq. (4.51) for $I = 0, 1$ are given by

$$\begin{aligned}
T^{I=0}_{\rm NNLO} =& \frac{3(D-F)(v_D-v_F)M_K^2}{F_K^2}\bar{u}(\boldsymbol{p}_4,s_4)\left(\gamma_5\frac{M_\Sigma+\not{p}_2-\not{p}_3}{u-M_\Sigma^2}\not{p}_3\gamma_5-\not{p}_1\gamma_5\frac{M_\Sigma+\not{p}_2-\not{p}_3}{u-M_\Sigma^2}\gamma_5\right)u(\boldsymbol{p}_2,s_2)\\
&-\frac{(D+3F)(v_D+3v_F)M_K^2}{3F_K^2}\bar{u}(\boldsymbol{p}_4,s_4)\left(\gamma_5\frac{M_\Lambda+\not{p}_2-\not{p}_3}{u-M_\Lambda^2}\not{p}_3\gamma_5-\not{p}_1\gamma_5\frac{M_\Lambda+\not{p}_2-\not{p}_3}{u-M_\Lambda^2}\gamma_5\right)u(\boldsymbol{p}_2,s_2)\\
&-\frac{4(w_1+w_2-w_3)M_K^2}{F_K^2}\bar{u}(\boldsymbol{p}_4,s_4)(\not{p}_1+\not{p}_3)u(\boldsymbol{p}_2,s_2) \qquad (6.34)\\
T^{I=1}_{\rm NNLO} =& \frac{(D-F)(v_D-v_F)M_K^2}{F_K^2}\bar{u}(\boldsymbol{p}_4,s_4)\left(\gamma_5\frac{M_\Sigma+\not{p}_2-\not{p}_3}{u-M_\Sigma^2}\not{p}_3\gamma_5-\not{p}_1\gamma_5\frac{M_\Sigma+\not{p}_2-\not{p}_3}{u-M_\Sigma^2}\gamma_5\right)u(\boldsymbol{p}_2,s_2)\\
&+\frac{(D+3F)(v_D+3v_F)M_K^2}{3F_K^2}\bar{u}(\boldsymbol{p}_4,s_4)\left(\gamma_5\frac{M_\Lambda+\not{p}_2-\not{p}_3}{u-M_\Lambda^2}\not{p}_3\gamma_5-\not{p}_1\gamma_5\frac{M_\Lambda+\not{p}_2-\not{p}_3}{u-M_\Lambda^2}\gamma_5\right)u(\boldsymbol{p}_2,s_2)\\
&-\frac{4(w_1-w_2+w_3)M_K^2}{F_K^2}\bar{u}(\boldsymbol{p}_4,s_4)(\not{p}_1+\not{p}_3)u(\boldsymbol{p}_2,s_2) \qquad (6.35)
\end{aligned}$$

and the invariant amplitudes read

$$\begin{aligned}
A^{I=0} =& \frac{6(D-F)v_-M_K^2}{F_K^2}\frac{(p_1\cdot p_4)+(p_2\cdot p_3)-M_K^2}{u-M_\Sigma^2}\\
&-\frac{2(D+3F)v_+M_K^2}{3F_K^2}\frac{(p_1\cdot p_4)+(p_2\cdot p_3)-M_K^2}{u-M_\Lambda^2} \qquad (6.36)\\
B^{I=0} =& -\frac{6(D-F)v_-M_K^2}{F_K^2}\frac{M_N+M_\Sigma}{u-M_\Sigma^2}\\
&+\frac{2(D+3F)v_+M_K^2}{3F_K^2}\frac{M_N+M_\Lambda}{u-M_\Lambda^2}-\frac{8M_K^2w^{I=0}}{F_K^2} \qquad (6.37)\\
A^{I=1} =& \frac{2(D-F)v_-M_K^2}{F_K^2}\frac{(p_1\cdot p_4)+(p_2\cdot p_3)-M_K^2}{u-M_\Sigma^2}\\
&+\frac{2(D+3F)v_+M_K^2}{3F_K^2}\frac{(p_1\cdot p_4)+(p_2\cdot p_3)-M_K^2}{u-M_\Lambda^2} \qquad (6.38)\\
B^{I=1} =& -\frac{2(D-F)v_-M_K^2}{F_K^2}\frac{M_N+M_\Sigma}{u-M_\Sigma^2}\\
&-\frac{2(D+3F)v_+M_K^2}{3F_K^2}\frac{M_N+M_\Lambda}{u-M_\Lambda^2}-\frac{8M_K^2w^{I=1}}{F_K^2}. \qquad (6.39)
\end{aligned}$$

Here we introduce the LECs in isospin space as

$$v_- = v_D - v_F, \qquad v_+ = v_D + 3v_F, \qquad (6.40)$$

$$w^{I=0} = w_1 - w_2 + w_3, \qquad w^{I=1} = w_1 + w_2 - w_3. \qquad (6.41)$$

The low-energy constants in the next-to-next-to-leading order of Lagrangian, $v_\pm$ are included in both isospin channels.

Applying the isospin-averaged kaon-nucleon amplitude to Eq. (6.12), we obtain the chiral condensate

Table 6.1 The property of the broad resonance states in the KN scattering with $S = +1$ and $I = 0$ around $\sqrt{s} = 1650$ MeV reported by Ref. [90]. The coupling strengths are obtained from the residue of the scattering amplitudes at the resonance positions [150].

Solution	Resonance (J^P)	mass [MeV]	width [MeV]	coupling strength [GeV^{-1}]
Solution 1	P_{01} ($\frac{1}{2}^+$)	1617	305	$5.26 - 2.62i$
Solution 2	P_{03} ($\frac{3}{2}^+$)	1678	463	$4.64 - 2.62i$

in terms of the LECs defined in chiral perturbation theory as

$$\frac{\langle \bar{u}u + \bar{s}s \rangle^*}{\langle \bar{u}u + \bar{s}s \rangle_0} = \left(1 + \frac{\rho_N}{2M_N M_K^2} \frac{3T^{I=1}(q=0) + T^{I=0}(q=0)}{4}\right) = 1 + \frac{(3b^{I=1} + b^{I=0})}{F_K^2}\rho_N. \tag{6.42}$$

Using this equation, the chiral condensate can be evaluated directly from the LECs determined from experiments within the linear density.

6.3.2 Including resonance state

As discussed in Section 3.2.3, the resonance state is reported in the $I = 0$ sector of KN scattering amplitude [90]. The resonance energies correspond to $P_{\rm lab} \sim 600$ MeV/c in the K^+N scattering. The resonance parameters are summarized in Table 6.1. Since these resonances have a large width, the resonance may contribute to the $I = 0$ scattering amplitude in a wide range of the energy around $P_{\rm lab} \sim 600$ MeV/c. In addition, most of the low-energy data for the $I = 0$ cross section are in these energies. Because resonances cannot be expressed in the perturbative expansion of energy, we take account of the resonance contribution explicitly into our amplitudes. The resonances state is introduced to the $I = 0$ amplitude by adding the following amplitude to the appropriate partial wave amplitude $T_{\ell=1\pm}$ defined in Eq. (4.13):

$$T^{\rm Pole} = \frac{g^2 k^2}{\sqrt{s} - W + i\Gamma/2} \tag{6.43}$$

where k is the c.m. momentum of the K^+N scattering, W and Γ are the mass and width of the resonance state, respectively, and g is the coupling strength of the resonance state to the K^+N $I = 0$ channel. The values of the coupling strengths are obtained as the residue of the scattering amplitudes at the resonance positions [150].

6.4 Results

In this section, we carry out the χ^2 fitting of the K^+N amplitude obtained by chiral perturbation theory to the experimental data and determine the LECs.

The reduced χ^2 function is defined as

$$\chi^2_{\rm d.o.f.} = \frac{1}{\#\text{d.o.f.}} \sum_i^N \left(\frac{y_i - f(x_i)}{\sigma_i}\right)^2 \tag{6.44}$$

Table 6.2 The values of the physical constants we use in this chapter.

M_N	M_K	M_Λ	M_Σ	F_K	D	F
938.9 MeV	495.6 MeV	1115.7 MeV	1193.2 MeV	110.0 MeV	0.80	0.46

where $y_i, f(x_i), \sigma_i$ and N are the experimental data, the theoretical calculations with the parameters, the errors of the data and the number of the data, respectively. #d.o.f. stands for the number of degree of freedom. In our analysis, we consider the partial waves up to the D-wave ($\ell = 2$). We restrict the energy region up to $P_{\rm lab} = 800$ MeV/c, where the inelastic contribution such as pion production starts to be significant.

The low-energy constants in the leading order of Lagrangian, D and F, have already been determined by the hyperon semi-leptonic decays at tree level [151]. We use the isospin-averaged hadron masses. These values are summarized in Table 6.2.

6.4.1 Determination of the low-energy constants

We determine the LECs, b^I, d^I, g^I, h^I, w^I for $I = 0, 1$, and $v_\pm$ appearing in both $I = 0$ and $I = 1$ amplitudes, simultaneously using the experimental data of the K^+p differential cross section between $P_{\rm lab} = 145$ MeV/c and 726 MeV/c [152], the $K^+n \to K^0p$ charge exchange differential cross sections between $P_{\rm lab} = 434$ MeV/c and 780 MeV/c [153, 154], $I = 1$ total cross section between $P_{\rm lab} = 145$ MeV/c and 788 MeV/c [92, 152, 155–158], and $I = 0$ total cross section. For the calculation for the K^+p scattering, we include the Coulomb correction discussed in Section 4.1.1. In this work, we consider four different cases for the fittings: FIT 1 uses Carroll 1973 [92] for the $I = 0$ total cross section, while FIT 2 employs Bowen 1970 [156]. Both cases do not introduce the broad resonance into the $I = 0$ amplitude. FIT 3 considers the P_{01} resonance by adding the resonance contribution (6.43) to the scattering amplitude, while FIT 4 takes account of the P_{03} resonance. In FIT 3 and FIT 4, we use Bowen 1970 for the $I = 0$ total cross section, because the resonance properties were obtained by using Bowen 1970 in Ref. [90]. In these fittings, we do not use the differential cross sections of the K^+n elastic scattering due to their large experimental uncertainties. The determined LECs for each case are summarized in Table 6.3. The table shows that the values of LECs for $I = 1$ in FIT 1, 2 and 4 are consistent with each other. This implies that the K^+p experimental data constrain the $I = 1$ KN amplitude very well.

In Figs. 6.2 and 6.3, we show our numerical results for the $I = 1$ total cross section and the K^+p elastic differential cross section calculated with the determined LECs, respectively, and compare them with the experimental observations. For the total cross section in Fig. 6.2 we use the scattering amplitude calculated only with the strong interaction, while the K^+p differential cross sections in Fig. 6.3 include the Coulomb corrections formulated in Section 4.1.1. In both figures, four sets of the determined LECs reproduce the experimental observations very well in the same manner. It is notable that chiral perturbation theory works well to reproduce the $I = 1$ KN amplitude in the energy region that we consider. Some deviations among four sets of the parameters get evident from $P_{\rm lab} = 500$ MeV/c in the K^+p differential cross section.

In Figs. 6.4 and 6.5, we show the $I = 0$ total cross section and the differential cross section for the charge exchange process $K^+n \to K^0p$ calculated with the determined LECs for each case, and we compare them with the experimental data. As stated above, for FIT 1 we use Carroll 1973 for the data of the $I = 0$ total cross section, while for FITs 2, 3 and 4 Bowen 1970 is used. Each fit reproduces the experimental data well. In particular, Fig. 6.5 shows that these four fits reproduce the experimental data well up to $P_{\rm lab} = 720$ MeV/c. Nevertheless, it should be emphasized that we find some deviations among the fits in the total cross sections in low energies below 300 MeV/c. This is because due to the lack of experimental data, the LECs are not constrained so much. In fact, as seen in Table 6.3, the values of LECs for $I = 0$ are different in the fits. To fix the low-energy behavior of the scattering amplitude with $I = 0$, experimental data below 300 MeV/c are extremely important. It is also interesting to mention that the total cross sections obtained by FIT 2 and FIT 4 are almost the same up to 600 MeV/c. In these fits, we use the same experimental data (Bowen 1970) but FIT 4 includes the P_{03} resonance contribution. Thus, our finding that FIT 2 and FIT 4 give a consistent result implies that the contribution of the P_{03} resonance can be absorbed into the LECs to reproduce the scattering amplitude up to 600 MeV/c. This situation can be understood by the fact that the obtained LECs for FIT 2 and FIT 4 are also almost equivalent but there are small deviations in the LECs for I=0. These differences in the LECs represent the contribution of the P_{03} resonance.

In Fig. 6.6, we show the partial wave decomposition of the $I = 1$ total cross section. In all fits except FIT 1, the S-wave contribution is dominant, while in FIT 1, the S-wave is the largest contribution at low momenta, but the contribution of the P-wave is as large as that of the S-wave at high momenta. The contribution of the D-wave is very small in each FIT.

In Fig. 6.7, we show the partial wave decomposition of the $I = 0$ total cross section. As seen in Fig. 6.7, each fit provides different contributions of the partial waves. In FITs 2, 3, and 4 the contribution of the D-wave is very small, while in FIT 1, the D-wave contribution is particularly large at higher momentum. In FITs 2, 3 and 4, P-waves give essential contributions, while the S-wave contribution is found to be minor in all the fits. In FIT 3, the contribution of the P_{01} partial wave is large reflecting the explicit introduction of the resonance contribution into the amplitude. The partial wave decompositions of FITs 2 and 4 are also consistent with each other. This tells us again that FITs 2 and 4 are equivalent.

In Fig. 6.8, we show our calculated results and the experimental data for the differential cross sections of the K^+n elastic scattering. Although the K^+n elastic scattering data are not used for the fitting, the K^+n elastic cross section should be reproduced according to the isospin symmetry, which is certainly good for hadronic reactions in these energies, because all of the theoretical calculations reproduce the cross sections of the K^+p elastic and $K^+n \to K^0p$ scatterings. Nevertheless, the experimental data are poorly reproduced in low energies and, especially, for higher energies the theoretical predictions are scattered among the fittings. Fig. 6.8 also shows that the difference between FIT 2 and FIT 4 can be seen at $\cos\theta_{\rm c.m.} = 1$ for $P_{\rm lab} > 680$ MeV/c, where the resonance contribution may be significant. This implies that forward scattering data for $P_{\rm lab} > 680$ MeV/c may give us important constraints on the wide resonance with $S = +1$.

Table 6.3 Determined low-energy constants. The values of the parameters except w^I are shown in unit of GeV^{-1}, and these of w^I are shown in units of GeV^{-2}. FIT 1 uses Carroll 1973 [92] as the $I = 0$ total cross section, while FIT 2 employs Bowen 1970 [156]. Both cases do not introduce the broad resonance into the $I = 0$ amplitude. FIT 3 considers the P_{01} resonance by adding the resonance contribution, while FIT 4 takes account of the P_{03} resonance. In FIT 3 and FIT 4, Bowen 1970 is used for the $I = 0$ total cross section.

Fitting	FIT 1	FIT 2	FIT 3	FIT 4
$b^{I=1}$	-1.07 ± 0.11	-1.13 ± 0.10	-0.11 ± 0.12	-1.08 ± 0.11
$d^{I=1}$	-2.05 ± 0.20	-2.08 ± 0.17	0.19 ± 0.19	-1.97 ± 0.17
$g^{I=1}$	-0.82 ± 0.22	-0.90 ± 0.18	-0.80 ± 0.20	-1.01 ± 0.19
$h^{I=1}$	3.70 ± 0.50	4.20 ± 0.60	0.90 ± 0.54	4.20 ± 0.60
$w^{I=1}$	-0.76 ± 0.11	-1.01 ± 0.10	-0.36 ± 0.10	-1.05 ± 0.10
$b^{I=0}$	-3.66 ± 0.30	1.40 ± 0.40	2.40 ± 0.48	2.30 ± 0.40
$d^{I=0}$	-9.20 ± 0.40	-0.30 ± 0.40	-1.40 ± 0.58	-0.60 ± 0.50
$g^{I=0}$	1.50 ± 0.50	6.10 ± 0.70	8.30 ± 0.95	8.10 ± 0.80
$h^{I=0}$	16.30 ± 0.70	-3.90 ± 0.80	-1.60 ± 0.96	-4.90 ± 0.80
$w^{I=0}$	-0.57 ± 0.29	4.19 ± 0.35	4.90 ± 0.46	5.00 ± 0.40
v_-	42.90 ± 1.70	12.70 ± 1.70	5.00 ± 0.19	10.1 ± 1.70
v_+	-7.60 ± 0.90	4.60 ± 0.90	-3.63 ± 0.93	4.70 ± 0.90
χ^2_{dof}	2.41	2.75	2.95	2.96

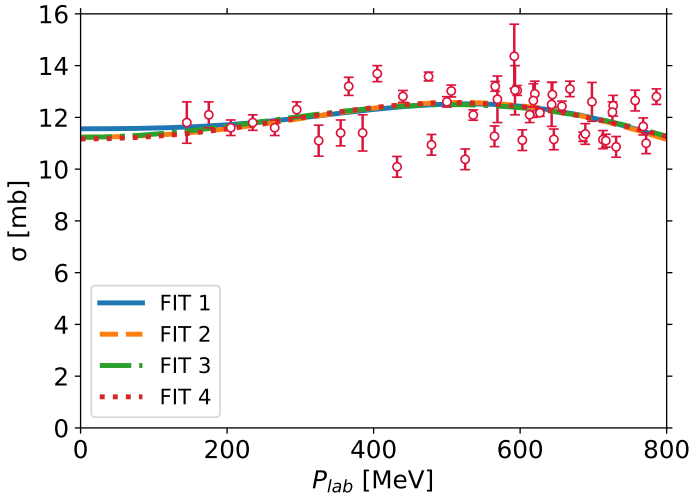

Fig.6.2 $I = 1$ K^+N total cross section calculated with the determined LECs in Table. 6.3 in comparison with the experimental data [92, 152, 155–158].

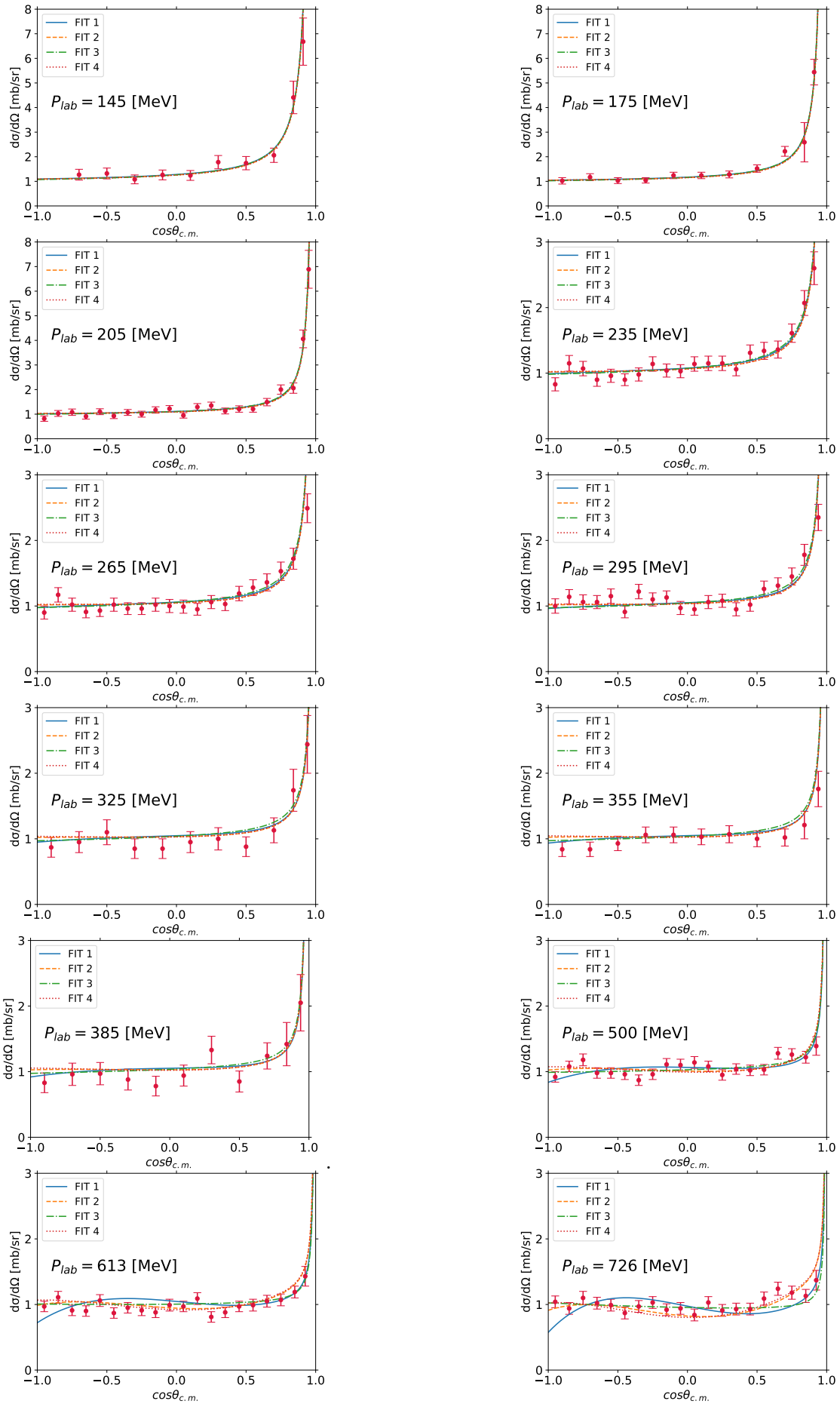

Fig.6.3 Calculated differential cross sections of the K^+p elastic scattering in comparison with the experimental data of Ref. [152].

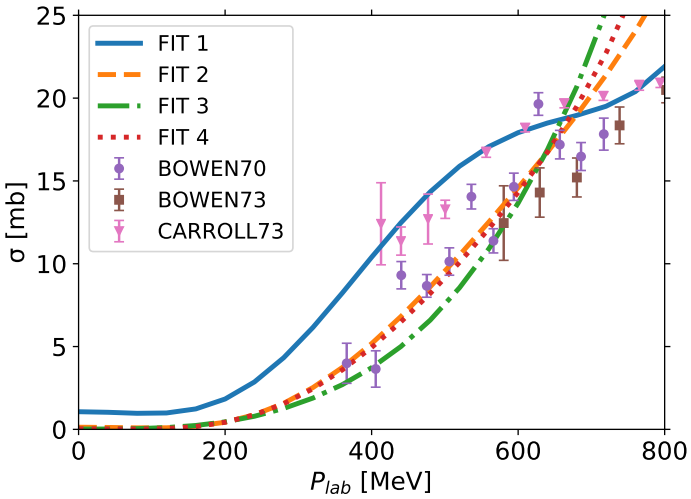

Fig.6.4 $I = 0$ K^+N total cross section calculated with the determined LECs in Table. 6.3 in comparison with the experimental data [92, 156, 158].

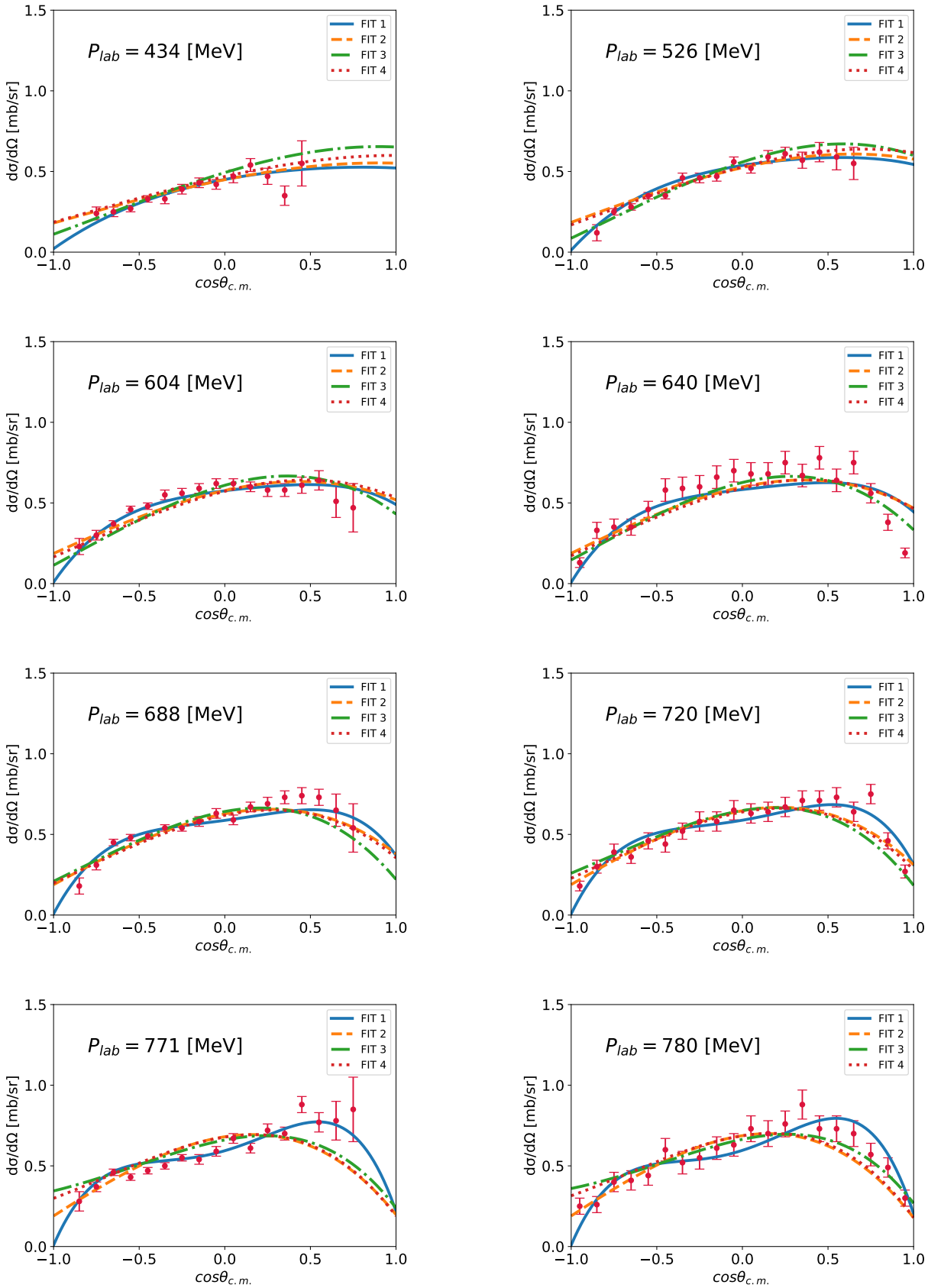

Fig.6.5 Calculated differential cross sections of $K^+n \to K^0p$ charge exchange scattering in comparison with the experimental data of Ref. [153, 154]. The momenta at the $P_{\rm lab} = 640, 720$ and 780 MeV/c are the data from Ref. [153]. The others are the data from Ref. [154].

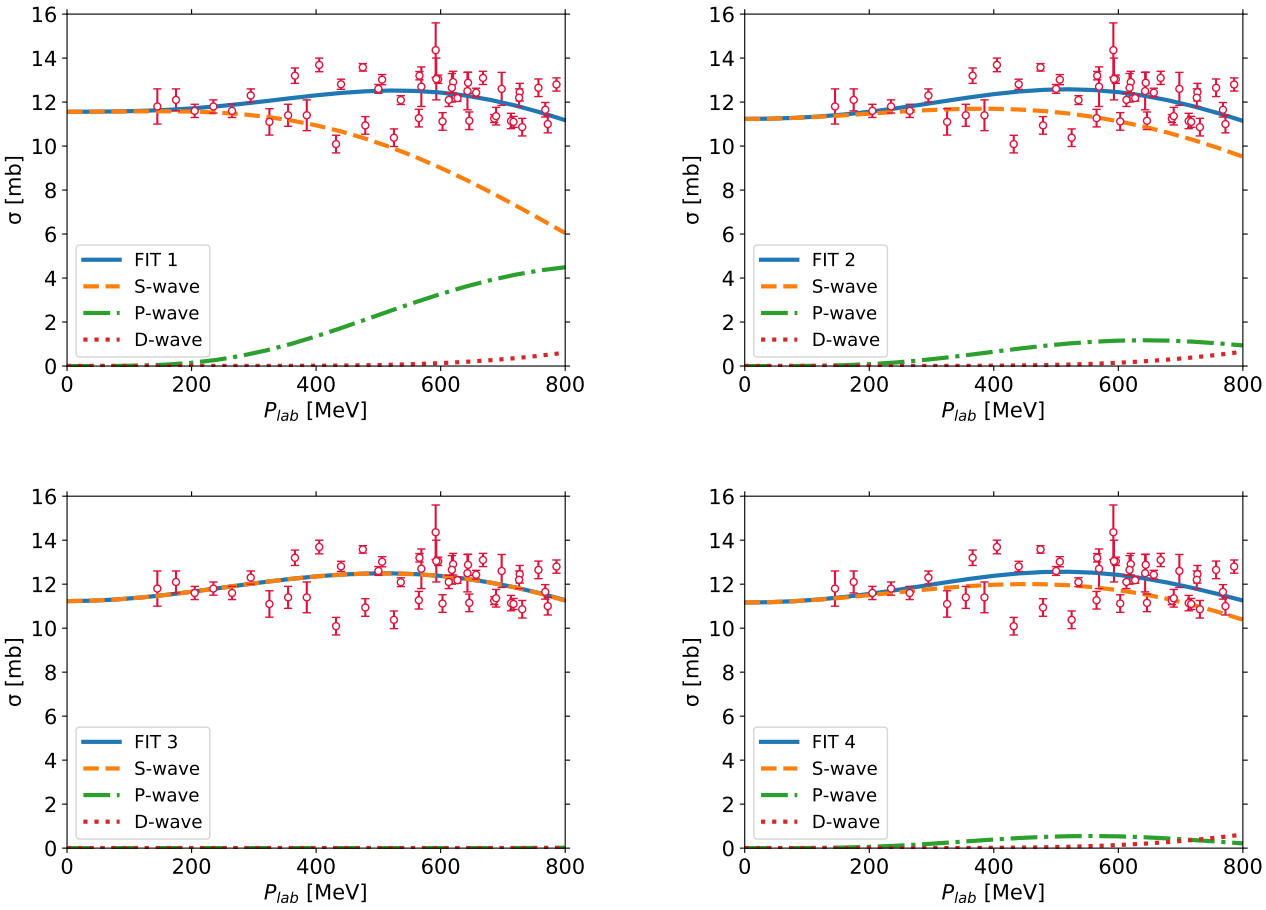

Fig.6.6 Partial wave contributions of $I = 1$ K^+N total cross section calculated with the determined LECs determined by each FIT.

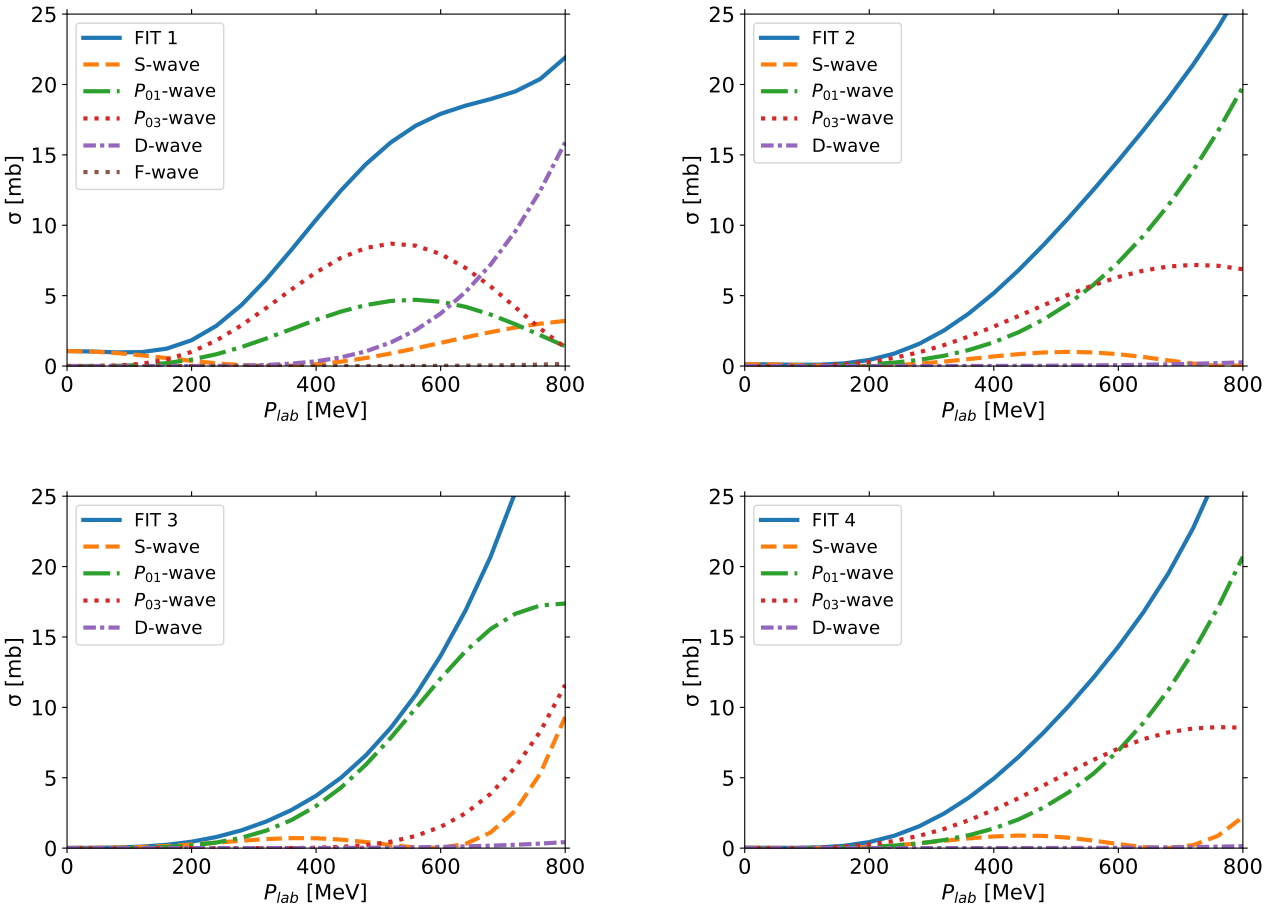

Fig.6.7 Partial wave contributions of $I = 0$ K^+N total cross section calculated with the determined LECs determined by each FIT.

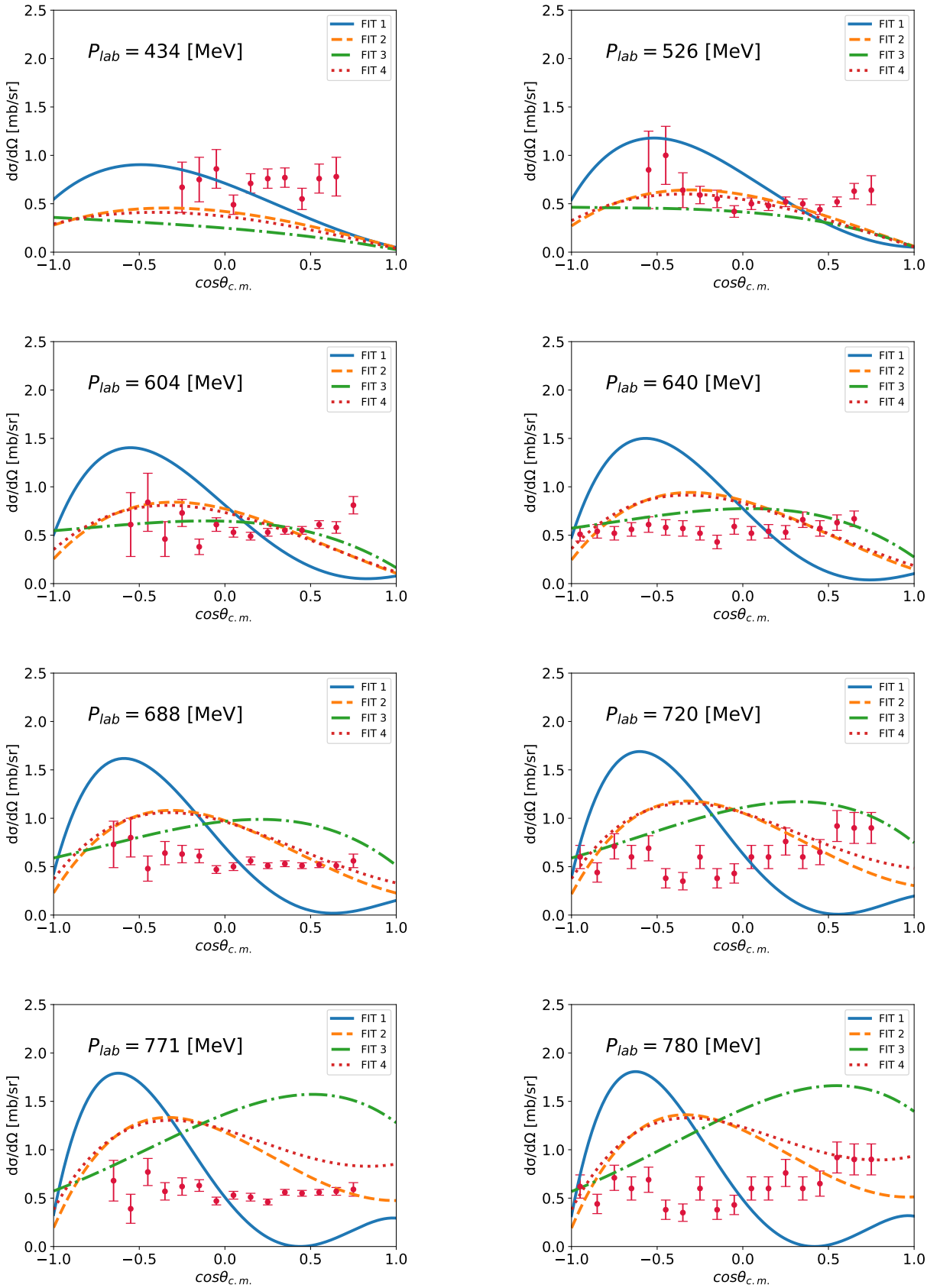

Fig.6.8 Calculated differential cross sections of K^+n elastic scattering in comparison with the experimental data of Ref. [154, 159]. The momenta at the $P_{\rm lab} = 640, 720$ and 780 MeV/c are the data from Ref. [159]. The others are the data from Ref. [154].

6.4.2 Behavior of in-medium chiral condensate with strange quarks

In this section, we discuss the behavior of in-medium chiral condensate with strange quarks Eq. (6.42) with the determined LECs in the previous sections. As seen in Eq. (6.42), the sign of $(3b^{I=1} + b^{I=0})$ determines whether the chiral condensate increases or decreases. It should be noted that the qualitative behavior of the chiral condensate is important here and the detailed value of $(3b^{I=1} + b^{I=0})$ is not focused in this chapter since the chiral condensate Eq. (6.42) is calculated under the linear density approximation.

We adopt the SU(3) low-energy constants obtained by other calculations and summarized in Table 6.4 in order to see the dependency of the parameter choice. The first was obtained by fitting to lattice QCD data of octet baryon masses [160]. The second set was obtained by Ref. [161] via fitting to experimental baryon octet data, this was also summarized by Ref. [162]. Since Ref. [161] only determined b_D and b_F, we fix b_0 so that $\langle \bar{u}u \rangle^*$ with the kaon decay constant F_K is reduced by 30% compared to in-vacuum at normal nuclear density ρ_0.

In order to see the density dependency of in-medium chiral condensate with strange, we plot Eq. (6.42) with our LECs in Table 6.3 together with Eq. (6.42) with the LECs in Table 6.4 as shown in Fig. 6.9. The behavior of the in-medium condensate is highly dependent on the choice of the parameter set. At $\rho_N = \rho_0$ the chiral condensate with the parameter sets in Table 6.4 is reduced by about 15∼23%, which is consistent with the results by FITs 2 and 4, which gives about 10∼20% reduction. As far as FIT 1 is concerned, the chiral condensate decreases very significantly compared to that with the LECs in Table 6.4. In contrast to these FITs, FIT 3 leads to the in-medium chiral condensate increased at $\rho_N = \rho_0$ compared to the in-vacuum condensate. This behavior is unnatural in terms of the partial restoration of DBχS at high density. FIT 3′ is discussed in the next section.

The choice of the experimental data of the $I = 0$ total cross section and the presence or absence of the resonance state in $I = 0$ K^+N scatterings have a significant impact on the determination of the LECs which is important for the behavior of the chiral condensate. Therefore we emphasize that in order to determine the behavior of the in-medium chiral condensate with strange quarks precisely, it is important to accurately determine many experimental values at the energy much lower than $P_{\rm lab} = 600$ MeV such that the effect of the resonance state needs not to be taken into account.

Table 6.4 SU(3) low-energy constants obtained by other calculations are shown in units of GeV^{-1}.

LEC	Ref. 1 [160]	Ref. 2 [161]
b_0	−0.609	−0.630
b_D	0.225	0.060
b_F	−0.404	−0.190

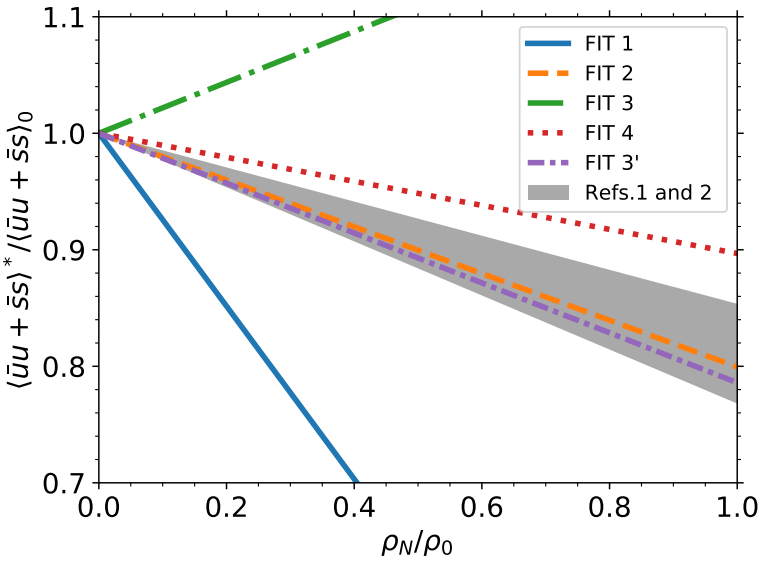

Fig.6.9 Density dependency of the in-medium chiral condensate with strange quarks calculated with our parameters in Tables 6.3 and 6.5 in comparison with the chiral condensate with the parameters in Table 6.4.

6.4.3 Another solution with the P_{01} resonance

We obtained FITs 1∼4 as the solution of the fitting for the K^+N cross sections. Unlike FITs 1, 2 and 4, FIT 3 does not provide the decreasing condensate at nuclear matter. We find another solution that minimizes Eq. (6.44) with the P_{01} resonance. This is named FIT 3′ and is shown in Table 6.5. Compared to the $I = 1$ LECs of FIT 3, those of FIT 3′ is closer to those of FITs 1, 2 and 4. The result of the calculation of in-medium chiral condensate using the LEC of FIT 3′ is shown in Fig. 6.9. It decreases compared to the chiral condensate in vacuum at $\rho_N = \rho_0$, as in the case with FITs 1,2 and 4. This behavior is consistent with the partial restoration of DBχS at high density. The fact that there is another solution with the P_{01} resonance for which $\chi^2_{\text{d.o.f.}}$ remains nearly unchanged indicates that the LECs with the smallest value of $\chi^2_{\text{d.o.f.}}$ may change as the experimental values increase in the future.

Table 6.5 Same as FIT 3 in Table 6.3 but the LECs that provide the minimized $\chi^2_{\rm d.o.f.}$. The LECs are shown in unit of GeV^{-1}.

Fitting	FIT 3′ (Bowen 1970 with P_{01})
$b^{I=1}$	-0.39 ± 0.12
$d^{I=1}$	0.69 ± 0.18
$g^{I=1}$	-1.07 ± 0.21
$h^{I=1}$	2.10 ± 0.50
$w^{I=1}$	-0.66 ± 0.10
$b^{I=0}$	-0.80 ± 0.50
$d^{I=0}$	-2.00 ± 0.60
$g^{I=0}$	1.00 ± 0.90
$h^{I=0}$	-3.90 ± 0.90
$w^{I=0}$	-0.10 ± 0.40
v_-	6.90 ± 0.19
v_+	-2.00 ± 0.90
$\chi^2_{\rm dof}$	3.00

6.4.4 Chiral condensate in SU(3) symmetric baryonic matter

As seen in the previous section, we discussed the chiral condensate including the strange quark component in symmetric nuclear matter consisting of the nucleons not including the strange quarks. In that sense, we discussed the SU(3) chiral condensate in the SU(2) symmetric baryonic matter. It is also interesting to further extend the chiral condensate in nuclear matter to that in the hypothetical hyperon matter and the SU(3) symmetric baryonic matter. Note, however, that chiral condensate in nuclear matter can be studied phenomenologically from the NG boson in heavy nuclei, as could be discussed from pionic atoms and pion-nuclei scattering, whereas it is difficult to evaluate the chiral condensate in hyperon matter phenomenologically.

Just as protons and neutrons are the same numbers in symmetric nuclear matter, we define SU(3) symmetric baryonic matter to have the same numbers of $1/2^+$ baryons in SU(3) octet, $p, n, \Lambda, \Sigma^+, \Sigma^0, \Sigma^-, \Xi^0$ and Ξ^-. We further define that there are the same numbers of Σ^+, Σ^0, and Σ^- in Σ-hyperon matter, and the same numbers of Ξ^0 and Ξ^- in Ξ-hyperon matter. Of course, only Λ exists in Λ-hyperon matter.

The chiral condensates $\langle \bar{u}u + \bar{d}d \rangle$ and $\langle \bar{u}u + \bar{s}s \rangle$ in nuclear matter and each hyperon matter such as

Λ-matter, Σ-matter and Ξ-matter are obtained in the same way as Section 6.2:

$$\frac{\langle \bar{u}u+\bar{d}d\rangle^*_N}{\langle \bar{u}u+\bar{d}d\rangle_0} = 1+\frac{(4b_0+2b_D-2b_F)}{F_\pi^2}\rho_B, \tag{6.45a}$$
$$\frac{\langle \bar{u}u+\bar{d}d\rangle^*_\Lambda}{\langle \bar{u}u+\bar{d}d\rangle_0} = 1+\frac{(12b_0+4b_D)}{3F_\pi^2}\rho_B, \tag{6.45b}$$
$$\frac{\langle \bar{u}u+\bar{d}d\rangle^*_\Sigma}{\langle \bar{u}u+\bar{d}d\rangle_0} = 1+\frac{(4b_0+4b_D)}{F_\pi^2}\rho_B, \tag{6.45c}$$
$$\frac{\langle \bar{u}u+\bar{d}d\rangle^*_\Xi}{\langle \bar{u}u+\bar{d}d\rangle_0} = 1+\frac{(4b_0+2b_D-2b_F)}{F_\pi^2}\rho_B, \tag{6.45d}$$

$$\frac{\langle \bar{u}u+\bar{s}s\rangle^*_N}{\langle \bar{u}u+\bar{s}s\rangle_0} = 1+\frac{(4b_0+3b_D-b_F)}{F_K^2}\rho_B, \tag{6.46a}$$
$$\frac{\langle \bar{u}u+\bar{s}s\rangle^*_\Lambda}{\langle \bar{u}u+\bar{s}s\rangle_0} = 1+\frac{2(6b_0+5b_D)}{3F_K^2}\rho_B, \tag{6.46b}$$
$$\frac{\langle \bar{u}u+\bar{s}s\rangle^*_\Sigma}{\langle \bar{u}u+\bar{s}s\rangle_0} = 1+\frac{2(2b_0+b_D)}{F_K^2}\rho_B, \tag{6.46c}$$
$$\frac{\langle \bar{u}u+\bar{s}s\rangle^*_\Xi}{\langle \bar{u}u+\bar{s}s\rangle_0} = 1+\frac{(4b_0+3b_D+b_F)}{F_K^2}\rho_B, \tag{6.46d}$$

where ρ_B is the density of the baryon number in each matter and we use the vertices of the meson-baryon T-matrices are summarized in Appendix D. The chiral condensates in the SU(3) symmetric baryonic matter are also obtained as:

$$\frac{\langle \bar{u}u+\bar{d}d\rangle^*_B}{\langle \bar{u}u+\bar{d}d\rangle_0} = \frac{1}{8}\left[2\frac{\langle \bar{u}u+\bar{d}d\rangle^*_N}{\langle \bar{u}u+\bar{d}d\rangle_0}+\frac{\langle \bar{u}u+\bar{d}d\rangle^*_\Lambda}{\langle \bar{u}u+\bar{d}d\rangle_0}+3\frac{\langle \bar{u}u+\bar{d}d\rangle^*_\Sigma}{\langle \bar{u}u+\bar{d}d\rangle_0}+2\frac{\langle \bar{u}u+\bar{d}d\rangle^*_\Xi}{\langle \bar{u}u+\bar{d}d\rangle_0}\right] \tag{6.47}$$
$$\frac{\langle \bar{u}u+\bar{s}s\rangle^*_B}{\langle \bar{u}u+\bar{s}s\rangle_0} = \frac{1}{8}\left[2\frac{\langle \bar{u}u+\bar{s}s\rangle^*_N}{\langle \bar{u}u+\bar{s}s\rangle_0}+\frac{\langle \bar{u}u+\bar{s}s\rangle^*_\Lambda}{\langle \bar{u}u+\bar{s}s\rangle_0}+3\frac{\langle \bar{u}u+\bar{s}s\rangle^*_\Sigma}{\langle \bar{u}u+\bar{s}s\rangle_0}+2\frac{\langle \bar{u}u+\bar{s}s\rangle^*_\Xi}{\langle \bar{u}u+\bar{s}s\rangle_0}\right] \tag{6.48}$$

where we relabel the chiral condensate in nuclear matter $\langle\rangle^*$ as $\langle\rangle^*_N$ to distinguish it from that in other baryonic matter. The SU(3) chiral condensate in the SU(3) symmetric baryonic matter is calculated as

$$\frac{\langle \bar{u}u+\bar{d}d+\bar{s}s\rangle^*_B}{\langle \bar{u}u+\bar{d}d+\bar{s}s\rangle_0} = \frac{2}{3}\left(\frac{\langle \bar{u}u+\bar{s}s\rangle^*_B}{\langle \bar{u}u+\bar{s}s\rangle_0}+\frac{1}{2}\frac{\langle \bar{u}u+\bar{d}d\rangle^*_B}{\langle \bar{u}u+\bar{d}d\rangle_0}\right)$$

where we assume that the in-vacuum condensates have the same value: $\langle \bar{u}u\rangle_0 = \langle \bar{d}d\rangle_0 = \langle \bar{s}s\rangle_0$ which seems to be valid according to the lattice QCD calculation [23].

As we saw in the previous section, to evaluate the chiral condensate in the nuclear matter, it is sufficient to determine the two-parameter pairs $b^{I=0,1}$, and for this purpose, the parameters were determined from KN scattering. On the other hand, the combinations of the LECs in Eq. (6.45) which cannot be rewritten in terms of the LECs in NLO of KN amplitudes, $b^{I=1} = b_0 + b_D$ and $b^{I=0} = b_0 - b_F$, should be normally determined from the meson-hyperon scatterings as well as the KN scattering. In our calculation here, we utilize FIT 2 of the obtained LECs $b^{I=0,1}$ from KN scattering in the previous section. Furthermore we use the relation formula between SU(2) and SU(3) LECs to fix b_0 [11]:

$$2b_0 + b_D + b_F = 2b_0 + b^{I=1} - b^{I=0} = 2c_1 \tag{6.49}$$

where c_1 is one of the SU(2) LECs. Here we use $c_1 = -0.59$ GeV^{-1} [81].

Firstly, we plot the behavior of $\langle \bar{u}u + \bar{d}d \rangle$ in nuclear matter, each hyperon matter and the SU(3) symmetric baryonic matter shown in Fig. 6.10. This calculation shows that the SU(3) flavor symmetry breaking for the baryon matter since the condensate $\langle \bar{u}u + \bar{d}d \rangle$ has no strange components but hyperon matter contains the strange quarks. The relative amount of up and down quarks in hyperon matter is less than in nuclear matter, so the condensate in hyperon matter is expected not to decrease more than that in nuclear matter. Fig. 6.10 shows that the chiral condensates in Λ-matter and Ξ-matter increase compared to the in-vacuum condensate, while the chiral condensate in Σ-matter decreases more than that in nuclear matter. Thus the results show a different behavior from the expectation. On the other hand, the condensate in the SU(3) symmetric baryonic matter is reduced but not more than that in nuclear matter, this is the expected behavior.

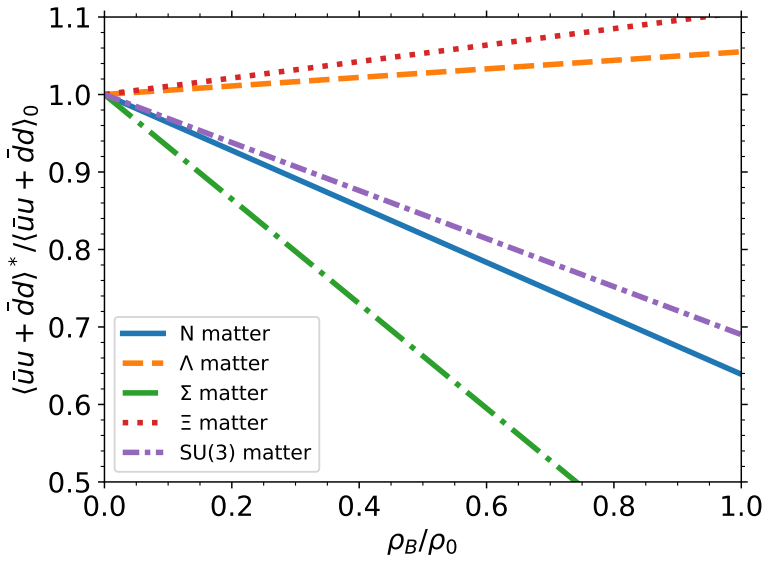

Fig.6.10 Baryon density dependencies of $\langle \bar{u}u + \bar{d}d \rangle$ in nuclear matter, each hyperon matter and the SU(3) symmetric baryonic matter.

Next, we plot the behavior of $\langle \bar{u}u + \bar{s}s \rangle$ in nuclear matter, each hyperon matter and the SU(3) symmetric baryonic matter shown in Fig. 6.11. The calculation shows that the chiral condensates in Λ-matter and Ξ-matter are reduced compared to the chiral condensate in nuclear matter, but the condensate in Σ-matter is not reduced compared to nuclear matter. Thus, since hyperon matter contains strange quarks, it would seem that the chiral condensate with strange components in hyperon matter would be reduced compared to chiral condensate in nuclear matter, but this is not necessarily the case. On the other hand, the condensate in the SU(3) symmetric baryonic matter is reduced compared to that in nuclear matter, this is the expected behavior.

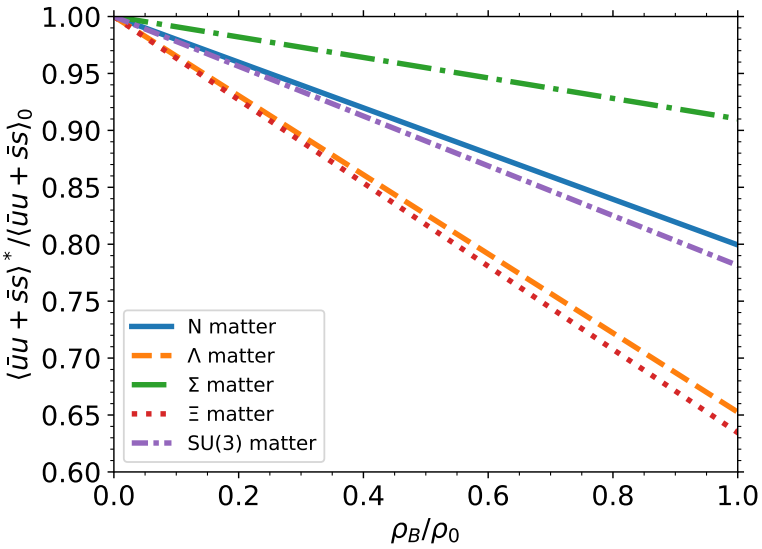

Fig.6.11 Same as Fig. 6.10, but $\langle\bar{u}u+\bar{s}s\rangle$.

For the SU(3) chiral condensate in the SU(3) symmetric baryonic matter, our result is seen in Fig. 6.12. The chiral condensate decreases by 25% at $\rho_B = \rho_0$. Thus the chiral symmetry is partially restored by 25% at $\rho_B = \rho_0$. This is consistent with the case of the SU(2) chiral condensate in nuclear matter.

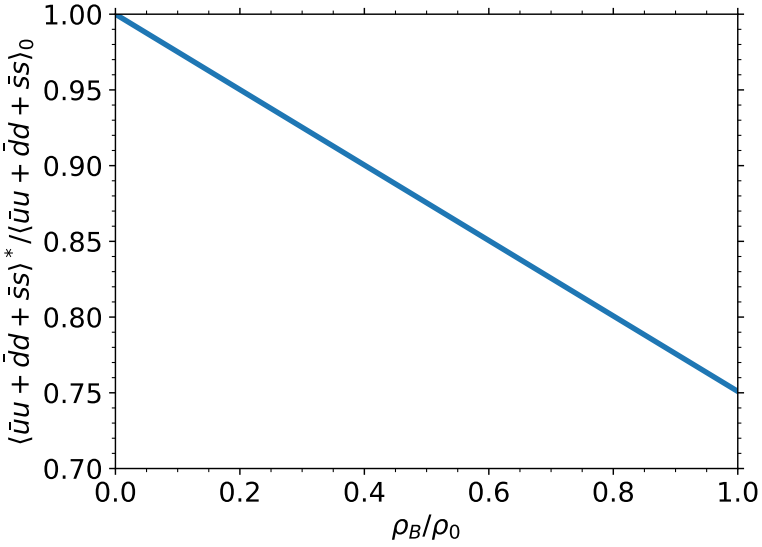

Fig.6.12 Baryon density dependencies of the SU(3) chiral condensate in the SU(3) symmetric baryonic matter with FIT 2 and Eq. (6.49).

It would be important to know the meson-hyperon interaction in order to investigate the SU(3) flavor symmetry breaking of $\langle\bar{u}u+\bar{d}d\rangle$ in the SU(3) baryonic matter and the SU(3) chiral condensate in the SU(3) symmetric baryonic matter. The meson-hyperon scattering could give important information on the limitation of the SU(3) LECs, complementary to the KN scattering.

6.4.5 Wave function renormalization of in-medium kaon

We also discuss the wavefunction renormalization of the kaon-nucleus using the obtained KN amplitudes. In our study, we construct the K^+N scattering amplitudes that are further developed from

Ref. [91]. So we calculate the wavefunction renormalization for the in-medium kaon using our K^+N scattering amplitudes constructed in the previous section. We use the isospin-averaged KN scattering amplitude for forward direction written as

$$T^{\rm ave}_{KN}(\omega,\theta=0)=\frac{1}{4}\big[3T^{I=1}_{KN}(\omega,\theta=0)+T^{I=0}_{KN}(\omega,\theta=0)\big]. \tag{6.50}$$

We obtain the optical potential of K^+-nucleus in the linear density approximation as

$$2M_K V_{\rm opt}(\omega^*_K)=\frac{\rho_N}{2M_N}T^{\rm ave}_{KN}(\omega^*_K,\theta=0) \tag{6.51}$$

where ω^*_K is the in-medium kaon energy. Now we assume that $V_{\rm opt}(\omega^*_K) << \omega_K$ and use the Klein-Gordon equation $\omega^{*2}_K-\omega^2_K-2M_KV_{\rm opt}(\omega^*_K)=0$ and its positive solution. Expanding the self-energy around $\omega^*_K=\omega_K$, we obtain

$$\begin{aligned}
V_{\rm opt}(\omega^*_K)&=V_{\rm opt}(\omega_K)+(\omega^*_K-\omega_K)\left.\frac{\partial V_{\rm opt}}{\partial\omega^*_K}\right|_{\omega^*_K=\omega_K}+\dots\\
&\simeq V_{\rm opt}(\omega_K)+\frac{M_K}{\omega_K}V_{\rm opt}(\omega_K)\left.\frac{\partial V_{\rm opt}}{\partial\omega^*_K}\right|_{\omega^*_K=\omega_K}\\
&=\left(1+\frac{M_K}{\omega_K}\left.\frac{\partial V_{\rm opt}}{\partial\omega^*_K}\right|_{\omega^*_K=\omega_K}\right)V_{\rm opt}(\omega_K)\equiv Z_K V_{\rm opt}(\omega_K), \qquad (6.52)\\
Z_K&\equiv 1+\frac{M_K}{\omega_K}\left.\frac{\partial V_{\rm opt}}{\partial\omega^*_K}\right|_{\omega^*_K=\omega_K} \qquad (6.53)
\end{aligned}$$

where Z_K is the wavefunction renormalization factor. The dependence of the momentum of kaon in nuclear matter P_{K^+} of the wavefunction renormalization factor Z_K at the normal nuclear density is shown in Fig. 6.13. Z_K with FIT 3′ is almost independent of P_{K^+} and gives almost 6% enhancement. On the other hand, those with all FITs expect FIT 3′ increases with respect to P_{K^+}. The degree of this increase depends on the choice of FIT. The density dependence of the wavefunction renormalization factor Z_K at the $P_{K^+}=488$ MeV/c is shown in Fig. 6.14. For the type of FIT, the enhancement ranges from 2% to 5% at the normal nuclear density. The K^+N interaction should be determined without ambiguity in terms of the investigation of the wavefunction renormalization for kaon in the nuclear matter. In the case of the in-medium pion, the wavefunction renormalization factor is enhanced by 40% at the normal nuclear density [144]. Compared to the case of the in-medium pion, our calculation gives a smaller enhancement at the normal nuclear density.

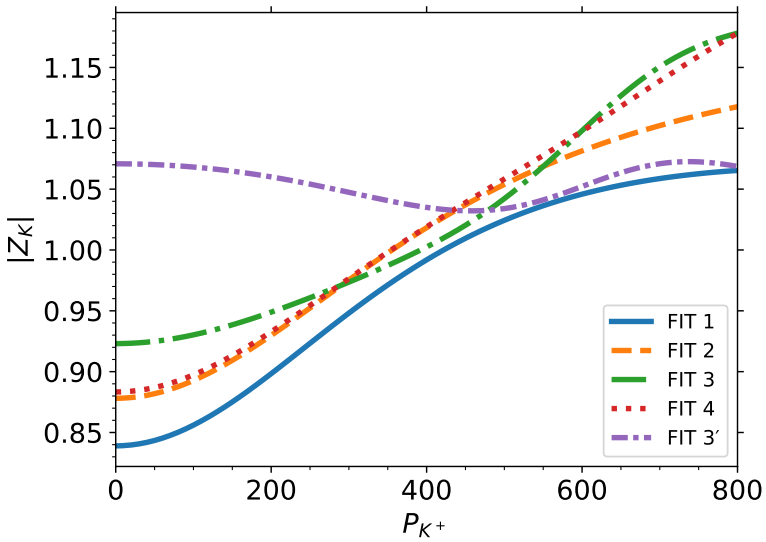

Fig.6.13 The dependence of the momentum of kaon in nuclear matter P_{K^+} of the absolute value of the wavefunction renormalization factor Z_K at the normal nuclear density.

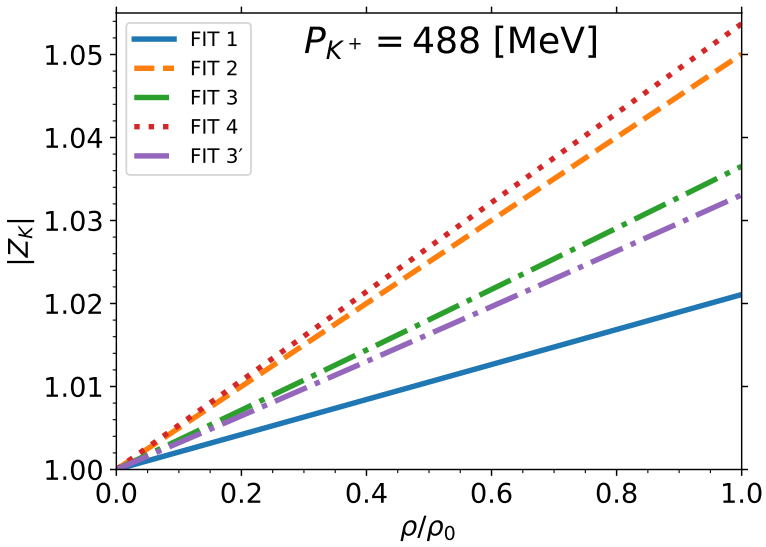

Fig.6.14 The density dependence of the absolute value of the wavefunction renormalization factor Z_K at the $P_{K^+} = 488$ MeV/c.

6.5 Summary

We have obtained the in-medium condensate that contains the kaon-nucleon scattering amplitude T_{KN} in the soft limit under the linear density approximation. We have utilized SU(3) chiral perturbation theory in order to calculate T_{KN}. Taking the soft limit, we have rewritten the condensate in terms of the low-energy constants (LECs) defined as SU(3) chiral perturbation theory.

We have estimated the LECs of SU(3) chiral perturbation theory using the experimental data of the K^+N elastic scatterings for the study of the chiral condensate including the strange components in nuclear matter. In order to improve extrapolation to the strange sector, we have utilized some terms from the next-to-next-to-leading order of the chiral Lagrangian, which contains the strange quark mass in addition to the chiral Lagrangian up to next-to-leading order. The LECs that appear here

characterize the interaction between K^+ and N. We have fitted them to reproduce the experimental data. We have performed the fitting for the LECs using the experimental data of the K^+p differential cross section, the $K^+n \to K^0p$ charge exchange differential cross sections, $I = 1$ total cross section, and $I = 0$ total cross section.

For $I = 0$ amplitude, there are two choices of the experimental data for the total cross section. Moreover, it has been reported that a resonance state could exist around $P_{\rm lab} = 600$ MeV at $I = 0$. Therefore, we have performed fitting considering the different experimental data and the presence of the resonance state. In particular, we have obtained the $I = 1$ amplitude which reproduces the experimental data at $P_{\rm lab} < 800$ MeV very well. For the $I = 0$ amplitude, since it has been reported that a resonance state exists around $P_{\rm lab} = 600$ MeV at $I = 0$, we have performed fitting the LECs in the case with/without the resonance state. We have determined the $I = 0$ amplitude to reproduce the $I = 0$ total cross section and the differential cross section of the $K^+n \to K^0p$ well, while the differential cross section of the K^+n elastic scattering not used for fitting has not been reproduced.

We have discussed the behavior of the in-medium chiral condensate with strange components based on the determined LECs. We have suggested that the choice of the experimental data for the $I = 0$ total cross section and whether the resonance state exists contribute to the behavior of the condensate in nuclear matter. We have also calculated the chiral condensates in hyperon matter and the SU(3) symmetric baryonic matter. In particular, we have indicated that the SU(3) flavor symmetry breaking was studied from $\langle \bar{u}u + \bar{d}d \rangle$ in hyperon matter and the SU(3) symmetric baryonic matter. Moreover, we have calculated $\langle \bar{u}u + \bar{d}d + \bar{s}s \rangle$ in the SU(3) symmetric baryonic matter and obtained the 25% restoration of the chiral symmetry in the case of SU(3) with our fitted LECs. This result is consistent with the case of the SU(2) condensate in nuclear matter. We have also indicated that the meson-hyperon scatterings are important to determine the SU(3) LECs.

We have calculated the wavefunction renormalization factor using the obtained T-matrix of KN. The dependence of the momentum of kaon in nuclear matter P_{K^+} of the wavefunction renormalization factor Z_K at the normal nuclear density depends on the FITs. It is important to determine the LECs in terms of wavefunction renormalization. In any FITs, the wavefunction renormalization factor for in-medium kaon has not increased as much as that for in-medium pion at the normal nuclear density.

We have emphasized that in order to determine the behavior of in-medium chiral condensate with strange precisely, it is important to accurately determine the experimental values at the energy much lower than $P_{\rm lab} = 600$ MeV such that the effect of the resonance state needs not to be taken into account, or to determine the existence of the resonance state.

Chapter 7

Kaonic atom and K^--nucleus interaction

7.1 Introduction: Two possible origins of the energy shift

K^--nucleus interaction is extracted by kaonic atoms which are bound states between K^- and nucleus mainly by Coulomb interaction, as well as pion-nucleus interactions for pionic atoms. Just as we discussed partial restoration of chiral symmetry in nuclear medium from the pion-nucleus interaction in Sec. 3.2.2, it may be possible to extract the information about partial restoration of chiral symmetry from the K^--nucleus interactions in the kaonic atom, but this has not currently been done[*1]. The K^--nucleus interaction is not as well understood as the pion-nucleus interaction. In particular, various arguments exist about K^--nucleus potential [96, 116], and while there are deep and shallow potentials as to their depth, they have not been determined.

The strong interaction effects on kaonic atoms can be seen in the energy shift from the pure Coulomb energy spectrum ΔE, and the absorption width Γ. The energy shift is defined by the following formula:

$$\Delta E = E_B - E_c \tag{7.1}$$

where E_c is the postulatory binding energy of the kaon and the atomic nucleus calculated by considering only the Coulomb potential and E_B is the real part of the authentic binding energy including both the effects of the strong and electromagnetic interactions. If $\Delta E > 0$ ($\Delta E < 0$) the strong interaction effect to the binding energy is attractive (repulsive).

The energy shift is found to be repulsive in all observed kaonic atoms. However, the strong interaction between K^-N is known to be attractive because $\Lambda(1405)$ is considered to be the $\bar{K}N$ bound state and therefore K^--nucleus potential is considered to be attractive as well as K^-N interaction. Hence we focus on the origin of the repulsive shift in kaonic atoms from the attractive strong interaction in this chapter In this study, we do not go into the depth of the K^--nucleus optical potential, but we focus on the feature that the shift of the binding energy due to the strong interaction is repulsive despite the K^--nucleus potential being attractive, i.e., the binding energy works in the direction of decreasing the absolute value of the binding energy.

We have two candidates for the origin of the repulsive shift. One is an effect of strong attractive interactions. If the attraction is so strong that some nuclear bound states are generated under the atomic states, the atomic states are repelled upwards by these bound states as a consequence of level

[*1] The kaon-nucleus scattering may currently be better suited for that discussion [91].

repulsion if the nuclear and atomic states have the same angular momentum. This mechanism is also seen in the $\bar{K}N$ system. The scattering length of the $\bar{K}N$ with $I = 0$ is known to have repulsive nature even though the $\bar{K}N$ interaction is attractive. This puzzle is solved by the presence of the $\Lambda(1405)$ resonance below the threshold of $\bar{K}N$. The coupling of $\Lambda(1405)$ and $\bar{K}N$ scattering states causes the level repulsion and consequently, the $\bar{K}N$ scattering length is seen as if $\bar{K}N$ were repulsively interacting. In this case, the real part of the optical potential may be more significant for the repulsive shift than the imaginary part.

The other is an effect of a large imaginary part of the optical potential. It works repulsively, because, for example, the 2nd order perturbation of the large imaginary part

$$E_n^{(2)} = \sum_{m \neq n} \frac{\langle \phi_n | i \,\mathrm{Im}\, V_{\mathrm{opt}} | \phi_m \rangle^2}{E_n - E_m} \tag{7.2}$$

may give a positive value. Therefore if the optical potential has a large imaginary part, it gives the repulsive energy shift. In other words, as discussed along the context of deeply bound antiproton atoms in Ref. [98], the large imaginary part suppresses the atomic wavefunction inside the nucleus, and consequently, the normalized wavefunction is pushed away to the outside of the nucleus. In this way, the large imaginary part plays an important role in the repulsive shift.

We study the global feature of the K^--nucleus potential, especially the role of the imaginary part, in the view of the kaonic atom by the following approach: Firstly, we determine optical potential parameters for each observed kaonic atom by solving the Klein-Gordon equation so as to reproduce the experimental data of the energy shift and the absorption width. Next, we confirm whether the obtained potential parameters describe also the other kaonic atoms by calculating the energy shifts and the absorption widths of various kaonic atoms using the parameters fitted by each kaonic atom and checking whether the calculated values are consistent with the experimental data.

7.2 Model of kaonic atom

In this section, we explain our formulation to calculate the binding energy of a kaonic atom. We solve the Klein-Gordon equation for the relative motion of K^- and a nucleus

We derive the equation of motion with the Coulomb potential $V_c(r)$ and the optical potential $V_{\mathrm{opt}}(r)$. We study the optical potential between kaon and the nucleus by solving the Klein-Gordon equation.

$$\Big[-\{E - V_c(r)\}^2 - \nabla^2 + \mu^2 + 2\mu V_{\mathrm{opt}}(r) \Big] \phi(\boldsymbol{r}) = 0, \tag{7.3}$$

with the Coulomb potential $V_c(r)$ of the electromagnetic interaction and the optical potential $V_{\mathrm{opt}}(r)$ of the strong interaction. The Coulomb potential is introduced as the zeroth component of the vector potential, and the optical potential is introduced as the scalar potential which is connected to the self-energy. The complex energy E is written as $E = \mu - E_B - i\Gamma/2$ with the reduced mass μ, the binding energy E_B and the absorption width Γ. We assume spherical potentials for $V_c(r)$ and $V_{\mathrm{opt}}(r)$, and the wavefunction $\phi(\boldsymbol{r})$ can be decomposed as $\phi(\boldsymbol{r}) = R_{n\ell}(r) Y_\ell^m(\Omega)$ with the radial wavefunction $R(r)$ and the spherical harmonics $Y_\ell^m(\Omega)$.

In order to see a global feature of the optical potential, we construct the K^--nucleus optical potential simply under the linear nuclear density approximation. The K^--nucleus optical potential $V_{\mathrm{opt}}(r)$

which is assumed to be proportional to nuclear density $\rho_N(r)$ is given by

$$V_{\rm opt}(r) = -(V_0 + iW_0)\frac{\rho_N(r)}{\rho_0} \tag{7.4}$$

where V_0 and W_0 are parameters of the strength of the strong interaction. These parameters are determined by two experimental values, which are the energy shift and the absorption width for each kaonic atom. We assume that the strength of the optical potential does not depend on nucleus. We use the Woods-Saxon form for the nuclear density $\rho_N(r)$ distribution:

$$\rho_N(r) = \frac{\rho_0}{1 + \exp[(r - R_B)/a]} \tag{7.5}$$

where R_B and a are the nuclear radius and diffuseness parameters. The parameters are taken from Refs. [163, 164] and summarized in Table 7.1.

The imaginary part of the optical potential produces nuclear absorption. We assume that the real part of the optical potential works attractively because of the fact that the K^-N interaction is attractive.

Microscopically, the dynamical effects of the $\bar{K}N$ interaction in the nucleus such as the presence of the $\Lambda(1405)$ resonance below the $\bar{K}N$ threshold, especially the energy dependence of the potential, are important to describe the K^- optical potential. Indeed, here we focus on the global feature of the optical potential for the kaonic atom and investigate it in the very narrow atomic energy range. We are interested in the existence or nonexistence of the nuclear states which affect the position of the atomic state. We do not intend to study the microscopic details of the kaon optical potential nor determine precisely the position of the nuclear bound states of the kaon which should be very sensitive to the dynamics of the $\bar{K}N$ interaction.

For the Coulomb potential $V_c(r)$, the charge distribution of the nucleus is taken into account as

$$V_c(r) = -\frac{e^2}{4\pi}\int \frac{\rho_p(r')}{|\boldsymbol{r} - \boldsymbol{r}'|}\mathrm{d}^3r', \tag{7.6}$$

where $\rho_p(r)$ is the proton density. We assume that the same density distribution as $\rho_N(r)$ for the proton density $\rho_p(r) = \rho_{p0}/(1 + \exp[(r - R_B)/a])$ with ρ_{p0} normalized as

$$\int \rho_p(r)\mathrm{d}^3r = Z, \tag{7.7}$$

with the proton number Z. The Coulomb energy E_c appears in Eq. (7.2) is obtained by $V_{\rm opt} = 0$.

In this calculation, we do not consider the effect of vacuum polarization. We have confirmed that this effect on the energy shift and the absorption width is at most 5% and these values are smaller than the experimental errors.

7.3 Result

In this section, we show numerical results calculated by using the approach shown in the previous section. First, we show the optical potential parameters V_0 and W_0 in various kaonic atoms. Then, we confirm their universality.

Table 7.1 Density parameters, the nuclear radius R_B and the diffuseness a, used in this calculation. The values are taken from Refs. [163, 164]

Nucleus	R_B[fm]	a[fm]
Mg	2.980	0.551
Al	2.840	0.569
Si	2.930	0.569
P	3.078	0.569
S	3.165	0.569
Cl	3.395	0.569
Co	4.080	0.569
Ni	4.090	0.569
Cu	4.200	0.569
Ag	5.300	0.532
Cd	5.380	0.563
In	5.357	0.563
Sn	5.300	0.583

Table 7.2 Observed data of the energy shift ΔE and the absorption width Γ. The values are taken from Refs. [165–167]. For the Cu kaonic atom, two data sets are employed; one data named Cu^1 is taken from Ref. [167], and the other data set named Cu^2 is taken from Ref. [166].

Atom	Transition	ΔE [keV]	Γ [keV]	Ref.
Mg	$4f \to 3d$	-0.027 ± 0.015	0.214±0.015	[166]
Al	$4f \to 3d$	-0.760 ± 0.050	0.490±0.160	[166]
Si	$4f \to 3d$	-0.130 ± 0.015	0.800±0.033	[166]
P	$4f \to 3d$	-0.330 ± 0.08	1.440±0.120	[165]
S	$4f \to 3d$	-0.550 ± 0.06	2.330±0.200	[165]
Cl	$4f \to 3d$	-0.770 ± 0.40	3.80±1.0	[165]
Co	$5g \to 4f$	-0.099 ± 0.106	0.64±0.25	[166]
Ni	$5g \to 4f$	-0.180 ± 0.070	0.59±0.21	[167]
Cu^1	$5g \to 4f$	-0.240 ± 0.220	1.650±0.72	[167]
Cu^2	$5g \to 4f$	-0.377 ± 0.048	1.35±0.17	[166]
Ag	$6h \to 5g$	-0.18 ± 0.12	1.54±0.58	[166]
Cd	$6h \to 5g$	-0.40 ± 0.10	2.01±0.44	[166]
In	$6h \to 5g$	-0.53 ± 0.15	2.38±0.57	[166]
Sn	$6h \to 5g$	-0.41 ± 0.18	3.18±0.64	[166]

Table 7.3 Obtained potential parameters for Cu^1 kaonic atom.

Used datum	Potential type	V_0[MeV]	W_0[MeV]
Cu^1	1	79.5	114.5
	2	78.0	20.0
	3	199.5	28.0

7.3.1 Determining potential parameters

Let us first determine the optical potential parameters V_0 and W_0 so as to reproduce the central value of each datum shown in Table 7.2. These data are taken from Refs. [165–167]. We will use two data sets of the Cu kaonic atom; one data named Cu^1 is taken from Ref. [167], and the other data set named Cu^2 is taken from Ref. [166].

We calculate the Klein-Gordon equation (7.3) with optical potential (7.4) and the Coulomb potential (7.6) for various kaonic atoms using the following values of the hadron masses,

$$M_{K^-} = 493.677 \text{ MeV}, \tag{7.8}$$
$$M_N = 938.919 \text{ MeV}. \tag{7.9}$$

Here we have taken the isospin average of the nucleon masses. We use a kaonic atom reduced mass given by

$$\mu = A\ M_N M_{K^-}/(A\ M_N + M_{K^-}), \tag{7.10}$$

with mass number A. Here we ignore the effect of the nuclear binding energy. We have confirmed that the effects are negligibly small.

Let us focus on a Cu kaonic atom as an example. In the Cu kaonic atom, the $4f$ orbit is the last orbit. The strong interaction for the $5g$ orbit may be ignored and the level shift and absorption width are extracted from the transition $5g \to 4f$. There are two data sets for the Cu kaonic atom, Cu^1 and Cu^2 shown in Table 7.2. We use the Cu^1 data set for this example. We search the potential parameters which reproduce the shift and absorption width, -0.240 keV and 1.650 keV in the range of $0 \text{ MeV} \leq V_0,\ W_0 \leq 300$ MeV. We obtain three potential parameters within this range. The result is shown in Table 7.3. These potentials provide the same repulsive shift and absorption width but have different features. The first potential has a larger imaginary part than its real part. The second has a larger real part than its imaginary part. The third has the largest real part of the three and a small imaginary part.

We calculate wavefunctions using these potentials and show those of the Cu kaonic atom in Figs. 7.1 and 7.2. Fig. 7.1 shows wavefunctions of the Cu kaonic atom in an atomic scale ($r = 0 \sim 100$ fm) while Fig. 7.2 shows wavefunctions of the kaonic atom in a nuclear scale ($r = 0 \sim 10$ fm). These potentials yield similar wavefunctions at the atomic scale, while the number of nodes that corresponds to the number of the nuclear bound states, is different from each other at the nuclear scale. The wavefunction obtained by Potential 1 has no nodes, the wavefunction by Potential 2 has one node and the wavefunction by Potential 3 has two nodes.

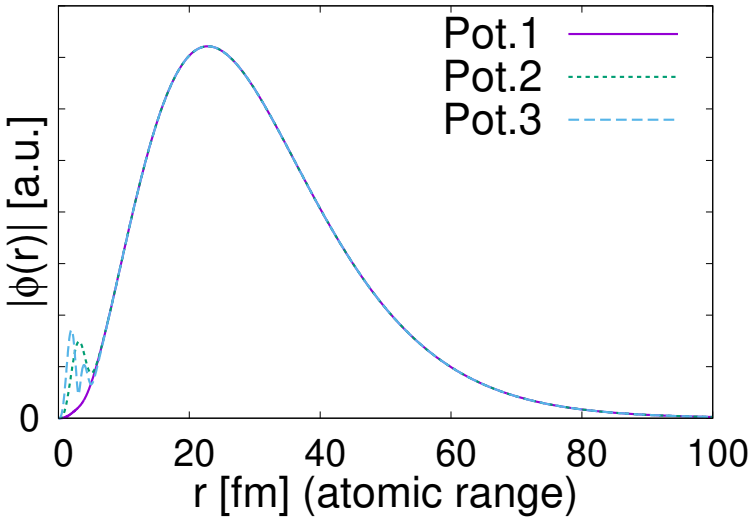

Fig.7.1 Wavefunctions squared of the atomic states with $\ell = 3$ (last orbit) calculated with Potentials 1, 2 and 3 for the Cu^1 kaonic atom in the atomic radial range.

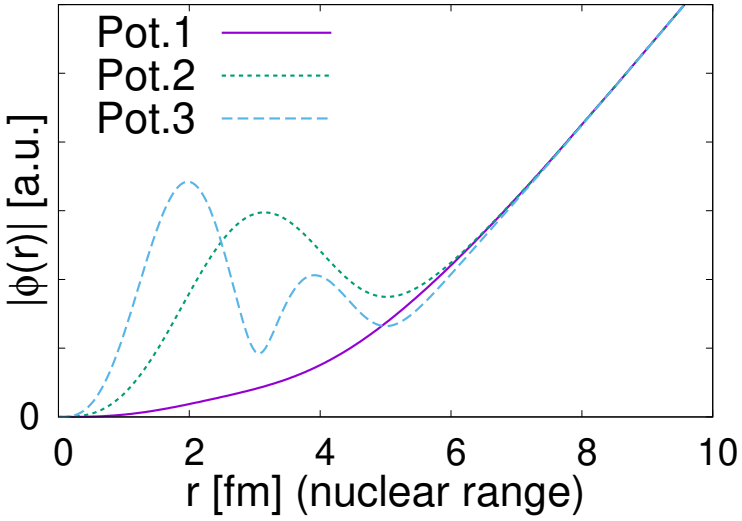

Fig.7.2 Same as in Fig.1, but in the nuclear radial range.

.

The Cu kaonic atom with Potential 1 has no nuclear states with the same angular momentum as the atomic state with $\ell = 3$ in which we are interested here. Thus, the nuclear states are not responsible for the repulsive shift in Potential 1. In order to see the role of the imaginary part of Potential 1 for the repulsive shift, we reduce the strength of the imaginary part of the potential W_0 by introducing a factor λ_1 as $\mathrm{Im}\, V_{\mathrm{opt}}(r) \rightarrow \lambda_1 \,\mathrm{Im}\, V_{\mathrm{opt}}(r)$ and changing λ_1 from 1 to 0.4 without changing the real part. For $\lambda_1 < 0.4$, the imaginary part of the potential becomes smaller and the strength of the real part remains unchanged so that it no longer approaches Potential 1 but Potential 2 behavior. Thus, for $\lambda_1 < 0.4$, the energy shift is caused by level repulsion due to the nuclear state of the K^--nucleus system. In this calculation we want to see the contribution of the imaginary part of the potential, so we consider $\lambda_1 \geq 0.4$. The energy shift and the absorption width for each λ_1 are plotted in Fig. 7.3. This figure shows that, as the strength of the imaginary part decreases, the energy shift also decreases. This implies that the large imaginary part is responsible for the repulsive shift in Potential 1.

Potentials 2 and 3 provide nuclear states with $\ell = 3$ below the atomic $4f$ state. We find one nuclear state with $\ell = 3$ for Potential 2 at $-E_B - i\Gamma/2 = (-5.8 - i22.4/2)$ MeV and two nuclear states for Potential 3 at $-E_B - i\Gamma/2 = (-102.5 - i57.0/2)$ MeV as the ground state and at $-E_B - i\Gamma/2 = (-17.7 - i32.0/2)$ MeV as a radial excited state. The detailed values of these spectra are not important. What we emphasize here is the fact that a shallow nuclear state exists with the same quantum number to the atomic state, and this nuclear state definitely couples to the atomic state and repels it up due to the level repulsion. In order to confirm this speculation, we introduce a parameter λ_2 in the optical potential as $V_{\rm opt}(r) \to \lambda_2 V_{\rm opt}(r)$ to change the position of the nuclear state. Changing λ_2 from 1.0 to 0.6, we find that the binding energy of the nuclear state gets smaller and negative for $\lambda_2 \leq 0.8$. The state with negative binding energy is a resonance thanks to the centrifugal barrier with $\ell = 3$. The nuclear state with the negative binding energy is located above the atomic state. In such a case, the energy shift of the atomic state gets attractive. This is because the atomic state lies below the nuclear state and the level repulsion pushes down the atomic state. We see this situation with $\lambda_2 = 0.6, 0.7, 0.8$ in Table 7.4. In this way, we conclude that in Potential 2 and 3 the nuclear state is responsible for the repulsive shift of the atomic state.

The reason that Potentials 2 and 3 have a smaller imaginary part than Potential 1 is as follows. The absorption width may be given by the expectation value of the imaginary part of the potential in the wavefunction of the atomic state as

$$\Gamma \sim \langle \text{Atom} | \, \text{Im}\, V_{\rm opt} \, | \text{Atom} \rangle \, . \tag{7.11}$$

As seen in Fig. 7.2, thanks to mixing with the nuclear states, the wavefunctions for Potentials 2 and 3 have a larger contribution than that of Potential 1 in the nuclear length scale. Because the optical potential has values in the nuclear range, the overlap integrals get sufficiently large even with small imaginary parts of the optical potential to reproduce the observed absorption width. In contrast, in order to reproduce the observed absorption width by the wavefunction without nodes, the optical potential necessarily has a large imaginary part. This mechanism appears in the case of Potential 1.

Now let us see the potential parameters obtained by other kaonic atoms. We find a very similar trend to the Cu case, that is, the potentials are classified into three categories; Potential 1 having a large imaginary part, Potential 2 having a small imaginary part and Potential 3 having a deep real part and a small imaginary part. Potential 1 provides no nuclear states with the same quantum numbers to the atomic state of interest, while Potentials 2 and 3 have nuclear states. We show the numerical results for the obtained potential parameters in Tables table 7.5, 7.6 and 7.7 for Potentials 1, 2 and 3, respectively. In Figs. 7.4 to 7.6, we plot the values of the potential parameters for each kaonic atom to see the atomic number dependence. One finds in Fig. 7.4 that the imaginary parts of Potential 1 are larger than those of the real parts independently of the atomic number and that the values themselves are scattered. For Potentials 2 and 3, Figs. 7.5 and 7.6 show that the real parts of the potentials are larger than their imaginary parts again independently of the atomic number and that the real parts tend to decrease as the atomic number increases.

In summary, we find that the observed data of the kaonic atoms suggest two types of optical potentials; one potential has a large imaginary part without giving nuclear states with the same quantum number to the atomic state (Potential 1), and the other (Potentials 2 and 3) has a sufficiently large real part to give a shallow nuclear bound state. For the origin of the repulsive shift of the kaonic

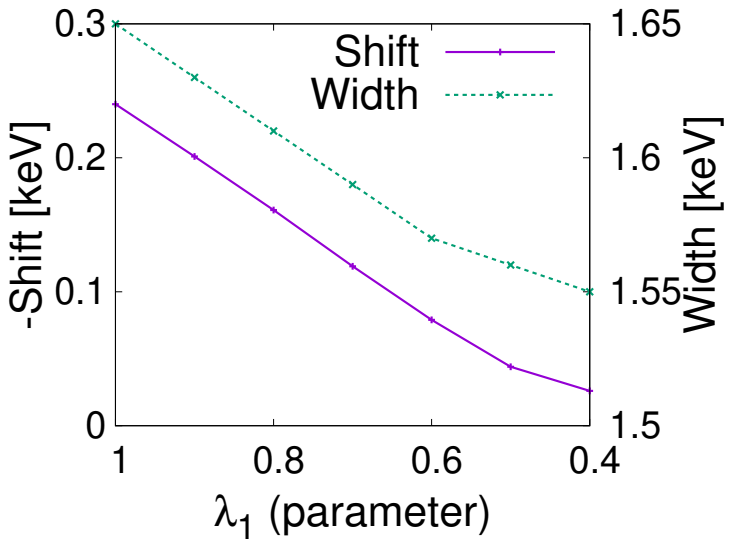

Fig.7.3 Energy shifts and absorption widths of the atomic state with $\ell = 3$ calculated for the Cu^1 kaonic atom by Potential 1 as a function of λ_1, which is introduced to control the strength of the imaginary part. The solid (dotted) line denoting the shift (width) uses the left (right) axis.

Table 7.4 Energy shifts and absorption widths of the atomic and nuclear states with $\ell = 3$ calculated for the Cu^1 kaonic atom by Potential 2 as a function of λ_2, which is introduced to control the strength of the potential. We the nuclear states get resonances, the energy shifts of the atomic states become attractive.

λ_2	kaonic atom		kaonic nucleus	
	$-$Shift [keV]	Width [keV]	E_B [MeV]	Width [MeV]
1.0	0.240	1.65	5.8	22.4
0.9	0.168	2.18	1.8	17.5
0.8	-0.216	2.57	-2.0	13.3
0.7	-0.648	2.05	-5.3	8.2
0.6	-0.696	1.19	-8.0	2.3

atom, in the former potential, the imaginary part works repulsively to the atomic state, while in the latter potential, the nuclear bound state repels up the atomic state.

7.3.2 Confirmation of universality

In the previous section, for each kaonic atom, two mechanisms are possible to explain the repulsive shifts of the atomic states. Here we pin down which scenario is realized in the observed kaonic atom by checking the universality of the optical potential obtained by one kaonic atom datum for other kaonic atoms. We calculate the energy shifts and the absorption widths for various kaonic atoms with the optical potential obtained in the previous section.

We show in Fig. 7.8 the energy shifts and the absorption widths of the $3d$ states of kaonic atoms calculated with Potential 1 in comparison with experimental data. Each line is calculated with a set of potential parameters (W_0, V_0) fitted by the data of a kaonic atom. This figure shows that all of the lines are with the errors of the experimental data, and we find that the calculation with Potential 1 is

Table 7.5 Determined potential parameters of Potential 1 for each kaonic atom.

Used datum.	V_0[MeV]	W_0[MeV]
Mg	24.5	79.0
Al	46.0	126.5
Si	61.5	120.5
P	67.0	142.0
S	79.0	142.0
Cl	79.0	142.0
Co	28.0	91.0
Ni	79.0	164.0
Cu^1	79.5	114.5
Cu^2	23.5	134.0
Ag	71.5	88.0
Cd	67.5	117.0
In	44.0	114.5
Sn	70.5	95.0

Table 7.6 Same as in Table 5, but of Potential 2.

Used datum.	V_0[MeV]	W_0[MeV]
Mg	128.0	24.0
Al	126.0	28.0
Si	116.5	31.0
P	100.5	26.5
S	93.0	27.0
Cl	84.0	26.5
Co	93.5	17.5
Ni	82.5	16.0
Cu^1	78.0	20.0
Cu^2	82.5	14.5
Ag	67.5	18.0
Cd	64.5	14.0
In	66.0	13.0
Sn	65.5	15.5

consistent with all of the observed experiments for the $3d$ states. In the same way, we plot the energy shifts and the absorption widths for the $4f$ states in Fig. 7.9 and for the $5g$ states in Fig. 7.10. In Fig. 7.11 we show the shifts calculated by all of the potentials obtained in the previous section, and we find that the calculations are consistent with the experimental data. This implies that the potential with a large imaginary part widely explains the kaonic atom data and can be the origin of the repulsive shift. This type of potential was found in Ref. [96] as $t_{\rm eff}\rho$. Recently the K^- optical potential has been reanalyzed in Ref. [128] by considering multinucleon absorption and the $\bar{K}N$ amplitude based

Table 7.7 Same as in Table 5, but of Potential 3.

Used datum.	V_0[MeV]	W_0[MeV]
Mg	305.0	24.5
Al	316.0	32.5
Si	301.0	35.5
P	270.0	36.5
S	258.0	38.0
Cl	231.0	38.0
Co	215.5	19.5
Ni	203.5	27.0
Cu^1	199.5	28.0
Cu^2	197.0	20.0
Ag	163.0	24.0
Cd	153.5	23.0
In	153.5	18.0
Sn	157.5	22.5

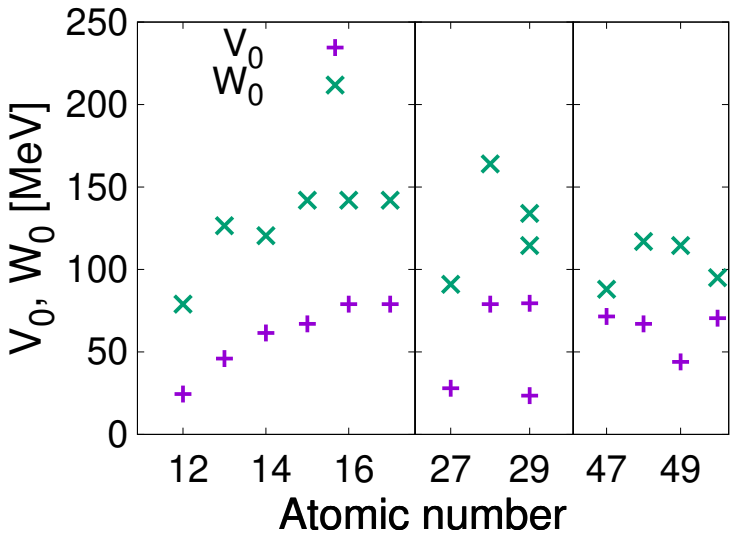

Fig.7.4 Atomic dependence of the potential parameters for Potential 1. The plus (+) and cross (×) signs denote the parameters for the real and imaginary parts, respectively.

on recent theoretical developments. There the optical potentials which were found to reproduce the K^- atom data have a larger imaginary part than its real part. Interestingly they have also found that most of the imaginary part comes from multinucleon absorption.

Actually, the real parts of the obtained optical potentials widely spread from 20 MeV to 80 MeV and are not determined as well as the imaginary parts. Thus, the real part of the optical potential is not sensitive to the spectra of the kaonic atoms. For precise determination of the optical potential, one should observe the nuclear states of the kaonic nucleus system.

The energy shifts and the absorption widths calculated with Potential 2 for the $3d$, $4f$ and $5g$ states of kaonic atoms are shown in Figs. 7.12 to 7.14, respectively, and in Fig. 7.15, we show all

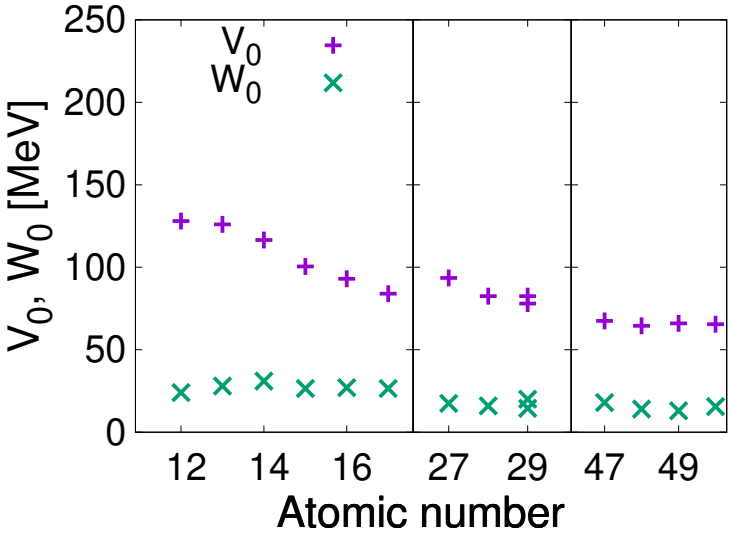

Fig.7.5 Same as in Fig.4, but for Potential 2.

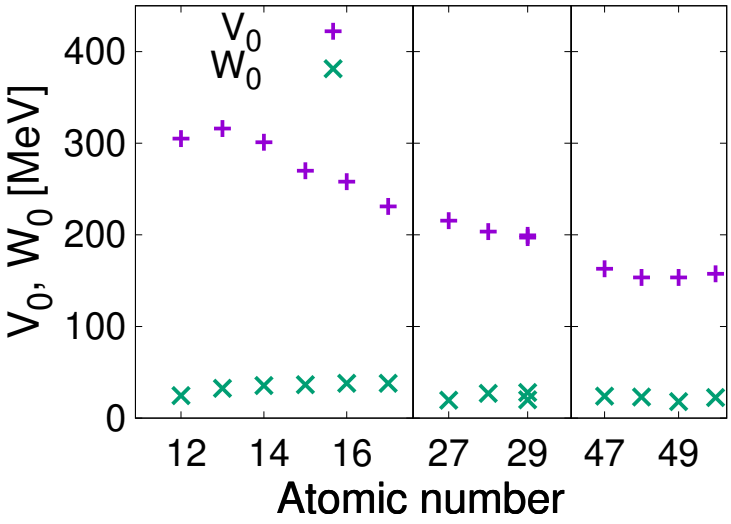

Fig.7.6 Same as in Fig.4, but for Potential 3.

of the calculation in one figure. These figures show that Potential 2 does not universally reproduce the observed shifts and absorption widths, and Potential 2 explains a specific kaonic nucleus only. Therefore, Potential 2 cannot be a solution to explain all of the energy shifts and absorption widths of the observed kaonic atoms, and the presence of the nuclear states is not responsible for the repulsive shift. For Potential 3, we find a discrepancy to the experiments in a similar way to Potential 2 as seen in the summary plot of Potential 3 given in Fig. 7.16.

The reason that Potentials 2 and 3 do not explain the repulsive shifts is as follows. A schematic figure of the explanation is shown in Fig. 7.7. If the level repulsion would be the origin of the repulsive shift, the atomic state should be sensitive to the position of the nuclear states because the mixing of these states determines the energy of the atomic state. Now each kaonic atom shares a common depth of the optical potential, but the potential size depends on the nuclear radius which is proportional to $A^{1/3}$. When the potential size is wider, the bound states have a deeper energy, which is an exercise of quantum mechanics for the bound states in a square-well potential. If the nuclear states get deeper,

the effects of the level repulsion become weaker, because the level mixing takes place when the levels are close energetically. As a consequence, the energy of the atomic state is strongly dependent on the atomic nuclide. Thus, this kind of potential cannot be universally applied for kaonic atoms. Actually, this type of potential was not found in the global fit performed in Ref. [96].

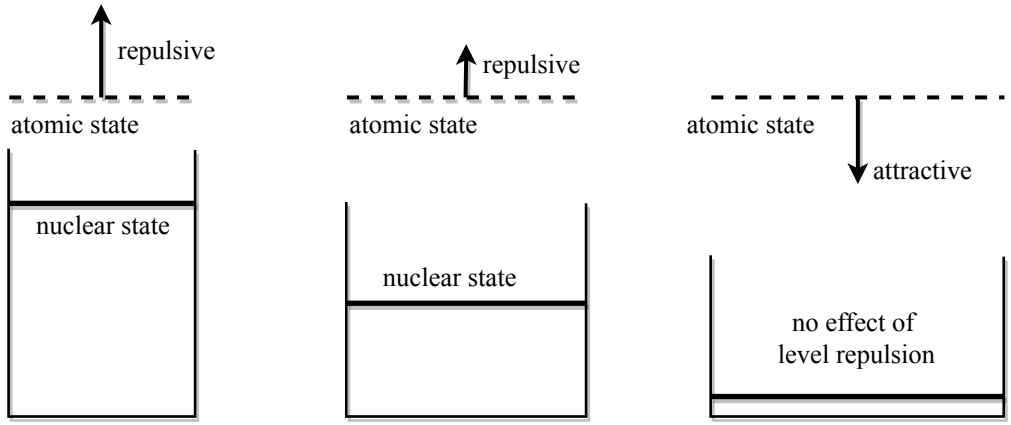

Fig.7.7 A schematic figure of repulsive energy shift due to level repulsion assuming a given potential parameter.

7.3.3 Other types of potential

In this section, we discuss two other types of optical potential in order to see the effect of the nuclear surface. One is a non-linear nuclear density potential, and the other is a linear nuclear density potential using other parameters of nuclear radius and diffuseness. These are accepted as optical potentials in the previous analysis [96].

Potential with non-linear density term

We study the optical potential of kaonic atoms with the non-linear term for nuclear density ρ_N. We have studied the optical potential of kaonic atoms under the linear nuclear density approximation in Eq. (7.4) in the previous section. We have found that the imaginary part of optical potential has an important role in the repulsive shift in kaonic atoms. Hence next we examine the optical potential which has a non-linear term, and confirm whether it provides the repulsive shift not by the level repulsion of nuclear states but by the imaginary part of the potential.

The phenomenological potential reported in Ref. [96] has non-linear density terms and is given by

$$V_{\rm opt}(r) = -\frac{4\pi}{2\mu}\left(1+\frac{M_K}{M_N}\right)a_{\rm eff}(\rho_N)\rho_N \tag{7.12}$$

and

$$a_{\rm eff}(\rho_N) = (-0.15+0.62i) + (1.66-0.04i)(\rho_N/\rho_0)^{0.21}\ {\rm fm} \tag{7.13}$$

where $a_{\rm eff}(\rho_N)$ is a density dependent effective scattering length. This potential amounts to $(-190 - i80)$ MeV at the nuclear center. The Real part of the potential is almost proportional to the non-linear term and the imaginary part is almost proportional to the linear term.

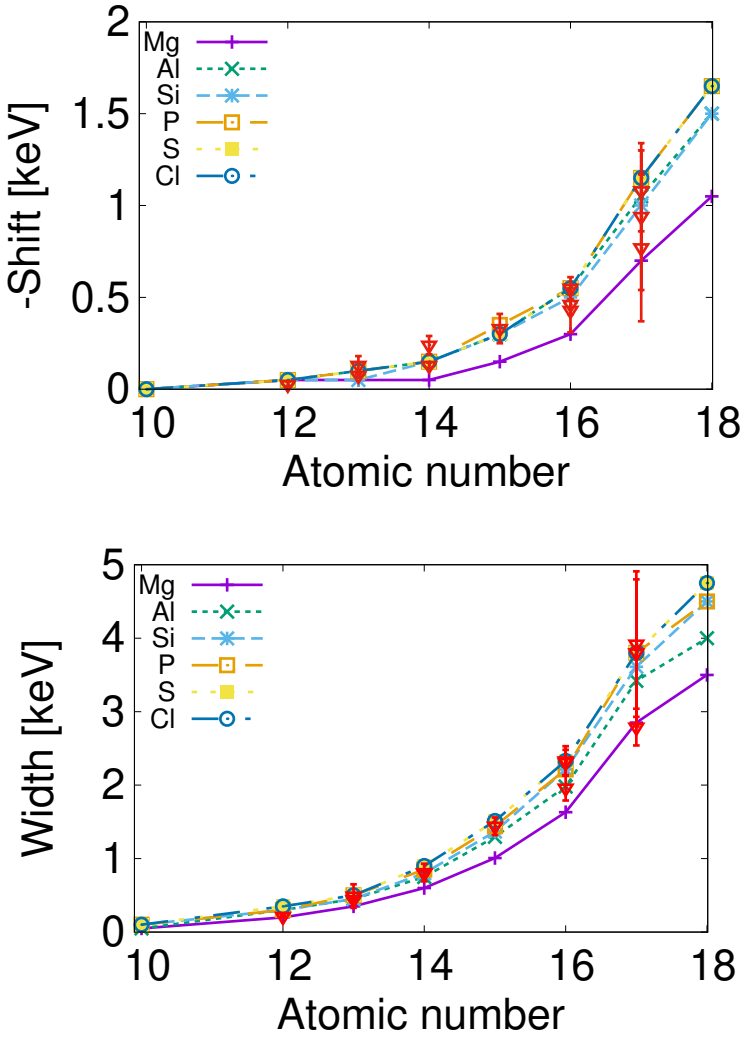

Fig.7.8 Energy shifts (upper plot) and absorption width (lower plot) of the kaonic atoms with $\ell = 2$ calculated with Potential 1. Each line corresponds to the results obtained by the potential parameters determined by the datum of the indicated atom. The points with error bars are the experimental data.

Here we take the following form to study the non-linear term effect :

$$V_{\rm opt}(r) = -V_0\left(\frac{\rho_N(r)}{\rho_0}\right)^{\alpha} - iW_0\left(\frac{\rho_N(r)}{\rho_0}\right), \tag{7.14}$$

where α is a parameter that characterizes the non-linear effect of the real part. We assume the real part of this potential is proportional to the non-linear term and the imaginary part is to the linear term. We determine the parameters V_0 and W_0 again from the observed shift and absorption width for the non-linear parameter α changed from $\alpha = 1$ (Potential 1) to $\alpha = 1.231$. We carry out the calculation in order to find the parameters V_0 and W_0 for the Cu kaonic atom for $\ell = 3$ and summarize the result in Table 7.8. This shows that the potential with $\alpha = 1.231$ has very similar potential parameters with the phenomenological potential obtained in Ref. [96]. It is also found that potentials with stronger nonlinearity have a deeper real part and a smaller imaginary part. It is interesting that this potential is continuously connected to Potential 1 with the parameter α. This fact implies that the phenomenological potential in Ref. [96] may have similar properties to Potential 1.

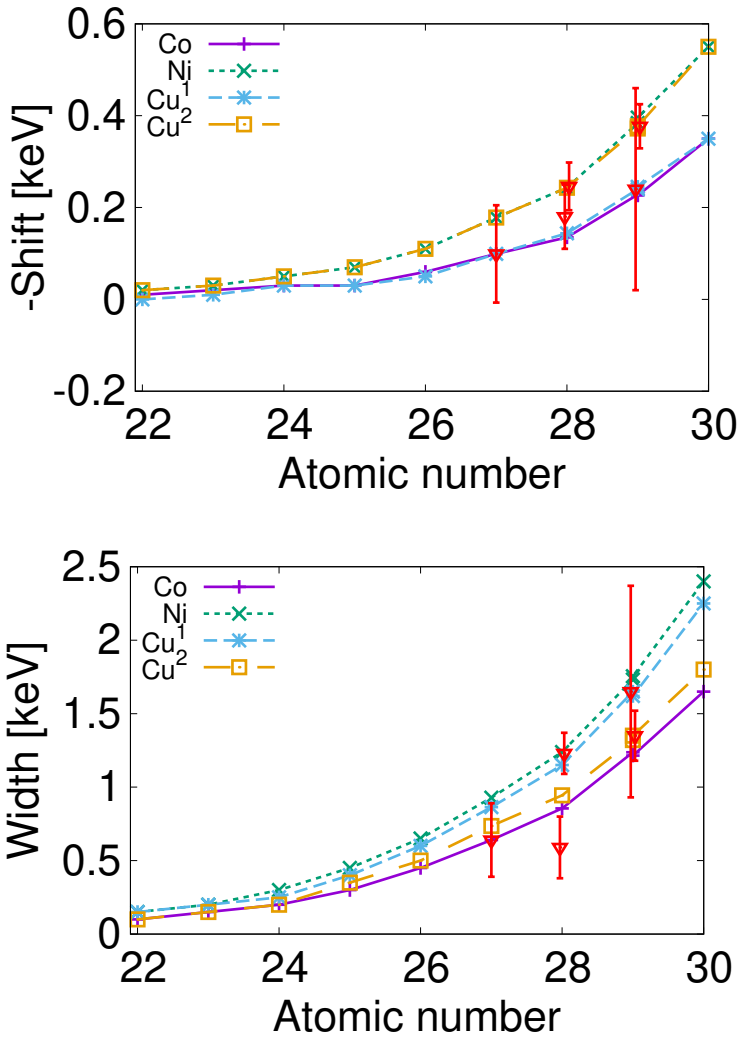

Fig.7.9 Same as in Fig. 7.8, but for the kaonic atoms with $\ell = 3$

In order to see the nature of the obtained potential, we calculate the energy spectrum of the kaonic nucleus with $\ell = 3$ using the following potential:

$$V_{\rm opt}(r) = -174.0\left(\frac{\rho_N(r)}{\rho_0}\right)^{1.231} - i\ 70.0\left(\frac{\rho_N(r)}{\rho_0}\right)\ {\rm MeV}. \tag{7.15}$$

This potential is the most similar to the phenomenological potential given in Ref. [96]. This potential provides nuclear states for $\ell = 3$ with $-E_B - i\Gamma/2 = (-52.1 - i85.1/2)$ MeV as the ground state and with $-E_B - i\Gamma/2 = (+12.8 - i69.5/2)$ MeV as a radial excited state with a negative binding energy and a large absorption width. The ground state has such deep binding energy that the nuclear state hardly influences the atomic states and its absorption width is also large. The excited state is a resonance with a negative binding energy trapped by the centrifugal barrier and is sitting above the atomic states. This feature is different from Potentials 2 and 3. The potential in Eq. (7.15) has very similar characteristics to Potential 1, which provides the repulsive shift by the effect of the imaginary part.

We discuss the universality of the potential in Eq. (7.15). We calculate the energy shifts and absorption widths for the various kaonic atoms using the optical potentials in 7.15. We confirm that

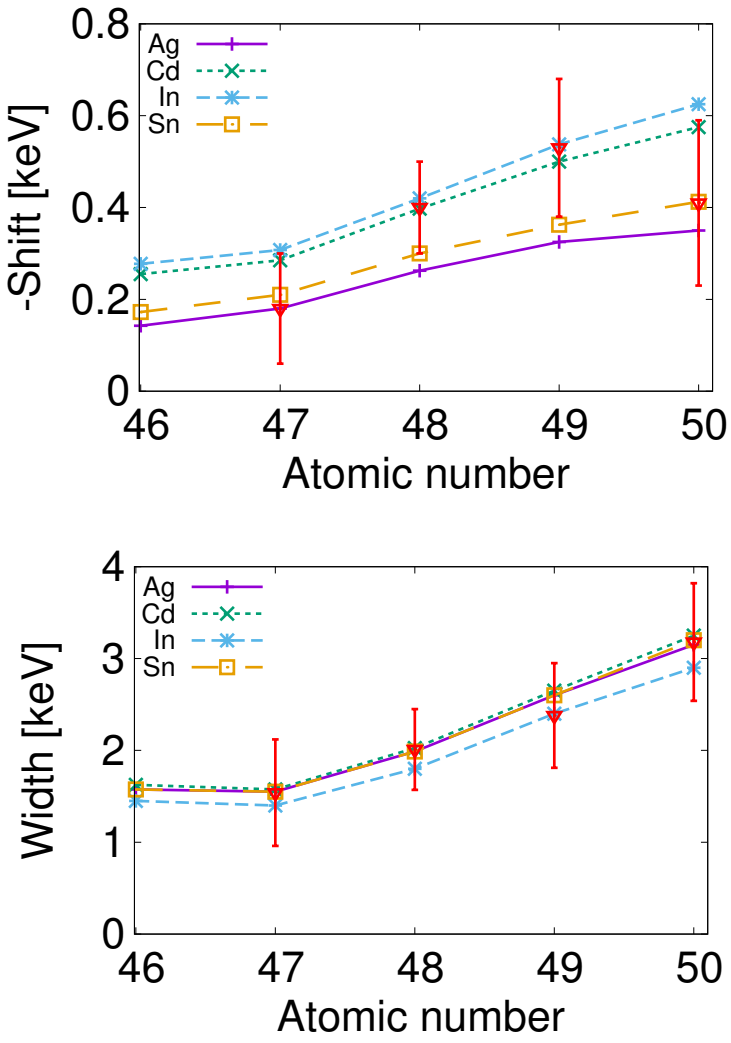

Fig.7.10 Same as in Fig. 7.8, but for the kaonic atoms with $\ell = 4$.

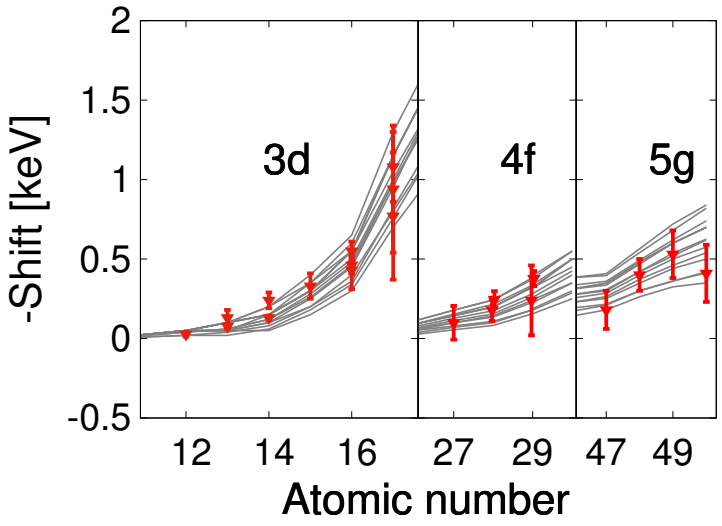

Fig.7.11 Summary of energy shifts of kaonic atoms in the last orbit calculated with Potential 1. The values are same as Figs. 7.8, 7.9 and 7.10.

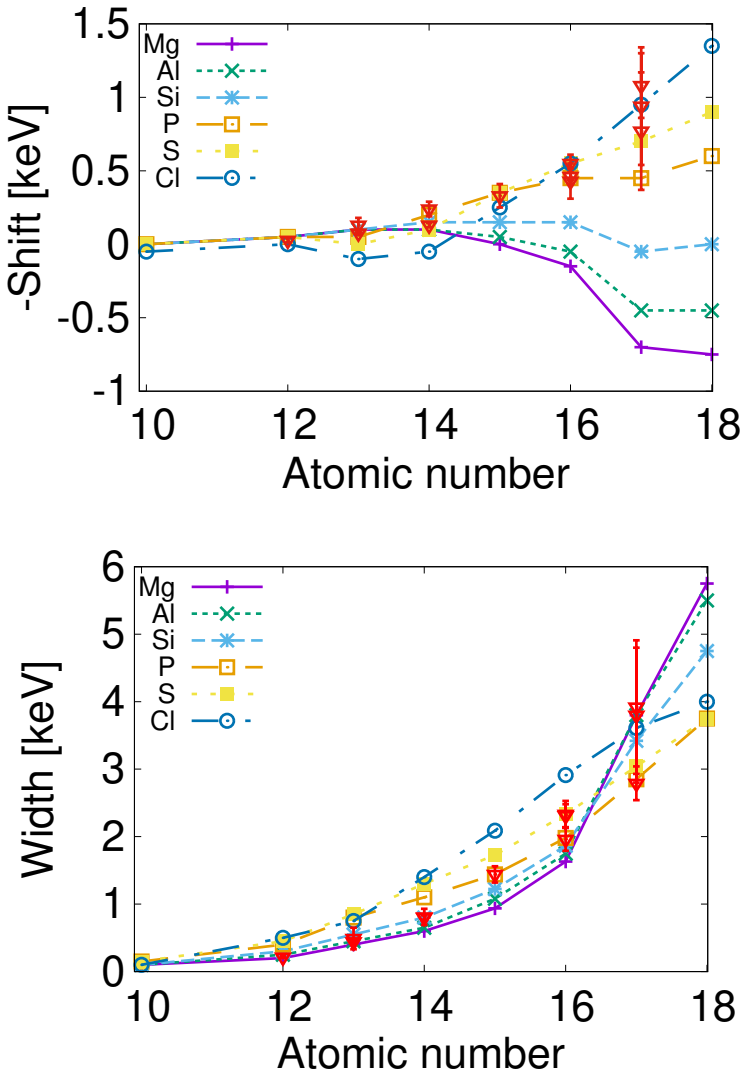

Fig.7.12 Same as in Fig. 7.8, but for Potential 2.

the potential reproduces the observed data seen in Table 7.2 within the experimental error as found for Potential 1 ($V_{\rm opt}(r) = -(79.5 + 114.5i)(\rho_N(r)/\rho_0)$ MeV) in the previous section. This is a natural result because the potential in Eq. (7.15) is similar to the phenomenological potential in Ref. [96] which has already the universality to reproduce a wide range of the observed kaonic atoms.

In Fig. 7.17 we plot the energy shifts and the absorption widths of the kaonic atoms with the last orbit $4f$ calculated by the potential in Eq. (7.15) and Potential 1 for Cu[1]. This figure shows that the potential in Eq. (7.15) provides almost the same atomic spectrum with Potential 1 and is consistent with the observation. Therefore, even though potentials with nonlinearity have a deeper real part, nuclear states play no significant role in the repulsive energy shift of the atomic state and have similar features with Potential 1, in which the imaginary part of the optical potential works essentially for the repulsive shift.

Another nuclear density parameter

In this section, we study the optical potential with another nuclear density parameter, which is originally used in Ref. [96] and referred to as "Unfolded" there. Here we list the density parameters

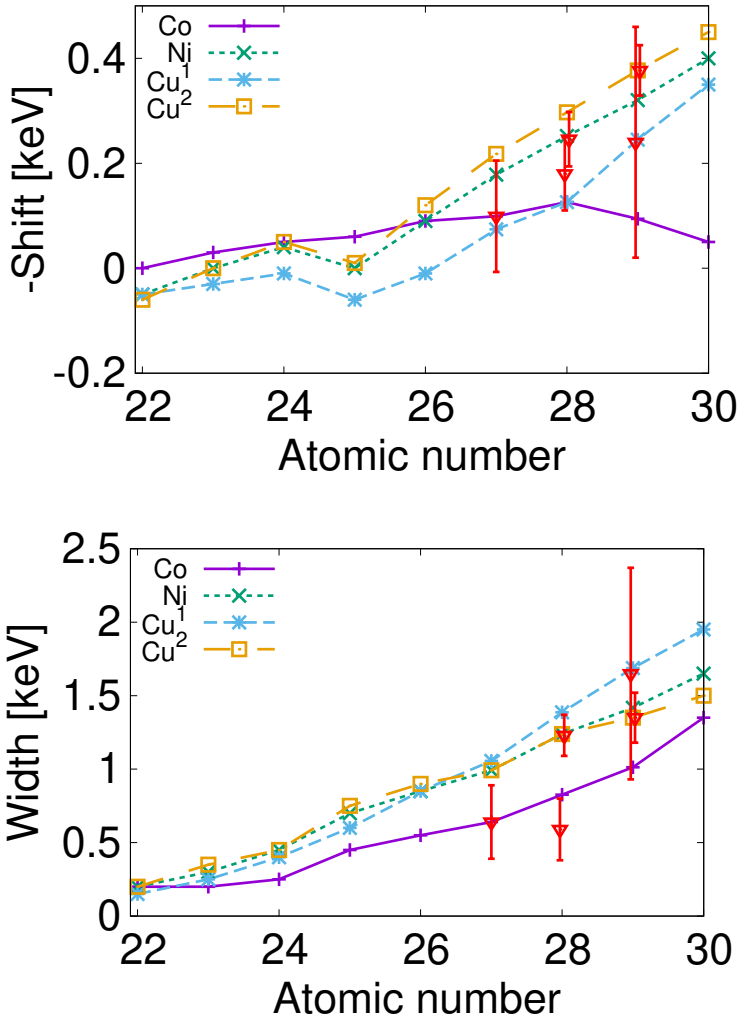

Fig.7.13 Same as in Fig. 7.12, but for the kaonic atoms with $\ell = 3$.

for the Co, Ni and Cu nuclei in Table 7.9. These density parameters have a bit larger radius R_B and a smaller diffuseness a. Using the "Unfolded" nuclear density parameter, we calculate the optical potential parameters for Cu to reproduce the Cu^1 datum in the linear density approximation and obtain the optical potential

$$V_{\rm opt}(r) = -(156.0 + i\ 122.0)\left(\frac{\rho_N(r)}{\rho_0}\right)\ \text{MeV}. \tag{7.16}$$

This potential again has a larger real part, which has an almost double depth in comparison with Potential 1, while the imaginary part is as large as Potential 1. In Fig. 7.17, we compare the energy shifts and absorption widths calculated by the potential in Eq. (7.16) and Potential 1 for Cu^1. Again we find that the potential in Eq. (7.16) and Potential 1 give the almost same atomic spectrum and the potential in Eq. (7.16) is consistent with the experiments for other nuclei than Cu, even though the real parts of these optical potentials are quite different. This implies that the potentials that successfully reproduce the observed energy shifts and absorption width of kaonic atoms widely have a large imaginary part and it is responsible for the repulsive shift, no matter how the real part of the optical potential is large.

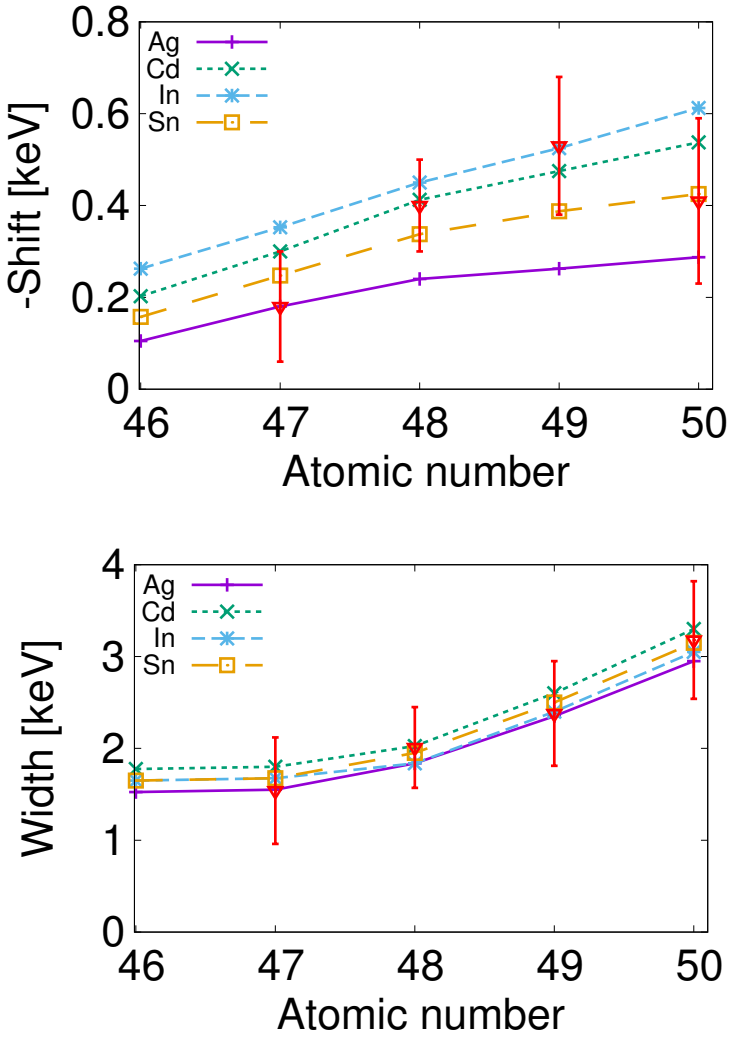

Fig.7.14 Same as in Fig. 7.12, but for the kaonic atoms with $\ell = 4$.

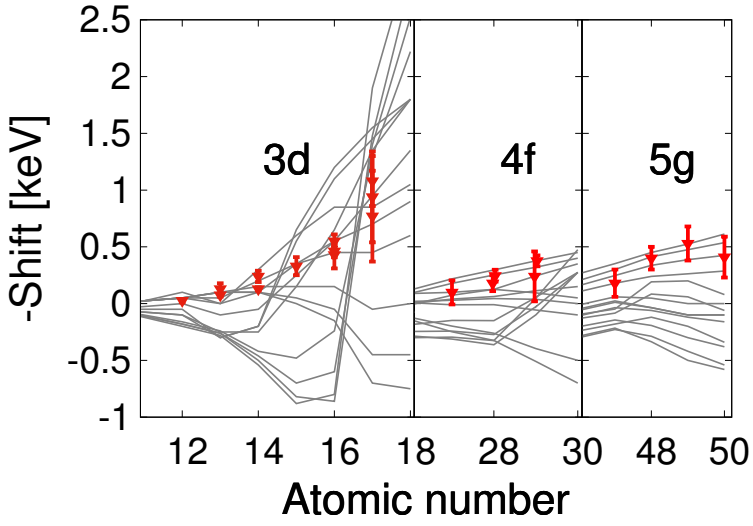

Fig.7.15 Same as in Fig. 7.11, but for Potential 2.

7.4 Summary

We have clarified the mechanism of the repulsive energy shifts for the last orbits of the kaonic atoms from the pure Coulomb spectrum. The repulsive shifts are observed universally in all of the observed

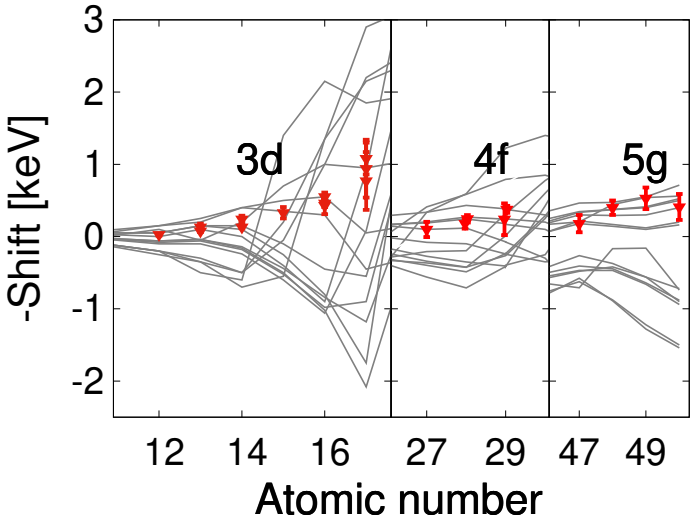

Fig.7.16 Same as in Fig. 7.11, but for Potential 3.

Table 7.8 Determined potential parameters for each α. The Cu^1 data are used to determine the parameter. The α parameter characterizes the nonlinearity of the density dependence.

α	V_0[MeV]	W_0[MeV]
1.000	79.5	114.5
1.033	90.0	109.0
1.066	101.0	105.0
1.099	114.0	99.0
1.132	127.0	94.0
1.165	141.0	89.0
1.198	157.0	81.0
1.231	174.0	70.0

Table 7.9 Unfolded nuclear parameters taken from Ref. [96]

Nuclei	R_B[fm]	a[fm]
Co	4.124	0.504
Ni	4.134	0.500
Cu	4.243	0.501

kaonic atoms. In order to investigate a global characteristic of the optical potential of kaonic atom, we have made good use of a simple potential proportional to the nuclear density ρ_N and have introduced two parameters for the strengths of the real and imaginary parts of the short-range optical potential, which may be regarded as averaged property seen from the atomic range. We have determined these potential parameters so as to reproduce the observed repulsive shift and absorption width for each kaonic atom datum. We have obtained two kinds of potentials for each datum based on the different mechanisms; in the first case (Potential 1), the potential has a large imaginary part and the imaginary part works repulsively, and in the second case (Potentials 2 and 3), the potential has a substantially large real part that yields nuclear bound states with the same angular momentum to the atomic

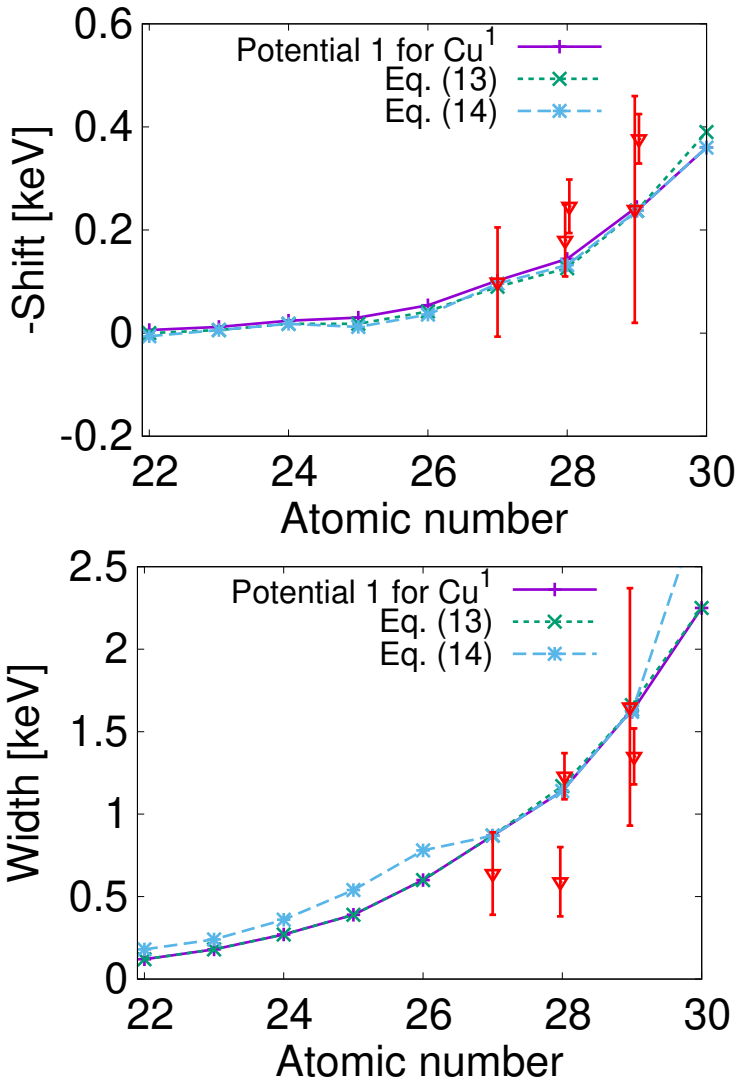

Fig.7.17 Energy shifts (upper plot) and absorption width (lower plot) of the kaonic atoms with $\ell = 3$ calculated with Potential 1 for Cu[1], Eq. (7.15) and Eq. (7.16). The solid, dashed and dotted lines denote the results obtained by Potential 1, Eq. (7.15) and Eq. (7.16), respectively. The points with error bars are the experimental data.

state and the nuclear states push up repulsively the atomic state. Having confirmed the universality of these potentials, we have found that Potential 1 which has a large imaginary part explains the experimental data globally, but Potentials 2 and 3 can explain only limited kaonic atoms. Therefore, we conclude that the origin of the repulsive shift in kaonic atoms does not come from level repulsion by the nuclear bound state, and that the imaginary part of the optical potential plays a significant role in the repulsive shift of kaonic atoms. This result implies that it would be somewhat difficult to observe nuclear states in heavier nuclei because of large nuclear absorption. Since the large absorption effect can be understood in connection with the resonance state, we hope that the kaon-nucleus interaction in the medium and heavy nuclei can be discussed more quantitatively, along with the refinement of our understanding of the $\bar{K}N$ and the $\Lambda(1405)$ resonance counted with it.

Chapter 8

Summary and Conclusion

In this dissertation, we have studied the SU(3) flavor symmetry and its breaking based on the hadron phenomena in the low-energy QCD. The kaon is characterized as a source of strangeness and is also a Nambu-Goldstone boson in the $\mathrm{SU}(3)_L \times \mathrm{SU}(3)_R$ chiral symmetry, and furthermore, as a hadron reflecting the effect of explicit symmetry breaking by the mass of the strange quark. Therefore we have focused on the hadron reactions induced by the kaon.

We have reviewed the symmetries of QCD, in particular flavor symmetry and chiral symmetry as symmetries related to the kaon. The flavor symmetry is the symmetry that mixes the light quark flavor and is justified by the fact that the masses of the light quark are less than the typical QCD scale $\Lambda_{\mathrm{QCD}} \sim 1$ GeV and can therefore be regarded as zero. The chiral symmetry is based on flavor symmetry and states that flavor transformation can be performed left-handed and right-handed independently. The chiral symmetry is dynamically broken and then the chiral condensate has a finite value and is also explicitly broken due to the finite quark masses, resulting in the Gell-Mann–Oakes–Renner relation. These symmetry breakings are associated with hadron phenomena. For example, the isospin symmetry breaking yields a difference in the $I = 1$ nucleon-nucleon scattering lengths. From the pionic atom which is the bound system between π^- and the nucleus, the restoration of the broken chiral symmetry is proved phenomenologically. Similar to these examples, we have studied the effects of the symmetry breaking in hadron phenomena induced by the kaon.

For the study of the isospin symmetry breaking, we have focused on the difference between the Λp and Λn in terms of the scattering length. The ΛN scattering is interesting to study the isospin symmetry breaking in systems containing strangeness, but there is not much information on ΛN scattering. The Λp scattering was studied via the $pp \to K^+\Lambda p$, while the Λn scattering is not enough understood. We have found that the $K^-d \to \pi^-\Lambda p$ and $K^-d \to \pi^0\Lambda n$ reactions with stopped kaon is useful as a tool to investigate the difference between the low-energy Λp and Λn interactions in terms of the scattering length. Since these reactions are isospin partners, their scattering amplitudes can be constructed in a similar manner. Isospin symmetry breaking effects can be included in the more basic amplitudes that construct the diagram. Using stopped kaons, the low-energy ΛN interaction is dominated by the spin-triplet configuration. We have found that the ΛN invariant mass spectra both for the Λp and Λn processes are sensitive to the ΛN scattering properties around the ΛN threshold, $E_{\Lambda p} < 30$ MeV and that one may extract the scattering lengths and the effective ranges from these spectra after restricting the angle between Λ and π in the final state in order to reduce the background contributions. We have also found that the ratio of the invariant mass spectra for the $K^-d \to \pi^-\Lambda p$

and $K^- d \to \pi^0 \Lambda n$ reactions works well to extract the qualitative tendency of the isospin symmetry breaking effects between the low-energy Λp and Λn scatterings. Even if it is difficult to extract the information on the ΛN scattering from the invariant mass spectrum itself, it may be possible to make qualitative arguments such as whether the scattering length of Λn is larger or smaller than that of Λp by studying the ratio of the reactions. Through this study, we were able to propose an experimental approach to contribute to understanding the breaking of isospin symmetry in the ΛN system which is not well understood by the reaction calculation of $K^- d \to \pi \Lambda N$.

For the SU(3) flavor symmetry breaking, we have studied the chiral condensate with strange quark components in nuclear matter without strangeness. For the phenomenological proof of the dynamical breaking of chiral symmetry (DBχS), the partial restoration of the chiral symmetry in nuclear matter is investigated. In particular, in the case of the flavor SU(2), the 30% decrease of the magnitude of $\langle \bar{u}u + \bar{d}d \rangle$ has already been confirmed in nuclear matter, then the chiral symmetry has been confirmed to be partially restored in nuclear matter. For the systematic study of DBχS, we have studied $\langle \bar{u}u + \bar{s}s \rangle$ in nuclear matter. $\langle \bar{u}u + \bar{s}s \rangle$ contains strange quark components while the nuclear matter does not. Therefore, unlike the in-medium $\langle \bar{u}u + \bar{d}d \rangle$, the in-medium $\langle \bar{u}u + \bar{s}s \rangle$ reflects the effect of the SU(3) flavor symmetry breaking. We have derived the in-medium chiral condensate with strange components based on the correlation function approach and the low-density theorem. As a result, we have obtained the in-medium condensate that contains the kaon-nucleon scattering amplitude T_{KN} in the soft limit under the linear density approximation. We have utilized the SU(3) chiral perturbation theory in order to calculate T_{KN}. Taking the soft limit, we have rewritten the condensate in terms of the low-energy constants (LECs) defined as the SU(3) chiral perturbation theory. We have obtained KN amplitude T_{KN} with the LECs of the SU(3) chiral perturbation theory using the experimental data of the K^+N elastic scatterings. In order to incorporate the flavor SU(3) breaking effect to the KN scattering amplitude, we have employed some terms from the next-to-next-to-leading order of the chiral Lagrangian which contains the strange quark mass. Moreover, we have included the resonance state with the broad decay width to the $I = 0$ sector. The choice of the experimental data for $I = 0$ total cross section and whether the resonance state exists have affected the determination of the LECs in KN amplitude. In the current status, the LECs are not determined uniquely due to the lack of experimental data at low energies, where the resonance state is not affected, therefore the behavior of the in-medium chiral condensate with strange components is not yet well determined. This study has concluded the need for KN scattering experiments at low energies to determine the LECs while avoiding the effect of the broad resonance. We have also performed the calculations of the chiral condensates in the hyperon matter and the SU(3) symmetric baryonic matter using the same formulation as for the chiral condensate in the nuclear matter. We have studied the SU(3) flavor symmetry breaking from $\langle \bar{u}u + \bar{d}d \rangle$ in hyperon matter and the SU(3) symmetric baryonic matter. Moreover, we have obtained the 25% restoration of the chiral symmetry in the case of SU(3) from $\langle \bar{u}u + \bar{d}d + \bar{s}s \rangle$ in the SU(3) symmetric baryonic matter with our fitted LECs. This result is consistent with the case of the SU(2) condensate in nuclear matter. We have also calculated the wavefunction renormalization factor which is related to the partial restoration of chiral symmetry using the obtained KN amplitude with each FIT of the LECs. In our calculation, we have found that the wavefunction renormalization factor for the in-medium kaon did not increase as much as that for the in-medium

pion at normal nuclear density. We have emphasized that it is important to determine the LECs in terms of the wavefunction renormalization. We have been able to conduct a theoretical study and propose the necessary experiment of K^+N scattering for a more systematic understanding of DBχS.

As well as the pion-nucleus interaction from the pionic atoms, the K^--nucleus interaction from kaonic atoms can be a phenomenological tool to prove the dynamical breaking of chiral symmetry, but at present, the K^--nucleus interaction is not as precisely understood as the pion-nucleus interaction. We have focused on the connection between the attractive real part of the K^--nucleus optical potential and the repulsive energy shift in the kaonic atom, and have aimed to understand the global nature of the K^--nucleus interaction from this viewpoint. In the case of the pionic atoms, both the energy shifts and the π^--nucleus strong interaction are repulsive, which is naturally understood. We have considered two mechanisms of the repulsive energy shifts for the last orbits of the kaonic atoms from the pure Coulomb spectrum. One candidate is the level repulsion between the atomic state and the nuclear state of the K^-- nucleus system. The other is the effect of the large imaginary part of the optical potential. In order to identify the origin of the repulsive shifts in kaonic atoms, we have obtained the optical potential parameters so as to reproduce the observed repulsive shift and absorption width for each kaonic atom datum. As a result, parameters derived from the former candidate do not give systematic experimental value reproduction, while parameters derived from the latter candidate give systematic experimental reproducibility. Therefore, we conclude that the origin of the repulsive shift in kaonic atoms does not come from level repulsion by the nuclear bound state, and that the imaginary part of the optical potential plays a significant role in the repulsive shift of kaonic atoms. This result implies that it would be somewhat difficult to observe nuclear states in heavier nuclei because of large nuclear absorption. Since the large absorption effect can be understood in connection with the resonance state, we hope that the K^--nucleus interaction in the medium and heavy nuclei can be discussed more quantitatively, along with the refinement of our understanding of the $\bar{K}N$ and the $\Lambda(1405)$ resonance counted with it. Together with the study of K^+-nucleus scattering, we hope that experiments on the heavy kaonic atom will be conducted to understand the role of strangeness in the nuclear medium. We hope that our study will be one of the starting points for such experiments.

In future studies, for the study of the isospin symmetry breaking in ΛN system, we will perform the extension of our formulation to finite momentum for initial kaon and incorporate P-wave interaction and the spin-flip configuration [168] to extract not only the information of the spin-triplet configuration but also that of the spin-singlet. For the study of the in-medium $\langle \bar{u}u + \bar{s}s \rangle$, it is interesting to analyze $K^+d \to KNN$ scattering in order to extract the information on the $I = 0$ sector of KN amplitude [169]. It is also important to make the in-medium chiral condensate more precise. It is interesting to evaluate the effect of the nonlinear term and the effect of the S-wave $\Lambda(1405)$ resonance on the chiral condensate. And it would be very interesting if chiral condensate can be experimentally evaluated from the study of the K^+-nucleus system as well as the pion-nucleus system, and we look forward to theoretical and experimental studies for this purpose. It is also interesting to determine the meson-hyperon interactions from the experiments of the scattering to give a limitation for the SU(3) LECs, complementary to the KN scattering. For future theoretical work on kaonic atoms, the study of the optical potential of kaonic helium isotopes, ^{3}He and ^{4}He, is in progress [170]. The purpose of this study is to extract the property of the optical potential from the experiment on kaonic helium isotopes,

J-PARC E62 experiment [171], in which the author of this dissertation participated. It would be also interesting to examine the connection between light kaonic atoms such as the kaonic helium and the heavier kaonic atom we have dealt with in our study.

We conclude that investigating the phenomena with strangeness induced by the kaon is a very effective way to understand flavor symmetry and its breaking phenomenologically. Experiments using kaon beams are being conducted at J-PARC in Japan. Further cooperation between the experimental study conducted at J-PARC and other accelerator facilities and theoretical study will continue to advance the physics of the light quark sector. While the physics of the light quark sector is moving toward a more precise understanding of SU(2) flavors, it is still a work in progress when even SU(3) flavors are considered. We hope that this study has contributed to the completion of the physics of light quark sectors.

Acknowledgements

First and foremost, I would like to express my deepest gratitude to my supervisor, Professor Daisuke Jido for his continuous support and guidance throughout my undergraduate study, master and doctoral programs. Furthermore, he gave me many opportunities to present my study at JPS meetings and workshops. Without his persistent guidance, my studies and dissertation would not have been possible. I would also like to thank Professor Tetsuo Hyodo (Tokyo Metropolitan University) who is my other supervisor in my master's program.

Secondly, I am grateful to my co-researchers, Professor Takatsugu Ishikawa (Research Center for Nuclear Physics, Osaka University), Doctor Stephan Hübsch (Tokyo Institute of Technology), Professor Natsumi Ikeno (Tottori University), Professor Junko Yamagata-Sekihara (Kyoto Sangyo University), and Professor Satoru Hirenzaki (Nara Women's University) for their fruitful discussions.

I would like to thank the examiners for my dissertation, Professor Ito, Professor Suyama, Professor Fujioka, and Professor Sekizawa, as well as the main examiner Professor Daisuke Jido, for their valuable advice and feedback.

I am very grateful to my labmate, Mister Taiju Amano, my senior, Doctor Kenji Aoki, and all the members of Nuclear Hadron Physics Group at Tokyo Institute of Technology and Tokyo Metropolitan University. I hope that Mister Yasunaga and Mister Hirama will further develop and deepen our studies. I also acknowledge the support by Grants-in-aid for Scientific Research of JSPS (20J20598).

Finally, I would like to express my special thanks to my family, Yutaka, Kanae, Rin, Hisako, Tadayoshi, Ritsuko, Shingo, Takeshi, Kumi, Eikichi, and Miyako.

Bibliography

[1] **Particle Data Group** Collaboration, R. L. Workman *et al.*, *Review of Particle Physics*, *PTEP* **2022** (2022) 083C01.

[2] Yuki, Akimoto. `https://higgstan.com`.

[3] Y. Iizawa, D. Jido, and T. Ishikawa, *$K^- d \to \pi\Lambda N$ reaction for studying charge symmetry breaking in the ΛN interaction*, *Phys. Rev. C* **106** (1, 2022) 045201, arXiv:2201.06737 [nucl-th].

[4] **HIRES Collaboration** Collaboration, A. Budzanowski *et al.*, *High resolution study of the Λp final state interaction in the reaction $p + p \to K^+ + (\Lambda p)$*, *Phys. Lett. B* **687** (2010) 31–35, arXiv:1003.0290 [nucl-ex].

[5] Y. Iizawa, S. Hübsch and D. Jido, *K^+N elastic scatterings for estimation of in-medium quark condensate with strange,*. in preparation.

[6] K. Suzuki *et al.*, *Precision spectroscopy of pionic 1s states of Sn nuclei and evidence for partial restoration of chiral symmetry in the nuclear medium*, *Phys. Rev. Lett.* **92** (2004) 072302, arXiv:nucl-ex/0211023.

[7] E. E. Kolomeitsev, N. Kaiser, and W. Weise, *Chiral dynamics of deeply bound pionic atoms*, *Phys. Rev. Lett.* **90** (2003) 092501, arXiv:nucl-th/0207090.

[8] D. Jido, T. Hatsuda, and T. Kunihiro, *In-medium Pion and Partial Restoration of Chiral Symmetry*, *Phys. Lett. B* **670** (2008) 109–113, arXiv:0805.4453 [nucl-th].

[9] E. Friedman *et al.*, *The In-medium isovector πN amplitude from low energy pion scattering*, *Phys. Rev. Lett.* **93** (2004) 122302, arXiv:nucl-ex/0404031.

[10] S. Goda and D. Jido, *Chiral condensate at finite density using the chiral Ward identity*, *Phys. Rev. C* **88** (2013) 065204, arXiv:1308.2660 [nucl-th].

[11] S. Hübsch and D. Jido, *Density dependence of the quark condensate in isospin-asymmetric nuclear matter*, *Phys. Rev. C* **104** (2021) 015202, arXiv:2103.08823 [nucl-th].

[12] E. G. Drukarev and E. M. Levin, *The QCD sum rules and nuclear matter*, *Nucl. Phys. A* **511** (1990) 679–700. [Erratum: Nucl.Phys.A 516, 715–715 (1990)].

[13] E. G. Drukarev and E. M. Levin, *Structure of nuclear matter and QCD sum rules*, *Prog. Part. Nucl. Phys.* **27** (1991) 77–134.

[14] Y. Iizawa, D. Jido, N. Ikeno, J. Yamagata-Sekihara, and S. Hirenzaki, *Origin of energy shift in kaonic atom and kaon-nucleus interaction*, arXiv:1907.05626 [nucl-th].

[15] H. D. Politzer, *Reliable Perturbative Results for Strong Interactions?*, *Phys. Rev. Lett.* **30** (1973) 1346–1349.

[16] D. J. Gross and F. Wilczek, *Ultraviolet Behavior of Nonabelian Gauge Theories*, *Phys. Rev.*

Lett. **30** (1973) 1343–1346.

[17] W. Heisenberg, *On the structure of atomic nuclei*, *Z. Phys.* **77** (1932) 1–11.

[18] M. Gell-Mann, *The Eightfold Way: A Theory of strong interaction symmetry,*.

[19] S. Okubo, *Note on unitary symmetry in strong interactions*, *Prog. Theor. Phys.* **27** (1962) 949–966.

[20] M. Gell-Mann and M. Levy, *The axial vector current in beta decay*, *Nuovo Cim.* **16** (1960) 705.

[21] S. L. Glashow and S. Weinberg, *Breaking chiral symmetry*, *Phys. Rev. Lett.* **20** (1968) 224–227.

[22] M. Gell-Mann, R. J. Oakes, and B. Renner, *Behavior of current divergences under SU(3) × SU(3)*, *Phys. Rev.* **175** (1968) 2195–2199.

[23] C. McNeile, A. Bazavov, C. T. H. Davies, R. J. Dowdall, K. Hornbostel, G. P. Lepage, and H. D. Trottier, *Direct determination of the strange and light quark condensates from full lattice QCD*, *Phys. Rev. D* **87** (2013) 034503, arXiv:1211.6577 [hep-lat].

[24] G. A. Miller and W. T. H. V. Oers, *CHARGE INDEPENDENCE AND CHARGE SYMMETRY*, pp. 127–167. arXiv:nucl-th/9409013.

[25] R. Machleidt and I. Slaus, *The Nucleon-nucleon interaction: Topical review*, *J. Phys. G* **27** (2001) R69–R108, arXiv:nucl-th/0101056.

[26] S. X. Nakamura, T. Ishikawa, and T. Sato, *Neutron-neutron scattering length from π^+ photoproduction on the deuteron*, arXiv:2003.02497 [nucl-th].

[27] **J-PARC E13 Collaboration** Collaboration, T. O. Yamamoto *et al.*, *Observation of Spin-Dependent Charge Symmetry Breaking in ΛN Interaction: Gamma-Ray Spectroscopy of ${}^{4}_{\Lambda}$He*, *Phys. Rev. Lett.* **115** (2015) 222501, arXiv:1508.00376 [nucl-ex].

[28] **Mainz A1 Collaboration** Collaboration, A. Esser *et al.*, *Observation of ${}^{4}_{\Lambda}$H Hyperhydrogen by Decay-Pion Spectroscopy in Electron Scattering*, *Phys. Rev. Lett.* **114** (2015) 232501, arXiv:1501.06823 [nucl-ex].

[29] T. A. Rijken, V. G. J. Stoks, and Y. Yamamoto, *Soft core hyperon - nucleon potentials*, *Phys. Rev. C* **59** (1999) 21–40, arXiv:nucl-th/9807082.

[30] T. A. Rijken, M. M. Nagels, and Y. Yamamoto, *Baryon-baryon interactions: Nijmegen extended-soft-core models*, *Prog. Theor. Phys. Suppl.* **185** (2010) 14–71.

[31] M. M. Nagels, T. A. Rijken, and Y. Yamamoto, *Extended-soft-core baryon-baryon model ESC16. II. Hyperon-nucleon interactions*, *Phys. Rev. C* **99** (2019) 044003, arXiv:1501.06636 [nucl-th].

[32] B. Holzenkamp, K. Holinde, and J. Speth, *A Meson Exchange Model for the Hyperon Nucleon Interaction*, *Nucl. Phys. A* **500** (1989) 485–528.

[33] A. Reuber, K. Holinde, and J. Speth, *Meson exchange hyperon - nucleon interactions in free scattering and nuclear matter*, *Nucl. Phys. A* **570** (1994) 543–579.

[34] J. Haidenbauer and U.-G. Meißner, *The Julich hyperon-nucleon model revisited*, *Phys. Rev. C* **72** (2005) 044005, arXiv:nucl-th/0506019.

[35] K. Tominaga, T. Ueda, M. Yamaguchi, N. Kijima, D. Okamoto, K. Miyagawa, and T. Yamada, *A one-boson-exchange potential for ΛN, ΛΛ and ΞN systems and hypernuclei*, *Nucl. Phys. A* **642** (1998) 483–505.

[36] K. Tominaga and T. Ueda, *Effective one-boson-exchange potential for ΛN and ΣN systems*

and hypertriton, Nucl. Phys. A **693** (2001) 731–754.

[37] M. Kohno, Y. Fujiwara, T. Fujita, C. Nakamoto, and Y. Suzuki, *Hyperon single particle potentials calculated from SU(6) quark model baryon baryon interactions,* Nucl. Phys. A **674** (2000) 229–245, arXiv:nucl-th/9912059.

[38] Y. Fujiwara, Y. Suzuki, and C. Nakamoto, *Baryon-baryon interactions in the SU(6) quark model and their applications to light nuclear systems,* Prog. Part. Nucl. Phys. **58** (2007) 439–520, arXiv:nucl-th/0607013.

[39] H. Garcilazo, T. Fernandez-Carames, and A. Valcarce, *ΛNN and ΣNN systems at threshold,* Phys. Rev. C **75** (2007) 034002, arXiv:hep-ph/0701275.

[40] Y. Fujiwara, C. Nakamoto, and Y. Suzuki, *Effective meson exchange potentials in the SU(6) quark model for NN and YN interactions,* Phys. Rev. C **54** (1996) 2180–2200.

[41] M. J. Savage and M. B. Wise, *Hyperon masses in nuclear matter,* Phys. Rev. D **53** (1996) 349–354, arXiv:hep-ph/9507288.

[42] C. L. Korpa, A. E. L. Dieperink, and R. G. E. Timmermans, *Hyperon nucleon scattering and hyperon masses in the nuclear medium,* Phys. Rev. C **65** (2002) 015208, arXiv:nucl-th/0109072.

[43] H. Polinder, J. Haidenbauer, and U.-G. Meißner, *Hyperon-nucleon interactions: A Chiral effective field theory approach,* Nucl. Phys. A **779** (2006) 244–266, arXiv:nucl-th/0605050.

[44] J. Haidenbauer, S. Petschauer, N. Kaiser, U. G. Meißner, A. Nogga, and W. Weise, *Hyperon-nucleon interaction at next-to-leading order in chiral effective field theory,* Nucl. Phys. A **915** (2013) 24–58, arXiv:1304.5339 [nucl-th].

[45] J. Haidenbauer, U. G. Meißner, and A. Nogga, *Hyperon–nucleon interaction within chiral effective field theory revisited,* Eur. Phys. J. A **56** (2020) 91, arXiv:1906.11681 [nucl-th].

[46] K.-W. Li, X.-L. Ren, L.-S. Geng, and B.-W. Long, *Leading order relativistic hyperon-nucleon interactions in chiral effective field theory,* Chin. Phys. C **42** (2018) 014105, arXiv:1612.08482 [nucl-th].

[47] K.-W. Li, X.-L. Ren, L.-S. Geng, and B. Long, *Strangeness $S = -1$ hyperon-nucleon scattering in covariant chiral effective field theory,* Phys. Rev. D **94** (2016) 014029, arXiv:1603.07802 [hep-ph].

[48] J. Song, K.-W. Li, and L.-S. Geng, *Strangeness $S = -1$ hyperon-nucleon interactions: Chiral effective field theory versus lattice QCD,* Phys. Rev. C **97** (2018) 065201, arXiv:1802.04433 [nucl-th].

[49] X. L. Ren, E. Epelbaum, and J. Gegelia, *Λ -nucleon scattering in baryon chiral perturbation theory,* Phys. Rev. C **101** (2020) 034001, arXiv:1911.05616 [nucl-th].

[50] S. Petschauer, J. Haidenbauer, N. Kaiser, U.-G. Meißner, and W. Weise, *Hyperon-nuclear interactions from SU(3) chiral effective field theory,* Front. in Phys. **8** (2020) 12, arXiv:2002.00424 [nucl-th].

[51] J. Haidenbauer, U.-G. Meißner, and A. Nogga, *Constraints on the Λ-Neutron Interaction from Charge Symmetry Breaking in the* ${}^{4}_{\Lambda}$He - ${}^{4}_{\Lambda}$H *Hypernuclei,* Few Body Syst. **62** (2021) 105, arXiv:2107.01134 [nucl-th].

[52] O. I. Dahl, N. Horwitz, D. H. Miller, J. J. Murray, and P. G. White, *Influence of the Lambdapi*

Resonance on Correlations in the Reaction $K^- + d \to \Lambda + \pi^- + p$, *Phys. Rev. Lett.* **6** (1961) 142–144.

[53] T. H. Tan, *Study of Hyperon-Nucleon Interaction in the Reaction* $K^- d \to \pi^- p\Lambda$ *at Rest*, *Phys. Rev. Lett.* **23** (1969) 395–398.

[54] D. Cline, R. Laumann, and J. Mapp, *Λp interaction near Σn threshold*, *Phys. Rev. Lett.* **20** (Jun, 1968) 1452–1455.

[55] G. Alexander, B. H. Hall, N. Jew, G. Kalmus, and A. Kernan, *Study of the Enhancement in the Λp Invariant Mass Near the $\Sigma\Lambda$ Threshold in $K^- d \to \Lambda p \pi^-$ Interactions Around 1.0 GeV/c*, *Phys. Rev. Lett.* **22** (Mar, 1969) 483–486.

[56] D. Eastwood, J. R. Fry, F. R. Heathcote, G. S. Islam, D. J. Candlin, G. Copley, G. R. Evaåns, J. R. Campbell, W. T. Morton, P. J. Negus, M. J. Counihan, D. P. Goyal, D. B. Miller, and B. Schwarzschild, *2130-MeV $\Lambda^0 p$ Mass Enhancement in the Reaction $K^- d \to \Lambda^0 p \pi^-$ at 1.45 and 1.65 GeV/c*, *Phys. Rev. D* **3** (Jun, 1971) 2603–2606.

[57] O. Braun, H. J. Grimm, V. Hepp, H. Strobele, C. Thol, T. J. Thouw, F. Gandini, C. M. Kiesling, D. E. Plane, and W. Wittek, *On the Lambda p Enhancement Near Sigma N Threshold*, *Nucl. Phys. B* **124** (1977) 45–60.

[58] R. M. A. Fujii, *bsorption of slow negative kaons in hydrogen and deuterium.*, *Nuovo Cim.* **8** (1958) 643–662.

[59] R. Karplus and L. S. Rodberg, *Inelastic final-state interactions: K^- absorption in deuterium*, *Phys. Rev.* **115** (Aug, 1959) 1058–1069.

[60] T. Kotani and M. Ross, *Analysis of K^- absorption in deuterium*, *Nuovo Cim.* **14** (1959) 1282–1309.

[61] A. E. Kudryavtsev, *MASS SPECTRUM OF (Λp) FROM THE REACTION $K^- d$ Yields $\pi^- \Lambda p$.*, *JETP Lett.* **90** (1, 1971) .

[62] E. Satoh, Y. Iwamura, and Y. Takahashi, *Theoretical study of a Λp resonance with two-channel formalism*, *Phys. Rev. Lett.* **35** (Oct, 1975) 1128–1131.

[63] G. Toker, A. Gal, and J. M. Eisenberg, *The $K^- d \to \pi^- \Lambda p$ reaction at low energies in the faddeev formalism*, *Phys. Lett. B* **88** (1979) 235–238.

[64] R. H. Dalitz, C. R. Hemming, and E. J. Morris, *THE (K-,pi-) STRANGENESS EXCHANGE REACTIONS ON DEUTERIUM*, *Nukleonika* **26** (1980) 1555.

[65] G. Toker, A. Gal, and J. M. Eisenberg, *The Y N Interactions and K^- Reactions on Deuterium at Low-energies*, *Nucl. Phys. A* **362** (1981) 405–430.

[66] R. H. Dalitz, *Λ and Σ Hypernuclear Physics*, *Nucl. Phys. A* **354** (1981) 101C.

[67] R. H. Dalitz and A. Deloff, *The $K^- d \to p \Lambda \pi^-$ Reaction*, *Czech. J. Phys. B* **32** (1982) 1021–1039.

[68] M. Torres, R. H. Dalitz, and A. Deloff, *K^- Absorption Reactions From Rest in Deuterium*, *Phys. Lett. B* **174** (1986) 213–218.

[69] H. Machner, J. Haidenbauer, F. Hinterberger, A. Magiera, J. A. Niskanen, J. Ritman, and R. Siudak, *Study of the Λp Interaction Close to the $\Sigma^+ n$ and $\Sigma^0 p$ Thresholds*, *Nucl. Phys. A* **901** (2013) 65–88, arXiv:1301.6089 [nucl-ex].

[70] D. Jido, E. Oset, and T. Sekihara, *Kaonic production of $\Lambda(1405)$ off deuteron target in chiral*

dynamics, *Eur. Phys. J. A* **42** (2009) 257–268, arXiv:0904.3410 [nucl-th].

[71] D. Jido, E. Oset, and T. Sekihara, *Kaon induced* $\Lambda(1405)$ *production on a deuteron target at DAFNE*, *Eur. Phys. J. A* **47** (2011) 42, arXiv:1008.4423 [nucl-th].

[72] D. Jido, E. Oset, and T. Sekihara, *The* $K^- d \to \pi\Sigma n$ *reaction revisited*, *Eur. Phys. J. A* **49** (2013) 95, arXiv:1207.5350 [nucl-th].

[73] J. Yamagata-Sekihara, T. Sekihara, and D. Jido, *Production of hyperon resonances induced by kaon on a deuteron target*, *PTEP* **2013** (2013) 043D02, arXiv:1210.6108 [nucl-th].

[74] N. Kaiser, P. B. Siegel, and W. Weise, *Chiral dynamics and the low-energy kaon - nucleon interaction*, *Nucl. Phys. A* **594** (1995) 325–345, arXiv:nucl-th/9505043.

[75] E. Oset and A. Ramos, *Nonperturbative chiral approach to s wave* $\bar{K}N$ *interactions*, *Nucl. Phys. A* **635** (1998) 99–120, arXiv:nucl-th/9711022.

[76] M. F. M. Lutz and E. E. Kolomeitsev, *Relativistic chiral SU(3) symmetry, large* N_c *sum rules and meson baryon scattering*, *Nucl. Phys. A* **700** (2002) 193–308, arXiv:nucl-th/0105042.

[77] E. Oset, A. Ramos, and C. Bennhold, *Low lying* $S = -1$ *excited baryons and chiral symmetry*, *Phys. Lett. B* **527** (2002) 99–105, arXiv:nucl-th/0109006. [Erratum: Phys.Lett.B 530, 260–260 (2002)].

[78] T. Hyodo, S. I. Nam, D. Jido, and A. Hosaka, *Flavor SU(3) breaking effects in the chiral unitary model for meson baryon scatterings*, *Phys. Rev. C* **68** (2003) 018201, arXiv:nucl-th/0212026.

[79] T. Hyodo, S.-i. Nam, D. Jido, and A. Hosaka, *Detailed analysis of the chiral unitary model for meson baryon scatterings with flavor SU(3) breaking effects*, *Prog. Theor. Phys.* **112** (2004) 73–97, arXiv:nucl-th/0305011.

[80] T. Hyodo and D. Jido, *The nature of the* $\Lambda(1405)$ *resonance in chiral dynamics*, *Prog. Part. Nucl. Phys.* **67** (2012) 55–98, arXiv:1104.4474 [nucl-th].

[81] J. Gasser, H. Leutwyler, and M. E. Sainio, *Sigma term update*, *Phys. Lett. B* **253** (1991) 252–259.

[82] N. Kaiser, P. de Homont, and W. Weise, *In-medium chiral condensate beyond linear density approximation*, *Phys. Rev. C* **77** (2008) 025204, arXiv:0711.3154 [nucl-th].

[83] U. G. Meissner, J. A. Oller, and A. Wirzba, *In-medium chiral perturbation theory beyond the mean field approximation*, *Annals Phys.* **297** (2002) 27–66, arXiv:nucl-th/0109026.

[84] T. Hatsuda and T. Kunihiro, *Critical Phenomena Associated with Chiral Symmetry Breaking and Restoration in QCD*, *Prog. Theor. Phys.* **74** (1985) 765.

[85] U. Vogl and W. Weise, *The Nambu and Jona Lasinio model: Its implications for hadrons and nuclei*, *Prog. Part. Nucl. Phys.* **27** (1991) 195–272.

[86] S. Weinberg, *Pion scattering lengths*, *Phys. Rev. Lett.* **17** (1966) 616–621.

[87] Y. Tomozawa, *Axial vector coupling renormalization and the meson baryon scattering lengths*, *Nuovo Cim. A* **46** (1966) 707–717.

[88] S. Hübsch, *Quark condensate and pion properties in isospin-asymmetric nuclear matter*. PhD thesis, Tokyo Institute of Technology, 2021.

[89] B. R. Martin, *Kaon-Nucleon Partial Wave Amplitudes Below 1.5-GeV/c for I=0 and 1*, *Nucl. Phys. B* **94** (1975) 413–430.

[90] K. Aoki and D. Jido, *KN scattering amplitude revisited in a chiral unitary approach and a possible broad resonance in $S = +1$ channel*, *PTEP* **2019** (2019) 013D01, arXiv:1806.00925 [nucl-th].

[91] K. Aoki and D. Jido, *K^+-nucleus elastic scattering revisited from perspective of partial restoration of chiral symmetry*, *PTEP* **2017** (2017) 103D01, arXiv:1705.07548 [nucl-th]. [Erratum: PTEP 2019, 069201 (2019)].

[92] A. S. Carroll, T. F. Kycia, K. K. Li, D. N. Michael, P. M. Mockett, D. C. Rahm, and R. Rubinstein, *Structure in the K^+ nucleon, $I = 0$ total cross-section below 1.1 GeV/c*, *Phys. Lett. B* **45** (1973) 531–534.

[93] D. Jido, *Mesons in Nuclei and Partial Restoration of Chiral Symmetry*, *JPS Conf. Proc.* **17** (2017) 081002, arXiv:1603.07083 [nucl-th].

[94] A. Kenji, *In-medium modification of Nambu-Goldstone boson properties induced by wavefunction renormalization under partial restoration of chiral symmetry*. PhD thesis, Tokyo Metropolitan University, 2019. https://irdb.nii.ac.jp/00891/0004338349.

[95] E. Friedman, A. Gal, and J. Mares, *Medium effects in K^+ nuclear interactions*, *Nucl. Phys. A* **625** (1997) 272–286, arXiv:nucl-th/9705026.

[96] E. Friedman, A. Gal, and C. J. Batty, *Density dependent K- nuclear optical potentials from kaonic atoms*, *Nucl. Phys. A* **579** (1994) 518–538.

[97] C. J. Batty, E. Friedman, and A. Gal, *Strong interaction physics from hadronic atoms*, *Phys. Rept.* **287** (1997) 385–445.

[98] E. Friedman and A. Gal, *In-medium nuclear interactions of low-energy hadrons*, *Phys. Rept.* **452** (2007) 89–153, arXiv:0705.3965 [nucl-th].

[99] C. J. Batty, *Optical Model Analysis of Exotic Atom Data. 1. Kaonic Atoms*, *Nucl. Phys. A* **372** (1981) 418–432.

[100] E. Friedman and A. Gal, *Narrow deeply bound K^- atomic states*, *Phys. Lett. B* **459** (1999) 43–48, arXiv:nucl-th/9902036.

[101] E. Friedman and A. Gal, *Kaonic atoms and in-medium K^-N amplitudes*, *Nucl. Phys. A* **881** (2012) 150–158, arXiv:1201.3770 [nucl-th].

[102] E. Friedman and A. Gal, *Kaonic atoms and in-medium K^-N amplitudes II: interplay between theory and phenomenology*, *Nucl. Phys. A* **899** (2013) 60–75, arXiv:1211.6336 [nucl-th].

[103] A. Gal, *Recent studies of kaonic atoms and nuclear clusters*, *Nucl. Phys. A* **914** (2013) 270–279, arXiv:1301.2145 [nucl-th].

[104] N. Barnea and E. Friedman, *Radial sensitivity of kaonic atoms and strongly bound anti-K states*, *Phys. Rev. C* **75** (2007) 022202, arXiv:nucl-th/0611020.

[105] A. Cieply, E. Friedman, A. Gal, and J. Mares, *Study of chirally motivated low-energy K^- optical potentials*, *Nucl. Phys. A* **696** (2001) 173–193, arXiv:nucl-th/0104087.

[106] V. Koch, *K^- - proton scattering and the $\Lambda(1405)$ in dense matter*, *Phys. Lett. B* **337** (1994) 7–13, arXiv:nucl-th/9406030.

[107] T. Waas, N. Kaiser, and W. Weise, *Low-energy anti-K N interaction in nuclear matter*, *Phys. Lett. B* **365** (1996) 12–16.

[108] T. Waas, N. Kaiser, and W. Weise, *Effective kaon masses in dense nuclear and neutron matter*,

Phys. Lett. B **379** (1996) 34–38.

[109] T. Waas and W. Weise, *S wave interactions of anti-K and eta mesons in nuclear matter*, *Nucl. Phys. A* **625** (1997) 287–306.

[110] J. Schaffner, J. Bondorf, and I. N. Mishustin, *In-medium production of kaons at the mean field level*, *Nucl. Phys. A* **625** (1997) 325–346, arXiv:nucl-th/9607058.

[111] A. Ohnishi, Y. Nara, and V. Koch, *Branching ratio change in K^- absorption at rest and the nature of the $\Lambda(1405)$*, *Phys. Rev. C* **56** (1997) 2767–2773, arXiv:nucl-th/9706084.

[112] M. Lutz, *Nuclear kaon dynamics*, *Phys. Lett. B* **426** (1998) 12–20, arXiv:nucl-th/9709073.

[113] K. Tsushima, K. Saito, A. W. Thomas, and S. V. Wright, *In-medium kaon and antikaon properties in the quark meson coupling model*, *Phys. Lett. B* **429** (1998) 239–246, arXiv:nucl-th/9712044. [Erratum: Phys.Lett.B 436, 453–453 (1998)].

[114] A. Sibirtsev and W. Cassing, *Anti-kaon production in proton nucleus reactions and the K-properties in nuclear matter*, *Nucl. Phys. A* **641** (1998) 476–498, arXiv:nucl-th/9805021.

[115] A. Ramos and E. Oset, *The Properties of anti-K in the nuclear medium*, *Nucl. Phys. A* **671** (2000) 481–502, arXiv:nucl-th/9906016.

[116] S. Hirenzaki, Y. Okumura, H. Toki, E. Oset, and A. Ramos, *Chiral unitary model for the kaonic atom*, *Phys. Rev. C* **61** (2000) 055205.

[117] A. Baca, C. Garcia-Recio, and J. Nieves, *Deeply bound levels in kaonic atoms*, *Nucl. Phys. A* **673** (2000) 335–353, arXiv:nucl-th/0001060.

[118] L. Tolos, A. Ramos, A. Polls, and T. T. S. Kuo, *Partial wave contributions to the anti-kaon potential at finite momentum*, *Nucl. Phys. A* **690** (2001) 547–566, arXiv:nucl-th/0007042.

[119] L. Tolos, A. Ramos, and A. Polls, *The Anti-kaon nuclear potential in hot and dense matter*, *Phys. Rev. C* **65** (2002) 054907, arXiv:nucl-th/0202057.

[120] C. L. Korpa and M. F. M. Lutz, *Kaon and antikaon properties in cold nuclear medium*, *Acta Phys. Hung. A* **22** (2005) 21–28, arXiv:nucl-th/0404088.

[121] L. Tolos, A. Ramos, and E. Oset, *Chiral approach to antikaon s and p-wave interactions in dense nuclear matter*, *Phys. Rev. C* **74** (2006) 015203, arXiv:nucl-th/0603033.

[122] J. Yamagata and S. Hirenzaki, *Kaon absorption from kaonic atoms and formation spectra of kaonic nuclei*, *Eur. Phys. J. A* **31** (2007) 255–262, arXiv:nucl-th/0612036.

[123] L. Tolos, D. Cabrera, and A. Ramos, *Strange mesons in nuclear matter at finite temperature*, *Phys. Rev. C* **78** (2008) 045205, arXiv:0807.2947 [nucl-th].

[124] W. Weise and R. Hartle, *Chiral SU(3) Dynamics and Antikaon-Nuclear quasibound States*, *Nucl. Phys. A* **804** (2008) 173–185, arXiv:0801.1467 [nucl-th].

[125] A. Cieply, E. Friedman, A. Gal, D. Gazda, and J. Mares, *K^- nuclear potentials from in-medium chirally motivated models*, *Phys. Rev. C* **84** (2011) 045206, arXiv:1108.1745 [nucl-th].

[126] T. Sekihara, J. Yamagata-Sekihara, D. Jido, Y. Kanada-En'yo, J. Yamagata-Sekihara, D. Jido, and Y. Kanada-En'yo, *Branching ratios of mesonic and nonmesonic antikaon absorptions in nuclear medium*, *Phys. Rev. C* **86** (2012) 065205, arXiv:1204.3978 [nucl-th].

[127] J. Yamagata-Sekihara, N. Ikeno, H. Nagahiro, D. Jido, and S. Hirenzaki, *Nuclear density probed by anti-kaon-nucleus systems and anti-kaon-nucleus interaction*, *Nucl. Phys. A* **914**

(2013) 344–348, arXiv:1212.3383 [nucl-th].

[128] E. Friedman and A. Gal, *K^-N amplitudes below threshold constrained by multinucleon absorption*, *Nucl. Phys. A* **959** (2017) 66–82, arXiv:1610.04004 [nucl-th].

[129] J. Yamagata, H. Nagahiro, Y. Okumura, and S. Hirenzaki, *Formation of kaonic atoms and kaonic nuclei by in-flight (K-,p) reactions*, *Prog. Theor. Phys.* **114** (2005) 301–316, arXiv:nucl-th/0503039. [Erratum: Prog.Theor.Phys. 114, 905–905 (2005)].

[130] **J-PARC E15** Collaboration, S. Ajimura *et al.*, *"K^-pp", a $\overline{K}$-Meson Nuclear Bound State, Observed in $^3He(K^-,\Lambda p)n$ Reactions*, *Phys. Lett. B* **789** (2019) 620–625, arXiv:1805.12275 [nucl-ex].

[131] R. H. Dalitz, T. C. Wong, and G. Rajasekaran, *Model calculation for Y*(0) (1405) resonance state*, *Phys. Rev.* **153** (1967) 1617–1623.

[132] K. Hashimoto, *K^+N PHASE SHIFTS FROM 600-MEV/C TO 1500-MEV/C*, *Phys. Rev. C* **29** (1984) 1377–1395.

[133] S. Scherer and M. R. Schindler, *A Primer for Chiral Perturbation Theory*, vol. 830. 2012.

[134] A. Pich, *Chiral perturbation theory*, *Rept. Prog. Phys.* **58** (1995) 563–610, arXiv:hep-ph/9502366.

[135] B. Kubis, *An Introduction to chiral perturbation theory*, in *Workshop on Physics and Astrophysics of Hadrons and Hadronic Matter*. 3, 2007. arXiv:hep-ph/0703274.

[136] G. Ecker, *Chiral perturbation theory*, *Prog. Part. Nucl. Phys.* **35** (1995) 1–80, arXiv:hep-ph/9501357.

[137] V. Bernard, N. Kaiser, and U.-G. Meissner, *Chiral dynamics in nucleons and nuclei*, *Int. J. Mod. Phys. E* **4** (1995) 193–346, arXiv:hep-ph/9501384.

[138] 青木健児, カイラル摂動論による核子-K^+ 中間子散乱と核媒質中におけるカイラル対称性の部分的回復, Master's thesis, 首都大学東京, 2016. https://irdb.nii.ac.jp/00891/0000795007.

[139] S. Weinberg, *Phenomenological Lagrangians*, *Physica A* **96** (1979) 327–340.

[140] J. Gasser and H. Leutwyler, *Chiral Perturbation Theory to One Loop*, *Annals Phys.* **158** (1984) 142.

[141] J. Gasser and H. Leutwyler, *Chiral Perturbation Theory: Expansions in the Mass of the Strange Quark*, *Nucl. Phys. B* **250** (1985) 465–516.

[142] J. A. Oller, M. Verbeni, and J. Prades, *Meson-baryon effective chiral lagrangians to $\mathcal{O}(q^3)$*, *JHEP* **09** (2006) 079, arXiv:hep-ph/0608204.

[143] J. A. Oller, *Chiral Lagrangians at finite density*, *Phys. Rev. C* **65** (2002) 025204, arXiv:hep-ph/0101204.

[144] S. Goda and D. Jido, *Pion properties at finite nuclear density based on in-medium chiral perturbation theory*, *PTEP* **2014** (2014) 033D03, arXiv:1312.0832 [nucl-th].

[145] H. C. Schroder *et al.*, *The pion nucleon scattering lengths from pionic hydrogen and deuterium*, *Eur. Phys. J. C* **21** (2001) 473–488.

[146] 比連崎悟, **中間子原子の物理**. 共立出版, 2017.

[147] T. B. Day and G. A. Snow, *Possible Explanation of Hyperfragment Suppression in K^-d Reactions*, *Phys. Rev. Lett.* **2** (Jan, 1959) 59–61.

[148] R. Machleidt, *The High precision, charge dependent Bonn nucleon-nucleon potential*

(CD-Bonn), *Phys. Rev. C* **63** (2001) 024001, arXiv:nucl-th/0006014.

[149] SAID partial-wave analysis. Averable at `http://gwdac.phys.gwu.edu/`.

[150] K. Aoki. In private communication.

[151] M. A. Luty and M. J. White, *Decouplet contributions to hyperon axial vector form-factors*, *Phys. Lett. B* **319** (1993) 261–268, arXiv:hep-ph/9305203.

[152] W. Cameron *et al.*, *K^+p Elastic Scattering from 130-MeV/c to 755-MeV/c*, *Nucl. Phys. B* **78** (1974) 93–109.

[153] G. Giacomelli *et al.*, *Differential cross-sections for K^+n charge-exchange scattering in deuterium between 0.64 and 1.51 Gev/c*, *Nucl. Phys. B* **42** (1972) 437–444.

[154] C. J. S. Damerell *et al.*, *K^+n Elastic and Charge Exchange Scattering Between 430-MeV/c and 940-MeV/c*, *Nucl. Phys. B* **94** (1975) 374–412.

[155] D. V. Bugg *et al.*, *Kaon-Nucleon Total Cross Sections from 0.6 to 2.65 GeV/c*, *Phys. Rev.* **168** (1968) 1466–1475.

[156] T. Bowen, P. K. Caldwell, F. N. Dikmen, E. W. Jenkins, R. M. Kalbach, D. V. Petersen, and A. E. Pifer, *Kaon-nucleon total cross-sections from 0.36 to 0.72 Gev/c*, *Phys. Rev. D* **2** (1970) 2599–2608.

[157] C. J. Adams *et al.*, *K^+p elastic scattering between 432 and 939 MeV/c*, *Phys. Rev. D* **4** (1971) 2637–2641.

[158] T. Bowen, E. W. Jenkins, R. M. Kalbach, D. V. Petersen, A. E. Pifer, and P. K. Caldwell, *K^+p and K^+d total cross-sections in the momentum range 0.57-1.16 GeV/c*, *Phys. Rev. D* **7** (1973) 22–26.

[159] **BGRT** Collaboration, G. Giacomelli *et al.*, *Differential cross-sections for K^+n elastic scattering between 0.64 GeV/c and 1.51 GeV/c*, *Nucl. Phys. B* **56** (1973) 346–355.

[160] L. Geng, *Recent developments in SU(3) covariant baryon chiral perturbation theory*, *Front. Phys. (Beijing)* **8** (2013) 328–348, arXiv:1301.6815 [nucl-th].

[161] B. Kubis and U. G. Meissner, *Baryon form-factors in chiral perturbation theory*, *Eur. Phys. J. C* **18** (2001) 747–756, arXiv:hep-ph/0010283.

[162] M. Holmberg and S. Leupold, *The relativistic chiral Lagrangian for decuplet and octet baryons at next-to-leading order*, *Eur. Phys. J. A* **54** (2018) 103, arXiv:1802.05168 [hep-ph].

[163] C. W. De Jager, H. De Vries, and C. De Vries, *Nuclear charge and magnetization density distribution parameters from elastic electron scattering*, *Atom. Data Nucl. Data Tabl.* **14** (1974) 479–508. [Erratum: Atom.Data Nucl.Data Tabl. 16, 580–580 (1975)].

[164] H. De Vries, C. W. De Jager, and C. De Vries, *Nuclear charge and magnetization density distribution parameters from elastic electron scattering*, *Atom. Data Nucl. Data Tabl.* **36** (1987) 495–536.

[165] G. Backenstoss *et al.*, *Strong interaction shifts and widths in light kaonic atoms*, *Phys. Lett. B* **38** (1972) 181–187.

[166] C. J. Batty *et al.*, *MEASUREMENT OF STRONG INTERACTION EFFECTS IN KAONIC ATOMS*, *Nucl. Phys. A* **329** (1979) 407–428.

[167] P. D. Barnes *et al.*, *Measurement of kaonic x-rays from al, si, ni and cu*, *Nucl. Phys. A* **231** (1974) 477–492.

[168] S. Yasunaga, Y. Iizawa, D. Jido, and T. Ishikawa, "$K^- d \to \pi\Lambda N$ reaction for studying the ΛN interaction with in-flight kaons." in progress.

[169] S. Hirama, Y. Iizawa, and D. Jido in progress.

[170] J. Yamagata-Sekihara and S. Hirenzaki, "Theoretical aspect of kaonic atoms - Optical potential from J-PARC E62 -." Talk at International workshop on Hadron physics with kaon beam and related topics (https://kds.kek.jp/event/43204/contributions/220718/).

[171] **J-PARC E62** Collaboration, T. Hashimoto *et al.*, *Measurements of Strong-Interaction Effects in Kaonic-Helium Isotopes at Sub-eV Precision with X-Ray Microcalorimeters*, *Phys. Rev. Lett.* **128** (2022) 112503.

Appendix A

Convention

The metric in Minkowski space is defined by

$$g^{\mu\nu} = \begin{pmatrix} 1 & & & \\ & -1 & & \\ & & -1 & \\ & & & -1 \end{pmatrix}. \tag{A.1}$$

The inner product of four vectors $x^\mu = (x^0, \boldsymbol{x})$ and $y^\mu = (y^0, \boldsymbol{y})$ is

$$x \cdot y = xy = x^\mu y_\mu = x_0 y_0 - \boldsymbol{x} \cdot \boldsymbol{y}. \tag{A.2}$$

We utilize Dirac matrices in Dirac–Pauli representation:

$$\gamma^0 = \begin{pmatrix} I_2 & 0 \\ 0 & -I_2 \end{pmatrix}, \qquad \gamma^i = \begin{pmatrix} 0 & \sigma_i \\ -\sigma_i & 0 \end{pmatrix}, \qquad \gamma^5 = \begin{pmatrix} 0 & I_2 \\ I_2 & 0 \end{pmatrix}. \tag{A.3}$$

Dirac matrices satisfy

$$\{\gamma^\mu, \gamma^\nu\} = 2g^{\mu\nu} I_4, \qquad \{\gamma^\mu, \gamma^5\} = 0, \qquad (\gamma^5)^2 = I_4, \qquad (\gamma^\mu)^\dagger = \gamma^0 \gamma^\mu \gamma^0, \qquad (\gamma^5)^\dagger = \gamma^5. \tag{A.4}$$

Dirac spinors are given by

$$\begin{aligned} u(\boldsymbol{p}, s) &= \sqrt{E+M} \begin{pmatrix} \chi_s \\ \frac{\boldsymbol{\sigma}\cdot\boldsymbol{p}}{E+M}\chi_s \end{pmatrix}, \\ \bar{u}(\boldsymbol{p}, s) &= \sqrt{E+M} \begin{pmatrix} \chi_s^\dagger & -\chi_s^\dagger \frac{\boldsymbol{\sigma}\cdot\boldsymbol{p}}{E+M} \end{pmatrix} \end{aligned} \tag{A.5}$$

with the mass M, the four momentum $p^\mu = (E, \boldsymbol{p})$, the energy $E = \sqrt{\boldsymbol{p}^2 + M^2}$ and the spin indices s. The Pauli spinor χ_s is defined by

$$\chi_{s=1} = \begin{pmatrix} 1 \\ 0 \end{pmatrix}, \qquad \chi_{s=-1} = \begin{pmatrix} 0 \\ 1 \end{pmatrix} \tag{A.6}$$

with the orthonormal and completeness conditions:

$$\chi_s^\dagger \chi_{s'} = \delta_{ss'}, \qquad \sum_s \chi_s \chi_s^\dagger = \begin{pmatrix} 1 & 0 \\ 0 & 1 \end{pmatrix}. \tag{A.7}$$

The Dirac spinor satisfies the Dirac equation:

$$(\not{p} - M) u(\boldsymbol{p}, s) = 0, \qquad \bar{u}(\boldsymbol{p}, s)(\not{p} - M) = 0 \tag{A.8}$$

The normalization of the Dirac spinor is

$$\bar{u}(\boldsymbol{p},s')u(\boldsymbol{p},s) = (E+M)\chi_s^\dagger\left(1-\frac{(\boldsymbol{\sigma}\cdot\boldsymbol{p})(\boldsymbol{\sigma}\cdot\boldsymbol{p})}{(E+M)^2}\right)\chi_r$$
$$= 2M\delta_{s's}, \tag{A.9}$$
$$u^\dagger(\boldsymbol{p},s')u(\boldsymbol{p},s) = 2E\delta_{s's}. \tag{A.10}$$

If we take the form of T-matrix as

$$T = \bar{u}(\boldsymbol{p}',s')\left[A+\frac{1}{2}(\not{k}+\not{k}')B\right]u(\boldsymbol{p},s), \tag{A.11}$$

the T-matrix can be written using Eq. (A.5) as

$$\begin{aligned}
T &= \bar{u}(\boldsymbol{p}',s')[A+\not{k}B]u(\boldsymbol{p},s)\\
&= \chi_{s'}^\dagger\left[(E+M)\left(A+B\omega+\frac{k_{\rm cm}^2B(1+\cos\theta)}{E+M}-\frac{k_{\rm cm}^2\cos\theta}{(E+M)^2}(A-B\omega)\right.\right.\\
&+ \left.\left. i\boldsymbol{\sigma}\cdot\boldsymbol{n}\;k_{\rm cm}^2\sin\theta\left(B-\frac{A-B\omega}{E+M}\right)\right)\right]\chi_s\\
&= \chi_{s'}^\dagger\left[(E+M)(A+B\omega)+k_{\rm cm}^2B+\frac{(E+M+\omega)B-A}{E+M}k_{\rm cm}^2\cos\theta\right.\\
&+ \left. i\boldsymbol{\sigma}\cdot\boldsymbol{n}\;\frac{(E+M+\omega)B-A}{E+M}k_{\rm cm}^2\sin\theta\right]\chi_s
\end{aligned} \tag{A.12}$$

where $\boldsymbol{n} = (\boldsymbol{k}'\times\boldsymbol{k})/|\boldsymbol{k}'\times\boldsymbol{k}|$. Here we use

$$\bar{u}(\boldsymbol{p}',s')u(\boldsymbol{p},s) = (E+M)\left(1-\frac{(\boldsymbol{\sigma}\cdot\boldsymbol{p}')(\boldsymbol{\sigma}\cdot\boldsymbol{p})}{(E+M)^2}\right)\delta_{s's} = (E+M)\left(1-\frac{\boldsymbol{p}'\cdot\boldsymbol{p}+i\boldsymbol{\sigma}\cdot(\boldsymbol{p}'\times\boldsymbol{p})}{(E+M)^2}\right)\delta_{s's}, \tag{A.13}$$

$$\bar{u}(\boldsymbol{p}',s')\gamma^0u(\boldsymbol{p},s) = (E+M)\left(1+\frac{(\boldsymbol{\sigma}\cdot\boldsymbol{p}')(\boldsymbol{\sigma}\cdot\boldsymbol{p})}{(E+M)^2}\right)\delta_{s's} = (E+M)\left(1+\frac{\boldsymbol{p}'\cdot\boldsymbol{p}+i\boldsymbol{\sigma}\cdot(\boldsymbol{p}'\times\boldsymbol{p})}{(E+M)^2}\right)\delta_{s's}, \tag{A.14}$$

$$\bar{u}(\boldsymbol{p}',s')\gamma^iu(\boldsymbol{p},s) = (E+M)\left(\frac{\boldsymbol{\sigma}\cdot\boldsymbol{p}'\sigma^i}{E+M}+\frac{\sigma^i\boldsymbol{\sigma}\cdot\boldsymbol{p}}{E+M}\right)\delta_{s's} = \left(p^{i'}+p^i-i\boldsymbol{p}'\times\boldsymbol{\sigma}+i\boldsymbol{p}\times\boldsymbol{\sigma}\right)\delta_{s's}. \tag{A.15}$$

Then we have the form of the T-matrix as

$$T = \chi_{s'}^\dagger[f-i(\boldsymbol{\sigma}\cdot\hat{\boldsymbol{n}})g]\chi_s \tag{A.16}$$
$$f = (E+M)(A+B\omega)+k_{\rm cm}^2B+\frac{(E+M+\omega)B-A}{E+M}k_{\rm cm}^2\cos\theta \tag{A.17}$$
$$g = -\frac{(E+M+\omega)B-A}{E+M}k_{\rm cm}^2\sin\theta. \tag{A.18}$$

For the calculation of the cross section, we need to consider spin summation. We should take an average over the degrees of freedom for the initial state and sum over the degrees of freedom for the final state. If we take the form of T-matrix as $T = \chi_{s'}^\dagger T'\chi_s$, then the differential cross section is

calculated as

$$\begin{aligned}\frac{\mathrm{d}\sigma}{\mathrm{d}\Omega} &= \frac{1}{64\pi^2 s}\frac{1}{2}\sum_{s'}\sum_{s}|T|^2 \\ &= \frac{1}{64\pi^2 s}\frac{1}{2}\sum_{s'}\sum_{s}|\chi^{\dagger}_{s'}\chi_s|^2|T'|^2 \\ &= \frac{1}{64\pi^2 s}\frac{1}{2}\sum_{s'}\sum_{s}|\delta_{s's}|^2|T'|^2 \\ &= \frac{1}{64\pi^2 s}|T'|^2. \end{aligned} \tag{A.19}$$

Appendix B

Loop integral

For the calculation of the $K^- d$ scattering amplitude, we need to calculate the following loop integral:

$$I \equiv -\int \frac{\mathrm{d}^3 q}{(2\pi)^3} \frac{1}{q^2+\mu^2} \frac{1}{(\boldsymbol{q}+\boldsymbol{Q})^2+M^2} \tag{B.1}$$

where $\mu = \sqrt{M_K^2 - q_0^2 - i\epsilon}$. The integral can be calculated as

$$I = -\frac{1}{2\pi^2} \int \mathrm{d}r\, r j_0(Qr) e^{-Mr} \int \mathrm{d}q\, \frac{q^2}{q^2+\mu^2} j_0(qr) \tag{B.2}$$

where j_n is the spherical Bessel function. For the integration with respect to q, we use

$$\int \mathrm{d}q\, \frac{q^2}{q^2+\mu^2} j_0(qr) = \frac{\pi}{2} \frac{e^{-\mu r}}{r}. \tag{B.3}$$

Then we have

$$\begin{aligned} I &= -\frac{1}{2\pi^2} \int \mathrm{d}r\, r j_0(Qr) e^{-Mr} \frac{\pi}{2} \frac{e^{-\mu r}}{r} \\ &= -\frac{1}{4\pi} \int \mathrm{d}r\, j_0(Qr) e^{-(M+\mu)r} \\ &= \frac{i}{8\pi Q} \ln\left(\frac{M+\mu+iQ}{M+\mu-iQ}\right). \end{aligned} \tag{B.4}$$

For $\mu^2 \geqq 0$:

$$\mathrm{Re}\, I = -\frac{i}{4\pi Q} \arctan\left(\frac{Q}{M+\mu}\right), \tag{B.5}$$

$$\mathrm{Im}\, I = 0. \tag{B.6}$$

For $\mu^2 \leq 0$:

$$\mathrm{Re}\, I = -\frac{i}{8\pi Q} \left(\arctan\left(\frac{Q-|\mu|}{M}\right) + \arctan\left(\frac{Q+|\mu|}{M}\right)\right), \tag{B.7}$$

$$\mathrm{Im}\, I = \frac{1}{16\pi Q} \ln\left(\frac{M^2+(Q^2-|\mu|^2)}{M^2+(Q^2+|\mu|^2)}\right). \tag{B.8}$$

This calculation used for Section 5.3.

Appendix C

Legendre polynomials

We use Legendre polynomial $P_\ell(x)$ and its derivative $P'_\ell(x)$ to perform the partial wave decomposition in Chapter 6. The first few Legendre polynomials we use are

$$P_0(x) = 1 \tag{C.1}$$
$$P_1(x) = x \tag{C.2}$$
$$P_2(x) = \frac{1}{2}\big(3x^2 - 1\big) \tag{C.3}$$
$$P_3(x) = \frac{1}{2}\big(5x^3 - 3x\big) \tag{C.4}$$
$$P_4(x) = \frac{1}{8}\big(35x^4 - 30x^2 + 3\big) \tag{C.5}$$
$$P_5(x) = \frac{1}{8}\big(63x^5 - 70x^3 + 15x\big). \tag{C.6}$$

The orthonormal relations for the Legendre polynomial and its derivative are given by

$$\int_{-1}^{1} P_\ell(x) P_{\ell'}(x)\,\mathrm{d}x = \frac{2}{2\ell+1}\delta_{\ell\ell'}, \tag{C.7}$$
$$\int_{-1}^{1} (1-x^2) P'_\ell(x) P'_{\ell'}(x)\,\mathrm{d}x = \frac{2}{2\ell+1}\ell(\ell+1)\delta_{\ell\ell'}, \tag{C.8}$$

respectively.

Appendix D

Vertices of meson-baryon Lagrangian related to the chiral condensate

For the meson-baryon amplitude T_{MB} related to the chiral condensate, we need these vertices:

$$[i\mathcal{L}_{\bar{p}p\pi^0\pi^0}] = -\frac{4iB_0m(2b_0+b_D+b_F)}{F_\pi^2} \tag{D.1a}$$

$$[i\mathcal{L}_{\bar{n}n\pi^0\pi^0}] = -\frac{4iB_0m(2b_0+b_D+b_F)}{F_\pi^2} \tag{D.1b}$$

$$[i\mathcal{L}_{\bar{\Lambda}\Lambda\pi^0\pi^0}] = -\frac{8iB_0m(3b_0+b_D)}{3F_\pi^2} \tag{D.1c}$$

$$[i\mathcal{L}_{\bar{\Sigma}^+\Sigma^+\pi^0\pi^0}] = -\frac{8iB_0m(b_0+b_D)}{F_\pi^2} \tag{D.1d}$$

$$[i\mathcal{L}_{\bar{\Sigma}^-\Sigma^-\pi^0\pi^0}] = -\frac{8iB_0m(b_0+b_D)}{F_\pi^2} \tag{D.1e}$$

$$[i\mathcal{L}_{\bar{\Sigma}^0\Sigma^0\pi^0\pi^0}] = -\frac{8iB_0m(b_0+b_D)}{F_\pi^2} \tag{D.1f}$$

$$[i\mathcal{L}_{\bar{\Xi}^0\Xi^0\pi^0\pi^0}] = -\frac{4iB_0m(2b_0+b_D-b_F)}{F_\pi^2} \tag{D.1g}$$

$$[i\mathcal{L}_{\bar{\Xi}^-\Xi^-\pi^0\pi^0}] = -\frac{4iB_0m(2b_0+b_D-b_F)}{F_\pi^2} \tag{D.1h}$$

$$[i\mathcal{L}_{\bar{p}pK^+K^-}] = -\frac{4iB_0(m+m_s)(b_0+b_D)}{F_K^2} \tag{D.2a}$$

$$[i\mathcal{L}_{\bar{n}nK^+K^-}] = -\frac{2iB_0(m+m_s)(2b_0+b_D-b_F)}{F_K^2} \tag{D.2b}$$

$$[i\mathcal{L}_{\bar{\Lambda}\Lambda K^+K^-}] = -\frac{2iB_0(m+m_s)(6b_0+5b_D)}{3F_K^2} \tag{D.2c}$$

$$[i\mathcal{L}_{\bar{\Sigma}^+\Sigma^+K^+K^-}] = -\frac{2iB_0(m+m_s)(2b_0+b_D+b_F)}{F_K^2} \tag{D.2d}$$

$$[i\mathcal{L}_{\bar{\Sigma}^-\Sigma^-K^+K^-}] = -\frac{2iB_0(m+m_s)(2b_0+b_D-b_F)}{F_K^2} \tag{D.2e}$$

$$[i\mathcal{L}_{\bar{\Sigma}^0\Sigma^0K^+K^-}] = -\frac{2iB_0(m+m_s)(2b_0+b_D)}{F_K^2} \tag{D.2f}$$

$$[i\mathcal{L}_{\bar{\Xi}^0\Xi^0K^+K^-}] = -\frac{2iB_0(m+m_s)(2b_0+b_D+b_F)}{F_K^2} \tag{D.2g}$$

$$[i\mathcal{L}_{\bar{\Xi}^-\Xi^-K^+K^-}] = -\frac{4iB_0(m+m_s)(b_0+b_D)}{F_K^2} \tag{D.2h}$$

$$[i\mathcal{L}_{\bar{p}pK^0\bar{K}^0}] = -\frac{2iB_0(m+m_s)(2b_0+b_D-b_F)}{F_K^2} \tag{D.2i}$$

$$[i\mathcal{L}_{\bar{n}nK^0\bar{K}^0}] = -\frac{4iB_0(m+m_s)(b_0+b_D)}{F_K^2} \tag{D.2j}$$

$$[i\mathcal{L}_{\bar{\Lambda}\Lambda K^0\bar{K}^0}] = -\frac{2iB_0(m+m_s)(6b_0+5b_D)}{3F_K^2} \tag{D.2k}$$

$$[i\mathcal{L}_{\bar{\Sigma}^+\Sigma^+K^0\bar{K}^0}] = -\frac{2iB_0(m+m_s)(2b_0+b_D-b_F)}{F_K^2} \tag{D.2l}$$

$$[i\mathcal{L}_{\bar{\Sigma}^0\Sigma^0K^0\bar{K}^0}] = -\frac{4iB_0(m+m_s)(b_0+b_D)}{F_K^2} \tag{D.2m}$$

$$[i\mathcal{L}_{\bar{\Sigma}^-\Sigma^-K^0\bar{K}^0}] = -\frac{2iB_0(m+m_s)(2b_0+b_D+b_F)}{F_K^2} \tag{D.2n}$$

$$[i\mathcal{L}_{\bar{\Xi}^0\Xi^0K^0\bar{K}^0}] = -\frac{4iB_0(m+m_s)(b_0+b_D)}{F_K^2} \tag{D.2o}$$

$$[i\mathcal{L}_{\bar{\Xi}^-\Xi^-K^0\bar{K}^0}] = -\frac{2iB_0(m+m_s)(2b_0+b_D+b_F)}{F_K^2} \tag{D.2p}$$

Appendix E

Isospin configuration

The physical meson and baryon fields are specified in terms of the magnitude of isospin and the third component of isospin and written as $|\Phi, U, I_3\rangle$ and $|B, U, I_3\rangle$, respectively. Isospin conventions for the hadrons with phase convention are given by

$$\left|\pi^+\right\rangle = -\left|\Phi, 1, 1\right\rangle, \quad \left|\pi^0\right\rangle = \left|\Phi, 1, 0\right\rangle, \quad \left|\pi^-\right\rangle = \left|\Phi, 1, -1\right\rangle, \tag{E.1}$$

$$\left|K^+\right\rangle = \left|\Phi, 1/2, 1/2\right\rangle, \quad \left|K^0\right\rangle = \left|\Phi, 1/2, -1/2\right\rangle, \quad \left|K^-\right\rangle = -\left|\Phi, 1/2, -1/2\right\rangle, \quad \left|\bar{K}\right\rangle = \left|\Phi, 1/2, 1/2\right\rangle, \tag{E.2}$$

$$|p\rangle = |B, 1/2, 1/2\rangle, \quad |n\rangle = |B, 1/2, -1/2\rangle, \tag{E.3}$$

$$|\Lambda\rangle = |B, 0, 0\rangle, \tag{E.4}$$

$$\left|\Sigma^+\right\rangle = -\left|B, 1, 1\right\rangle, \quad \left|\Sigma^0\right\rangle = \left|B, 1, 0\right\rangle, \quad \left|\Sigma^-\right\rangle = -\left|B, 1, -1\right\rangle \tag{E.5}$$

$$\left|\Xi^0\right\rangle = \left|B, 1/2, 1/2\right\rangle, \quad \left|\Xi^-\right\rangle = -\left|B, 1/2, -1/2\right\rangle. \tag{E.6}$$

The KN states are decomposed by the isospin basis:

$$\left|K^+p\right\rangle = |KN, 1, 1\rangle, \tag{E.7}$$

$$\left|K^+n\right\rangle = \frac{1}{\sqrt{2}}(|KN, 1, 0\rangle + |KN, 0, 0\rangle), \tag{E.8}$$

$$\left|K^0p\right\rangle = \frac{1}{\sqrt{2}}(|KN, 1, 0\rangle - |KN, 0, 0\rangle), \tag{E.9}$$

$$\left|K^0n\right\rangle = |KN, 1, -1\rangle. \tag{E.10}$$

Thus the T-matrix of the KN scattering are also decomposed by the T-matrix in isospin basis:

$$T_{K^+p} = \left\langle K^+p\right| T \left|K^+p\right\rangle = \langle KN, 1, 1| T |KN, 1, 1\rangle = T^{I=1}, \tag{E.11}$$

$$T_{K^+n} = \left\langle K^+n\right| T \left|K^+n\right\rangle = \frac{1}{\sqrt{2}}(\langle KN, 1, 0| + \langle KN, 0, 0|)T\frac{1}{\sqrt{2}}(|KN, 1, 0\rangle + |KN, 0, 0\rangle) = \frac{1}{2}(T^{I=1} + T^{I=0}), \tag{E.12}$$

$$T_{K^+n\to K^0p} = \left\langle K^0p\right| T \left|K^+n\right\rangle = \frac{1}{\sqrt{2}}(\langle KN, 1, 0| - \langle KN, 0, 0|)T\frac{1}{\sqrt{2}}(|KN, 1, 0\rangle + |KN, 0, 0\rangle) = \frac{1}{2}(T^{I=1} - T^{I=0}). \tag{E.13}$$

Isospin averaged amplitudes of the kaon-baryon scattering:

$$T_{KN}^{\text{ave}} = \frac{3T_{KN}^{I=1} + T_{KN}^{I=0}}{4}, \tag{E.14a}$$

$$T_{K\Lambda}^{\text{ave}} = T_{K\Lambda}^{I=1/2} \tag{E.14b}$$

$$T_{K\Sigma}^{\text{ave}} = \frac{4T_{K\Sigma}^{I=3/2} + 2T_{K\Sigma}^{I=1/2}}{6}, \tag{E.14c}$$

$$T_{K\Xi}^{\text{ave}} = \frac{3T_{K\Xi}^{I=1} + T_{K\Xi}^{I=0}}{4}. \tag{E.14d}$$

The kaon-SU(3) baryon amplitude:

$$T_{KB}^{\text{SU(3) ave}} = \frac{1}{8}[2T_{KN}^{\text{ave}} + T_{K\Lambda}^{\text{ave}} + 3T_{K\Sigma}^{\text{ave}} + 2T_{K\Xi}^{\text{ave}}]. \tag{E.15}$$